10-2015

Multiwavelength Imaging of Planetary Nebulae: Resolving & Disentangling Structure

Marcus J. Freeman
mjf6441@rit.edu

Multiwavelength Imaging of Planetary Nebulae: Resolving & Disentangling Structure

Marcus J. Freeman

A dissertation submitted in partial fulfillment of the requirements for the degree of

Ph.D. *in* Astrophysical Sciences and Technology

in the College of Science, School of Physics and Astronomy

Rochester Institute of Technology

October, 2015

Rochester Institute of Technology

Ph.D. Dissertation

Multiwavelength Imaging of Planetary Nebulae: Resolving & Disentangling Structure

---

Author:

Marcus J. Freeman

Advisor:

Dr. Joel H. Kastner

A dissertation submitted in partial fulfillment of the requirements

for the Degree of Doctor of Philosophy in Astrophysical Sciences and Technology

School of Physics and Astronomy

College of Science

Approved by _____

Prof. Andrew Robinson Date

Director, Astrophysical Sciences and Technology

Certificate of Approval

Astrophysical Sciences and Technologies

R·I·T | *College of* Science

Rochester, NY, USA

The Ph.D. Dissertation of Marcus J. Freeman has been approved
by the undersigned members of the dissertation committee as satisfactory for the degree of
Doctor of Philosophy in Astrophysical Sciences and Technology.

Dr. Jan van Aardt, Committee Chair	Date
Dr. Joel H. Kastner, Dissertation Adviser	Date
Dr. Andrew Robinson	Date
Dr. Adam Frank	Date

For my parents, Tracey McGrail and Jerry Freeman

Per ardua ad astra (Through adversity to the stars)

ABSTRACT

Planetary nebulae (PNe) represent the late stages of low-mass stellar evolution. The formation of the myriad of PNe morphologies involves processes that are present in many other astrophysical systems such as the wind-blown bubbles of massive stars. In this dissertation we present the results of an X-ray study of PNe, and two modeling projects that incorporate the resulting data with the goal of furthering our understanding of their X-ray properties and morphologies, and the 3D multiwavelength structure of PNe. This work expands the *Chandra* Planetary Nebula Survey (ChanPlaNS), which was designed to investigate X-ray emission from PNe, from 35 to 59 objects. The results from Cycle 14 Chandra observations of 24 PNe brought the overall ChanPlaNS diffuse X-ray detection rate to $\sim$ 27% and the point source detection rate to $\sim$ 36%. The detection of diffuse X-ray emission is unmistakably associated with young ($\lesssim 5 \times 10^3$ yr), compact ($R_{\rm neb} \lesssim 0.15$ pc) PNe that exhibit closed elliptical structures and high electron densities ($n_e \gtrsim 10^3$ cm^{-3}). Utilizing the ChanPlaNS data for 14 PNe that exhibit diffuse X-ray emission, we constructed simple, spherically symmetric two-phase models using the astrophysical modeling tool, *SHAPE*. Our models consisted of a hot bubble and swept-up shell with the intent of investigating the X-ray morphology of these objects and the extinction caused by the swept-up shell. We compared simulated and observed radial profiles and we conclude that while most ($\sim$ 79%) PNe are best described by a limb-darkened X-ray morphology, this is due to nebular extinction of an intrinsically limb-brightened hot bubble structure. Expanding upon our two-phase model, we used *SHAPE* to generate a 3D model of the brightest diffuse X-ray PN, BD+30°3639, with the model constrained by previously published multiwavelength data extending from the radio to the X-ray regimes. Our aim was to investigate the multiwavelength 3D morphology of this well-studied nebula and draw connections with other PNe. We interpreted kinematic and observational data to best fit our model with observations and found that the inherent structure shares similarities with several other PNe, suggesting a common evolutionary path.

CONTENTS

DECLARATION

I, MARCUS J. FREEMAN ("the Author"), declare that no part of this dissertation is substantially the same as any that has been submitted for a degree or diploma at the Rochester Institute of Technology or any other University. I further declare that this work is my own. Those who have contributed scientific or other collaborative insights are fully credited in this dissertation, and all prior work upon which this dissertation builds is cited appropriately throughout the text. This dissertation was successfully defended in Rochester, NY, USA on ...

Modified portions of this dissertation have previously been published by the Author in peer-reviewed papers appearing in *The Astrophysical Journal* (ApJ):

- **Chapter 3** is based on the paper Freeman et al. (2014), entitled *The Chandra Planetary Nebula Survey (CHANPLANS). II. X-Ray Emission from Compact Planetary Nebulae* (2014, ApJ, 794, 99), co-authored by Roldolfo Montez, Jr., Joel H. Kastner (the Dissertation adviser), and the ChanPlaNS Collaboration.

ACKNOWLEDGEMENTS

As with any great project, it is impossible to conquer anything alone. I'd like to acknowledge NASA, *Chandra* X-ray Center, the Laboratory for Multiwavelength Astrophysics, and the Astrophysical Sciences and Technology program at RIT for providing me with funding for this project. I would also like to thank my advisor, Joel Kastner, who never lost faith in me throughout my various projects, and always managed to find time to work through whatever problems came up.

My parents, Tracey McGrail, Jerry Freeman, and Donna Funteral, were my greatest supporters throughout my dissertation. Without them I would have never made it this far, nor would I have endeavored to become the man I am today. They serve as my inspiration and my greatest cheerleaders. I am also extremely thankful for all of my friends who supported me through my time at RIT. Whether it were my fellow graduate students or my longtime friends, they all managed to help me in one way or another throughout my graduate student career. Last, but most definitely not least, I would like to acknowledge Triana Almeyda, for her tireless support and understanding.

LIST OF PUBLISHED WORK

1. *The Chandra Planetary Nebula Survey (CHANPLANS). II. X-Ray Emission from Compact Planetary Nebulae.*
   Marcus J. Freeman, Rodolfo Montez, Jr., Joel H. Kastner, and the ChanPlaNS Collaboration (2014, ApJ, 794, 99).

LIST OF TABLES

LIST OF FIGURES

CHAPTER 1

INTRODUCTION TO PLANETARY NEBULAE

1.1 Planetary Nebulae

As the near-end stages of intermediate mass (∼1-8 $M_\odot$) stars, planetary nebulae (PNe) serve as windows into the evolution and the chemical enrichment of the universe. Throughout the progenitor star's journey up the asymptotic giant branch (AGB), it continuously sheds mass at rates from $\sim 10^{-7}$ to 10^{-5} $M_\odot$ yr^{-1} through a dusty, molecule-rich stellar wind ($v_w \sim 10 - 30$ km s^{-1}). Once helium has been exhausted in the core of the AGB star, it sheds its tenuous outer layers, revealing the compact core. The fast wind ($v_w \simeq$ 500-1500 km s^{-1}) of the central star collides with the previously ejected AGB wind, compressing it into a shell. As the newly revealed core evolves towards a white dwarf (WD), the effective temperature of its observable photosphere increases, and when its temperature passes 30 kK its UV radiation becomes strong enough to ionize the surrounding material, creating the PN that we are familiar with. The nebula continues to expand at a rate of $\sim$ 40 km s^{-1} and remains visible for 1-3$\times 10^4$ years before it begins to fade as the central star cools (Jacob et al., 2013).

Models of the formation of PNe (Kwok et al., 1978; Schmidt-Voigt & Koppen, 1987; Marten & Schönberner, 1991; Villaver et al., 2002; Perinotto et al., 2004; Toalá & Arthur, 2014) assert that

Figure 1.1: False color images of planetary nebulae. These nebulae represent a medley of morphologies from round to highly bipolar. Top row, left to right: Abell 39 (WIYN/NOAO/NSF), IC 418 (NASA/ESA/STScI/AURA/R. Sahai), and NGC 2392 (Eskimo Nebula; NASA/ESA/STScI). Middle row, left to right: NGC 6720 (Helix Nebula; NASA/ESA/R. O'Dell), NGC 6543 (Cat's Eye Nebula; NASA/ESA/HEIC/STScI/AURA), and NGC 7009 (NASA/ESA/B. Balick et al.). Bottom row, left to right: NGC 5189 (NASA/ESA/STScI/AURA), NGC 7027 (NASA/ESA), and Hb 5 (HST/NASA/B. Balick).

their structure is strongly impacted by interacting stellar winds (ISW). From the assumption of isotropic winds in these models, we expect PNe to be spherical, but in actuality, spherical nebulae are the exception and not the rule (De Marco, 2009). *Hubble Space Telescope (HST)* observations of a variety of PNe have revealed that the structures of PNe are not so simple, as seen in Fig. 1.1. The shapes of PNe range from multiple-shelled ellipsoids to tight-waisted bipolar structures with large lobes, and still others that feature multipolar outflows and extremely asymmetrical structures. The menagerie of PNe optical emission line morphologies demonstrates that the formation of PNe is far more complicated than the original ISW model predicts. A modified model from Kahn & West (1985) included an aspherical mass distribution to account for axisymmetric and bipolar nebulae. This generalized interacting stellar winds (GISW) theory turned out to also conflict with observations and became a subject of controversy (Balick & Frank, 2002).

More advanced modeling coupled with better observations has since provided a better understanding of the physical structures of PNe, and opened up the field of shaping mechanisms from winds to jets, disks, and the most popular hypothesis, binaries (Frank et al., 1993). PNe remain a confounding set of objects that require further investigation. There are plenty of mysteries yet to solve, such as the role of the central stellar engine and binary companions in shaping the overall 3-dimensional structure and whether or not there exists a common evolutionary model as proposed by the ISW.

1.2 Distance

We know of over 3400 PNe in the Milky Way, but given the density of PNe in the solar neighborhood (~ 50 kpc^{-3}; Cahn & Amd, 1978; Frew, 2008), we expect the true number to be much higher. The detection of PNe is largely driven by optical observations of emission lines like [O III] or Hα, which are heavily obscured and absorbed toward the Galactic Center and the Galactic Disk, making it difficult to find such objects there. For the known PNe, this obscuration by interstellar material (ISM) also makes determining the intrinsic physical parameters of these objects problematic. This

is compounded with a lack of well constrained distance measurements to PNe.

Currently, primary distance measurements that have uncertainties $< 10\%$ only exist for less than one percent of all of the observed Galactic PNe (Frew et al., 2015). This results in the calculation of distances to most PNe based on statistical measurements, and depending on the method can result in varying distances from one paper to the next (Golovatyi & Demchyna, 2014; Zijlstra, 2015; Frew et al., 2015). A variety of approaches have been proposed to determine PNe distances based on a plethora of different assumptions. For example, the Shklovsky method assumed a constant ionized mass for the PN shell (Minkowski & Aller, 1954; Shklovsky, 1956), which then could be used in conjunction with mean density estimates from [O II] or [S II] observations. This proves to be problematic given that the ionized mass within a PN is not constant throughout its lifetime, resulting in over and underestimates for young and old PNe respectively.

Alternatively, assuming a variable mass, the optical thickness of the nebula can be related to the total ionized mass. The optical thickness is inferred from the 5 GHz radio density and then related to the mass, which can be related to the size (Daub, 1982). This same method was tweaked to assume a continuous function of linear radius and use the surface brightness (Maciel & Pottasch, 1980; Pottasch, 1980), or the brightness temperature to estimate the distance (Zhang, 1995; Phillips, 2002, 2004a).

Another method examined PNe that were evolving with constant luminosity and were expected to have similar absolute bolometric magnitudes, and similar central stars with masses close to 0.6 $M_{\odot}$. With the star's mass and a determination of the stellar temperature, the absolute magnitude could be calculated and compared with the apparent magnitude from observations, leading to a distance measurement (Phillips, 2005). Still others made more specific assumptions, such as the angular size of the waist of all Type I bipolar PNe are the same, or use the angular diameter of the He II Strömgren zone (Phillips, 2004b). The latter method can only be applied to optically thick PNe.

The vast array of distance determinations has led to an equally vast list of physical parameters for many nebulae that do not necessarily agree with one another. With the help of astrometry from

Gaia, we will be able to obtain primary distance measurements to many of the Galactic PNe. More accurate distance measurements will lead to better calibrated physical parameters such as radius, mass, luminosity, age of the nebulae, luminosity and mass of the central stars of the PN (CSPNe), and PNe distribution. These parameters are essential for understanding the evolution of PNe, as well as the evolution of the galaxies they reside in. For the purposes of this dissertation, we assume distances determined via the Hα surface brightness - radius ($S_{\mathrm{H}\alpha}$-r) relation which makes use of the Hα flux, angular size, and reddening toward the PNe to determine the distance (Frew et al., 2015). Specifically, we assume distance values from Frew (2008).

1.3 Low-Mass Stellar Evolution

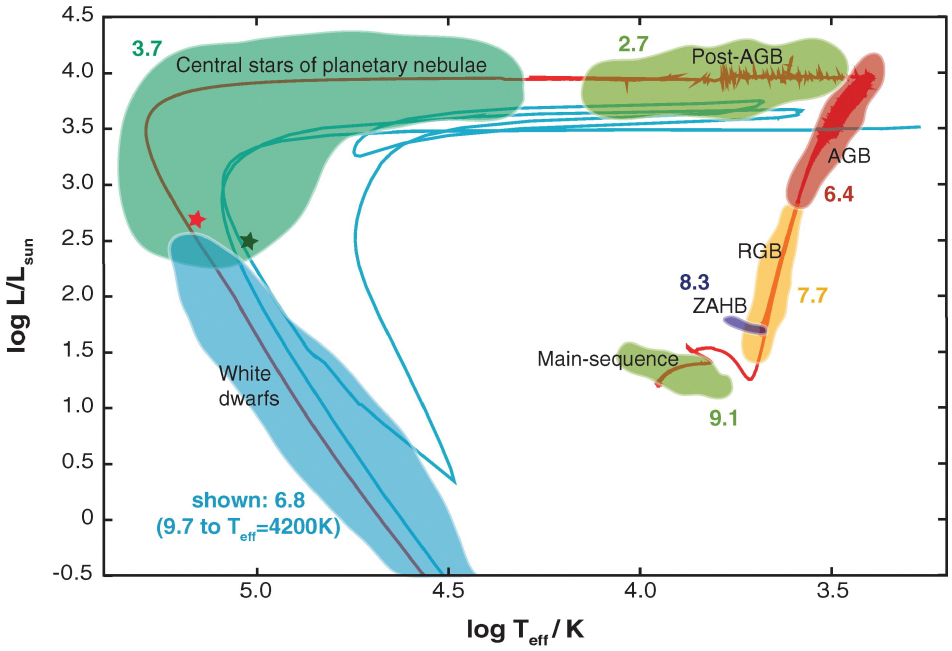

Figure 1.2: Schematic Hertzsprung-Russell (HR) diagram illustrating low mass star evolution from the main sequence to becoming a white dwarf, from (Herwig, 2005).

For massive stars (>8 $M_{\odot}$), the final stages of their evolution results in a violent eruption in the form of a supernova, leaving behind a neutron star or black hole. Less massive stars (1-8 $M_{\odot}$)

will evolve to become PNe through less explosive means, with the central star eventually becoming a white dwarf. Most of the star's life is spent on the main sequence where it burns hydrogen (Fig. 1.2). Low mass stars spend the bulk of their lives here (1-10 Gyr) burning hydrogen in the core, which keeps the star in hydrostatic equilibrium, where radiation pressure outward from the fusion process balances the inward gravitational pressure.

The star eventually ceases hydrogen fusion in its core, resulting in gravitational collapse which contracts the core and heats it up. Hydrogen continues burning in a shell around the helium core and radiation pressure begins to drive the stellar envelope outward, cooling the star and making it redder and brighter. This stage marks the beginning of the red giant phase. As hydrogen burning continues, more helium is deposited into the core, and contraction continues, leading to rising core temperatures. Eventually the core heats to 10^8 K and begins to fuse helium via the Triple-α process.

The ignition of this core burning process is called the Helium Flash, and marks the end of the red giant phase as the star begins to get hotter and bluer, moving horizontally across the HR diagram (Fig. 1.2). Both hydrogen and helium burning continue, building up carbon and oxygen in the core. Once all of the helium is spent in the core, fusion ceases again and there is nothing to balance against gravitational pressure, resulting in another phase of of core collapse. As the core collapses it heats up, however the core temperature is never high enough to ignite carbon fusion, resulting in a degenerate core of carbon and oxygen. Surrounding this core is a shell of helium and another shell of hydrogen. This is where the star begins to ascend the asymptotic giant branch (AGB), which marks the crucial final stage before the creation of the PN (Herwig, 2005).

1.3.1 Stellar Winds

Burning continues on the hydrogen shell as the core contracts, and helium burning occurs periodically on the underlying shell, resulting in smaller helium flashes. These flashes can also dredge up the products of previous helium burning, such as carbon, nitrogen, and oxygen, and inject them into the stellar envelope. The outer edges of the stellar envelope are cool enough to form dust which is efficiently driven away from the star by the radiation pressure from hydrogen

and helium burning. The dust transfers momentum to the enriched gas and carries it away in a wind which has a speed on the order of 10s of km s^{-1} and at the upper part of the AGB leads to mass loss rates up to $M_\odot$ yr^{-1}. The star loses a significant fraction of its mass this way, up to 80%, leading to the loss of the stellar envelope and the end of the AGB phase.

The central core continues to contract under gravitational pressure and increase in temperature as it evolves towards becoming a WD. With the increase in temperature comes an increase in UV radiation, which penetrates into the AGB wind, ionizing the ejecta and creating the PN. As the radius of the central star decreases, the escape velocity increases, resulting in a faster stellar wind, with velocities ranging from 500 to 1500 km s^{-1}. The region closest to the central star is dominated by the unencumbered, fast wind. This wind plows into the previously ejected material in the slower AGB wind, compressing it and forming it into a thin shell. The collision of the fast wind with the AGB ejecta results in shocks that heat the fast wind gas to temperatures $> 10^6$ K, forming a "hot bubble" capable of producing soft X-rays ($0.3 \sim 1$ keV). The hot bubble and swept-up shell are separated by a contact discontinuity, across which heat conduction can occur, which may be responsible for lowering the temperature of the hot bubble from predicted values of $\sim 10^7$ K to observed values of $\sim 10^6$ (Steffen et al., 2008; Toalá & Arthur, 2014).

The pressure from the hot bubble and the fast wind expand the PN at a rate of $\sim$ 40 km s^{-1} (Jacob et al., 2013). As the nebula expands the central star continues to heat up, towards temperatures of $\sim$ 100 kK. Once the star can no longer contract it begins to cool down and becomes a WD. At this time, the PN has expanded and become more diffuse, becoming optically thin to UV radiation, and eventually fades away.

1.3.2 Wolf-Rayet Type Stars

There exists a subclass of central stars of PNe that are H-deficient and exhibit fast stellar winds ($v_w \gtrsim 10^3$ km s^{-1}) that result in high mass-loss rates ($\gtrsim 10^{-6}$ $M_\odot$ yr^{-1}). Typically this subclass of star has strong emission lines from the products of helium burning (C, N, and O), which makes their spectra similar to a class of massive stars known as Wolf-Rayet (WR) stars. This subclass of

low mass WR stars is identified as [WR]-type and is divided into three different types: the oxygen type [WO] , the carbon type [WC], and the nitrogen type [WN] (sometimes supplemented by an intermediate [WN/WC] classification; van der Hucht et al., 1981; DePew et al., 2011).

Multiple evolutionary paths are theorized for these stars. One theory suggests that the formation of H-deficient [WR] stars is based on the timing of the thermal pulse via the Asymptotic Giant Branch Final Thermal Pulse (AFTP), the Late Thermal Pulse (LTP) or the Very Late Thermal Pulse (VLTP). The first serves as the finale to the AGB phase, while the LTP occurs after the star has left the AGB but continues to burn hydrogen. Finally, the VLTP occurs when the star is already beginning to cool along the WD evolutionary track (Herwig, 2001). Alternatively, [WR] stars are theorized to form from binary interactions, possibly being the product of a binary merger (De Marco & Soker, 2002; De Marco, 2008; Hajduk et al., 2010).

Given the similarities to their more massive cousins, which produce wind-blown bubbles of their own (Toalá & Arthur, 2011b; Toalá et al., 2012; Zhekov & Park, 2011; Zhekov, 2014), PN around [WR]-type central stars are expected to share similar traits. The higher mass loss and wind speeds are expected to result in more pronounced limb-brightened morphologies, as the much higher wind from the [WR] star sweeps up the previous AGB wind. This also has been proposed for the diffuse X-ray morphologies for both WR and [WR]-type stars (Wrigge et al., 1994; Wrigge, 1999; Wrigge et al., 2005; Toalá et al., 2012).

1.4 Shaping Paradigms

Originally the notion was that PNe formed from a sudden mass-loss event much like supernovae, but modeling and observations since then has proven that not to be the case (Kwok et al., 1978; Schönberner & Steffen, 2003). A variety of methods have been proposed for the generation of PNe, and the creation of the assortment of morphologies that appear to make every nebula unique. Below, we discuss some of the various theories of PNe shaping.

1.4.1 Winds

Previously we discussed how the wind of the AGB star and the central star work together to create a PNe, however this was under the assumption that such winds are homogeneous and isotropic. While there do exist PNe that appear to fit this configuration (e.g. Abell 39, Fig. 1.1, top left), most PNe do not exhibit such well defined spherical structures. If the AGB wind is inhomogeneous and has clumpy structure, instabilities can form, resulting in asymmetrical features. Such structures are found in the circumstellar envelopes of AGB stars (e.g. IRC+10216; Leão et al., 2006), and could lead to non-uniform density distributions that result in multipolar nebulae (Steffen et al., 2013). Additionally, if the central star were to have a binary companion, a secondary wind or accretion onto the companion could create spiral-like structures. Such structures have been seen in AGB stars like R Scl (Maercker et al., 2012), which could explain some of the spiral-like filamentary structures seen in PNe like the Saturn Nebula.

1.4.2 Tori and Disks

An initial model suggested by Frank et al. (1993) placed a torus in the equatorial plane of the nebula. The results of their hydrodynamical simulations reproduced observed PNe at a variety of inclinations, positing that with the inclusion of a disk or torus that the ISW model is still a reasonable approach. A disk or torus would collimate the AGB and central star winds in the polar direction, resulting in a tight or hidden waist in optical observations. Circumstellar disks have been detected around post-AGB stars and the central stars of PNe such as the Egg Nebula. In fact, 18% of PNe central stars have been found with dusty disks (Clayton et al., 2014). The origin of this disk is still unconfirmed, but is possibly linked to accretion of dust from the AGB phase, the destruction of Kuiper Belt objects, or the presence of a binary companion. Clayton et al. (2014) surveyed the central stars of several PNe and found that 8 out of the 13 stars that had disks were either binaries or suspected binaries.

Figure 1.3: ESO Very Large Telescope image of Fleming 1. The outer regions of this nebula shows symmetric jet structures indicative of a binary at its heart. (Credit: ESO/H. Boffin)

1.4.3 Jets

An inhomogeneous wind should result in asymmetrical PNe more often than axisymmetrical nebulae. Jets could be responsible for the creation of bipolar nebulae that exhibit a well defined, collimated structure. An alternative launching mechanism for the AGB shell could be the launching of a jet from within the stellar envelope. Such a jet would be launched along the poles of the star, accelerating the polar material outward faster than the equatorial material (Akashi & Soker, 2013). This would result in a highly elliptical or bipolar nebula similar to Fleming 1, which shows evidence for a jet (Fig. 1.3). The jet structure of Fleming 1 has a axisymmetric, spiral-like structure with minor oscillations in it, which are attributed to a central binary (Boffin et al., 2012). Other axisymmetic structures and disturbances could be the result of the precession of the jet after the formation of the nebula (Sahai & Trauger, 1998; Bujarrabal et al., 2001).

Jet structures are not often visible in many PNe with bipolar structures. Spectroscopic observations have revealed high velocity outflows at speeds ~ 100 km s^{-1} in several PNe, which serves as indirect evidence of a jet. Furthermore, bullet-like and ansae structures found on opposite sides of the central star are also attributed to some sort of jet and are associated with bipolar nebulae. Jets can generate instabilities in the surrounding shell of the AGB star which will result in dense

clumps forming along the flow. Clumps like these are seen in NGC 6302, suggesting that a jet may have played some role in its formation (Akashi & Soker, 2013).

1.4.4 Magnetic Fields

Collimation of bipolar nebulae may also be explained by the ejection of ionized material along magnetic field lines. Stars are expected to have magnetic fields during their main sequence lifetime, and these fields can cause accretion or ejection of material. A remnant magnetic field from the time that the central star spent on the main sequence could be responsible for some of the axisymmetric morphologies seen in PNe. Alternatively, this magnetic field could be produced as a result of a rapidly rotating stellar core within a slowly rotating envelope, resulting in the creation of a dynamo and a corresponding magnetic field (Jordan et al., 2012)

Models of dynamo generation from single and binary stars by Nordhaus et al. (2007) showed that if certain conditions are met, single stars could generate necessary magnetic fields, though common envelope binaries are far more likely to produce such fields. The addition of a secondary star results in additional energy and momentum which can boost the magnetic field. Magnetic fields up to 1 G have been measured, via polarization of radio maser emission, in the envelopes of AGB stars, and on the order of a few mG in proto-PN (Vlemmings, 2007, and refs. therein). However, surveys searching for magnetic fields emanating from the central stars of PNe have only found a few with detectable fields, of which only one is a suspected binary (Leone et al., 2011, 2014).

1.4.5 Binaries

The shapes of PNe were once exclusively linked to post-AGB stages of evolution, but it is becoming more and more apparent that the AGB phase may have a larger impact on the eventual evolution of the PN. Many AGB stars are expected to have companion stars, which is expected to impact not only the evolution, but the morphology of the subsequent PN. This Binary Hypothesis (De Marco, 2009) has infiltrated nearly all forms of explanation for PNe shaping. Whether it is

by accreting material to form a jet or a disk, or adding extra energy to the system and a stronger magnetic field, binaries play an important role in the evolution of PNe.

It is well known that most stars form in pairs, which further supports this hypothesis. Observations of AGB stars have found many with companions that have already begun to play a role in the deformation of the stellar envelope (Leão et al., 2006; Mayer et al., 2014). Binary companions can also hide themselves by falling into the envelope of the central star. This common envelope binary is expected to accelerate the loss of the AGB envelope by injecting additional energy and momentum. It is in this phase of evolution that jets can form and launch the stellar envelope away from the binary (Soker, 2004; Nordhaus et al., 2007; Tocknell et al., 2014; De Marco et al., 2015).

As a result of the common envelope phase, the orbit of the core of the AGB star and the companion star shrinks, and in some cases can lead to coalescence. When this happens, the companion star disappears, leaving behind a single star. The only evidence of a companion ever existing is believed to be within the nebula itself. Not only does the morphology inform us of this, but also the chemical composition of the central star. This is how [WR]-type central stars are believed to have formed (De Marco & Soker, 2002; De Marco, 2008; Hajduk et al., 2010).

1.5 PNe across the spectrum

The interesting morphologies of PNe are not limited to the optical emission line observations. PNe have been observed across the electromagnetic spectrum and have revealed complicated structures at every wavelength. Being able to observe PNe at a range of wavelengths is crucial for understanding their evolution, from their past to their possible future.

1.5.1 Radio/Millimeter

PNe are typically found with radio emission from the dense envelope around the main nebula. Free-free emission from the ionized portions of the circumstellar envelope make PNe bright radio sources (Gruenwald & Aleman, 2007; Planck Collaboration et al., 2015). Observations of the 21

cm hydrogen line shows extended halos that surround nebulae and represent the gas previously ejected by the AGB star. Molecular emission from CO is also associated with shells around many PNe, but there are also cases that reveal atypical distributions of CO in the form of bullets or high velocity outflows (see Chapter 5). Radio observations have proven useful for determining electron temperatures within nebulae and the level of intervening interstellar extinction (Terzian, 1968).

1.5.2 Infrared

The infrared (IR) part of the spectrum probes many complex dust and gas features within the nebula. Far-IR observations reveal large amounts of mass ejected at earlier stages of the central star's evolution that surround the main nebula. In particular, most of the mass of the nebula is expected to be found in dust in this wavelength regime. The *Herschel* Planetary Nebula Survey (HerPlaNS) investigated 11 PNe at wavelengths longer than 51 μm to investigate the spatial distribution of electron density, temperature, and elemental abundances. These data can provide insight into the progenitor star's mass loss history and the molecular makeup of such nebulae (Ueta et al., 2014; Aleman et al., 2014).

In the mid-IR, observations typically reveal emission from polycyclic aromatic hydrocarbons (PAHs) which are expected to form within photodissociation regions (PDRs), as well as [Ne II], and the warm dust continuum (Latter et al., 1995; Chu et al., 2011). The intrinsic physical structure of the nebula is best seen at these wavelengths since they do not suffer from absorption. Additionally, the emission shows evidence of stratification, with the cooler dust appearing on the edges of the nebula while the warmer components appear deeper, and in some cases, coincident with the optical emission.

The presence of CO is commonly associated with H_2 emission, found towards the outer edges of PDRs where the molecular hydrogen can be shielded from the UV radiation. This envelope of molecular hydrogen is steadily dissociated as UV radiation begins to leak out of the main nebula as it continues to expand. The presence of H_2 emission has also been used as an indicator of bipolar structure of PNe (Zuckerman & Gatley, 1988; Kastner et al., 1996). This near-IR emission can show

structures vastly different than those seen in J, H, and K images, which often show morphology similar to that visible in the optical. Additionally this part of the spectrum allows for an in-depth look at the thermal plasma, thermal dust, and hot stellar continuum (Whitelock, 1985; Weidmann et al., 2013).

1.5.3 Optical

As the energy increases in the electromagnetic spectrum, we begin to probe deeper and deeper into the PNe. The ionization structure of such nebulae is revealed by the optical emission lines where the gas in the lowest ionization state is found further away from the central star, while the highly ionized gas is found closer to it (Sabbadin et al., 2006). The stratification of ions is a good tracer of the evolutionary state of the nebula, as well as its age and chemical makeup of the progenitor star. PNe are bright emission line sources, and are typically discovered in other galaxies by their Hα, and more commonly [O III] fluxes.

1.5.4 Ultraviolet

The UV radiation from the central stars of PN is responsible for ionizing the surrounding gas and illuminating the structures that we find so beautiful. This means that many PNe, particularly the young and compact objects, remain optically thick to UV radiation for some time. As the nebula gets older, the outer layers are not efficiently shielded from the UV radiation and also become ionized. Observations taken by the International Ultraviolet Explorer (IUE) have revealed high-excitation emission lines, yielded electron densities, and have detected and provided information about the properties of the stellar winds (Feibelman, 1998).

1.5.5 X-rays

X-ray observations of PNe performed by the *Chandra* Planetary Nebula Survey (ChanPlaNS) have revealed that more than 50% of PNe display X-ray emission (Kastner et al., 2012; Freeman et al., 2014, Chapter 3). In the cases where we find point source emission from the CSPNe, we

believe it to be an indicator of activity that corresponds with the presence of a companion star, or in some cases a wind and/or a hot photosphere of the proto-WD (Montez et al., 2015b). The softer, diffuse emission is associated with the hot bubble, though this appears to only be present during the early stages of PNe evolution. (Kastner et al., 2012; Freeman et al., 2014; Montez et al., 2015a). The diffuse X-ray emission of PNe and wind-blown bubbles of massive Wolf-Rayet (WR) stars share similar characteristics (García-Segura et al., 1996b,a; Freyer et al., 2003; Toalá & Arthur, 2011b; Toalá et al., 2012; Dwarkadas & Rosenberg, 2013). For wind-blown bubbles like S308, the X-ray emission is brightest along the inner limb of the optical bubble, which is analogous to some PNe that host [WR]-type CSPNe.

1.6 Dissertation Synopsis

In this dissertation we tackle the emerging multiwavelength picture of PNe, with a heavy emphasis on X-rays, in order to better understand the structure, kinematics, and shaping of PNe. Through ChanPlaNS we were able to investigate not only the presence of possible binary companions to the central stars of PNe, but also place limits on the evolutionary timescale associated with the wind-shaping phase of PNe. Our results have also helped us constrain the physical properties of PNe that are expected to host diffuse X-ray emission, helping to inform future X-ray observations.

To model the physical structure of PNe, we use the astrophysical modeling tool *SHAPE*. We include previously published multiwavelength data, and for the first time in *SHAPE*, X-ray emission and absorption models. The use of 3D modeling can help us better understand the morphology of PNe, and the origin of such shapes. Using kinematic data, we can reconstruct the intrinsic shape of a PN, and by incorporating multiwavelength observations, we can see how the various regions of of the nebula interact with one another. Additionally, having a 3D model permits us to directly compare the intrinsic, deprojected structure of one nebula with the projected structure of another, helping to understand commonalities in contrast with object specific aspects of PN shaping. By

doing this, we can relate multiple different projected morphologies to a possible unified evolution model.

This dissertation is organized as follows. In Chapter 2 we briefly describe and discuss our analysis methods, including the procedures for reducing *Chandra* data and the astrophysical modeling tool *SHAPE*. In Chapter 3 we explore the theoretical models for X-ray emission from PNe as well as the insights from *Chandra* observations. Chapter 4 details the set up and results of modeling diffuse X-ray emission from planetary nebulae using a simple, spherically symmetric toy model. In Chapter 5 we delve into the construction of a 3D morpho-kinematic model of the well-studied, X-ray luminous PN BD+30°3639 based on multiwavelength observations and compare it to other well-studied PNe. We conclude with a summary and discussion of future work in Chapter 6.

CHAPTER 2

X-RAY DATA AND ANALYSIS

2.1 X-rays

To observe hot objects such as massive stars, AGN, or the hot bubbles within PNe, we look for X-ray emission. Unfortunately, this part of the electromagnetic spectrum is heavily absorbed by the Earth's atmosphere, requiring space based observatories. Due to the expense of launching a telescope into space, many observatories have to consider trade-offs between having large collecting areas or better resolution. Regardless of the final configuration, all X-ray telescopes need to be designed to appropriately collect X-ray photons. Due to their energetic nature, X-rays typically penetrate and, depending on the thickness, are absorbed by the material they come in contact with rather than reflected. However, if the incident angle of the X-ray is small with respect to the surface, they can be reflected towards a detector. Typically, X-ray telescopes utilize mirror configurations consisting of concentric shells in paraboloid and hyperboloid shapes, to increase the effective collecting area of the telescope.

Though the method of collecting incident photons differs from optical and infrared radiation, X-ray astronomy can also make use of proportional counters (PCs), micro channel plates (MCPs), or charge coupled devices (CCDs) to detect incoming photons. PCs produce an output energy that

is proportional to the incident radiation while MCPs convert incident X-rays into an electron cloud, which is amplified for detection purposes. One of the advantages of CCDs in application to X-ray astronomy is that CCDs can record the location, time, and energy with which an X-ray photon strikes the detector in the form of event lists. This is useful considering that most astrophysical X-ray sources have low photon arrival, hence detection, rates. With so few counts it is imperative to collect as much information as possible from each photon.

2.2 X-ray Satellite Observatories

There have been many space based X-ray observatories that have contributed to the field of high energy astrophysics. It is important to understand the capabilities of each in order to select the appropriate telescope to observe a particular type of object. Parameters like resolution, field of view, and energy range become deciding factors for choosing the right X-ray observatory. Below we briefly discuss the characteristics of some of the most successful observatories.

2.2.1 Past Observatories

Einstein

The second High Energy Astrophysical Observatory (HEAO-2) was renamed *Einstein* by NASA after launch in 1978. *Einstein* was the first imaging X-ray telescope put into orbit, and was capable of observing extended and faint objects. The X-ray observatory served for almost three years in space, and in that time it managed to alter our view of the X-ray sky. *Einstein* made use of a single Wolter grazing incidence telescope with four instruments that could be moved into the focal plane as desired. The Imaging Proportional Counter used a proportional counter with a field of view of $75'$ over an energy range of 0.4-4.0 keV. The High Resolution Imager (HRI) used a micro-channel plate detector with a spatial resolution of $2'$, field of view of $25'$, and an effective energy range of 0.15-3.0 keV. The Solid State Spectrometer and the Focal Plane Crystal Spectrometer both had a field of view of $6'$ but operated at 0.5-4.5 and 0.42-2.6 keV respectively. Lastly, *Einstein* also

included the Objective Grating Spectrometer, which could be used with the HRI. *Einstein* provided the first studies of supernova remnants, galaxies, and galaxy clusters in the X-ray, which led to better understandings of their gas morphologies (Giacconi et al., 1979).

The Roentgen Satellite *ROSAT*

The Roentgen Satellite (*ROSAT*) was launched in 1990 with the intent of performing an all sky X-ray and extreme ultraviolet survey. *ROSAT* utilized 4 Wolter concentric mirrors to scatter the incoming X-rays towards three instruments, two position-sensitive proportional counters (PSPCs) and a high resolution imager (HRI) for a field of view of 2°. Similar to MCPs, PSPCs use a window gas counter where incoming X-ray photons are absorbed by the gas and create an electron cloud proportional to the photon energy in an energy range of 0.1-2.5 keV. The electrons fall onto a cathode grid which detects the position of the event to within 120 micrometers. The HRI used a photocathode to convert the X-ray photons into electrons, followed by a MCP which produced an electron cloud onto a crossed anode grid. To detect extreme UV photons, an XUV telescope with three grazing incidence mirrors was installed and aligned with the XRT. The Wide-Field Camera (WFC) was used to collect the XUV photons using a MCP similar to the HRI (Trümper et al., 1991).

ASCA

Japan's fourth cosmic X-ray astronomy mission, the Advanced Satellite for Cosmology and Astrophysics (*ASCA*), was created in partial cooperation with the United States. *ASCA* was launched in 1993 and served as the first X-ray satellite to employ CCDs for the detection of X-rays. The satellite served for over seven years in space, and provided both broad-band (0.4-10 keV) imaging and good spectral resolution with the added bonus of a large effective area. Four X-ray telescopes made up the eyes of *ASCA*, each composed of 120 nested gold-coated aluminum foil shells, which directed X-ray photons towards two different types of detectors: a Gas Imaging Spectrometer (GIS), and a Solid-state Imaging Spectrometer (SIS). The GIS used two imaging

proportional counters to observe a field of view of $50'$ from 0.8-12 keV. The SIS was comprised of two CCDs with a field of view of $22' \times 22'$ with an energy range of 0.4-12 keV. During its lifetime, *ASCA* observed crucial broad iron lines from active galactic nuclei that provided evidence for strong gravity near the supermassive black hole (Tanaka et al., 1994).

2.2.2 Active Observatories

XMM-Newton

The X-ray Multi-Mirror Mission (*XMM-Newton*) was launched by the European Space Agency (ESA) in 1999. *XMM-Newton* was constructed as part of ESA's Horizon 2000 Science Programme. It was designed with a large effective area with the goal of collecting long exposures with high sensitivity. Additionally, the space observatory included the first optical monitor on an X-ray mission. The satellite contains three co-aligned gold-coated Wolter grazing incidence telescopes which make use of three types of instruments. The European Photon Imaging Cameras (EPIC-MOS) contain 7 CCDs each with a field of view of $33' \times 33'$ over an energy range of 0.1-15 keV. An additional European Photon Imaging Camera uses an array of 12 CCDs for spectro-imaging over the same energy range, with a field of view of $27.5' \times 25.7'$. For spectroscopy, the Reflection Grating Spectrometer (RGS) works in conjunction with EPIC-MOS and is mounted under two of the three telescopes. The RGS uses gratings to deflect light onto an array of 9 EPIC-MOS CCDs over an effective energy range of 0.35-2.5 keV with a field of view of $5'$[1]

The *Chandra* X-ray Observatory

Initially commissioned as the Advanced X-ray Astrophysics Facility (*AXAF*), the *Chandra* X-ray Observatory (CXO) was launched in 1999 and was designed to address several problems facing the X-ray community. The observatory was required to have a large telescope area, high observing efficiency with spatially resolved spectroscopy of modest resolution, and a long operational lifetime. A key requirement was high spatial resolution; the telescope has a point spread function of less

[1] "XMM-Newton Users Handbook", Issue 2.13, 2015 (ESA: XMM-Newton SOC)

than $0.5''$ which varies with the location of the source in the telescope field of view. This last requirement is one of the key elements that results in the high demand for *Chandra* observing time (Schwartz, 2004). For the purposes of this work, *Chandra* provides the necessary spatial resolution to disentangle point-like emission from diffuse emission, unlike that of *ROSAT* and *XMM-Newton*. This is especially important given the small angular size of some PNe in the *Chandra* Planetary Nebula Survey sample (see Chapter 3).

The High Resolution Mirror Assembly (HRMA) accomplishes this feat and consists of four sets of nested mirrors. Originally designed with six mirror shells (2 were eliminated prior to launch), the *Chandra* mirrors serve as the next step in technology from those that were used on ROSAT and the *Einstein* missions. The HRMA allows for previously observed X-ray point sources to be reclassified as extended objects with distinct and complex internal structure. At its focal plane are two imaging instruments: the High Resolution Camera (HRC) and the Advanced Camera for Spectroscopy (ACIS). The HRC makes use of micro channel plates while ACIS uses CCDs. The HRC is effective over an energy range of 0.1-10 keV and has an imaging field of view of $30' \times 30'$ and a spectroscopic field of view of $7' \times 97'$. ACIS has an energy range of 0.2-10 keV and is split into an imaging array (I) and a spectroscopic array (S) as well. ACIS-I is composed of 4 front illuminated CCD chips with a total field of view of $16' \times 16'$ while ACIS-S has 6 CCD chips (4 front illuminated, 2 back illuminated) for a field of view of $8' \times 48'$. *Chandra* also includes both a High Energy Transmission Grating (HETG) and a Low Energy Transmission Grating (LETG), which can be used with ACIS or HRC.

The *Swift* Gamma-Ray Burst Mission

In 2004, the *Swift* Gamma-Ray Burst (GRB) mission was launched with the goal of identifying GRBs and observing them using additional telescopes in other parts of the spectrum. In particular, the X-ray telescope (XRT) is used to gather information about the GRB or afterglow's position quickly and accurately, as well as deliver moderate resolution spectra and high time resolution lightcurves. Beyond corroborating GRB positions, the XRT is also used for pointed observations,

examining X-ray emission over an energy range of 0.2-10 keV with a field of view of $23.6' \times 23.6'$. A 600×602 silicon CCD array sits at the focal plane of the telescope to collect the X-ray photons after they scatter off the grazing incidence mirrors (Gehrels, 2004).

Suzaku

Launched in 2005, the *Suzaku* observatory was actually the second generation of the Astro-E telescope, which was lost at launch in 2000. The X-ray telescope was developed by the Japanese Institute of Spaces and Astronautical Science (ISAS) in conjunction with US support. Unlike previous X-ray telescopes, *Suzaku* featured the first X-ray micro-calorimeter in space which was designed to provide high energy resolution spectroscopy. The satellite features five nested, gold-coated grazing incidence telescopes that focus photons towards the spectrometer, imaging spectrometer, and hard X-ray detector. The X-ray spectrometer makes use of the micro-calorimeter and has a field of view of $2.9' \times 2.9'$ and an effective energy range of 0.3-12 keV. The imaging spectrometer uses CCDs to achieve an field of view of $18' \times 18'$ over the same energy range as the X-ray spectrometer. The hard X-ray detector operates over an energy range of 10-600 keV and uses a crystal scintillator and silicon diodes. The field of view for the hard X-ray detector depends on the incident radiation: $34' \times 34'$ for energies < 100 keV, and $4.5^\circ \times 4.5^\circ$ for energies > 100 keV (Madejski, 2005).

2.3 X-ray Data Reduction

All X-ray data used in this dissertation comes from *Chandra* observations of planetary nebulae. Here we will discuss data reduction techniques applied to our set of *Chandra* data.

2.3.1 Reprocessing

Data received from *Chandra* arrives in the form of primary and secondary data files downloaded from the *Chandra* X-ray Center (CXC). To create a consistent set of processed results, we begin our data reduction by reprocessing the data using the *Chandra Interactive Analysis of Observations*

(CIAO version 4.35[2]) command `chandra_repro`. This script reads the data and generates a bad pixel file and event file using the latest calibrations for *Chandra* available (CALDB). Additionally, this procedure makes use of sub pixel event reposition (SER), which can improve the determination of the location of photons within individual pixels, effectively optimizing the spatial resolution (Li et al., 2004).

Reprocessing of observations is important because over time calibration algorithms have changed resulting in less optimized data. By reprocessing all the data that we make use of, including archival data, we make sure that all data products are consistent with one another and make use of the most up-to-date calibration data (e.g. bad pixel locations, CCD quantum efficiencies, focal plane geometry, etc.).

2.3.2 Source detection

To determine possible sources within the field of view of each observation we use the wavelet-based source detection task `wavdetect` (Freeman et al., 2002) in CIAO. We search for sources using wavelength size scales of 1, 2, 4, 8, and 16 pixels within $4'$ of the central star of our target PN for on-axis sources. Rebinning is necessary for off-axis sources due to the growing PSF size with increasing off-axis angle. This requires that for targets more than $4'$ off-axis we rebin the image to 4×4 ($\sim 2''$ pixels) rather than 1×1 ($0.492''$ pixels). The sources detected by `wavdetect` are only recorded if they lie above a $\sim 3\sigma$ significance threshold. The results are then cross-correlated with the optical USNO-B1 (Monet et al., 2003) and near-infrared 2MASS[3] catalogs of point sources. Those sources that correspond with those lists and lie within $10''$ of the target PN are then identified and recorded.

Extended sources are identified by eye, via visual inspection of energy filtered images. Soft energy band images from 0.3-2.0 keV remove moderate contamination from background photons and highlight diffuse emission. Such an image is created using the `dmcopy` task and filtering the

[2] http://cxc.harvard.edu/ciao/

[3] Two Micron All Sky Survey, which is a joint project of the University of Massachusetts and the Infrared Processing and Analysis Center/California Institute of Technology

ENERGY and PI columns of the *Chandra* event list. This may be enhanced by rebinning or smoothing images to highlight the extended features. For some objects, the recorded photons (or counts) attributed to the source lie below 10 counts, which has led to detections that are not as well defined. Still, for many PNe with high enough counts per unit solid angle above the background we are able to confidently confirm diffuse X-ray emission.

2.3.3 Source event statistics and spectral extraction

To calculate the statistics of X-ray point sources attributed to the central stars of PNe (Chapter 3), we select a 3.5″ radius region centered on the central star. From this region we are able to extract source photon statistics (number, mean, median, and lower and upper quartile photon energies) and the source spectrum. Typically, the median of an observed quantity is dependent upon the instrument, particularly the instrumental energy response. However, for a collection of objects observed with the same instrument, the median photon energy can serve as a measurement of plasma temperature and intervening absorption (Getman et al., 2010).

Additionally, we extract spectra and statistics from the region around the central star that corresponds to the extent of nebula. The size of the these regions is governed by optical morphologies of each individual nebula. Regions are also generated from adjacent areas on the same ACIS chip which are intended to be source-free regions. These regions serve as background regions and are scaled for calibration of the source regions for fitting of X-ray spectra to determine physical parameters such as plasma temperature, intervening absorption, and elemental abundances.

Spectra are extracted from event lists by using `specextract` and the source and background regions, which uses the most recent calibration files to calibrate the resulting spectra. Using the spectral analysis tool `xspec`, we can fit the spectra with an appropriate emission model (Fig. 2.1). Typical models that describe X-ray emission sources are blackbody, Bremsstrahlung, and optically thin, thermal plasma models. The parameters of each model can be adjusted to provide a better fit to the data, with the goal of minimizing the reduced χ^2 value which provides an estimate of the goodness-of-fit.

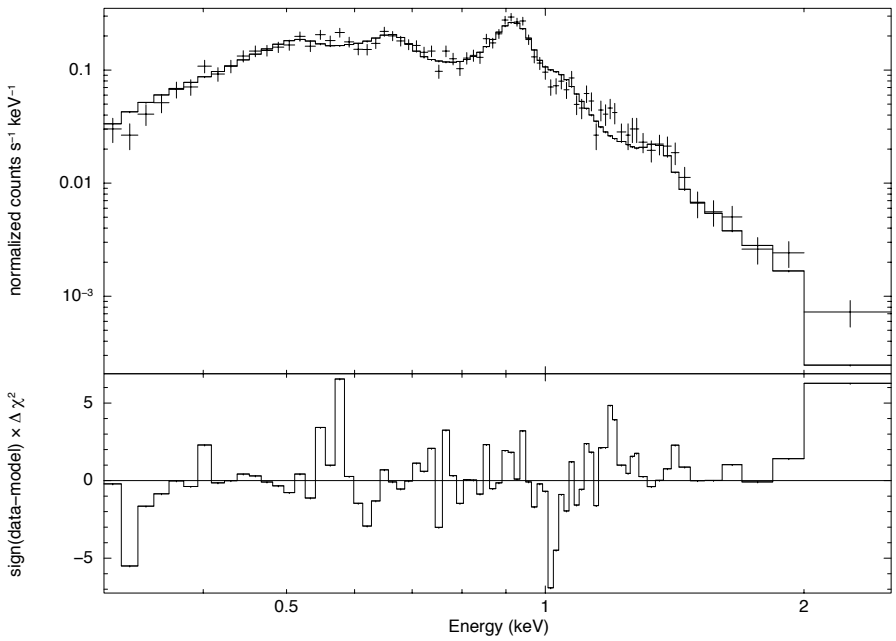

Figure 2.1: Example spectra of BD+30 generated using `specextract`. Here we have fit the X-ray emission with an optically thin, thermal plasma model, assuming intervening photoelectric absorption. The crosses represent the *Chandra* data and the solid line is the model. The lower panel displays the residuals of the model subtracted from the data.

2.3.4 Output

The output of this reduction pipeline can be seen in Fig. 2.2, and is described in more detail in Chapter 3 and Kastner et al. (2012). The images produced show a *Chandra* soft-band X-ray image centered on the PN and filtered to reveal any diffuse emission present (0.3-2.0 or 0.5-1.3 keV; left panel) and the positions of detected broad-band (0.3-8.0 keV) X-ray sources, USNO-B1 catalog stars, and 2MASS point source catalog sources are overlaid on an Hα image (right panel). The optical images were collected from the *Hubble Space Telescope (HST)* archive[4] and the SuperCOSMOS Hα Survey (SHS).

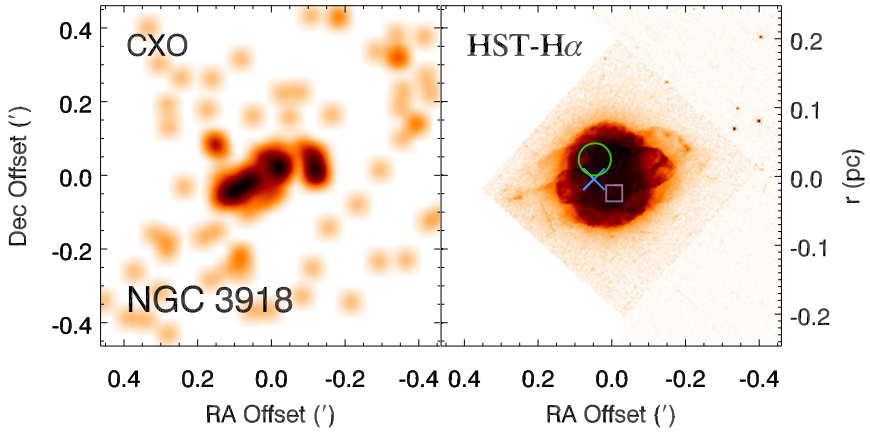

Figure 2.2: Example output from the ChanPlaNS reduction pipeline for NGC 3918. The *left panel* shows the *Chandra*/ACIS soft-band (0.3-2.0) keV image, smoothed with a Gaussian function with 3″ FWHM, centered on the SIMBAD coordinates of the PN (which lies on back-illuminated CCD S3). The *right panel* shows an optical image obtained from *HST* overlaid with the positions of detected broad-band (0.3-8.0 keV) X-ray sources (crosses), USNO catalog stars (circles), and 2MASS Point Source Catalog IR sources (squares). The size of the cross is proportional to the number of X-ray photons detected (Freeman et al., 2014).

[4] http://archive.stsci.edu/hst

2.4 *SHAPE*: 3D Astrophysical Modeling Software

To extend the modeling of X-rays into 3-dimensional space, we used the 3D morpho-kinematic tool *SHAPE*, a software package developed for astrophysical modeling (Steffen & López, 2006; Steffen et al., 2011). *SHAPE* allows for the handling of various parameters of a structural model of an astrophysical source interactively, such that one can adjust the position and orientation of the object on the sky, as well as a simulated slit for spectroscopy or generating radial surface brightness profiles, and the image system spatial and spectral resolution in order to better simulate observations. To produce the synthetic images, *SHAPE* calculates radiative transfer using ray-casting and the necessary input parameters such as temperature, density, and other physical parameters. It is worth noting that for the models produced by *SHAPE* heating mechanisms are not taken into account, meaning that physical attributes such as temperature, density, and ionization state are treated as input parameters. This project represents the first attempt to incorporate X-rays into a *SHAPE* 3D model and use the simulated output for comparison with *Chandra* observations.

To model radiative transfer, *SHAPE* uses the standard "textbook" theory, which is briefly summarized here. The amount of energy that is radiated through an area dA with normal n with solid angle $d\Omega$ centered about k with a frequency between ν and $\nu + d\nu$ (independent of time) is:

$$dE = I_\nu k \cdot n \cdot dA \cdot d\Omega \cdot d\nu \,, \tag{2.1}$$

where I_ν is the specific intensity with units of J m^{-2} s^{-1} Hz^{-1} ster^{-1}. As the light ray travels through the medium, it has the possibility of having energy added to it or energy removed from it. Where intensity is added to the beam, via emission, the amount of intensity is defined as

$$dI_\nu = j_\nu ds \,, \tag{2.2}$$

where j_ν is the emission coefficient with units of J m^{-3} s^{-1} Hz^{-1} ster^{-1}, and ds is the distance over which the beam has traveled in meters. For the alternative case, where intensity is removed

from the beam, or pure absorption, the intensity is defined as

$$dI_\nu = -\kappa_\nu I_\nu ds\,, \tag{2.3}$$

where κ_ν is the absorption coefficient with units of m^{-1}. Taking both absorption and emission into account, the total intensity change over a distance ds can be written as

$$\frac{dI_\nu}{ds} = j_\nu - \kappa_\nu I_\nu\,. \tag{2.4}$$

Integrating over s provides the emergent intensity of the beam, yielding

$$I_\nu = e^{-\tau_\nu} I_0 + \int_0^{\tau_\nu} e^{-\tau_\nu} S_\nu dt\,, \tag{2.5}$$

where τ_ν is the optical depth, and $S_\nu = j_\nu/\kappa_\nu$.

SHAPE takes the source function S_ν to be constant along ds for each individual cell on the 3-dimensional grid. This allows for an easier solution to the equation of radiative transfer and the resulting emergent intensity of the object.

The intensity is then used to generate synthetic images, which are rendered using one of four different renderers: *particle*, *grid*, *mesh*, or *physical*. The *particle*, *grid*, and *mesh* renderers assume that the object being modeled is optically thin, while the *physical* renderer incorporates opacity and radiative transport effects. For the purposes of this dissertation, we have made use of the *particle*, *mesh*, and *physical* renderers to demonstrate the effects of nebular absorption on X-ray emission and morphology (Chapter 4), and to investigate the intrinsic morphology of BD+30°3639, compared to the projected morphology which has suffered extinction due to opacity effects (Chapter 5). To calculate a synthetic image, the emission from each cell is integrated along the line of sight, while to generate position-velocity diagrams and radial profiles, the emission is extracted along a simulated spectrometer slit. Observations can be directly compared with the synthetic images in *SHAPE* by importing them and using them as a reference. *SHAPE* offers a *differencing* feature which subtracts

an imported observed image from the synthetic image, providing a method to investigate synthetic differences between the data and the model (Steffen et al., 2011).

2.5 Chapter Summary

In this chapter we presented an overview of observing and reducing X-ray data. We discussed the nature of X-ray observations and described a few of the prominent X-ray observatories. In particular, we covered our analysis techniques used in reducing *Chandra* data for the *Chandra* Planetary Nebula Survey (ChanPlaNS). This pipeline has been used to generate images and identify point sources as well as collect statistics such as median energy, counts, and count rate. We also highlighted the 3D modeling software *SHAPE*, and its capabilities to simulate observations from rendered objects. It should be noted that *SHAPE* has not been previously used in conjunction with X-ray data, hence our analysis presented here will represent a new and alternative technique.

CHAPTER 3

X-RAY EMISSION FROM PLANETARY NEBULAE

3.1 The *Chandra* Planetary Nebula Survey

Models describing the structure of PNe (Kwok et al., 1978; Schmidt-Voigt & Koppen, 1987; Marten & Schönberner, 1991; Villaver et al., 2002; Perinotto et al., 2004; Toalá & Arthur, 2014) posit that fast ($v_{\rm w} \simeq$ 500-1500 km s^{-1}) winds emanating from the pre-WD will collide with the previously ejected AGB envelope, sweeping up the AGB ejecta into a thin shell. These wind collisions result in shocks that heat the fast wind gas to temperatures $> 10^6$ K, creating a "hot bubble" capable of producing soft X-rays ($0.3 \sim 1$ keV). A binary companion to the central star of the PN (CSPN) is capable of further influencing the PN shape via formation of an accretion disk (Soker & Rappaport, 2000), transfer of angular momentum, the generation of a strong magnetic dynamo at the CSPN (Nordhaus et al., 2007), or in the case of a close binary, the formation of jets (Soker & Livio, 1994; Miszalski et al., 2011; Corradi et al., 2011; Boffin et al., 2012; Tocknell et al., 2014). While some CSPNe with hot photospheres ($\gtrsim$ 100 kK) are capable of emitting soft X-rays, many CSPNe exhibit hard X-rays (> 1 keV) that cannot be attributed to photospheric emission alone (Montez & Kastner, 2013; Montez et al., 2015b). Such hard X-rays might be expected, however, when a hot, compact companion accretes material, as suggested for some white

dwarfs with hard X-ray emission (Bilíková et al., 2010), or from the corona of a "rejuvenated" late-type companion of a post-common envelope binary CSPN (Montez et al., 2010). There is also the possibility that a "hard excess" could result from material infall from a debris disk around the CSPN, similar to the debris disk discovered around the central star of the Helix Nebula and possibly linked to its hard X-ray emission (Su et al., 2007). Alternatively, the hard X-ray emission might emerge from shocks within the stellar wind, via a process similar to that observed in O and B stars (Cassinelli et al., 1994).

The *Chandra* Planetary Nebulae Survey (ChanPlaNS) was designed to place constraints on the frequency of appearance and range of X-ray spectral characteristics of X-ray-emitting PN central stars and the evolutionary timescales of wind-shock-heated bubbles within PNe. The initial ChanPlaNS program consisted of observations of 21 high-excitation PNe selected from among the ~ 120 known PNe within ~ 1.5 kpc of Earth, along with another 14 PNe previously observed by *Chandra* that fall within this volume (Kastner et al., 2012, henceforth known as K12). The initial results included more than a dozen new detections of X-ray point sources and placed new constraints on the physical conditions, timescales, and frequency of hot bubbles. The survey recently continued with a 670 ks *Chandra* Cycle 14 Large Program of an additional 24 compact ($R_{\rm neb} \lesssim 0.4$ pc) PNe selected from among the volume-limited sample. In this chapter, we describe the results of the ChanPlaNSsurvey observations of these compact PNe in the context of the overall volume-limited sample of PNe.

3.2 Observations and Data Reduction

3.2.1 Sample: Compact ($R_{\rm neb} \lesssim 0.4$ pc) planetary nebulae within ~ 1.5 kpc

The PNe that constitute the sample observed with *Chandra*, listed in Table 3.1, were primarily selected so as to further probe the onset, evolutionary timescale, and properties of diffuse X-ray sources within PNe. Hence, we selected objects on the basis of their relatively small physical dimensions, as ascertained via optical imaging. More specifically, we chose the 24 Cycle 14 Table 3.1

objects from the compilation of solar-neighborhood PNe in (Frew, 2008) such that the resulting merged Cycle 12+14+archival sample would constitute a representative, volume-limited ($D \lesssim 1.5$ kpc) sample of PNe with inner bubble or inner shell radii $\lesssim 0.4$ pc (excluding very low surface brightness PNe, which typically have faint central stars). We estimate that our completeness in surveying compact ($R_{\rm neb} \lesssim 0.4$ pc) nebulae within ~ 1.5 kpc is 90%, based on the solar neighborhood census of PNe recently compiled by Frew et al. (2014b). The chosen nebular radius roughly corresponds to a dynamical PN lifetime of $\lesssim 10^4$ yr — approximately twice the apparent hot bubble dissipation timescale inferred from Cycle 12 plus archival *Chandra* data shown in K12 — assuming typical PN expansion velocities of $\sim$40 km s^{-1} (Jacob et al., 2013). Basic PN and CSPN data for the sample objects can be found in Table 3.1.

3.2.2 Observations

All Cycle 14 PNe were observed with the back-illuminated (BI) CCD of *Chandra*'s Advanced CCD Imaging Spectrometer (ACIS). The use of CCDs as X-ray detectors provides determinations of incident photon energies as well as locations, which in turn allows for filtering of images by photon energy. *Chandra*/ACIS-S3 has an energy sensitivity of $\sim$ 0.3-8.0 keV, with a field of view of $\sim 8' \times 8'$ and pixel size $0.492''$. The BI CCD S3 has greater low-energy (< 1 keV) sensitivity compared to the front-illuminated ACIS-I array, extending sensitivity down to ~ 0.2 keV for high soft photon fluxes, albeit with uncertain calibration (Montez & Kastner, 2013). Additionally, use of S3 facilitates subpixel event repositioning (SER) in processing so as to better sample the High Resolution Mirror Assembly core of the point spread function (Li et al., 2004). Observation IDs, dates, and exposure times for the Cycle 14 ChanPlaNS observations are listed in Table 3.2.

All data were reduced using CIAO (version 4.5). Data reduction made use of the ChanPlaNS pipeline which is detailed in Chapter 2. Briefly, this pipeline consists of the following steps: reprocessing of the primary and secondary data files and the application of SER using `chandra_repro`; detection of sources in the full field of view of each observation using `wavdetect`; calculation of statistics from a $3.5''$ radius region centered on the CSPN, to place constraints on possible X-ray

Table 3.1: Planetary Nebulae within 1.5 kpc[a] Observed by *Chandra*

Name	PN G	morph.[b] (F08/SMV11)	D (kpc)	R (pc)	age (10^3 yr)	T_* (kK)	sp. type	comp.[c]	H_2[d]	X-rays[e]
Abell 65	017.3−21.9	Eafm:/Ls	1.17	0.30	17.5[f]	114[g]	O(H)	(Y)	...	N
HaWe 13	034.1−10.5	Efp?/Esip	1.01	0.18	...	68	hgO(H)	...	...	N
Hb 5	359.3−00.9	Bps/Bcbmph	1.70	0.13	1.5[h]	172	...	...	Y	D
HbDs 1	273.6+06.1	Er? /Is	0.80	0.29	...	119[i]	O(H)	...	...	P
He 2-11	259.1+00.9	Ebps/Bcbsip	1.14	0.24	0.7[j]	108[j]	...	K5V[j]	...	N
IC 1295	025.4−04.7	Efm:/Es(b/ti)	1.23	0.30	11	98	hgO(H)	...	...	N
IC 2149	166.1+10.4	E/Bsh	1.52	0.04	2	42	Of(H)	...	N	N
IC 4637	345.4+00.1	Eam/Estp	1.30	0.05	2	50	O(H)	(Y?)	...	N
IC 5148/50	002.7−52.4	Rm /Rsiph	0.85	0.27	5	110	hgO(H)	...	...	N
M 1-26	358.9−00.7	R/Mcbsih	1.20	0.02	1	33	Of(H)	...	...	N
M 1-41	006.7−02.2	Bs/(I/B)	1.47	0.15	...	187	...	...	Y	N
NGC 1501	144.5+06.5	Es/Esph	0.72	0.09	2	135	[WC4]	...	...	D
NGC 2899	277.1−03.8	Baps/Bosbp	1.37	0.37	14	215[k]	...	F5V:	Y	N
NGC 3918	294.6+04.7	Ems(h)/Lsbairh	1.84	0.08	3	150	O(H)?	...	...	D
NGC 6026	341.6+13.7	Ef/Ish	1.31	0.16	6	35	O7(H)	WD?	...	N
NGC 6072	342.1+10.8	Ba/Mcot	1.39	0.23	23	140	...	...	Y	N
NGC 6153	341.8+05.4	Es/Esah	1.10	0.07	4	109	Of(H)?	...	N	D
NGC 6337	349.3−01.1	Epr /Rsarh	0.86	0.10	12	105	...	(Y)	...	P
NGC 6369	002.4+05.8	Ebpr(h:)/Mcst	1.55	0.12	3	66	[WO3]	...	Y	D
NGC 6894	069.4−02.6	Emr/Eh	1.31	0.17	4	100	...	...	...	N
NGC 7076	101.8+08.7	Ea/Esh	1.47	0.20	5	80	...	...	...	N
NGC 7354	107.8+02.3	Emp/Esaph	1.60	0.09	3	96	...	...	N	N
Sh 2-71	035.9−01.1	Bs/Lsbp	1.14	0.30	14	157	...	...	N	N
Sp 1	329.0+01.9	Rr/Rsh	1.13	0.20	6	72	O(H)	(Y)	...	P

Notes.
[a]PN and central star data compiled from (Frew, 2008, and references therein) unless otherwise noted.
[b]Morphologies as listed in Frew (2008, F08): B: bipolar, E: elliptical, R: round, a: asymmetry present, b: bipolar core present, f: filled (amorphous) center, m: multiple shells present, p: point symmetry present, r: ring structure dominant, s: internal structure noted, (h): distinct outer halo. Morphologies following an abbreviated and very slightly modified version of the classification system described in Sahai et al. (2011) (SMV11; see their Table 2): B: bipolar, M: multipolar, E: elongated, I: irregular, R: round, L: collimated lobe pair, S: spiral arm, c: closed outer lobes, o: open outer lobes; s: CSPN apparent, b: bright (barrel-shaped) central region, t: bright central toroidal structure; p: point symmetry, a: ansae, i: inner bubble, h: halo; r: radial rays; (/): alternate possibilities.
[c]"(Y)" = known binaries with unknown companion types; "(Y?)" = possible binary; otherwise the type of the companion star is as listed (De Marco, 2009).
[d]"Y" = near-IR H_2 detected; "N" = near-IR H_2 not detected (Bernard-Salas & Tielens, 2005; Bohigas, 2001; Webster et al., 1988; Ramos-Larios et al., 2013; Kastner et al., 1996, and references therein).
[e]X-ray results key: P = point source; D = diffuse source; N = not detected.
[f]Huckvale et al. (2013)
[g]Hillwig et al. (2015)
[h]López et al. (2012)
[i]Herald & Bianchi (2011)
[j]Jones et al. (2014a)
[k]Drew et al. (2014)

point source emission; and generation of annotated two-panel images displaying a filtered *Chandra* X-ray image highlighting the predominately soft X-ray (0.3-2.0 keV) nature of the nebulae and

Table 3.2: Log of *Chandra* Observations

Name	OBSID	date	exposure (ks)
Abell 65	14583	2013-08-22	29.7
HaWe 13	14578	2013-07-15	18.6
Hb 5	14596	2013-10-18	29.1
HbDs 1	14575	2013-08-10	19.5
He 2-11	14581	2013-08-10	29.6
IC 1295	14585	2013-08-04	29.7
IC 2149	14593	2012-12-30	28.7
IC 4637	14586	2014-03-08	29.6
IC 5148/50	14576	2013-04-07	19.7
M 1-26	14584	2013-08-10	29.6
M 1-41	14591	2013-03-02	29.6
NGC 1501	14574	2012-12-08	19.7
NGC 2899	14589	2013-05-28	29.6
NGC 3918	14597	2013-07-31	30.0
NGC 6026	14588	2013-06-29	29.6
NGC 6072	14590	2014-01-23	29.6
NGC 6153	14579	2014-01-17	28.6
NGC 6337	14577	2013-08-04	19.7
NGC 6369	14594	2013-02-18	29.6
NGC 6894	14587	2013-12-13	29.2
NGC 7076	14592	2013-03-29	29.6
NGC 7354	14595	2013-12-26	29.6
Sh 2-71	14582	2013-10-07	29.6
Sp 1	14580	2013-01-24	29.4

the best available optical (Hα or R band) image obtained from the *Hubble* Legacy Archive[1], the Wisconsin-Indiana-Yale-NOAO (WIYN) 0.9m telescope (see K12), the SuperCOSMOS H-Alpha Survey (SHS; Parker et al., 2005; Frew et al., 2014a), or the Digitized Sky Survey (DSS[2]), as indicated in the panels (Fig. 3.1).

3.3 Results

Results from the Cycle 14 *Chandra* observations listed in Table 3.2 are illustrated in Figs. 3.1-3.3 and are summarized in Tables 3.1 and 3.3. The last column of Table 3.1 states whether the PN was detected and, if so, the type of X-ray emission detected (point-like, diffuse, or both). As in

[1]http://archive.stsci.edu/hst
[2]http://archive.stsci.edu/dss

K12, our conservative estimate for our sensitivity limits for diffuse and hard (soft) point-like X-ray sources are $\sim 10^{30}$ and $\sim 10^{29}$ ($\sim 10^{31}$) erg s^{-1}, respectively, at a distance of 1.5 kpc.

Table 3.3: Planetary Nebulae X-ray Point Source Characteristics

Name	N[a] (photons)	C[b] (ks^{-1})	median E[c] (keV)	E range[d] (keV)
Abell 65[e]	1	0.02 ± 0.05	0.96	0.96-1.09
HaWe 13	...	< 0.21	...	...
Hb 5[f]	15:	0.51 ± 0.09:	0.94:	0.81-1.03
HbDs 1	10	0.49 ± 0.06	0.65	0.56-0.78
He 2-11	...	< 0.14	...	...
IC 1295	...	< 0.13	...	...
IC 2149	...	< 0.14	...	...
IC 4637	...	< 0.14	...	...
IC 5148/50	...	< 0.20	...	...
M 1-26	...	< 0.15	...	...
M 1-41	...	< 0.14	...	...
NGC 1501[g]	...	< 0.20:	...	...
NGC 2899	...	< 0.14	...	...
NGC 3918[g]	21:	0.71 ± 0.06:	0.85:	0.66-1.03
NGC 6026[e]	1	0.05 ± 0.08	1.16	0.90-2.31
NGC 6072	...	< 0.14	...	...
NGC 6153[g]	...	< 0.14:	...	...
NGC 6337	39	1.99 ± 0.07	1.27	1.03-1.73
NGC 6369[g]	8:	0.27 ± 0.07:	1.06:	0.96-2.38
NGC 6894	...	< 0.14	...	...
NGC 7076	...	< 0.14	...	...
NGC 7354	...	< 0.14	...	...
Sh 2-71	...	< 0.14	...	...
Sp 1	11	0.37 ± 0.07	0.93	0.83-1.33

Notes.
[a]Number of source photons, after background subtraction.
[b]Source photon count rate.
[c]Median source photon energy.
[d]Source photon energy range (25th through 75th percentiles).
[e]Uncertain point source detections at the positions of known binaries. See §3.3.3.
[f]There is no point source apparent within Hb 5.
[g]Point source counts, count rate (or upper limit), median energy, and energy ranges are uncertain due to presence of diffuse emission component.

Table 3.4 (an update of Table 4 from K12) lists X-ray detection statistics broken down by PN morphology, H_2, detection/nondetection fraction, and known central star binarity for the entire ChanPlaNS sample. Figs. 3.3 and 3.4 represent updates of Figs. 5 and 6, respectively, in K12. In Fig. 3.3, various observed parameters for the sample PNe − optical morphology, H_2 de-

Table 3.4: Planetary Nebulae: *Chandra* X-ray Detection Statistics

category[a]	N[b]	N_{PX}[c]	N_{DX}[c]
Entire sample	59	21 (36%)	16 (27%)
Round/elliptical, F08	47	19 (40%)	14 (30%)
Bipolar, F08	12	2 (17%)	2 (17%)
Round/elliptical/irregular, SMV11	37	14 (38%)	9 (24%)
Bipolar/multipolar, SMV11	22	7 (32%)	7 (32%)
near-IR H_2 not detected	19	9 (47%)	10 (53%)
near-IR H_2 detected	18	3 (17%)	4 (22%)
known binary CSPN	19	11 (58%)	2 (11%)

Notes.
[a]Morphologies as listed and defined in column 3 of Table 1 and associated footnotes; CSPN binary detections and H_2 detections as listed, respectively, in columns 9 and 10 of Table 1.
[b]Total number of sample PNe in each category.
[c]Number of PNe in each category displaying point-like and/or diffuse X-ray emission in *Chandra* imaging (K12).

tection/nondetection, X-ray detection/nondetection, and X-ray source type − are illustrated in a plot of CSPN effective temperature vs. nebular radius. In Fig. 3.4, we plot median X-ray photon energy against nebular radius. In Fig. 3.5, which has no counterpart in K12, we further illustrated PN X-ray detections and nondetections in the form of plots of PN distances and ratios of [O III] to Hβ fluxes against nebular densities for all (59) ChanPlaNS sample PNe.

3.3.1 Cycle 14 detections of X-rays from PNe

We have detected five of the Table 3.1 PNe in diffuse X-ray emission: Hb 5, NGC 1501, NGC 3918, NGC 6153, and NGC 6369 (Fig. 3.2). The last four objects are first time detections; Hb 5 was detected previously by *XMM-Newton* (Montez et al., 2009, see below). These detections represent a $\sim$ 21% (5/24) detection rate of hot bubbles within the Cycle 14 sample. When these detections are combined with the previous ChanPlaNS observations, the ChanPlaNS detection rate of PNe hot bubbles now stands at $\sim$ 27% (16/59). Two of the newly detected objects, NGC 1501 and NGC 6369, host Wolf-Rayet-type (WR) CSPNe, which brings the ChanPlaNS diffuse detection rate of such objects to 100% (5/5). The detection rate of diffuse X-ray emission from [WR]-type CSPNe remains high when including PNe beyond $\sim$ 1.5 kpc (see Kastner et al., 2008). These diffuse X-ray detections follow the previously-established trend that diffuse X-ray PNe generally display

compact ($R_{\rm neb} \lesssim 0.15$ pc), elliptical optical morphologies (Fig. 3.3; K12). A notable exception is Hb 5, which has a bipolar morphology.

The Table 3.1 detections of X-ray point sources within three Cycle 14 PNe, HbDs1, NGC 6337, and Sp 1, constitutes a $\sim$ 13% detection rate of CSPNe within the recently observed Cycle 14 sample. These Cycle 14 detections bring the overall ChanPlaNS detection rate of CSPNe to $\sim$ 36% (21/59). Two of the three new CSPNe (within NGC 6337 and Sp 1) are known binaries, which brings the overall ChanPlaNS detection rate of all CSPN that are known to be binaries (as of writing this paper) to 60% (Table 3.4).

3.3.2 PNe displaying diffuse X-ray emission

The diffuse X-ray emitting PNe detected in the Cycle 14 sample are displayed in Fig. 3.2 and are described briefly below. As is evident in Figs. 3.3 and 3.4 and Table 3.4, these detections reinforce previous ChanPlaNS results indicating that PNe displaying diffuse X-rays are predominantly elliptical in morphology with $R_{\rm neb} \lesssim 0.15$ pc; furthermore, diffuse X-ray PNe generally lack detections of near-IR H_2 emission. In a forthcoming paper (Montez et al., 2015a, in prep), we present a global analysis of the ChanPlaNS diffuse X-ray sources. Here, we describe the properties of the diffuse X-ray PNe detected during Cycle 14 observations.

Classical hot bubbles

NGC 3918 appears to host multiple shells, and is similar in optical and X-ray morphology to multiple-shell, diffuse X-ray PNe such as NGC 6543 (K12). Three-dimensional models of the nebula vary in their interpretations of its morphology. Clegg et al. (1987) modeled NGC 3918 as a biconical nebula within an optically thin sphere, while a spindle-like structure was favored by both Corradi et al. (1999) and Ercolano et al. (2003). Like NGC 1501, the shell of the nebula shows enhanced [O III]/Hα emission resulting from the inner shell expanding into the outer shell (Guerrero et al., 2013), while the inner shell confines the diffuse X-ray emission.

NGC 6153 is also an elliptical nebula that hosts multiple shells, and is thought to be the product

of a high mass (4.5 $M_{\odot}$) progenitor (Pottasch & Bernard-Salas, 2010). Often compared to NGC 7009, NGC 6153 is indeed morphologically similar, both in the optical and X-ray; however NGC 6153 lacks the ansae found in NGC 7009. The diffuse X-ray emission is confined to the inner shell, as is the case with NGC 3918 and similar multiple-shell, diffuse X-ray PNe (K12).

PNe with [WR]-type CSPNe

Both NGC 1501 and NGC 6369 harbor [WR]-type central stars and diffuse X-ray emission. NGC 1501 is an elliptical nebula with a [WR]-type central star within a complex, filamentary internal structure. The central star has been reclassified many times between [WO] and [WC] type. Based on emission lines detected in the optical spectrum, the CSPN appears to be [WO4] (Crowther et al., 1998; Ercolano et al., 2004); however, the star also displays an infrared excess from J through all *Spitzer* IRAC bands, which is indicative of circumstellar dust, as is common for [WC]-type stars (Bilíková et al., 2012). NGC 1501 shows enhanced [O III]/Hα emission along the surface of the nebular shell, which is evidence for shocks along the skin (Guerrero et al., 2013). Similarly, the X-ray emission appears to trace shocks inside the primary nebular shell.

In contrast to the elliptical shell and filamentary internal structure of NGC 1501, NGC 6369 appears to have a spherical main nebular shell described as a barrel, with bipolar outflows (Ramos-Larios et al., 2012). This structure is similar to that of NGC 40 (Montez et al., 2005). Where [O III] and Hα are dim in NGC 6369, the nebula is bright in [N II], displaying a ring of emission along the inner shell. The bright optical shell is filled with H_2 and surrounded by a photodissociation region (Ramos-Larios et al., 2013), and the shell encloses the diffuse X-ray emission around the [WO]-type central star (Peña et al., 2013). The correspondence of the X-ray emission and the nebular shell, and lack of emission from the blowouts, suggests that emission is generated by the strong winds of the CSPN colliding with the progenitor red giant wind, as is the case for NGC 40 (Montez et al., 2005).

The bipolar planetary nebula, Hb 5

Hb 5 is a bipolar nebula with large lobes ($\sim 27''$) extending east and west and a tight waist with a bright core that contains secondary expanding lobes. The smaller lobes ($\lesssim 12''$) may result from an interaction between a fast, low-density wind and an inhomogeneous, high density circumstellar shell (López et al., 2012). Diffuse X-ray emission was previously detected serendipitously by *XMM-Newton* (Montez et al., 2009). The emission in the *XMM* images appeared coincident with the peak optical emission around the core and possibly along the Hα emission in the lobes, although *XMM*'s resolution was insufficient to determine if the X-ray emission is extended.

The recent *Chandra* observations also detected a bright, compact X-ray core, coincident with the peak optical emission. There is no apparent X-ray point source from the CSPNe contributing to the core emission. Additionally, X-ray emission was tentatively detected along the tip of the eastern lobe, which appears optically blueshifted, while no apparent emission is seen from the western, redshifted lobe which may be attributed to extinction by intervening nebular material (López et al., 2012).

3.3.3 PNe displaying point-like X-ray emission at central stars

The three Cycle 14 X-ray point source detections (HbDs1, NGC 6337, Sp 1) continue the trend, noted in K12, that soft ($\sim 0.6 - 1.0$ keV) X-ray sources likely indicate the presence of CSPN photospheric emission and/or wind shocks, while hard ($\gtrsim 1.0$ keV) sources appear related to the presence of binary companions to CSPNe (Fig. 3.4; Montez et al., 2015b, in prep). Below are brief summaries of each of the Table 3.1 PNe with newly detected point-like X-ray emission.

HbDs1 is an irregularly elliptical nebula around the hot blue star LSS 1362 ($T_{\rm eff} = 116$ kK; Herald & Bianchi, 2011). The nebula has enhanced Hα emission along its northern and southern limbs. The magnetic field properties of the CSPN have been debated. A kG field was inferred by Jordan et al. (2005, 2012) from spectropolarimetric data taken with the ESO Very Large Telescope; however, more recent FORS2 observations showed no evidence of such a strong field (with upper limits of $B < 600$ G; Leone et al., 2011; Bagnulo et al., 2012; Leone et al., 2014; Steffen et al., 2014).

The detected X-ray point source has a median energy of 0.65 keV, which may indicate self-shocking within the stellar winds previously detected at the CSPN (Herald & Bianchi, 2011; Guerrero & De Marco, 2013), possibly combined with photospheric emission (see Montez & Kastner, 2013).

NGC 6337 is seen as a ring nebula with radial filaments. This PN harbors a nearly face-on ($i \lesssim 15°$) close binary (0.17 d period) central star system (Hillwig et al., 2010). It is likely that the nebula is viewed nearly pole-on as well, suggesting a bipolar structure with a narrow waist around the binary (García-Díaz et al., 2009). The close binary is most likely the product of a common envelope phase (De Marco et al., 2011), leaving behind a pre-WD and a cool main-sequence star (Hillwig et al., 2010). The X-ray point source associated with this binary has a median energy of 1.27 keV, the hardest emission detected from a point source in the ChanPlaNS sample thus far. This hard X-ray detection provides strong support for a model in which the X-rays originate from a cool, coronally active companion (see §3.4.3).

Sp 1 appears similar to NGC 6337; this PN is also a diffuse ring on the plane of sky and harbors a close binary (2.9 d period) at its center (Bond & Livio, 1990; Jones et al., 2012; Bodman et al., 2012). Spatiokinematical modeling of the nebular shell shows that the nebula is a nearly pole-on hourglass shape (Jones et al., 2012). This is borne out by modeling of the CSPN by Bodman et al. (2012), which indicates a G0 or F8 main sequence companion with an orbital inclination of $10° < i < 20°$, consistent with the generation of a near pole-on nebula. UV spectra of the CSPN show evidence for stellar winds (Patriarchi & Perinotto, 1991), which could be at best partly responsible for the X-ray point source at the CSPN. However, the median energy for the X-rays from the Sp 1 CSPN is 0.93 keV, making it one of the harder X-ray sources in the ChanPlaNS sample, and suggesting that the companion dominates the detected emission.

3.3.4 X-ray nondetections

Table 3.3 lists the point source X-ray characteristics (net counts, count rates, median photon energies, and photon energy ranges) of each PN in the Cycle 14 sample. To obtain these results, the 0.3-3.0 keV background counts were extracted from a source-free region near the central star. These

background counts were scaled to the point source extraction radius of 3.5″, and then subtracted from the counts of the same extraction region centered on the CSPN, to obtain the net source counts (or source count upper limits). Sources with less than 6 net counts are classified as undetected. Two sources lie below this background-subtracted limit, Abell 65 and NGC 6026, but could be considered as tentative detections; there are $\sim$ 4 (source+background) counts found near their CSPNe, both of which have known companion stars. There are a few sources above the net count limit that we consider to be doubtful as point source detections: Hb 5, NGC 3918 and NGC 6369. Contamination from the diffuse X-ray emission in NGC 3918 makes it difficult to determine the contribution from a possible point source at the CSPN in the circular source region. NGC 6369 is a luminous, albeit reddened, PN that lies near the limit of our volume-limited sample, at a distance of 1.55 kpc (Monteiro et al., 2004). Additionally, the diffuse X-ray emission of NGC 6369 is not concentrated at the CSPNe, which makes it unlikely to contaminate a point source detection. Finally, as previously noted, Hb 5 appears to have no point-like emission within the CSPN extraction region.

Several PNe that were undetected appear to fit within morphology trends typical of previous ChanPlaNS point source and diffuse X-ray detections. IC 5148/50 is undetected, yet it has a morphology similar to Sp 1, suggesting that it may be a pole-on hourglass and, hence, could be the product of a binary system. In optical images, NGC 6894 has the multiple-shell structure of a hot bubble from which we would expect to see diffuse X-ray emission, though it is important to note that the central star is faint and on the WD cooling track. Similarly, NGC 7354 hosts multiple elliptical shells and ansae, similar to NGC 3918 and NGC 6153; however no X-ray photons were detected from the innermost bubble of NGC 7354. These nondetections appear to place stringent limits on the timescales for X-ray emitting hot bubbles within PNe (§3.4.2) − although we note that NGC 7354 is quite heavily reddened and, hence, any soft X-rays from its interior might suffer considerable absorption.

The objects with no detectable X-ray emission have varying morphologies (round, elliptical, bipolar), with at least half exhibiting inherent asymmetries. IC 4637 is an example of a PNe that

falls within the range of nebular properties for the diffuse X-ray detections (K12), but was not detected. Specifically, IC 4637 has a radius of 0.05 pc and elliptical morphology (Frew, 2008). Additionally, IC 2149 is a young, compact bipolar nebula with an elliptical central shell and may be the product of a low mass progenitor and/or binary evolution (Vázquez et al., 2002). Upper limit estimates for X-ray luminosity L_X for each of these sources (Montez et al., 2015a, in prep) will help place constraints on the sizes, plasma densities, and morphologies of X-ray emitting nebulae.

3.4 Discussion

The sample of 59 PNe within $\sim$ 1.5 kpc observed to date by *Chandra* constitutes a representative set of X-ray observations of mostly compact and, hence, predominately relatively young PNe within the solar neighborhood. Adding the 24 PNe observed in Cycle 14 to the initial sample (see K12) reduces the overall PN X-ray detection rate from $\sim$ 70% to $\sim$ 54% (32/59). This decrease most likely reflects the composition of the initial ChanPlaNS sample; these objects were chosen based on the presence of bright high excitation lines indicative of hot CSPNe ($T_{\rm eff} \gtrsim 10^5$ K) and/or structure that resulted from rapid evolution (K12), while the Cycle 14 objects were chosen to complete the X-ray census of compact ($R_{\rm neb} < 0.4$ pc) PNe within $\sim$ 1.5 kpc. Nevertheless, the Cycle 14 results underscore trends apparent in the X-ray properties of PNe, as we discuss in the following subsections.

3.4.1 Diffuse X-ray emission from [WR]-type CSPNe

The CSPNe that are H-deficient and display spectroscopic evidence for fast stellar winds and high mass-loss rates (up to 10^{-6} $M_\odot$ yr^{-1}; Crowther et al., 1998; DePew et al., 2011) are classified as [WR]-type because of their similarity, as a class, to luminous WR stars. The primary difference between the two classes is that the [WR]-type stars descend from intermediate mass (1-8 $M_\odot$) stars, whereas "classical" WR stars are the descendants of massive ($>$ 25-30 $M_\odot$) stars (Crowther et al., 2006). In total there are 5 known [WR]-type CSPNe in the ChanPlaNS sample: NGC 1501 and

NGC 6369 from Cycle 14 (Table 3.1), as well as NGC 40, NGC 2371, and BD +30°3639 from Cycle 12 and archival observations (K12). All 5 of these [WR]-type CSPN objects display diffuse X-ray emission. The only consistent morphological similarity among all of the [WR] type CSPNe is that their main bubbles appear elliptical (Frew, 2008). In each case, the diffuse X-ray emission is enclosed by the central optical bubble, although the morphology of the X-ray emission varies considerably from object to object.

BD +30°3639: The unusually bright, diffuse emission fills the central bubble, perhaps as a consequence of its very young age ($\sim 10^3$ yr; Frew, 2008).

NGC 40: The emission appears within a partial ring that traces the inner edge of the bright optical rim of the nebula (Montez et al., 2005).

NGC 2371: The diffuse emission is contained within the bright nebular rim but does not seem to follow any significant optical feature, and is highly asymmetric.

NGC 1501: The X-ray emission traces the rim of the nebula, echoing the limb-brightened morphology of WR star wind-blown bubble S308 (Toalá et al., 2012).

NGC 6369: The diffuse emission is asymmetrical and strongest along the northern limb of the central bubble.

The X-ray results for most of the above PNe, with the possible exception of NGC 2371, reveal some potential similarities between PNe with [WR]-type CSPNe and the wind-blown bubbles of massive WR stars. When massive ($\geq 10\,M_{\odot}$) stars enter the WR evolutionary phase, they are subject to copious mass loss through stellar winds (Crowther, 2007), thereby enriching the interstellar medium (ISM) in the products of nucleosynthesis. Depending upon the initial mass of the star, WR wind speeds can be quite high ($v_w > 1000$ km s^{-1}; Wrigge & Wendker, 1996). WR star progenitors have masses in the range 25-75 $M_{\odot}$ (Crowther, 2007); thus, most are believed to remain in the general area where they are formed, where remnants of the clouds from which they were created still exist, allowing for the energetic WR stellar winds to sweep up the surrounding ISM. The large

wind speeds and high mass loss rates (10^{-6} to 10^{-5} $M_{\odot}$ yr^{-1}) of WR stars thereby evacuate large cavities consisting of hot ($\sim 10^6$ to 10^7 K) shocked wind gas within the swept-up ISM shell (Wrigge & Wendker, 1996).

Observations of wind-blown bubbles have only revealed diffuse X-rays in two in objects, NGC 6888 and S 308. These two are described as having temperatures on the order of 10^6 K with luminosities around 10^{34} ergs s^{-1} resulting from a limb brightened morphology (Toalá & Arthur, 2011a). The diffuse X-rays are emitted by the cooling of the hot WR wind as it comes in contact with the cool ISM, as predicted by the model of stellar bubbles described by Weaver et al. (1977). Toalá & Arthur (2011b) describe two different models for emission used to explain the lack of detection of X-rays from other bubbles. The first model suggests that the X-ray emission is the result of a short-lived phase of the wind-blown bubble evolution, during the early stages of its formation as is suspected in PNe. The second model posits that there is soft X-ray emission present, however strong absorption due to neutral hydrogen is responsible for the lack of detection. Based on simulations performed by Toalá & Arthur (2011a), they find that the first model describes the case where the red supergiant (RSG) wind does not make it far from the WR star, and breaks up into clumps which interact with the shocked fast wind, heating up the gas to X-ray temperatures of millions of Kelvin. The problem with this model is that it requires we catch the wind-blown bubble in this early phase, which would suggest that most bubbles we find are past this phase in their evolution. In the second model they find that the RSG wind isn't as dense and expands further from the star, pushing the interaction region out to the limb of the bubble, as seen in NGC 6888 and S 308. Here they suggest that the soft X-ray emission is not observed because of absorption by surrounding nebular gas, which is also a problem for the first model if such a wind-blown bubble were in its earliest phase.

The X-ray limb-brightening in massive WR star wind-blown bubbles, such as S308, is the result of the hot WR wind cooling as it comes in contact with the the previously ejected red (or yellow) supergiant or luminous blue variable material (García-Segura et al., 1996a,b; Freyer et al., 2003; Toalá & Arthur, 2011b; Toalá et al., 2012; Dwarkadas & Rosenberg, 2013). A similar process occurs

in PNe, wherein the X-ray emission is contained within the ejected AGB envelope and does not come in direct contact with the ISM. The question remains: *is the diffuse X-ray emission from [WR] CSPNe limb-brightened or not?* We explore this question further in Chapter 4.

3.4.2 Diffuse X-ray emission and PN size, age, and electron density

The diffuse X-ray emission from hot bubbles in PNe is evidently confined to early phases in PN evolution. In K12, we pointed out that the central bubbles of PNe with diffuse emission tend to have elliptical, nested-shell morphologies and radii $\lesssim 0.15$ pc (Fig. 3.3 and Tables 3.1 and 3.4). This radius limit corresponds to dynamical ages $\lesssim 5 \times 10^3$ yr, roughly a quarter of the $(21 \pm 5) \times 10^3$ yr mean visibility time of PNe (Jacob et al., 2013). Our Cycle 14 detections and nondetections thereby reinforce the inference, made in K12, that diffuse X-ray emission is restricted to the most compact nebulae. We note that the correlation of diffuse X-rays with elliptical morphology is ambiguous (Table 3.4), but it remains the case that PNe with closed structures (whether bubbles or lobes) are more likely to be detected as diffuse X-ray sources.

From Fig. 3.5 we see, furthermore, that with the exception of NGC 2371, all ChanPlaNS PNe with diffuse X-ray emission have nebular densities $n_e \gtrsim 1000$ cm^{-3}, as determined via their Hα line luminosities and nebular radii which are in turn determined from the Hα surface brightness vs. radius relation (Frew, 2008; Frew et al., 2014b). In contrast, the diffuse X-ray detection rate is essentially independent of distance and nebular excitation. Since PN density and radius are correlated, the remarkably sharp n_e boundary between diffuse X-ray detections and nondetections in Fig. 3.5 further underscores the notion of a limit on the timescale for energetic (nebula-shaping) wind interactions in PNe. Moreover, Fig. 3.5 suggests that, from spectroscopy of density-sensitive lines (e.g. [OII], [SII]), it is possible to ascertain whether a PN might currently be in a wind-collision phase, when we would expect to see diffuse X-ray emission. Nevertheless, the duration of the wind-interaction phase is a complex problem that must account for (1) luminosity of the central star (e.g. Hb 5 high, NGC 5148 low), (2) expected hydrogen column density, and (3) spectral type of the central star (i.e. whether [WR] or not).

This density limit may explain the X-ray nondetection of nebulae like NGC 6894 and NGC 6804 (K12), which appear morphologically similar to known diffuse X-ray emitters. NGC 6894 has a nebular radius of 0.17 pc and NGC 6804 has a nebular radius of 0.19 pc, both of which have a density $\log n_e \sim 2.7$. Thus, evidently, both NGC 6894 and NGC 6804 lie close to, but just below, the $\log n_e$ X-ray detection threshold. It is important to keep in mind that electron density is not a good indicator of PN evolutionary state. Fast evolving stars achieve low luminosities at still quite high nebular densities, but remain undetected in diffuse X-rays (Steffen et al., 2008). Upper limit estimates and observations of additional nebulae similar to these − with $n_e \gtrsim 1000$ cm^{-3} and closed optical morphologies (multiple shells, well-defined inner bubbles) − will allow us to answer questions about diffuse emission such as: *What is the lifetime of the hot bubble shaping phase? How does it relate to the mass of the CSPN progenitor? What is the relationship between diffuse X-ray emission and the final mass of the core, i.e. the WD remnant?* We aim to revisit the question of diffuse X-ray dependence on age in Chapter 4 (also see Schönberner et al., 2014; Montez et al., 2015a, in prep.).

3.4.3 Binary detections/nondetections

Six additional known binary CSPNe were observed in Cycle 14, all of which are close binaries ($p < 3$ d). Two of these six, NGC 6337 and Sp 1, had detectable point source X-ray emission. Both PNe appear to have nearly pole-on hourglass structures. The median energy for both point sources is relatively hard ($\gtrsim 1.0$ keV), which implies that the CSPN X-ray emission is due to late-type companions that display elevated levels of coronal activity. These binary, X-ray-luminous CSPNe are therefore similar to the CSPNe in DS 1, HFG 1, and LoTr 5, which are thought to be systems in which mass transfer from PN progenitor to late-type companion has spun up the companion (Jeffries & Stevens, 1996; Soker & Kastner, 2002; Montez et al., 2010); alternatively, in many or most of these cases of X-ray-emitting binary CSPNe, it is possible the coronal activity of the companion is due to tidal locking that has resulted in rapid, synchronous rotation (a possibility we further explore in Montez et al., 2015b). NGC 6337 and Sp 1 represent the two most compact (and

therefore youngest) PNe harboring X-ray point sources at known binary CSPNe in the ChanPlaNS sample (Fig. 3.4). The periods of the close binaries within Abell 65 (1.00 d; Bond & Livio, 1990; Shimansky et al., 2009; Hillwig et al., 2015), He 2-11 (0.61 d; Jones et al., 2014b), and NGC 6026 (0.53 d; Hillwig et al., 2010) lie between those of NGC 6337 (0.17 d; Hillwig et al., 2010) and Sp 1 (2.91 d; Bond & Livio, 1990), but no point source X-ray emission was detected from the former three PNe. This leaves us with unanswered questions: *What is the relationship between binary period/separation and X-ray point source emission? What are the characteristics of secondaries within binaries that do exhibit X-ray emission?*

IC 5148/50 is a potentially significant nondetection, given its morphological similarity to Sp 1. Based on imagery alone, Sp 1 appears to have a spherical morphology, but spatiokinematcial modeling reveals this is a projection effect and its intrinsic shape is that of a pole-on hourglass (Jones et al., 2012). Such bipolar structures are likely to be the products of binary interactions (see, e.g., Balick & Frank, 2002, and references therein). The nondetection of IC 5148/50 may indicate that, while it is morphologically similar to Sp 1, structurally it may be quite different. From Hα, [N II], and [O III] observations (Hua et al., 1998) it is clear that IC 5148/50 hosts not only internal elliptical structure but also a helical structure. Observations of H_2 (Kastner et al., 1996) and/or spatially resolved, high-resolution emission line spectroscopy (for use in spatiokinematical modeling) are necessary to determine whether or not IC 5148/50 has inherently bipolar vs. elliptical structure. The CSPN of IC 5148/50 also has no infrared excess indicative of an unresolved cool companion (De Marco et al., 2013; Douchin et al., 2014).

It is possible that many other, similarly X-ray-luminous CSPN have gone undetected in our sample of PNe. From Fig. 3.5 we see that the fraction of PNe with detected point-like X-ray emission is strongly dependent on distance. All sample PNe within $\lesssim$ 0.6 kpc have point-like emission, whereas beyond 1.3 kpc the detection fraction drops to $\sim$ 35%. This drop in detection fraction is likely the result of increased interstellar extinction obscuring the softer X-ray point sources, and furthermore implies that we lack the sensitivity necessary to detect even the (harder) binary CSPNe at distances much beyond $\sim$ 1 kpc. Further discussion concerning the implications

of the distance dependence of the X-ray detection rate of CSPNe can be found in Montez et al. (2015b).

3.5 Chapter Summary

We present results from the most recent set of observations obtained by the *Chandra* Planetary Nebula Survey (ChanPlaNS), the first comprehensive X-ray survey of PNe in the solar neighborhood (within $\sim$ 1.5 kpc). The survey was designed to place constraints on the frequency of appearance and range of X-ray spectral characteristics of X-ray-emitting PN central stars and the evolutionary timescales of wind-shock-heated bubbles within PNe. ChanPlaNS began with a combined Cycle 12 and archive *Chandra* survey of 35 PNe. ChanPlaNS continued via a *Chandra* Cycle 14 Large Program which targeted all (24) remaining known compact ($R_{\rm neb} \lesssim 0.4$ pc), young PNe that lie within $\sim$ 1.5 kpc. The highlights of the ChanPlaNS Cycle 14 results include the following:

- The overall X-ray detection rate for relatively compact ($\lesssim$ 0.4 pc) PNe within $\sim$ 1.5 kpc observed thus far by *Chandra* is $\sim$ 54%.
- Nearly 40% of the ChanPlaNS sample PNe host X-ray-luminous point sources at their CSPNe. This includes three new detections of CSPNe X-ray sources within the Cycle 14 sample PNe.
- Roughly 60% of the known binaries within the ChanPlaNS sample display point-like X-ray emission, including first-time Cycle 14 detections of X-rays from the CSPNe of NGC 6337 and Sp 1.
- All PNe with [WR]-type CSPN within the ChanPlaNS sample observed thus far (BD +30°3639, NGC 40, NGC 2371, NGC 1501, NGC 6369) display diffuse X-ray emission. With the exception of NGC 2371, all of these PNe have elliptical morphologies. In each case,

the diffuse X-ray emission resembles the limb-brightened morphology of wind-blown bubbles blown by massive WR stars.

- The addition of the Cycle 14 results brings the overall ChanPlaNS diffuse X-ray detection rate to $\sim 27\%$.

- It has become clearer that diffuse X-ray emission is associated with young ($\lesssim 5 \times 10^3$ yr) PNe with compact ($R_{\rm neb} \lesssim 0.15$ pc), closed structures and high central electron densities ($n_e \gtrsim 1000$ cm^{-3}). Typically, such nebulae display nested-shell elliptical morphologies and rarely show H_2 emission and/or pronounced butterfly structures. Hb 5 is a notable exception.

- The ChanPlaNS detection rate of diffuse X-ray emission from PNe within ~ 1.5 kpc appears largely independent of distance and excitation, if the latter is measured via the flux ratio of [O III] and Hβ lines.

- In contrast, the ChanPlaNS detection rate of point-like X-ray emission from PNe within ~ 1.5 kpc appears strongly dependent on distance, reflecting the relatively low intrinsic X-ray luminosities of CSPNe combined with the effects of interstellar extinction.

We note that in addition to the need to acquire data for a larger sample of PNe − particularly high-n_e PNe and those harboring known binary central stars − we must carry out estimations of upper limits on L_X in order to reaffirm our claims and to properly answer our open questions. Further analysis of these and future ChanPlaNS data and results describing both point-like X-ray emission from CSPNe (Montez et al., 2015b) and diffuse X-ray emission from PNe (Montez et al., 2015a, in prep) will continue to refine models of PN shaping mechanisms, X-ray emission timescales, and the role of binarity in PN formation and evolution.

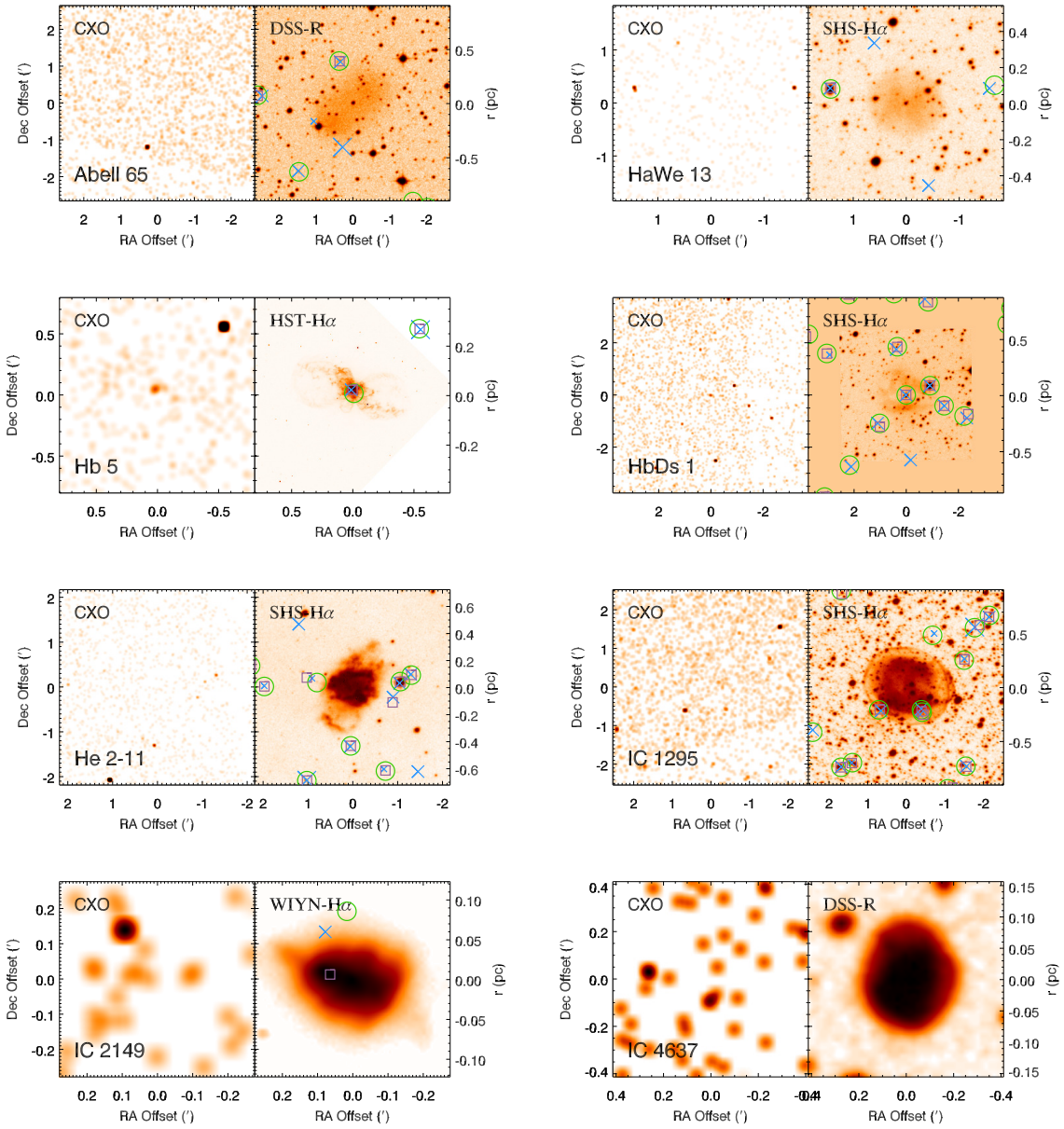

Figure 3.1: ChanPlaNS pipeline output for the Table 3.1 PNe. Two panels are presented for each PN. The *left panel* of each pair shows the *Chandra*/ACIS soft-band (0.3-2.0) keV image, smoothed with a Gaussian function with 3″ FWHM (1″ FWHM for M 1-26, or 6″ FWHM for images larger than 5′ on a side), centered on the SIMBAD coordinates of the PN (which lies on back-illuminated CCD S3). The *right panel* shows an optical image (obtained from *HST*, WIYN, the SuperCOSMOS H-alpha Survey, or the DSS, as indicated) overlaid with the positions of detected broad-band (0.3-8.0 keV) X-ray sources (crosses), USNO catalog stars (circles), and 2MASS Point Source Catalog IR sources (squares). The size of the cross is proportional to the number of X-ray photons detected.

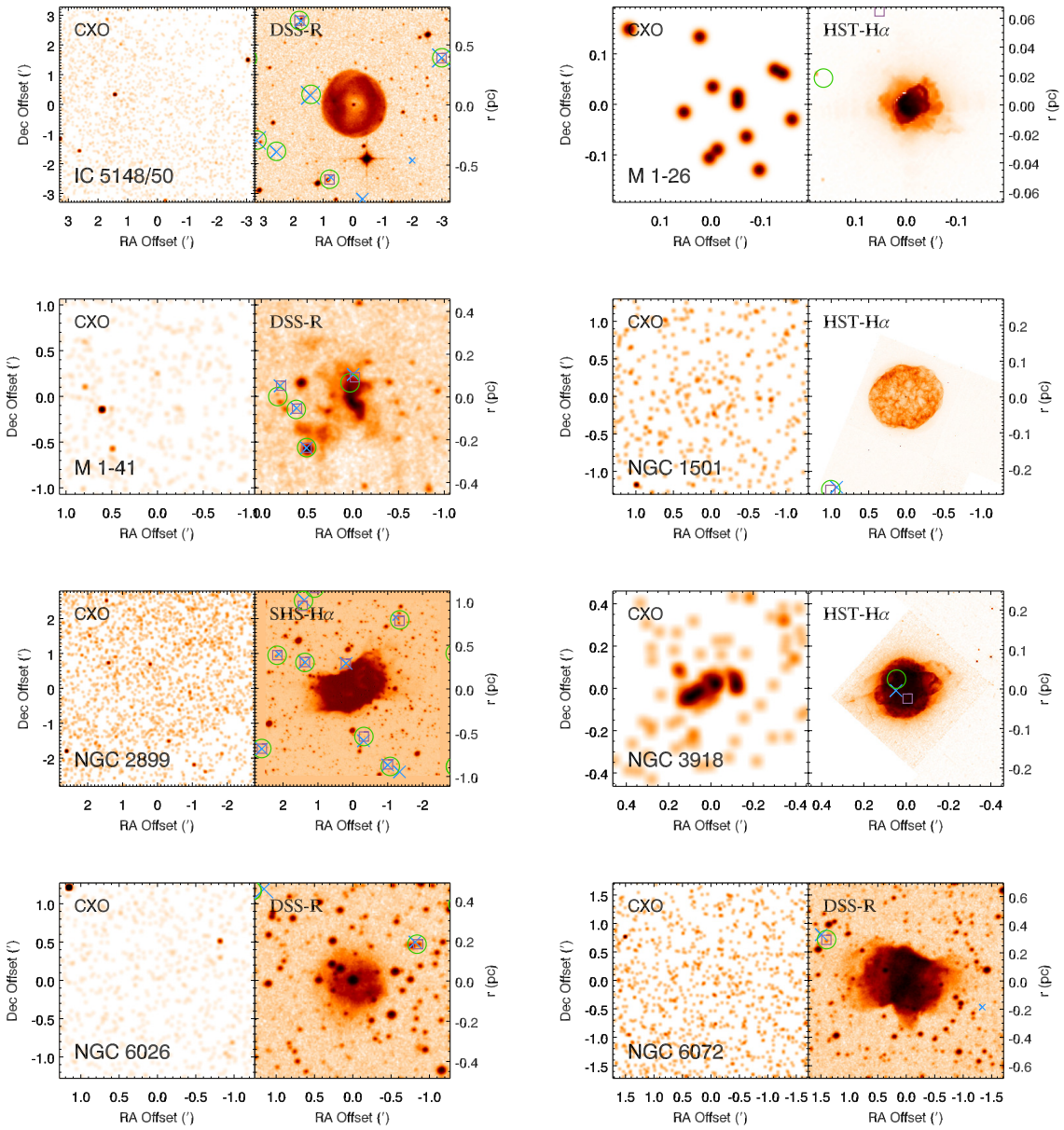

Figure 3.1: (cont.)

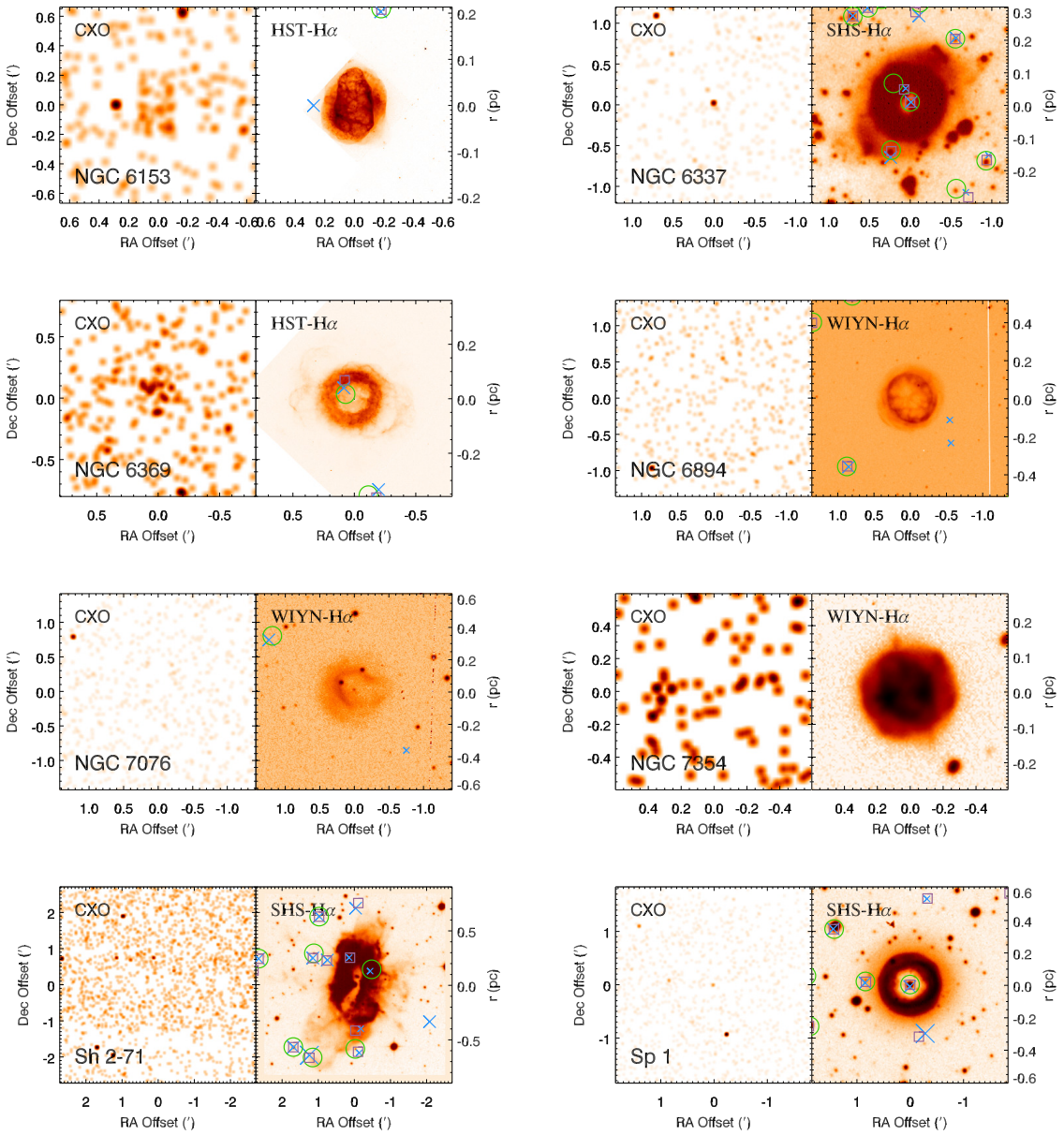

Figure 3.1: (cont.)

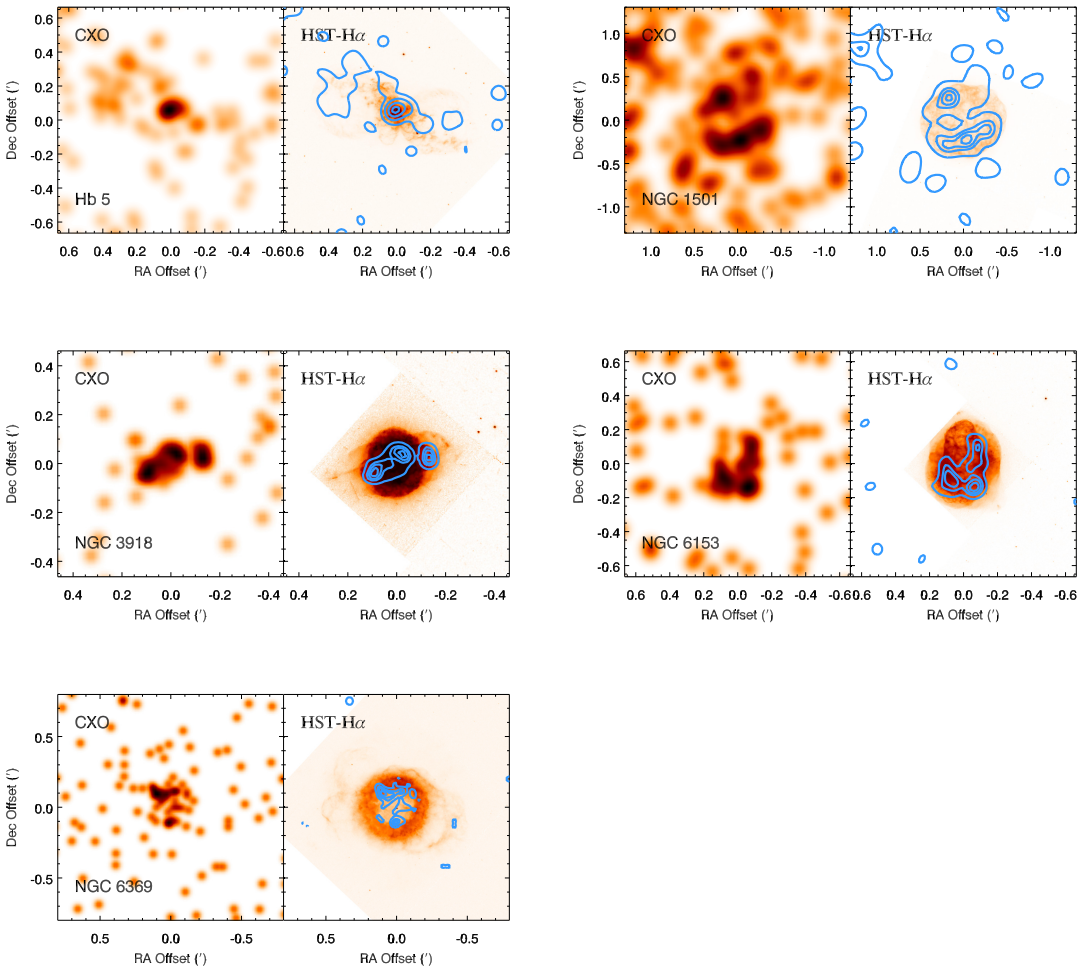

Figure 3.2: Images of Table 3.1 PNe in which diffuse X-ray emission has been detected by *Chandra*. The left and right panel for each PN display, respectively, *Chandra* 0.5-1.2 keV images filtered to efficiently remove the soft background and *Chandra* contours overlaid on optical images. The *Chandra* images of Hb 5, NGC 1501, and NGC 6153 have been smoothed with a 12.5″ FWHM Gaussian, while the *Chandra* images of NGC 3918 and NGC 6369 have been smoothed with a FWHM of 3″. The contour levels of all but Hb 5 are 30, 60, 75, and 90% of the maximum X-ray surface brightness (Hb 5 has contour levels of 10, 30, 60, and 90%).

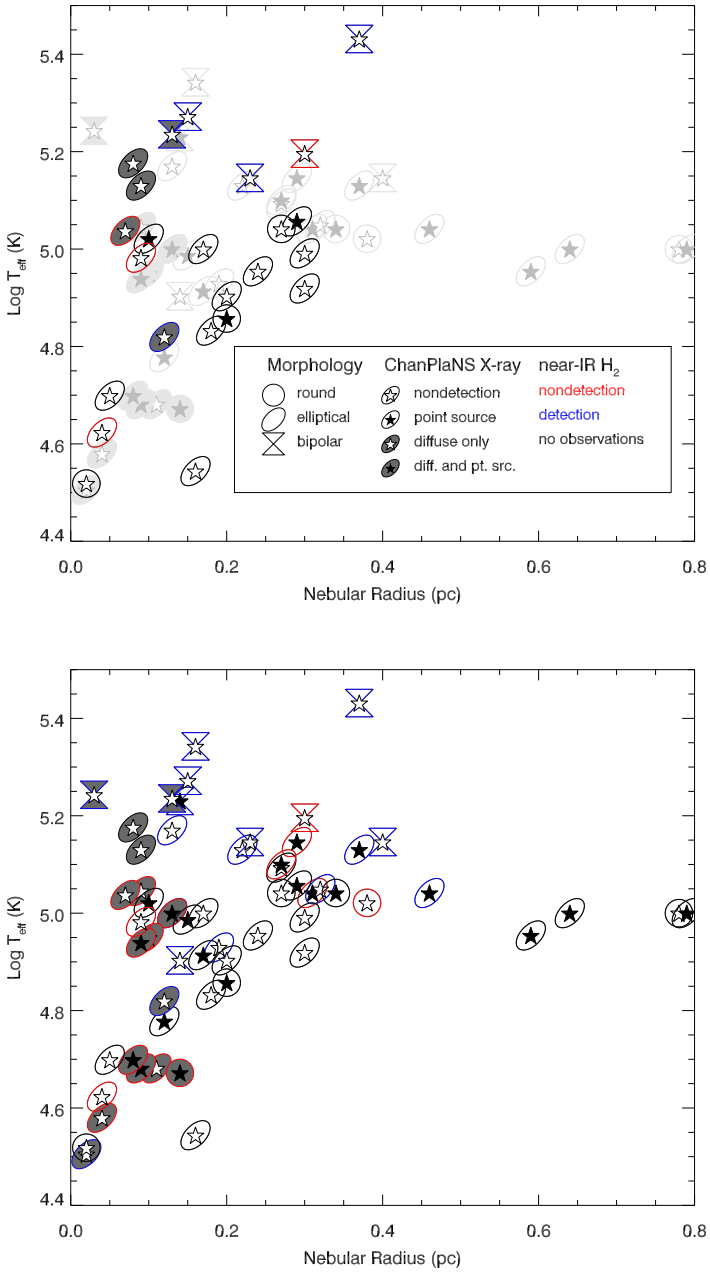

Figure 3.3: Plots of CSPN $T_{\rm eff}$ vs. PN radius for all ChanPlaNS observed objects, with symbols indicating presence or absence of diffuse or point-like X-ray emission, as well as PN morphology and presence or absence of H_2 emission. In the top panel, the highlighted objects represent Cycle 14 data and the light gray objects represent Cycle 12 and archival data (K12).

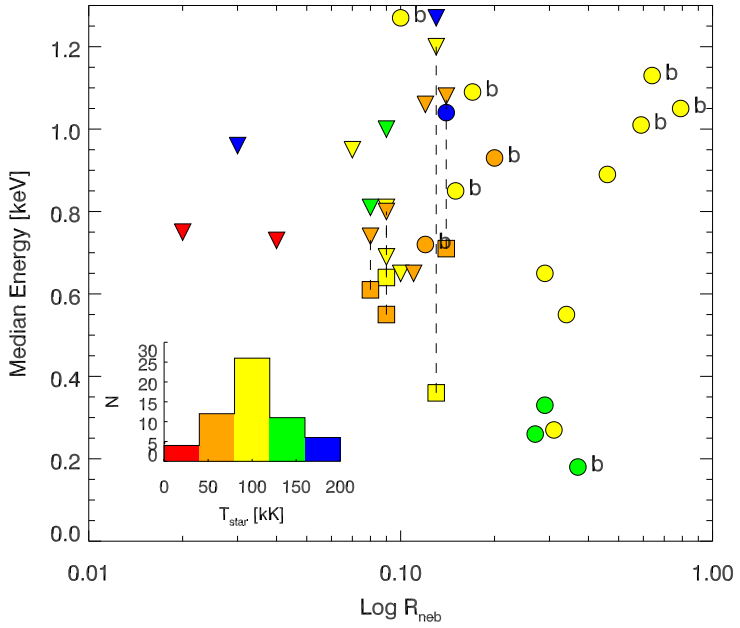

Figure 3.4: Median X-ray photon energy vs. nebular radius for all Cycle 12+14+archival sample PNe detected as X-ray sources. Symbol shapes indicate the nature of the PN X-ray source (triangles: diffuse sources; circles: CSPN point sources; squares: diffuse+CSPN sources) and are color-coded according to CSPN $T_{\rm eff}$, whose distribution for the observed sample is shown in the inset histogram. Known binary CSPNe are indicated by "b". The dashed line connects the diffuse+CSPN emission with the corresponding diffuse emission for sources that exhibit both types of emission.

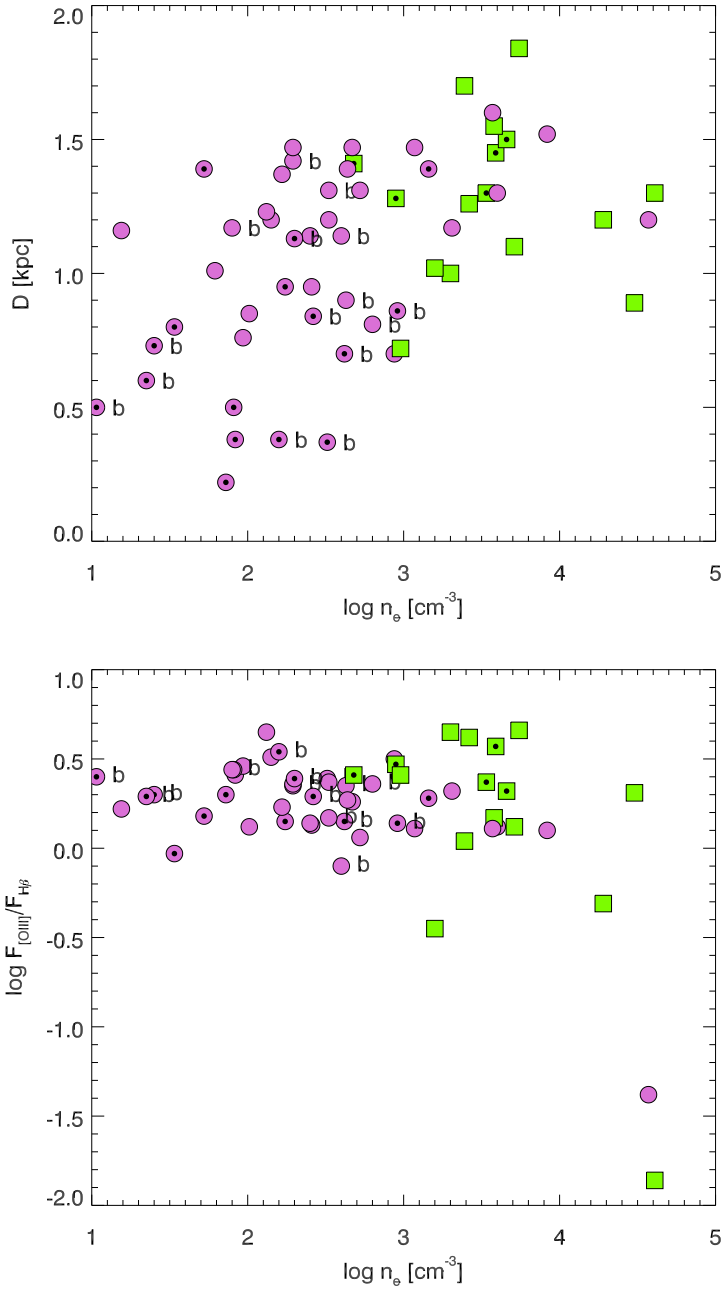

Figure 3.5: Distance (*top*) and ratio of [O III] to Hβ fluxes (*bottom*) vs. the log of electron density n_e for PNe detected (green squares) and not detected (purple circles) as ChanPlaNS diffuse X-ray sources. A bullet within each symbol indicates that the CSPNe was detected as a point-like X-ray source. A "b" next to a symbol indicates the CSPN is a known binary.

CHAPTER 4

MODELING DIFFUSE X-RAY EMISSION OF PLANETARY NEBULAE

4.1 Introduction

The myriad of PNe morphologies are in part the result of shaping caused by the proto-WD wind. Once the AGB star has exhausted its fuel, it sheds its outer envelope, revealing the hot core which ionizes the AGB ejecta. The fast (500-1500 km s^{-1}) wind of the proto-WD collides with the AGB material, sweeping it up into a dense shell. This collision of the fast wind with the AGB ejecta causes shocks which reach temperatures $> 10^6$ K, capable of emitting soft X-rays ($0.3 \sim 1$ keV).

The *Chandra* Planetary Nebula Survey (ChanPlaNS), an X-ray survey of PNe in the solar neighborhood, has revealed that close to 30% of all PNe display diffuse X-ray emission from the hot bubble (see Chapter 3; Kastner et al., 2012). The morphology of this emission is an intriguing mystery. The formation of a PN hot bubble is expected to share many similarities with those of wind-blown bubbles from massive WR stars, which display diffuse X-ray emission that appears brighter towards the inner edge of the optical emission (e.g. García-Segura et al., 1996b,a; Freyer

et al., 2003; Toalá & Arthur, 2011b; Toalá et al., 2012; Dwarkadas & Rosenberg, 2013). This is a result of the density profile of the central stellar wind, which increases sharply as it plows into the surrounding material along the the rim of ionized gas. The diffuse X-ray emission of PNe only appear to share this morphology in particular cases like NGC 40, while others like BD+30°3639 darken towards the limb of the bubble. It is unclear as to whether this range of X-ray morphologies reflects different intrinsic structures for the shocked fast wind gas in different PNe, or is due to different degrees of absorption by the dense swept-up shell.

The metals in the ionized region serve as efficient absorbers of X-rays, concealing the true X-ray flux and emission shape. X-ray spectral analysis can offer some insight into the impact of the absorbing column $N_{\rm H}$ that obscures the emission, but the source of the absorption has yet to be clearly defined as nebular or interstellar. Typically, the $N_{\rm H}$ values determined from X-ray spectra are higher than assumed from reddening measurements based on Hβ (Frew, 2008; Montez et al., 2015a, in prep). This suggests enhanced metal abundances in the absorbing material, but does not offer much insight into its nature or location with respect to the PN X-ray source.

To address the question raised in Chapter 3 concerning the intrinsic structures of the diffuse X-ray emitting regions of PNe, we constructed basic models for 14 of the ChanPlaNS PNe with detected diffuse X-ray emission, four of which host [WR]-type central stars (CSPNe) (Table 4.1). We created a two-phase, spherically symmetric model of the PNe, consisting of a hot bubble interior (X-ray emitting region) and a shell of swept-up AGB material (absorbing material). By varying the density of the swept-up shell we can study the effect on the projected X-ray radial emission profile (REP) and determine the best fit for each PN. This also allows us to estimate the mean density of the shell, as well as the approximate hydrogen column density, $N_{\rm H}$, of the shell itself.

In §4.2 we will briefly overview the subsample of targets selected for modeling, followed by a description of the two-phase model in §4.3. We will discuss our *SHAPE* toy model and data analysis methods in §4.4, which will include information about the *Chandra* data we will be comparing our models with. In §4.5 we will present the results of our analysis, followed by discussion of these results in §4.6. Lastly, we will summarize the chapter in §4.7.

4.2 Target CSPNe

Table 4.1: ChanPlaNS PNe within 1.5 kpc[a] with Diffuse X-ray Emission

No.	Name	PN G	morph.[b] (F08/SMVII)	D (kpc)	R (pc)	age (10^3 yr)	T_* (kK)	sp. type	comp.[c]	H_2[d]	X-rays[e]
1	BD+30°3639	064.7+05.0	Er/Ecsarh	1.30	0.02	1	32	[WC9]	...	Y	D[f]
2	IC 418	215.2−24.2	Em(h:)/Ecspih	1.20	0.04	3	38	Of(H)	...	N	D
3	NGC 40	120.0+09.8	Eas(h)/Bbsh	1.02	0.11	4	48	[WC8]	...	N	D[g]
4	NGC 1501	144.5+06.5	Es/Esph	0.72	0.09	2	135	[WC4]	...	...	D
5	NGC 2392	197.8+17.3	Rm/Rsai	1.28	0.14	3	47	Of(H)	dm?	N	D,P
6	NGC 3242	261.0+32.0	Em(h)/Ecspaih	1.00	0.10	4	89	O(H)	...	N	D
7	NGC 3918	294.6+04.7	Ems(h)/Lsbairh	1.84	0.08	3	150	O(H)?	...	...	D
8	NGC 6153	341.8+05.4	Es/Esah	1.10	0.07	4	109	wels	...	N	D
9	NGC 6369	002.4+05.8	Ebpr(h:)/Mcst	1.55	0.12	3	66	[WO3]	...	...	D
10	NGC 6543	096.4+29.9	Emps(h)/Mcspa	1.50	0.09	5	48	Of-WR(H)[h]	...	N	D,P[i]
11	NGC 6826	083.5+12.7	Emp(h)/Ecsah	1.30	0.08	5	50	O3f(H)	...	N	D,P
12	NGC 7009	037.7−34.5	Emps(h)/Lbspa	1.45	0.09	3	87	O(H)	...	N	D,P
13	NGC 7027	084.9−03.4	Bs/Mctspih	0.89	0.03	1.4	175	...	...	Y	D[j]
14	NGC 7662	106.5−17.6	Emp(h)/Esah	1.26	0.09	3	111	O(H)[k]	...	N	D

Notes.
[a]PN and central star data compiled from Frew (2008), and references therein.
[b]Morphologies as listed in Frew (2008) (F08): B: bipolar, E: elliptical, R: round, a: asymmetry present, b: bipolar core present, f: filled (amorphous) center, m: multiple shells present, p: point symmetry present, r: ring structure dominant, s: internal structure noted, (h): distinct outer halo. Morphologies following an abbreviated and very slightly modied version of the classification system described in Sahai et al. (2011) (SMV11; see their Table 2): B: bipolar, M: multipolar, E: elongated, I: irregular, R: round, L: collimated lobe pair, S: spiral arm, c: closed outer lobes, o: open outer lobes; s: CSPN apparent, b: bright (barrel-shaped) central region, t: bright central toroidal structure; p: point symmetry, a: ansae, i: inner bubble, h: halo; r: radial rays; (/): alternate possibilities.
[c]"(Y)" = known binaries with unknown companions types; "(Y?)" = possible binary; otherwise the type of the companion star is as listed (De Marco, 2009).
[d]"Y" = near-IR H_2 detected; "N" = near-IR H_2 not detected (Bernard-Salas & Tielens, 2005; Bohigas, 2001; Webster et al., 1988; Ramos-Larios et al., 2013; Kastner et al., 1996, and references therein).
[e]X-ray results key: P = point source; D = diffuse source.
[f](Kastner et al., 2000)
[g](Montez et al., 2005)
[h](Mendez et al., 1990)
[i](Chu et al., 2001; Guerrero et al., 2001)
[j](Kastner et al., 2001)
[k](Herald & Bianchi, 2011)

ChanPlaNS established that nearly 30% of PNe observed by *Chandra* display diffuse X-ray emission (see Chapter 3). The objects in Fig. 4.1 and Table 4.1 represent 14 compact ($R_{\rm neb} \lesssim 0.15$ pc) PNe from the ChanPlaNS sample that display such emission. These PNe were originally chosen for the ChanPlaNS sample for either their compact size or because they are considered "high-excitation" objects with hot central stars. Together, this sample includes PNe with varying

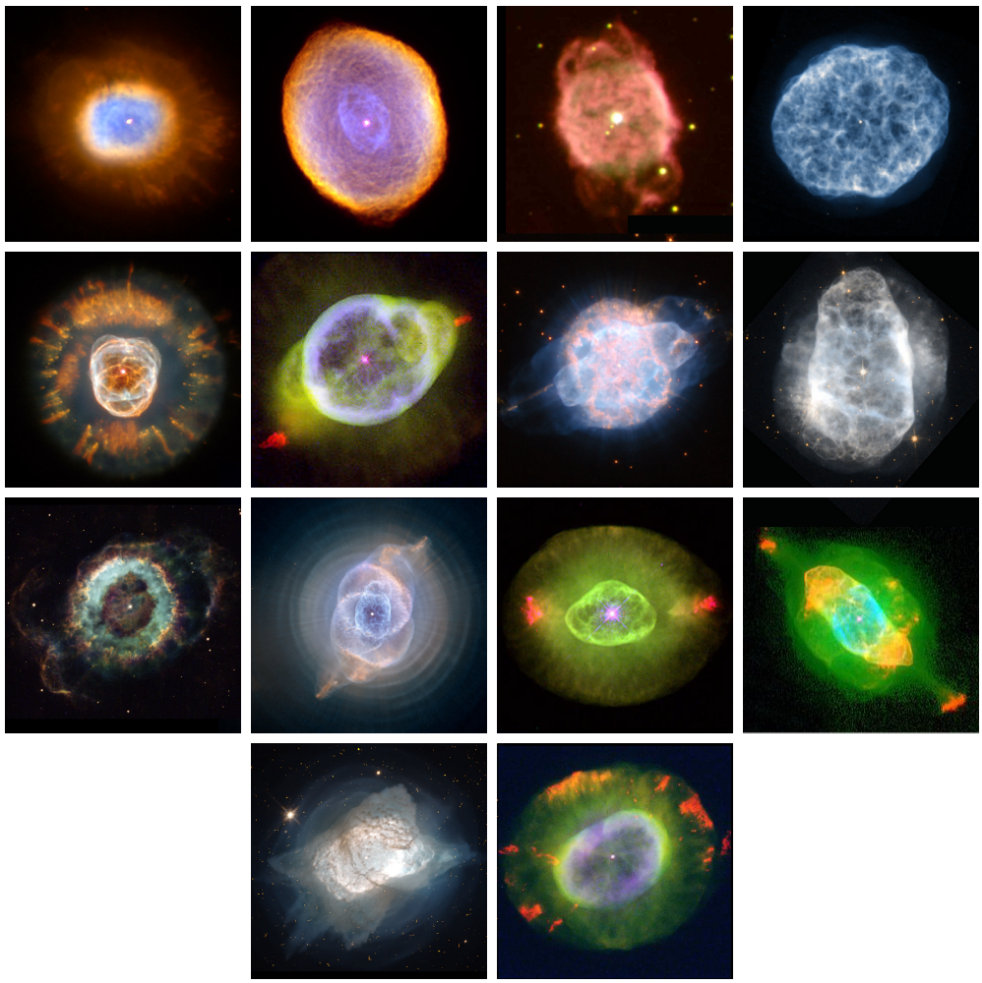

Figure 4.1: Images of Table 4.1 PNe (credit: HST/NASA/ESA). Top row, left to right: BD+30°3639, IC 418, NGC 40 (NSF/AURA/NOAO/WIYN), and NGC 1501. Second row, left to right: NGC 2392, NGC 3242, NGC 3918, and NGC 6153. Third row, left to right: NGC 6369, NGC 6543, NGC 6826, and NGC 7009. Bottom row, left to right: NGC 7027 and NGC 7662.

physical parameters that can provide insight into the wind-shaping phase of PN evolution which is characterized by the presence of diffuse X-ray emission. This stage of the evolutionary path for PNe appears to be limited to high density ($n_e \gtrsim 1000$ cm^{-3}), young ($\lesssim 5 \times 10^3$ yr) nebulae with closed elliptical structures (Freeman et al., 2014). Based on the ages of the Table 4.1 objects, we expect our targets to represent various stages of this wind-shaping phase.

Not included here are Hb 5 and NGC 2371, both of which are ChanPlaNS sample PNe that also exhibit diffuse X-ray emission, however the nature of their emission and the nebulae themselves present some difficulties. The X-ray emission from NGC 2371 is highly asymmetric, which proves problematic for our analysis in this chapter where we consider spherically symmetric diffuse emission from the hot bubble. Hb 5 is a highly bipolar nebula, the only ChanPlaNS sample object with this morphology associated with diffuse X-ray emission, and as such makes it a peculiar PNe and not consistent with the others of our subsample. The majority of the diffuse X-ray emission is confined to a small central region around the central star, though there is evidence for additional emission along the rim of the blueshifted lobe (see Chapter 3).

4.3 The Two-Phase PNe Toy Model

The standard model of PN formation via the interacting stellar winds model (Kwok et al., 1978; Schmidt-Voigt & Koppen, 1987; Marten & Schönberner, 1991) posits a system that is composed of four distinct regions: the undisturbed fast proto-WD wind, the hot bubble, the swept-up AGB shell, and the undisturbed AGB wind (Fig. 4.2, left). The collision of the proto-WD wind with the AGB wind creates both a forward and reverse shock. The reverse shock separates the interior undisturbed wind from the hot bubble, while the forward shock separates the swept-up shell from the undisturbed AGB wind. The hot bubble is expected to reach temperatures $T_{\rm hb} \sim 10^7$ K, based on the wind speeds attributed to the central stars (500-1500 km s^{-1}), however X-ray observations reveal temperatures closer to 10^6 K. One explanation for the cooler temperatures is thermal conduction across the interface between the swept-up shell and the hot bubble (Steffen et al., 2008).

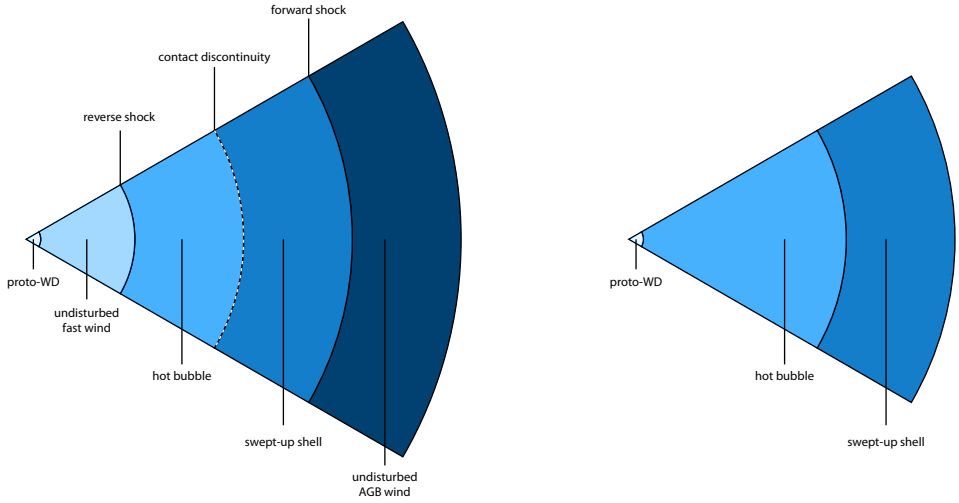

Figure 4.2: Schematic diagram of a PN (not to scale). *Left:* The typical 4-phase model of a wind-blown PN described by Weaver et al. (1977); Kwok et al. (1978) which includes the undisturbed fast wind, hot bubble, swept-up shell, and the undisturbed AGB wind. *Right:* Our 2-phase toy model of a PNe which is limited to the hot bubble and the swept-up shell.

Thermal conduction involves the diffusion of cooler, swept-up material along magnetic field lines into the hot bubble. The orientation of the magnetic field with respect to the contact discontinuity determines the efficiency of this process. Even a weak tangential magnetic field can contribute to thermal conduction, leading to an increase in the density and lowering the temperature of the hot bubble to observed values of $\sim 10^6$ K (Soker, 1994; Toalá & Arthur, 2014).

On the other side of this contact discontinuity, the dense swept-up AGB shell is expected to be cooler ($T_{\rm ss} \sim 10^4$ K) and emit primarily in optical emission lines. The X-rays emitted by the hot bubble gas can be scattered or absorbed by the gas in this region. Using a simplistic model for the potential scattering events, or the absorbing column, $N_{\rm H} \sim n_e \Delta R$, where n_e is the electron density, and ΔR is the thickness of the swept-up shell, we can estimate the column density of the swept-up shell.

Previously, $N_{\rm H}$ has been estimated using $c_{{\rm H}\beta}$ to determine the reddening to the central star caused by the interstellar medium (Bernard-Salas & Tielens, 2005; Frew, 2008), however these val-

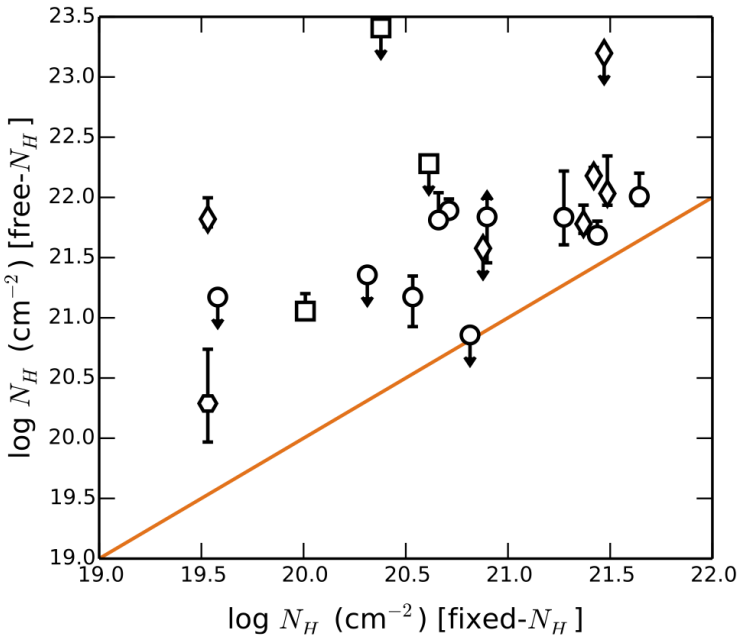

Figure 4.3: Column densities $N_{\rm H}$ estimated from $c_{{\rm H}\beta}$ measurements (x-axis) and X-ray spectral fitting (y-axis), from Montez et al. (2015b). Known binary CSPNe are represented by diamonds and hot CSPNe with WR or PG1159 spectral type are identified with squares. The hexagon represents the Helix Nebula.

ues appear systematically lower than those determined from fitting X-ray spectra of PNe (Fig. 4.3; Montez et al., 2015b). This absorption excess is may be to the nebular material itself. By constructing a simplistic model of a PNe we can investigate what effect the swept-up shell has on the X-ray morphology of a PN.

Our basic, spherically symmetric PNe model contains two phases: the hot bubble and the swept-up shell (Fig. 4.2, right). We ignore the undisturbed winds from the CSPN and the progenitor AGB star in order to focus our analysis on the X-ray emitting region and the obscuring, dense swept-up shell where the gas-phase metals will have the most impact on the X-ray flux. Additionally, our model does not account for the contact discontinuity, which is expected to have some impact on the X-ray emission based on hydrodynamical models of PNe evolution (Toalá & Arthur, 2014). That being said, we believe that the swept-up shell will dominate the X-ray extinction and we can therefore ignore the contact discontinuity for our purposes.

4.4 Data analysis

4.4.1 Toy model set-up

We approach the problem of X-ray nebular extinction by setting up our two-phase toy model for each of the 14 PNe with diffuse X-ray emission from the ChanPlaNS sample (Table 4.1) using the astrophysical modeling tool *SHAPE* (see Chapter 2). The radius of the hot bubble $R_{\rm hb}$ for each object is measured by placing a circular aperture over the *Chandra* image that encompasses all the diffuse emission. The radius of the swept-up shell $R_{\rm ss}$ is measured by placing a circular aperture over the Hα *HST* image for the same nebula. In *SHAPE* we construct a hot bubble sphere with radius $R_{\rm hb}$ and a surrounding shell with an inner radius equal to $R_{\rm hb}$ and an outer radius of $R_{\rm ss}$. The density distribution of all the hot bubbles is scaled from the density models of Steffen et al. (2008) seen in Fig. 4.4, to fit the edge of the hot bubble with our $R_{\rm hb}$ for each PN with a minimum density of 1 cm^{-3}. This distribution assumes heat conduction is present, and is responsible for increasing the density towards the edge of the hot bubble. Thermal conduction is also responsible

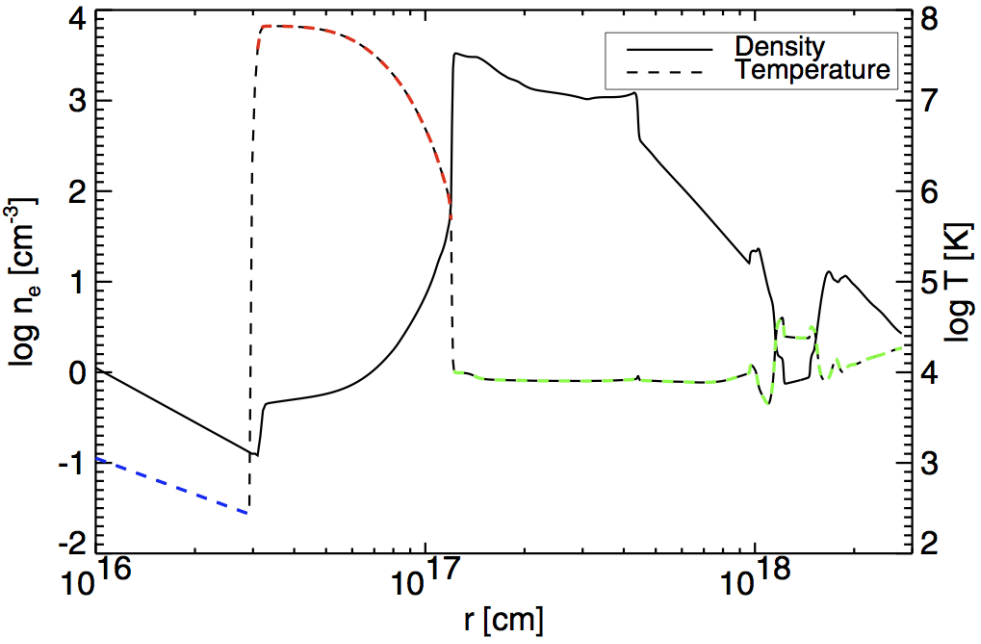

Figure 4.4: Radial profiles of electron density and temperature for a PN with a central star of $T_{\rm eft} \simeq 71600$ at an age of 5640 yr, from Steffen et al. (2008). The reverse wind shock, which forms the inner boundary of the hot bubble at $r \simeq 3 \times 10^{16}$ cm, and the outer edge (the contact discontinuity) is at $r \simeq 1.3 \times 10^{17}$ cm.

for cooling the plasma to an average temperature of 2 MK, which corresponds to spectral fits of many PNe (Chu et al., 2003; Guerrero, 2006; Kastner, 2007).

Measurements of temperature-sensitive emission lines of [O III] and [N II] indicate an average nebular temperature of 10^4 K for the ionized regions of PNe (Gutierrez-Moreno et al., 1986; Acker et al., 1989; Koeppen et al., 1991; Zhang et al., 2004), so we adopt this temperature for the swept-up shell. The density distribution is defined as

$$n_{\rm ss}(R) = n_{\rm peak}\left(\frac{R_{\rm hb}}{R}\right)^{\alpha}, \tag{4.1}$$

where $n_{\rm peak}$ is the peak density for the swept-up shell and α is varied over values of 2, 1.5, 1 and 0 (distributions A, B, C and D respectively, Fig. 4.5). We vary the value of $n_{\rm peak}$ from 10^2 to 10^9 cm^{-3} for the swept-up shell for each density distribution and each PN to find the best fit to the observed *Chandra* data. An `apec` thermal plasma emission model from `xspec` assuming solar abundances serves as the emission model for the hot bubble (Fig. 4.6). Typically, X-ray absorption is handled by assuming ISM abundances for the surrounding material. In the case of the swept-up shell, we know that the temperature is higher, and therefore the ionization state of the gas is very different than that of the ISM. However, estimates of the abundances are not well constrained and often require modifications to correct for discrepancies (Stasińska, 2002; Gonçalves et al., 2012). For the purposes of our toy model, we assume an ISM abundance for the swept-up shell, and we hence adopt the `wabs` photoelectric absorption model (Fig. 4.7; Morrison & McCammon, 1983). We do not consider self-absorption of the X-ray emitting region, nor emission from the swept-up shell.

4.4.2 X-ray Radial Emission Profiles (REPs)

From ChanPlaNS we have chosen 14 of the diffuse X-ray emitters (Table 4.1) to compare with our toy models. We generated X-ray REPs for each object by first filtering the *Chandra* image to

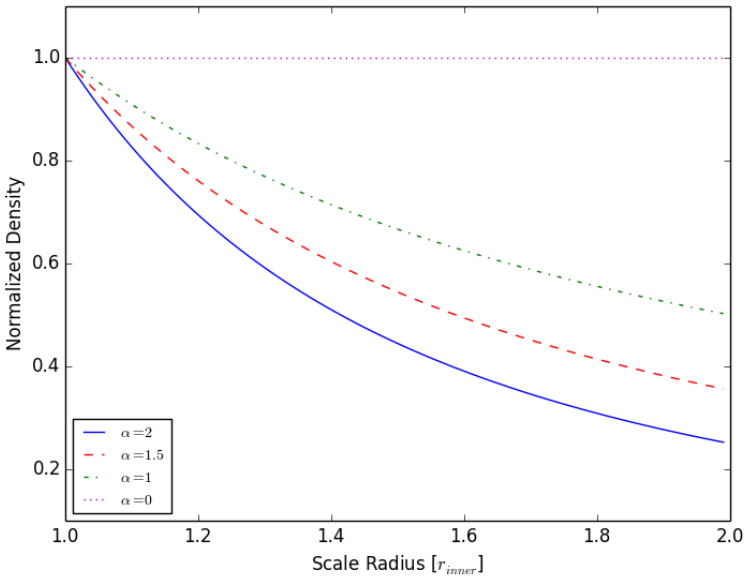

Figure 4.5: Density models A ($\alpha = 2$), B ($\alpha = 1.5$), C ($\alpha = 1$), and D ($\alpha = 0$) plotted as a function of the inner shell radius ($R_{\rm hb}$).

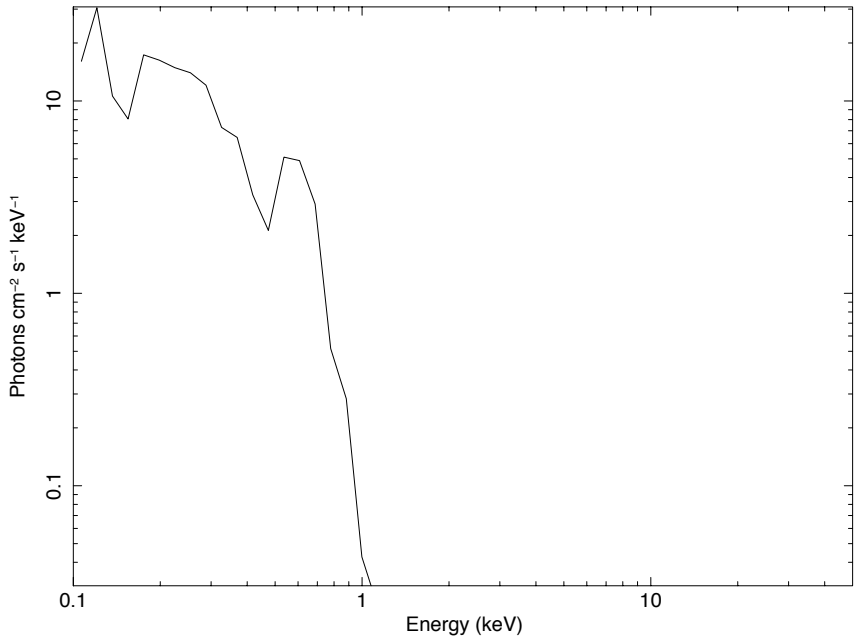

Figure 4.6: Thermal plasma model with solar abundances and plasma temperature of 2 MK from `xspec`.

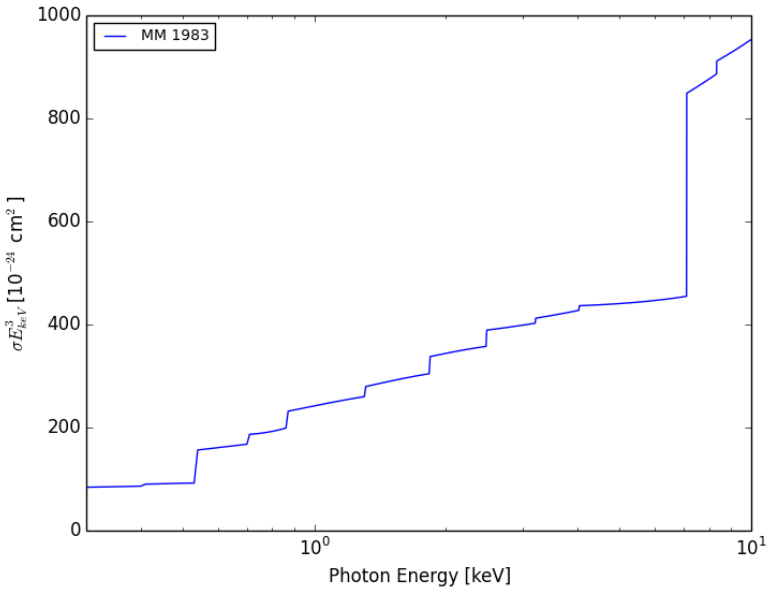

Figure 4.7: Morrison & McCammon (1983) photoelectric absorption model of X-rays by the ISM.

the energy range that best displays the diffuse emission while ignoring background photons[1], and then setting up multiple elliptical apertures to encompass the emission. The radius reported for each annulus is taken to be that of the semi-major axis. For those objects with both point-like and diffuse X-ray emission, the innermost elliptical region is excised around the central source. It is important to mention that some PNe suffer from low photon counts, which make fitting the REPs difficult given that they can appear sparsely populated by emission resulting in a noisy distribution. We will further discuss this effect in §4.5.1.

For the *SHAPE* toy models we used the synthetic observations as the basis of the REP. Given the spherical symmetry of the models, we chose to use a single slit placed on the center of the nebula out to the edge of the swept-up shell $R_{\rm ss}$ to extract the REP. This profile is then normalized to its peak intensity value, as is the *Chandra* REP, and the two are compared. By varying $n_{\rm peak}$ we aim to find the best fit density and corresponding $N_{\rm H}$ that reproduces the observed X-ray REP

[1] 0.3-2.0 keV for Cycle 12 and archival objects, and 0.5-1.2 keV for Cycle 14 objects

as a measure of extinction by the swept-up shell.

4.4.3 Goodness-of-fit

Once we have generated the synthetic REPs for our toy models over a range of peak densities (10^2-10^9 cm^{-3}), we quantitatively evaluate which peak density value best fits the observed REP. To account for the inherent statistical uncertainties of photon counting, we run a set of 1000 Monte Carlo simulations for the *Chandra* REP, resampling the data within a normal distribution based on the uncertainties. Each simulation is compared with the *SHAPE* REP and repeated for each density over our range of values. The goodness-of-fit for each profile with the observed data is evaluated using two different techniques: cross-correlation and Kolmogorv-Smirnov testing.

Cross-correlation

More commonly used for analyzing time series and data with variability (e.g. light curve analysis), cross-correlation analysis can also be applied to other varieties of regularly binned datasets. To measure how well the *Chandra* data (x) correlates with the *SHAPE* model (y) we compute the cross-correlation coefficient,

$$r = \frac{\sum_{i=1}^{N}(x_i - \bar{x})(y_i - \bar{y})}{\left(\sqrt{\sum_{i=1}^{N}(x_i - \bar{x})^2}\right)\left(\sqrt{\sum_{i=1}^{N}(y_i - \bar{y})^2}\right)}, \tag{4.2}$$

where there are N pairs of (x, y). Here N is defined by the number of data points in the *Chandra* REP, which in this case is equivalent to the number of elliptical annuli covering the X-ray data. When x and y are perfectly correlated, $r = 1$; when they are perfectly anticorrelated, $r = -1$. If there is no correlation between the two data sets then $r = 0$ (Peterson, 2001).

Kolmogorov-Smirnov test

A common test of the degree to which two datasets differ is the Kolmogorov-Smirnov (KS) test. The KS test uses the maximum difference between two functions of data as the statistic,

$$D = \sup_x |F_1(x) - F_2(x)|\,, \tag{4.3}$$

where $F_1(x)$ and $F_2(x)$ represent the *Chandra* and *SHAPE* data respectively. When the two datasets are in agreement we expect D to be close to 0, while if they disagree, then D should be large.

Error analysis

As a result of the Monte Carlo simulations, both the cross-correlation method and the KS test yield a distribution of values for each density. We fit a gaussian to the distributions of r and D values for each density to retrieve the peak value and standard deviation. These are then used to determine the range of maximum and minimum r and D values respectively. We calculate the centroid of the r and D distributions, considering only values within $0.8r_{\rm peak}$ or $1.2D_{\rm min}$, which define our upper and lower limits. The centroids then give our best fit peak density value.

To investigate how well our goodness-of-fit works for our models, we examined the relation between the cross-correlation coefficient r and the KS test value D for each nebula. In Figs. 4.8 and 4.9 we find that PNe that have larger numbers of observed counts have higher r values and lower D values, corresponding to the best fits. As the number of counts decreases we see the inverse, where r decreases and D decreases. Based on this relation, where $r \sim 1 + D$, we choose to analyze the REP fits based on the cross-correlation value.

4.5 Results

In *SHAPE* we varied $n_{\rm peak}$ logarithmically between 10^2 to 10^9 cm^{-3} for each PN model, repeating this range of densities for each of the four density distributions for the swept-up shell. From

Table 4.2: *SHAPE* Toy Model Physical Parameters

No.	Name	D [kpc]	$R_{\rm hb}$ [pc]	$R_{\rm ss}$ [pc]	Best Fit $\log n_{\rm peak}$ [cm^{-3}]	Best Fit $\log N_{\rm H}$ [cm^{-2}]	r	Δr
A								
1	BD+30°3639	1.30	0.02	0.03	$6.46^{+0.55}_{-0.24}$	$22.95^{+1.97}_{-0.86}$	0.92	0.00
2	IC 418	1.20	0.02	0.05	$8.19^{+1.49}_{-0.29}$	$25.15^{+4.58}_{-0.88}$	0.83	0.22
3	NGC 40	1.02	0.10	0.19	$4.71^{+2.71}_{-0.29}$	$22.14^{+12.74}_{-1.36}$	0.37	0.08
4	NGC 1501	0.72	0.09	0.11	$4.53^{+2.53}_{-0.31}$	$21.21^{+11.86}_{-1.46}$	0.42	0.15
5	NGC 2392	1.28	0.06	0.16	$6.22^{+0.62}_{-0.25}$	$23.71^{+2.37}_{-0.96}$	0.90	0.07
6	NGC 3242	1.00	0.05	0.10	$7.62^{+1.14}_{-0.29}$	$25.16^{+3.76}_{-0.95}$	0.70	0.45
7	NGC 3918	1.84	0.09	0.15	$7.40^{+0.10}_{-0.08}$	$24.70^{+0.33}_{-0.26}$	0.73	0.67
8	NGC 6153	1.10	0.08	0.10	$5.06^{+0.58}_{-0.24}$	$21.82^{+2.52}_{-1.03}$	0.35	0.16
9	NGC 6369	1.55	0.10	0.25	$5.78^{+0.48}_{-0.22}$	$23.44^{+1.93}_{-0.91}$	0.49	0.22
10	NGC 6543	1.50	0.07	0.12	$5.58^{+0.73}_{-0.27}$	$22.81^{+2.99}_{-1.10}$	0.84	0.06
11	NGC 6826	1.30	0.05	0.10	$7.07^{+0.59}_{-0.23}$	$24.31^{+2.04}_{-0.79}$	0.71	0.24
12	NGC 7009	1.45	0.10	0.13	$5.53^{+0.58}_{-0.25}$	$22.49^{+2.35}_{-1.00}$	0.57	0.09
13	NGC 7027	0.89	0.04	0.08	$7.18^{+1.23}_{-0.30}$	$24.31^{+4.15}_{-1.00}$	0.91	0.08
14	NGC 7662	1.26	0.05	0.10	$7.18^{+1.28}_{-0.29}$	$24.34^{+4.34}_{-0.99}$	0.73	0.33
B								
1	BD+30°3639	1.30	0.02	0.03	$6.46^{+0.51}_{-0.23}$	$22.96^{+1.81}_{-0.83}$	0.92	0.00
2	IC 418	1.20	0.02	0.05	$8.01^{+1.53}_{-0.29}$	$24.97^{+4.78}_{-0.91}$	0.81	0.29
3	NGC 40	1.02	0.10	0.19	$4.71^{+2.71}_{-0.29}$	$22.14^{+12.73}_{-1.37}$	0.36	0.08
4	NGC 1501	0.72	0.09	0.11	$4.47^{+2.47}_{-0.31}$	$21.15^{+11.68}_{-1.47}$	0.42	0.14
5	NGC 2392	1.28	0.06	0.16	$6.42^{+0.81}_{-0.28}$	$23.90^{+3.03}_{-1.06}$	0.89	0.05
6	NGC 3242	1.00	0.05	0.10	$7.56^{+1.25}_{-0.29}$	$25.10^{+4.17}_{-0.96}$	0.70	0.63
7	NGC 3918	1.84	0.09	0.15	$7.27^{+0.43}_{-0.20}$	$24.57^{+1.44}_{-0.69}$	0.73	0.78
8	NGC 6153	1.10	0.08	0.10	$5.08^{+0.48}_{-0.22}$	$21.84^{+2.05}_{-0.95}$	0.36	0.18
9	NGC 6369	1.55	0.10	0.25	$5.74^{+0.43}_{-0.22}$	$23.40^{+1.77}_{-0.89}$	0.49	0.17
10	NGC 6543	1.50	0.07	0.12	$5.45^{+0.61}_{-0.25}$	$22.69^{+2.53}_{-1.02}$	0.85	0.05
11	NGC 6826	1.30	0.05	0.10	$7.07^{+0.60}_{-0.23}$	$24.31^{+2.05}_{-0.78}$	0.74	0.26
12	NGC 7009	1.45	0.10	0.13	$5.46^{+0.55}_{-0.24}$	$22.42^{+2.27}_{-1.00}$	0.55	0.10
13	NGC 7027	0.89	0.04	0.08	$7.46^{+1.56}_{-0.31}$	$24.59^{+5.14}_{-1.03}$	0.92	0.07
14	NGC 7662	1.26	0.05	0.10	$7.48^{+1.64}_{-0.30}$	$24.64^{+5.39}_{-0.97}$	0.70	0.50
C								
1	BD+30°3639	1.30	0.02	0.03	$6.45^{+0.55}_{-0.25}$	$22.95^{+1.96}_{-0.87}$	0.91	0.03
2	IC 418	1.20	0.02	0.05	$8.02^{+1.54}_{-0.29}$	$24.97^{+4.79}_{-0.89}$	0.81	0.31
3	NGC 40	1.02	0.10	0.19	$4.71^{+2.71}_{-0.29}$	$22.13^{+12.73}_{-1.38}$	0.37	0.08
4	NGC 1501	0.72	0.09	0.11	$4.53^{+2.53}_{-0.31}$	$21.22^{+11.86}_{-1.45}$	0.43	0.15
5	NGC 2392	1.28	0.06	0.16	$6.20^{+0.73}_{-0.27}$	$23.69^{+2.77}_{-1.05}$	0.90	0.07
6	NGC 3242	1.00	0.05	0.10	$7.61^{+1.70}_{-0.30}$	$25.15^{+5.63}_{-0.98}$	0.69	0.58
7	NGC 3918	1.84	0.09	0.15	$7.55^{+0.25}_{-0.15}$	$24.84^{+0.81}_{-0.50}$	0.74	0.71
8	NGC 6153	1.10	0.08	0.10	$5.24^{+0.54}_{-0.24}$	$22.00^{+2.26}_{-1.01}$	0.35	0.19
9	NGC 6369	1.55	0.10	0.25	$5.69^{+0.39}_{-0.21}$	$23.35^{+1.61}_{-0.86}$	0.49	0.21
10	NGC 6543	1.50	0.07	0.12	$5.45^{+0.60}_{-0.25}$	$22.68^{+2.52}_{-1.04}$	0.84	0.05
11	NGC 6826	1.30	0.05	0.10	$7.07^{+0.59}_{-0.23}$	$24.30^{+2.03}_{-0.81}$	0.73	0.22
12	NGC 7009	1.45	0.10	0.13	$5.46^{+0.61}_{-0.24}$	$22.41^{+2.51}_{-1.00}$	0.52	0.12
13	NGC 7027	0.89	0.04	0.08	$7.65^{+1.80}_{-0.31}$	$24.77^{+5.83}_{-1.00}$	0.91	0.07
14	NGC 7662	1.26	0.05	0.10	$7.66^{+1.88}_{-0.29}$	$24.82^{+6.10}_{-0.95}$	0.71	0.43
D								
1	BD+30°3639	1.30	0.02	0.03	$6.36^{+0.52}_{-0.24}$	$22.86^{+1.86}_{-0.86}$	0.90	0.03
2	IC 418	1.20	0.02	0.05	$7.71^{+1.41}_{-0.29}$	$24.67^{+4.52}_{-0.92}$	0.80	0.00
3	NGC 40	1.02	0.10	0.19	$4.70^{+2.70}_{-0.30}$	$22.13^{+12.72}_{-1.40}$	0.36	0.08
4	NGC 1501	0.72	0.09	0.11	$4.53^{+2.53}_{-0.32}$	$21.21^{+11.84}_{-1.48}$	0.42	0.15
5	NGC 2392	1.28	0.06	0.16	$6.03^{+0.73}_{-0.27}$	$23.51^{+2.85}_{-1.05}$	0.89	0.05
6	NGC 3242	1.00	0.05	0.10	$7.31^{+1.31}_{-0.29}$	$24.86^{+4.47}_{-0.98}$	0.69	0.59
7	NGC 3918	1.84	0.09	0.15	$7.12^{+0.34}_{-0.18}$	$24.42^{+1.17}_{-0.62}$	0.73	0.72
8	NGC 6153	1.10	0.08	0.10	$5.08^{+0.48}_{-0.22}$	$21.84^{+2.04}_{-0.96}$	0.35	0.17
9	NGC 6369	1.55	0.10	0.25	$5.64^{+0.64}_{-0.26}$	$23.30^{+2.65}_{-1.08}$	0.47	0.21
10	NGC 6543	1.50	0.07	0.12	$5.26^{+0.48}_{-0.22}$	$22.49^{+2.06}_{-0.93}$	0.86	0.05
11	NGC 6826	1.30	0.05	0.10	$7.07^{+0.59}_{-0.23}$	$24.30^{+2.04}_{-0.79}$	0.78	0.24
12	NGC 7009	1.45	0.10	0.13	$5.37^{+0.52}_{-0.23}$	$22.33^{+2.18}_{-0.97}$	0.55	0.08
13	NGC 7027	0.89	0.04	0.08	$6.62^{+0.92}_{-0.28}$	$23.75^{+3.31}_{-1.01}$	0.89	0.10
14	NGC 7662	1.26	0.05	0.10	$7.31^{+1.61}_{-0.29}$	$24.47^{+5.40}_{-0.97}$	0.72	0.43

the synthetic data, we created X-ray REPs at each $n_{\rm peak}$ to compare with the *Chandra* REP. After running our Monte Carlo simulations comparing the synthetic REPs with the observed REP, we find the best fit result, which can be found in Table 4.2 for all 14 PNe. The corresponding best fit, normalized X-ray REP for each PN for the various density models can be found in Figs. 4.10-4.23. The normalized *SHAPE* REP is fitted to the *Chandra* data, and compared with *HST* Hα observations where available.

The column density is calculated using the determined shell thickness ΔR and the best fit density. We find that our best fit $N_{\rm H}$ values are not dependent on the location of each PN in the galaxy. Fig. 4.24 shows high $N_{\rm H}$ PNe can be found both in and above the plane of the galaxy. When we compare the distance to each nebula and the corresponding best fit $N_{\rm H}$ there also does not appear to be any dependence on the distance (Figs. 4.25 and 4.26). We conclude that there is no clear tendency for more distant PNe to have larger $N_{\rm H}$ values.

4.5.1 PNe with Poor Photon Statistics

One of the limitations of X-ray observations is that count rates of PNe can be quite low. As a result of this, there are PN in our sample that have few detectable photons. This makes fitting of a REP difficult, resulting in cross-correlation values with large uncertainties, and hence large uncertainties in our density fits. NGC 40, NGC 1501, and NGC 6369 occupy a region of Figs. 4.8 and 4.9 where $r < 0.5$ and $D > 0.8$, suggesting that our observations are not confidently fit by the model REPs. On the other hand, NGC 3918 falls in the middle of the pack but has very large uncertainties, calling into question the validity of its fits. To address this problem may require incorporating Poisson-based models to account for the limited counts that we have for these objects.

4.5.2 Comparison with the Frew Catalog

Of the 14 ChanPlaNS PNe that were modeled, 11 ($\sim$79%) display a projected X-ray REP that is best fit by a limb-darkened *SHAPE* model. The three that do display limb-brightened morphology are NGC 40, NGC 1501, and NGC 6153 with corresponding densities of $\sim 5.0 \times 10^4$, $\sim 3.4 \times 10^4$,

and $\sim 1.2 \times 10^5$ cm^{-3} respectively. The peak densities extracted from the *SHAPE* modeling (Table 4.2) for all the sample PNe are consistently high ($n_{\rm peak} \gtrsim 10^4$ cm^{-3}) when compared to those reported in Frew (2008) (Figs. 4.27 and 4.28). We do find a consistent trend wherein PNe with high densities from Frew (2008) also have high densities from our fitted toy models.

As the model density profile becomes shallower (moving from *A* to *D*), we see that most PNe require lower peak densities to fit the observed data. We expect such a trend, wherein PNe with thicker shells have more available mass to attenuate an equivalent amount of X-ray emission. However, we find that the peak density of the nebula with the thickest shell, NGC 6369, varies little between the radial density profile models (Figs. 4.29 and 4.30), whereas the peak density of NGC 7027 decreases by nearly an order of magnitude between models *C* and *D*. At the same time, the peak density of the BD+30 shell does not vary greatly between our four radial density distributions. Given that it has the thinnest shell of all the PNe in our sample, this is not a surprising result as the radial density profiles do not vary greatly over such a small change in radius. The X-ray emission of NGC 6369 is confined to the inner ring of the nebula but has extended optical emission that appears in lobes outside of the main ring, while both NGC 7027 and BD+30 host emission confined to an inner shell that lies close to the outer edges of the optical emission. The estimates of the thickness of the nebular shell are based on 2D projections of the optical nebula, which may overestimate its size and simplify its structure, especially for NGC 7027 which appears to have a complex optical morphology.

The nebular density is expected to decrease with increasing nebular radius. This is evident from the fact that the nebular density is typically derived from

$$n_e \sim \frac{M_i}{\frac{4}{3}\pi R_{\rm neb}^3}\,, \tag{4.4}$$

where M_i is the ionized mass (Frew, 2008). For our toy models, we obtain the peak density corresponding to the radial profile that correlates best with the observed *Chandra* data, and therefore this density is independent of radius. Although our values of n_e are obtained using different meth-

ods, our results show a trend in Fig. 4.31 of decreasing nebular density with increasing radius, similar to that found by Frew (2008). If we scale the $R - n_e$ relation of Frew (2008) by 3.25 magnitudes, we see that our density fits do indeed follow this trend. Figs. 4.32 and 4.33 show that most of our PNe lie within $\log n_{e,\mathrm{FREW}} + 3.25 \pm 0.75$, with the exception of NGC 3918. The flat density model (D) best matches the Frew (2008) density values as it requires lower densities for several of the PNe with radii below 0.10 pc.

The diffuse X-ray emission phase of PNe evolution has only been detected for PNe with estimated dynamical ages $\lesssim 5 \times 10^3$ yr (see Ch. 3; Freeman et al., 2014). During this time, the wind from the CSPNe is expected to have a large impact on the shaping of the nebula. Across this timeframe the fitted density has a relatively flat trend with large scatter (Figs. 4.34 and 4.35), indicating that the density of the swept-up shell does not change significantly throughout this period of evolution. Six PNe have kinematic ages around 3000 yr, and the corresponding density values range from $\sim 10^5$-10^8 cm^{-3}. This age range appears to split into two distinct groups with IC 418, NGC 3918, and NGC 7662 representing the denser group ($\sim 10^{7}$-^{8} cm^{-3}), while NGC 2392, NGC 6369, and NGC 7009 have lower densities ($\sim 10^{5.5}$-$10^{6.5}$ cm^{-3}). This trend appears to split the entire sample across the 5×10^3 yr period, with a range of $\sim 10^{6.5}$-10^{7} cm^{-3} where no PNe are found, with the exception of NGC 7027, which only falls in this range when assuming a flat density.

Alternative estimates of the hydrogen column density of our sample PNe are determined by measurements of Hβ emission. Figs. 4.36 and 4.37 compare Hβ column density estimates with those fit here. For PNe with higher estimated N_{H} from Hβ observations we see lower N_{H} values, and vice versa. Our N_{H} estimates are typically higher, with a maximum difference of ~ 5 orders of magnitude. Only two PNe lie close to their corresponding Frew (2008) estimated values: NGC 1501 and NGC 6153, which coincidently have limb-brightened morphologies and poor photon statistics. Indeed, given the large uncertainties, most of our column density values are consistent with those estimated from Hβ observations. Still, it appears that our N_{H} determination method reveals an additional density component that is not evident from Hβ measurements. Our N_{H} values appear to show a slight decline with increasing nebular radius (Figs. 4.38 and 4.39), which corresponds

to the lower densities at larger radii. This may point to a similar ionized mass across the PNe in our sample. If the ionized mass is constant then larger nebulae will have lower densities, and consequently lower column densities.

Additionally, we compare our column density values with those derived from X-ray spectral fits by Montez et al. (2015a, in prep). Figs. 4.40 and 4.41 compare their results with ours, revealing again that our toy models imply column densities orders of magnitude above those estimated by other means. The values estimated by Montez et al. (2015a, in prep) show a much larger range and larger uncertainties for several PNe. The upper limits of a few PNe are very large, which could possibly put our estimates in better agreement with one another. We assume the same base `vapec` thermal plasma model as Montez et al. (2015a, in prep), however our temperature is fixed to 2 MK and the abundances are set to solar. Variations in the elemental abundances, as well as different temperatures may be in part the reason for this discrepancy.

4.5.3 PNe with [WR]-type CSPNe

Four PNe in our sample, BD+30°3639, NGC 40, NGC 1501, and NGC 6369 host [WR]-type central stars, and the X-ray morphologies appear to be split between those with heavy extinction and those with very little extinction. We find no evidence that the X-ray morphologies of PNe with [WR]-type central stars are systematically different from those with "normal" (H-rich) central stars. BD+30°3639 is the youngest of the PNe in the sample, and displays an X-ray morphology that darkens towards the optical rim. The best fit density is $\sim 2.9 \times 10^6$ cm^{-3} which puts it on the upper edge of the low density group. Meanwhile, the oldest PN with a [WR]-type CSPNe is NGC 40, which exhibits a limb-brightened morphology and a lower density of $\sim 5.0 \times 10^4$ cm^{-3}. NGC 1501 exhibits a limb-brightened morphology as well, with a best fit density of $\sim 3.5 \times 10^4$ cm^{-3} . These two are among the least dense PNe in our sample, consistent with their (limb-brightened) X-ray morphologies. Lastly NGC 6369, like BD+30, shows a limb-darkened X-ray profile with a best fit density of $\sim 6.0 \times 10^5$ cm^{-3}. It is also the only PNe in the ChanPlaNS sample with a [WO]-type central star and has a shell thickness more than twice that of the other PNe with

[WR]-type CSPNe.

4.6 Discussion

The sample of 14 PNe with diffuse X-ray emission represent a subset of mostly compact and young PNe in the local solar neighborhood. We made use of *SHAPE* to model a spherically symmetric version of a PN with a hot bubble and a swept-up shell to investigate the impact of the nebular material on the X-ray morphology as well as test an alternate method of determining the nebular density. We found that most of our sample (11/14) show radial profiles that darken towards the inner rim of the optical emission, which is indicative of moderate to heavy extinction present in the swept-up shell. In the following subsections we discuss apparent trends we have identified as a result of our analysis.

4.6.1 Limb-Brightening vs -Darkening

The intrinsic density profile of the hot bubble is expected to increase as it approaches the interface with the swept-up shell (Steffen et al., 2008; Toalá & Arthur, 2014). However, this X-ray limb-brightened morphology does not appear to be the norm for PNe; in fact quite the opposite is true. Most of our sample display limb-darkening, where the peak of the projected X-ray REP is closer to the center of the nebula rather than at the edge of the hot bubble. PNe with this morphology also show the X-ray emission fading as the Hα profile increases. Our fit for NGC 6153 is in opposition to this. The best fit profile is limb-brightened with an r value of ~ 0.34 and the peak of the emission extending beyond the optical peak (Fig. 4.17). This fit however is shallow, indicating that if the fit is to be believed it does suffer from extinction due to the surrounding shell. NGC 40 and NGC 1501 also display limb-brightening, with NGC 1501 in particular showing almost no X-ray emission in the interior of the hot bubble (Fig. 4.13). NGC 40 appears to have a double peaked structure, with a secondary peak interior to the brightness peak at the limb similar to NGC 6153 (Fig. 4.12). The poor photon statistics in the X-ray images of these PNe and the corresponding

low r fits make it difficult to confidently state that these objects are truly limb-brightened.

Our results indicate a trend of decreasing intensity with increasing PN radius (Fig. 4.32 and 4.33) although the densities we determine are systematically larger than those reported in Frew (2008) (Fig. 4.27 and 4.28). This trend is best fit with a limb-brightened hot bubble with its X-ray emission attenuated by the surrounding swept-up material. While we see similar trends between our results and previously estimated values, the 3+ order of magnitude difference is a large offset that is indicative of major discrepancies between physics models for these objects. The random nature of poor photon statistics can be blamed in individual cases for poor fitting, but the overall discrepancy is robust, pointing to another cause for the high peak density fits. The "over-density" that we are seeing in our fit results may point to an additional absorber that we have not accounted for, such as self-absorption from the hot bubble gas which was not included in this analysis, or it may suggest that the extinction contribution from the other regions cannot be neglected.

Alternatively, we have not accounted for deviations from ISM abundance for the swept-up shell or for absorption related to dust. Through preliminary testing of varying the swept-up shell abundances we have seen that increasing the oxygen abundance reduces the best fit density. Being able to account for the abundances of each individual element would provide a better REP to compare and thus result in a more accurate estimate of the density of the swept-up shell. Additionally, adding a very weak dust component with a gas-to-dust ratio of $\sim 10^{-8}$ does bring the fitted density closer to estimated values. Further modeling is required to adequately address the importance of including a dust component in the swept-up shell.

4.6.2 Swept-up Shell Density Distribution

Density distributions of r^{-2} are typically assumed for the AGB wind, but the swept-up shell should not have such a steep decay. As modeled by Steffen et al. (2008) in Fig. 4.4, the initial density distribution of the swept-up shell is relatively flat before falling off. Of the four density models that we used to fit the swept-up shell profile, the flat profile (D) resulted in density fits closest to previously estimated values. A flat or constant distribution of the swept-up shell is an

unlikely scenario for the entire shell, especially for larger shells that are less compressed by the fast stellar wind. Additionally, the complex mass loss history of each individual star is unique, which could result in clumpier wind structure, creating an inhomogeneous shell, or one of multiple epochs of mass loss corresponding to a wide range of densities as a function of distance from the central star. A more complex density distribution for the swept-up shell is required to improve our model of the extinction surrounding the hot bubble.

4.6.3 CSPNe and Nebular Extinction

Four PNe in our sample have X-ray point sources located at their CSPNe: NGC 2392, NGC 6543, NGC 6826, and NGC 7009. For each of these PNe we ignored the central regions of the nebula when attempting to better fit the diffuse REP. From our cross-correlation analysis we find that r for NGC 6826 is around 0.55, but upon visual inspection of the fit it does not appear to be good. This may have to do with the X-ray emission from the central star contaminating the fit, requiring that we adjust the size of the inner annulus such that we remove more of the CSPN contamination.

The three remaining PNe with point-like X-ray emission all display limb-darkened morphologies. Depending on the energy, the point-like X-ray emission can be linked to either a binary companion ($E_{\rm med} \gtrsim 1.0$ keV) or with wind shocks or photospheric emission ($E_{\rm med} \sim 0.6$-1.0 keV) (see Chapter 3, also Kastner et al., 2012; Freeman et al., 2014; Montez et al., 2015b,a, in prep). Both NGC 7009 and NGC 6543 have lower median point source energies (0.7 and 0.59 keV respectively), which could be linked to wind shocks or photospheric emission from the CSPNe. It is unclear whether or not these wind shocks would have any impact on the shape of the hot bubble so far from central star, or if the photospheric emission could alter the shape of the emission either. It is striking how similar their projected X-ray REPs appear to one another given the differences between the two nebulae.

[WR]-type CSPNe

Of the 14 PNe in our sample, four have [WR]-type central stars. In Chapter 3 we posited that PNe with [WR]-type CSPNe share similarities with the wind-blown bubbles around massive WR stars. Both systems are expected to show limb-brightened morphologies, however our current sample suggests otherwise. Both BD+30 and NGC 6369 display limb-darkened morphologies while NGC 40 and NGC 1501 are limb-brightened. The projected X-ray morphology of NGC 40 and NGC 1501 may be the result of poor photon statistics, but it is clear that they differ from BD+30 and NGC 6369. Both NGC 40 and NGC 1501 have well-defined upper density limits around 10^5 cm^{-3}, which represents the turn over from a limb-brightened to limb-darkened nebula for these two nebulae. This upper limit is similar to the best-fit density for NGC 6153 ($\sim 1.2 \times 10^5$ cm^{-3}) which looks to have a double peak structure, similar to that of NGC 40. Also, NGC 6153 hosts a weak emission line star (wels) which is very similar to [WC]-type stars (Parthasarathy et al., 1998).

The central star of NGC 6369 is [WO]-type while those of the other three are [WC], which also appears to have little effect on the fitted density. The nebular density of NGC 6369 is $\sim 2.5 \times 10^5$ cm^{-3} which lies in between the extremes of BD+30 with 2×10^6 cm^{-3} and NGC 1501 with $\sim 3 \times 10^3$ cm^{-3}. However, it is worth noting that BD+30 is believed to have previously been a [WO]-type star based on the silicate dust envelope surrounding the nebula, which may link the fitted peak densities of this PN and NGC 6369. The switch from [WO] to [WC] may have been the result of some major mass loss event or merger, which would inject additional material into the surrounding nebula, acting as an additional layer of absorption.

The four PNe with [WR]-type CSPNe appear to be a part of the low density branch of a bimodal density distribution with BD+30 representing the densest of the group. Given the higher mass loss rates and faster wind speeds of [WR]-type CSPNe compared to H-rich CSPNe, we expect these PN to evolve more quickly, preventing mixing between the fast wind and the surrounding shell (Tylenda, 1996). This would result in lower densities overall compared to PNe without [WR]-type CSPNe.

4.7 Normalized N_{H} Estimates

The initial results of our analysis revealed best-fit density values 2-3 orders of magnitude above those determined from Hα surface brightness measurements from Frew (2008). By making adjustments to the *SHAPE* toy model, such that the best-fit column density for BD+30 is scaled to $N_{\mathrm{H}} = 2.4 \times 10^{21}$ cm^{-2}, determined from X-ray spectral fitting from Yu et al. (2009), we were able to generate the results seen in Figs. 4.42-4.47.

We see that many of the objects have best-fit densities (Figs. 4.44 and 4.45) and ionized mass estimates (Figs. 4.46 and 4.47) that fall within the limits of the Frew (2008) values, while some still exhibit an over-density and very high mass estimates. These high peak density and mass values may be due to some additional absorber that we are not considering here, or possibly that these offsets point to less efficient thermal conduction at the contact discontinuity in these nebulae. Less material being transferred across the boundary between the hot bubble and the swept-up shell would reduce the density at the edge of the hot bubble, resulting in a radial profile that appears limb-darkened without the need for additional nebular material. Comparing the stellar types, ages, and distances of the nebulae with high density and mass values does not reveal any common traits, suggesting that the fault may lie in our toy model. Further investigation is required.

4.7.1 Emission Line Diagnostics

Estimates of electron densities of gaseous nebulae can be determined through a variety of methods. From spectroscopic measurements of various density sensitive line ratios, such as the [S II] $\lambda\lambda$6716, 6731 and [O II] $\lambda\lambda$3726, 3729 doublets (Keenan, 1991; Osterbrock & Ferland, 2006), densities have been estimated for various PNe. However, it is difficult to obtain quality spectra where the doublets can be separated from one another (Gutierrez-Moreno et al., 1986). When such observations are not available, the density can be estimated from the Hα flux, radius, and distance to a PN, given an estimate of the volume filling factor (Pierce et al., 2004; Frew, 2008).

A representative sample of density values determined via various density diagnostics compared

Table 4.3: Electron Density Estimates via Various Methods

Name	log $n_{e,[\mathrm{S\ II}]}$ (Keenan, 1991)	log $n_{e,[\mathrm{O\ II}]}$	log $n_{e,\mathrm{H}\alpha}$ (Frew, 2008)	log $n_{e,SHAPE}$ This work	log $n^{\mathrm{a}}_{e,SHAPE(\mathrm{scaled})}$ This work
IC 418	4.5	4.5[b]	4.28	7.71	6.20
NGC 7027	4.6	4.7[c]	4.48	6.62	5.59
BD+30°3639	4.0	3.7[d]	4.61	6.36	4.72

Notes.
[a]Estimates based on scaling column density of BD+30 to the value determined via X-ray spectral fitting by Yu et al. (2009).
[b]Gutierrez-Moreno et al. (1986)
[c]Middlemass (1990)
[d]Kaler (1986)

with those determined from our toy models can be found in Table 4.3. The values estimated by Keenan (1991) in column 2 were determined using the [S II] doublet, those in column 3 used [O II] (Gutierrez-Moreno et al., 1986; Middlemass, 1990; Kaler, 1986), column 4 used the Hα flux (Frew, 2008), column 5 are the best-fit values determined from our toy model, and column 6 represent best-fit values from our toy model when scaled to fit the column density value for BD+30 determined from X-ray spectral fitting. We see that the values determined from the [S II] and [O II] doublets are similar, while the mean values determined from Hα are lower for IC 418 and NGC 7027, and much higher for BD+30 (Frew, 2008).

The disparity in these values points to differences in the methods in which they are determined. The diagnostics of both the [S II] and [O II] doublets do not reveal large variations; however, when compared with the Hα and *SHAPE* values we see that the different density determination methods may be probing different regions of the nebula. The low degree of ionization of [S II], [O II], and Hα are likely characteristic of the outer, lower-density regions of these nebulae, whereas our *SHAPE*-derived values should be less sensitive to any ionization stratification of the metals present in the swept-up shell. This may contribute to the higher density values, as we are probing the entire shell, as opposed to just the outer layers where [S II] and [O II] are typically found.

4.8 Chapter Summary

We present results from modeling of X-ray emission from PNe targeted by the *Chandra* Planetary Nebula Survey. The sample of 14 ChanPlaNS PNe represent a set of compact and relatively young PNe that exhibit diffuse X-ray emission, four of which have [WR]-type CSPNe. We constructed two-phase toy models of all 14 PNe using *SHAPE*, which consist of a spherically symmetric X-ray emitting hot bubble and swept-up shell capable of absorbing the X-ray emission. The analysis of the diffuse X-ray morphology of both the models and the *Chandra* was designed to investigate effect of nebular extinction on the intrinsic X-ray morphology, as well as what effect the CSPN type may have on the observed X-ray morphology.

Based on best fits of our models to the observed X-ray data, we find that ∼79% of the PNe in our sample display a projected radial emission profile that opposes the assumed X-ray density profile which increases towards the rim of the hot bubble. In contrast, the projected X-ray REPs for many of the PNe peak close to the center of the nebula and decrease toward the limb. This morphology is indicative of a nebula that suffers from moderate to heavy nebular extinction of a hot bubble with a limb-brightened density distribution, which is corroborated by the high n_e and $N_{\rm H}$ values we have calculated ($\gtrsim 10^4$ cm^{-3} and $\gtrsim 10^{21}$ cm^{-2}, respectively). These values are much higher than those determined from measurements of Hβ emission (Bernard-Salas & Tielens, 2005; Frew, 2008).

The source of this extinction in our model is the dense shell of AGB material that was plowed up by the wind of the CSPN. The lack of additional absorption components such as dust or the appropriate nebular abundances may be responsible for the "over-density" discrepancy that we find. Nevertheless, we do see the same $n_e - R_{\rm neb}$ relationship as Frew (2008) using independent methods. Further modeling is required to incorporate variable abundances and a dust component. Additionally, poor photon statistics have contributed to poor fitting. Either deeper *Chandra* observations or Poisson-based models are required to enhance our fitting method for these photon starved nebulae.

From our analysis, it appears that the type of stellar engine that drives the wind and thus formation of the PNe has no apparent effect on the shape of the X-ray emission, given that we see PNe with [WR]-type CSPNe that display limb-brightening and others that show limb-darkening. More information about the progenitor stars, such as the initial mass and binary status, as well as information about the evolution history of these nebulae is required to make a more definitive conclusion as to what effect the central engine has.

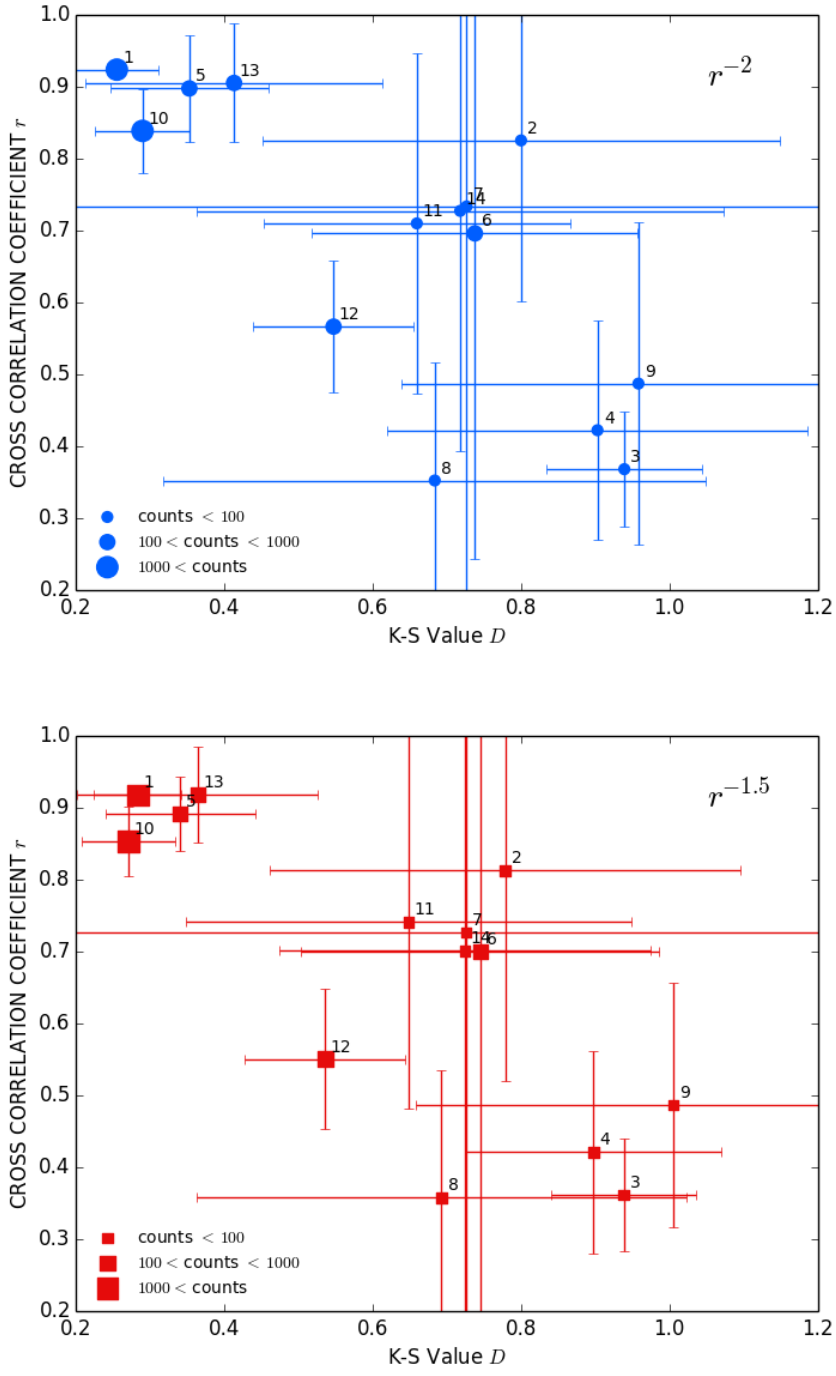

Figure 4.8: Cross-correlation coefficient r versus the KS value D for density models A and B. We find a linear trend between the two goodness-of-fit tests, where $r \sim 1 + D$. Additionally, we note that for PNe with high counts r approaches 1 and D approaches 0.

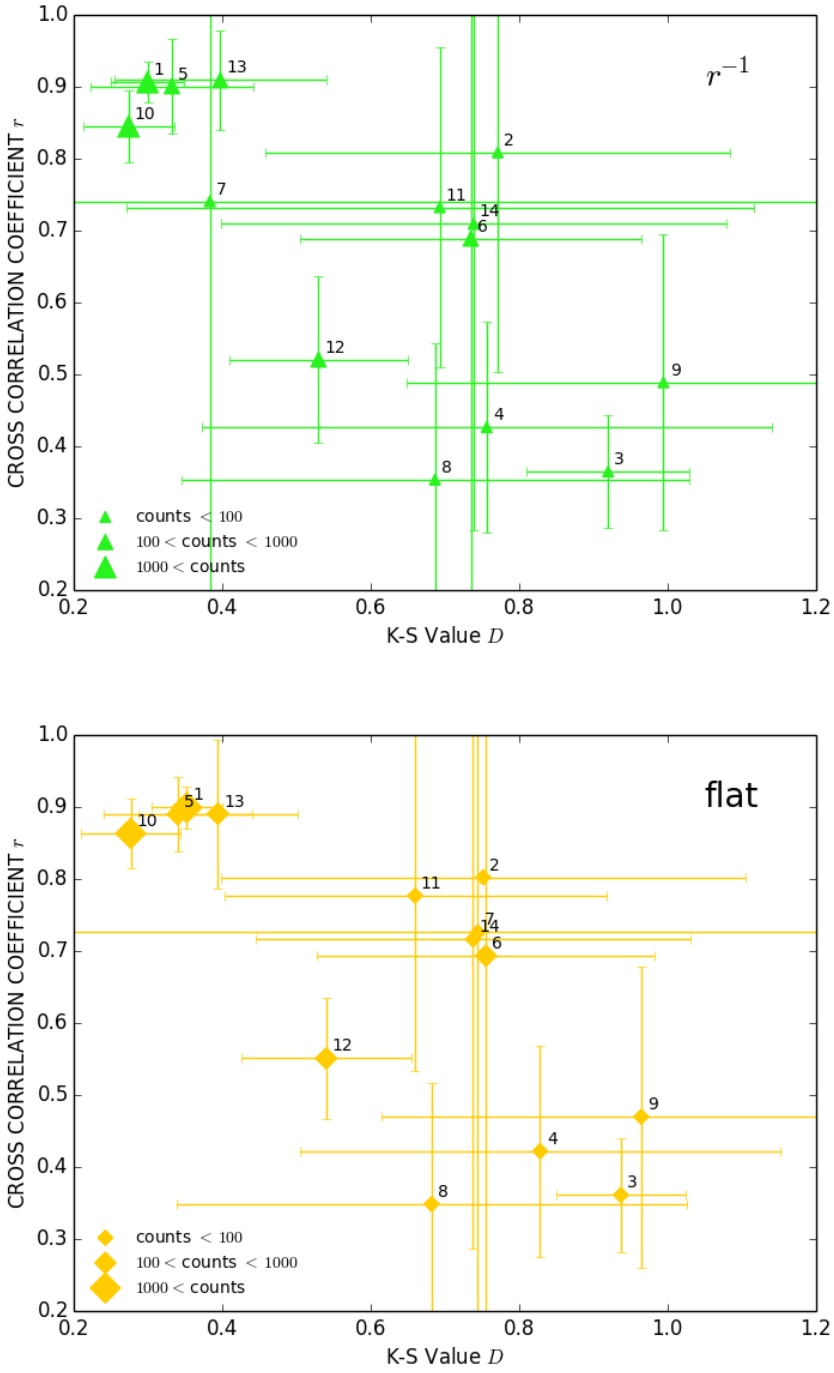

Figure 4.9: As in Fig. 4.8 for density models C and D.

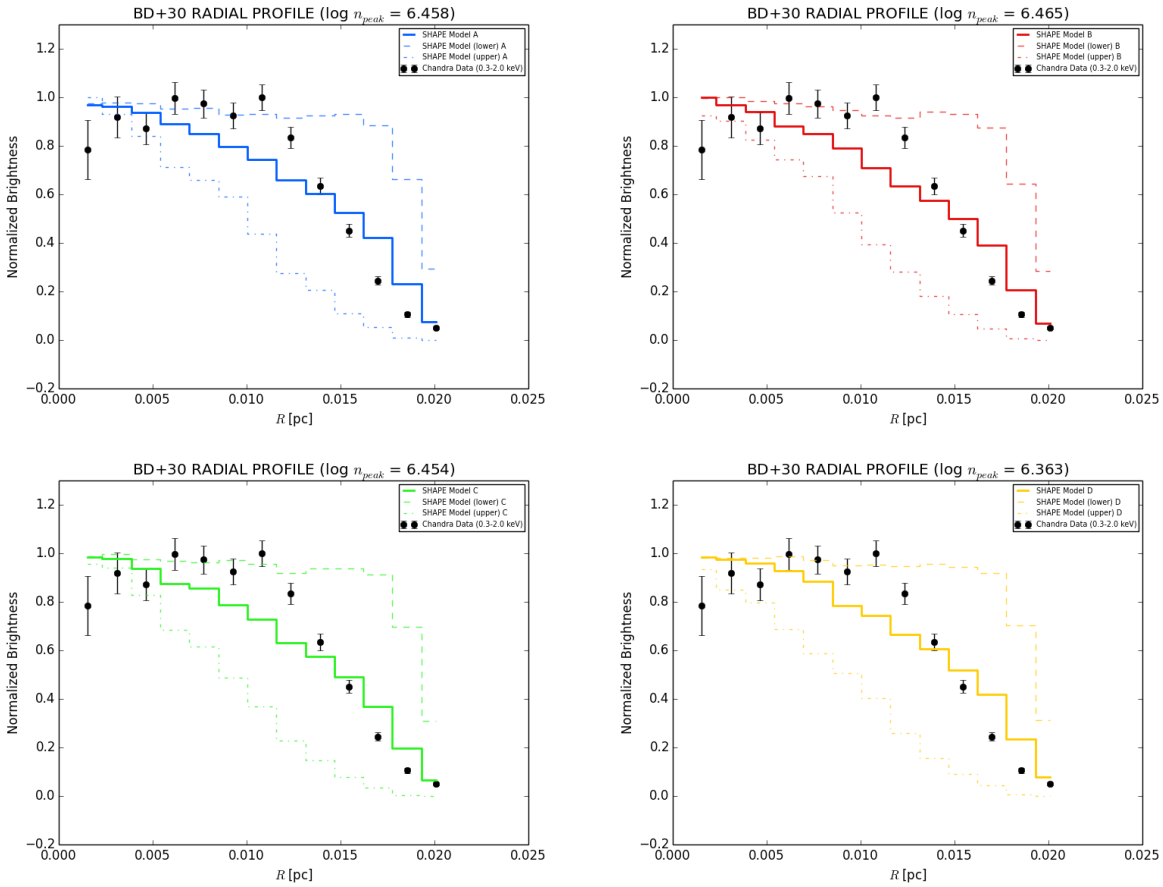

Figure 4.10: Best fit REP for the four density models used for BD+30. The filled circles represent the *Chandra* radial profile, while the solid line represents the *SHAPE* REP. REPs for upper (dashed) and lower (dot dashed) limits for the best-fit are also displayed for each density model. The top row shows the r^{-2} (A) and $r^{-1.5}$ (B) models, while the bottom row shows the r^{-1} (C) and flat density distribution (D) models.

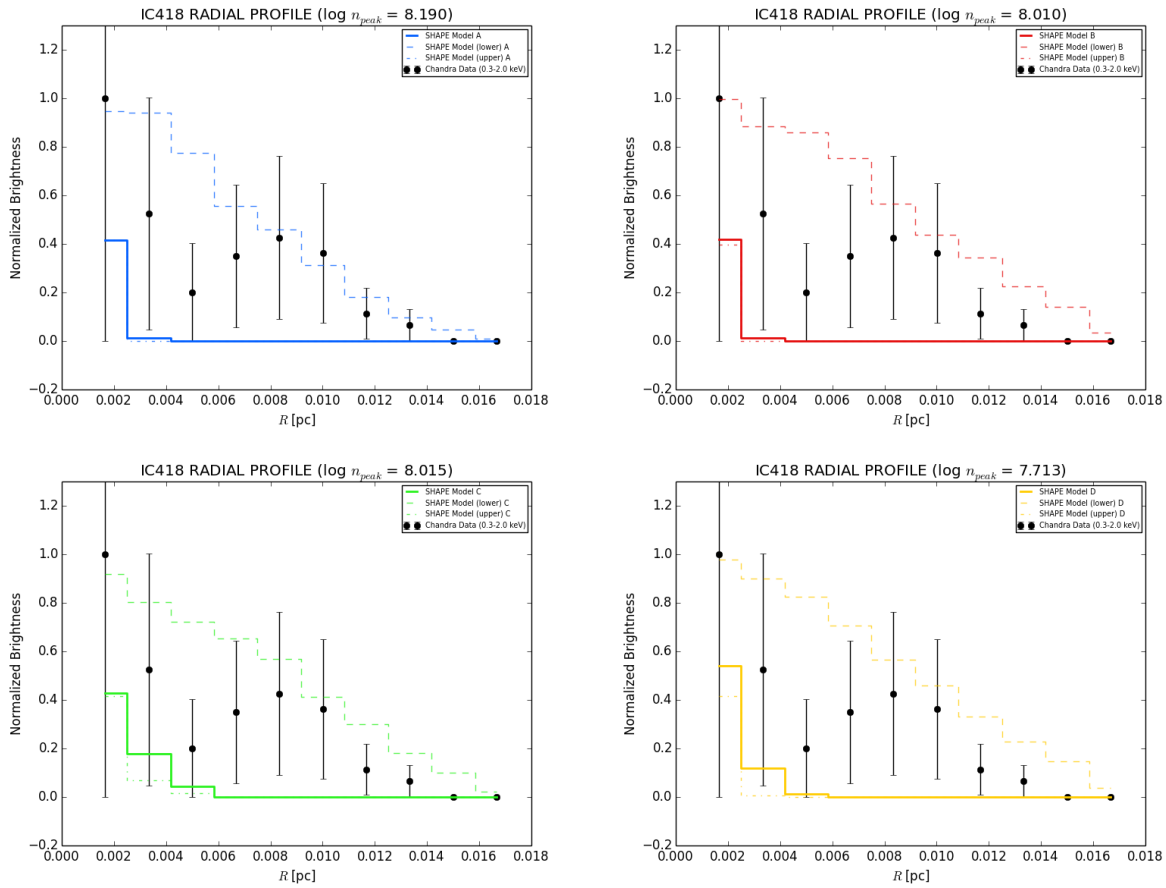

Figure 4.11: Best fit REP for the four density models used for IC 418. The configuration of this figure follows that of Fig. 4.10.

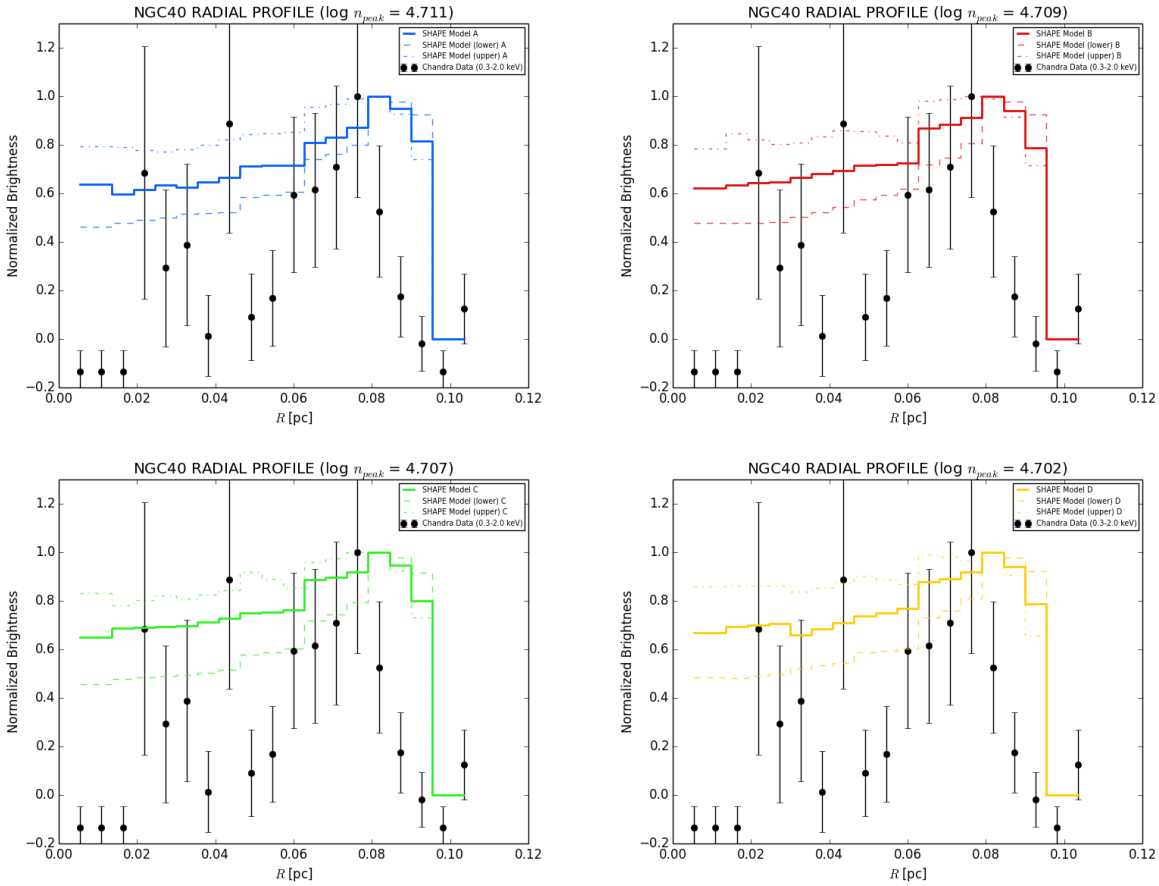

Figure 4.12: Best fit REP for the four density models used for NGC 40. The configuration of this figure follows that of Fig. 4.10.

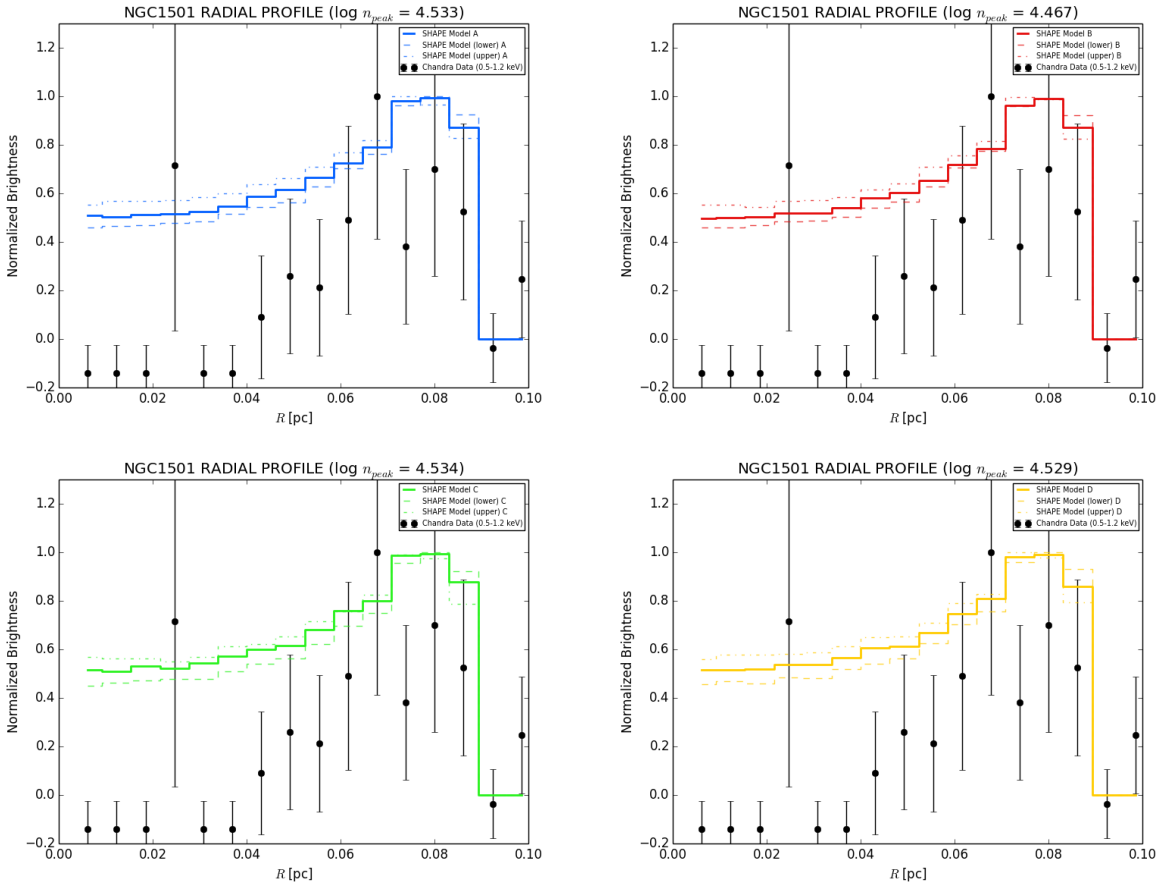

Figure 4.13: Best fit REP for the four density models used for NGC 1501. The configuration of this figure follows that of Fig. 4.10.

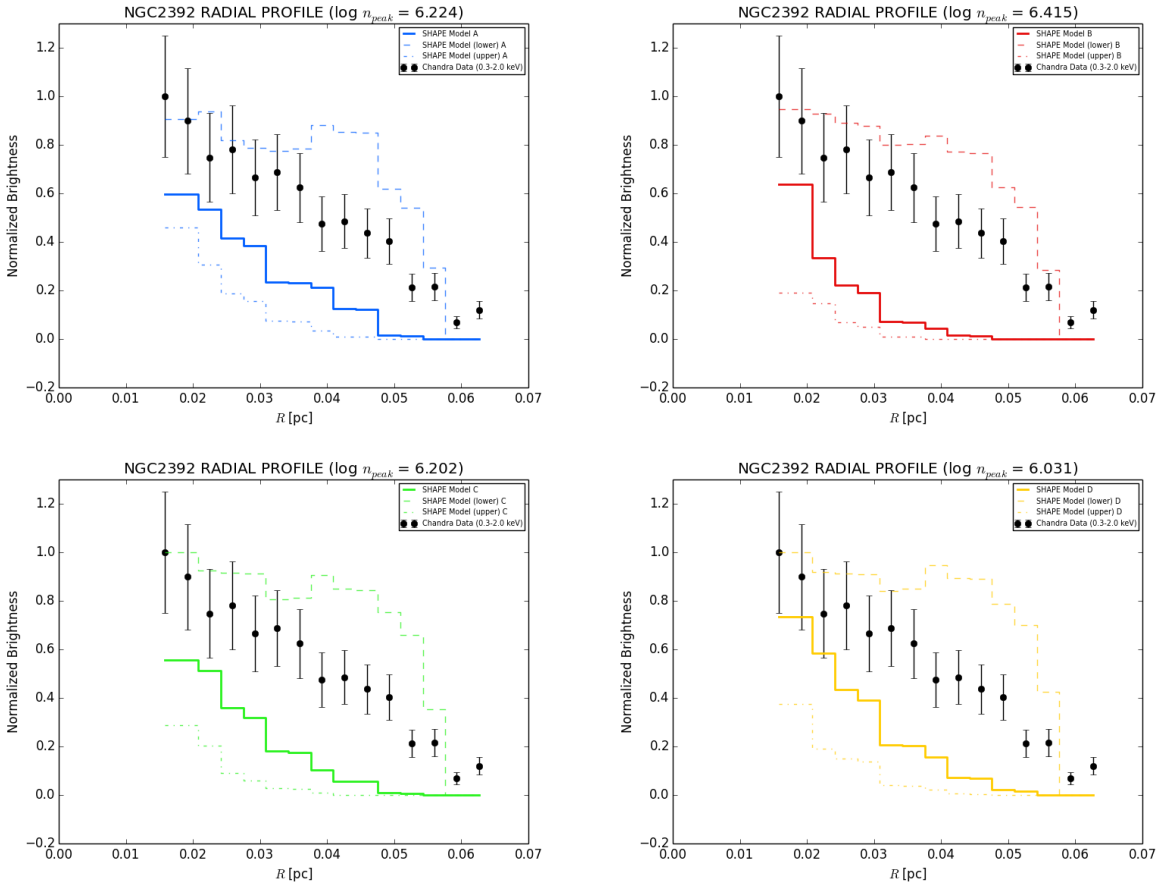

Figure 4.14: Best fit REP for the four density models used for NGC 2392. The configuration of this figure follows that of Fig. 4.10.

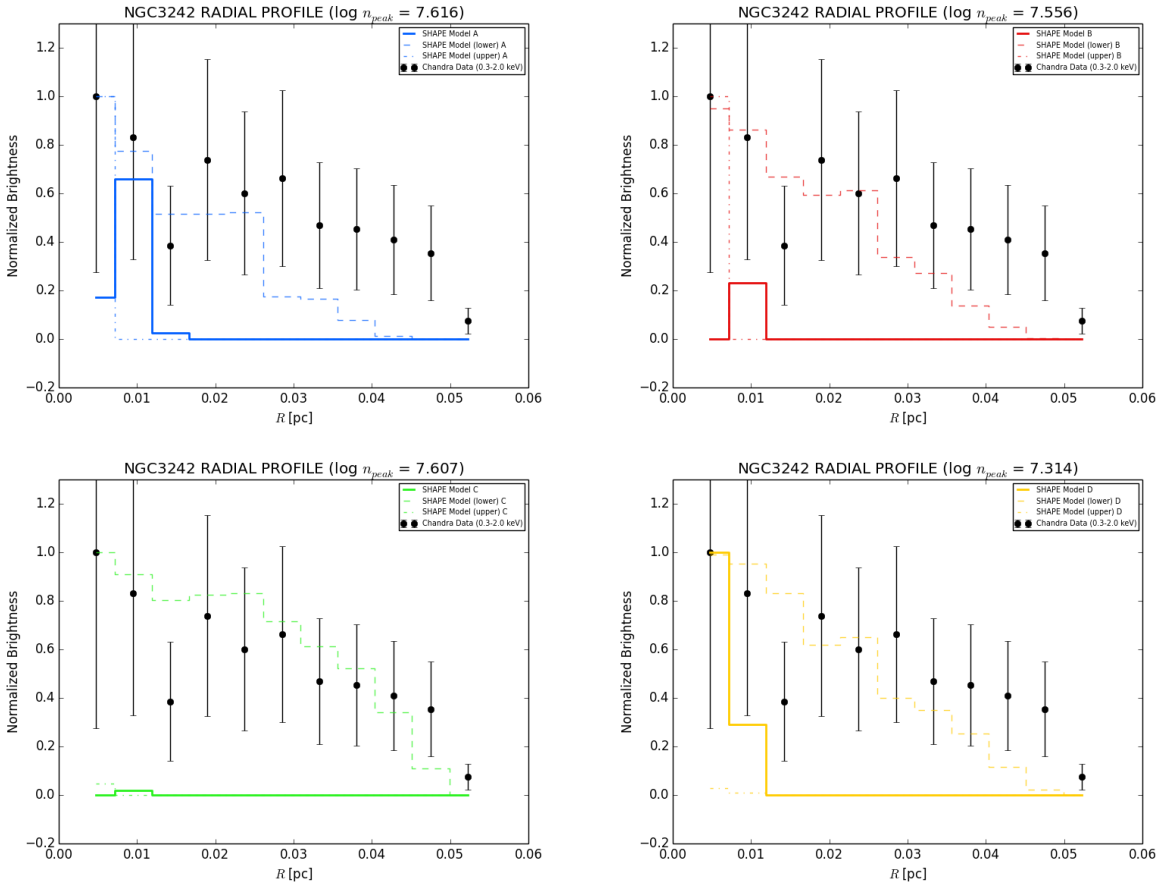

Figure 4.15: Best fit REP for the four density models used for NGC 3242. The configuration of this figure follows that of Fig. 4.10.

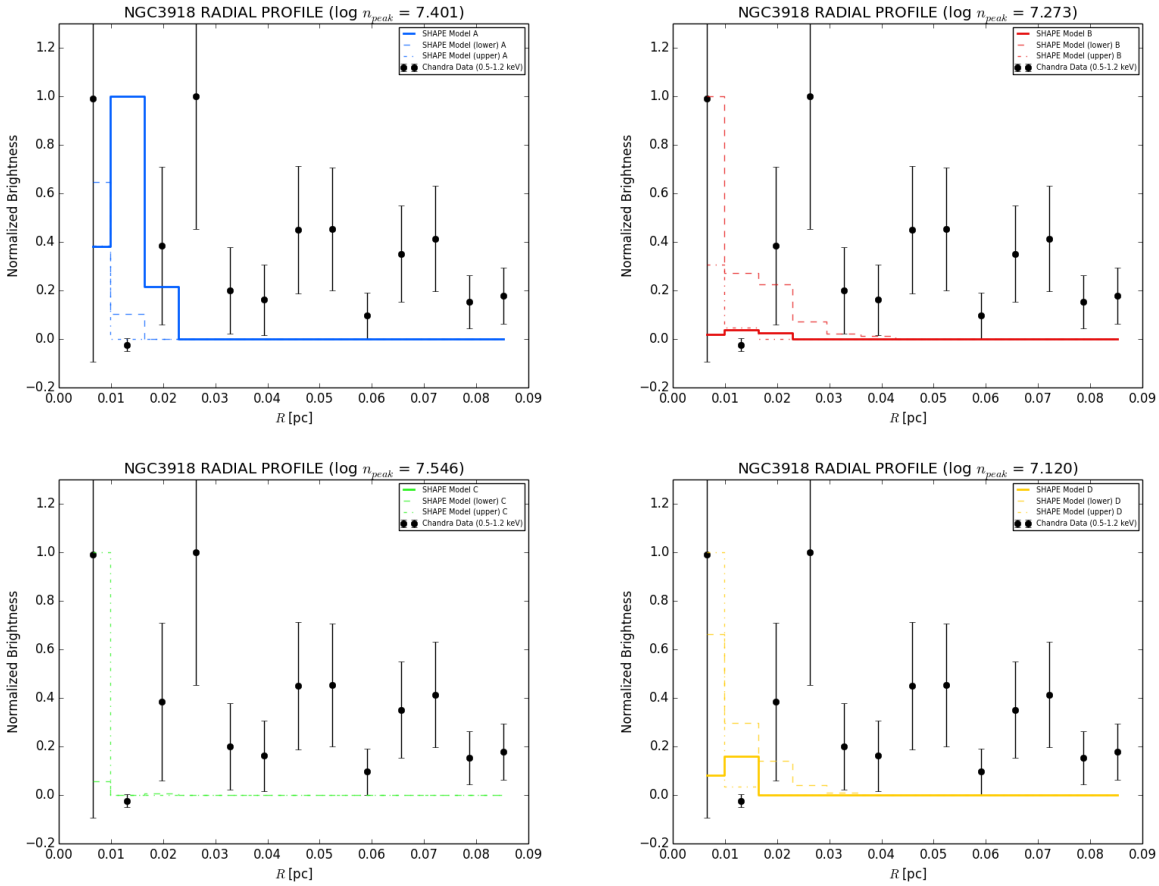

Figure 4.16: Best fit REP for the four density models used for NGC 3918. The configuration of this figure follows that of Fig. 4.10.

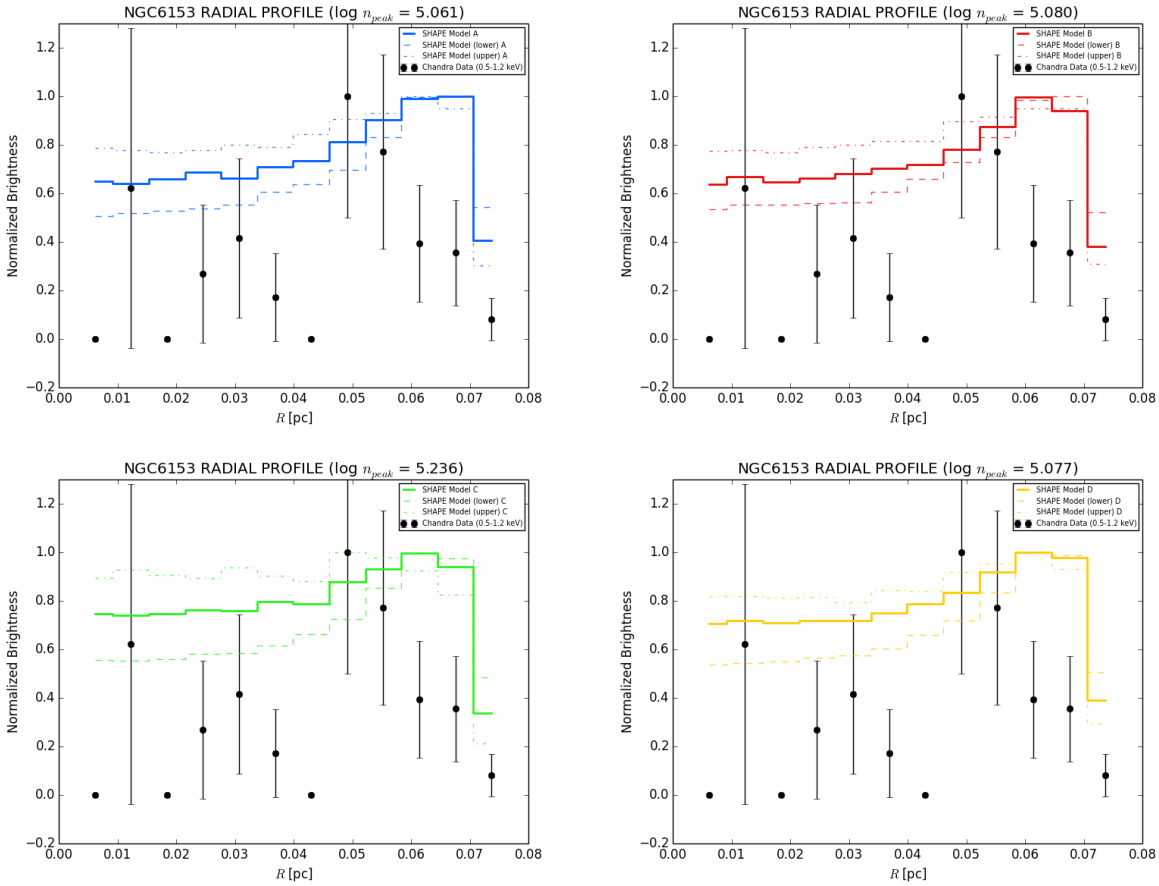

Figure 4.17: Best fit REP for the four density models used for NGC 6153. The configuration of this figure follows that of Fig. 4.10.

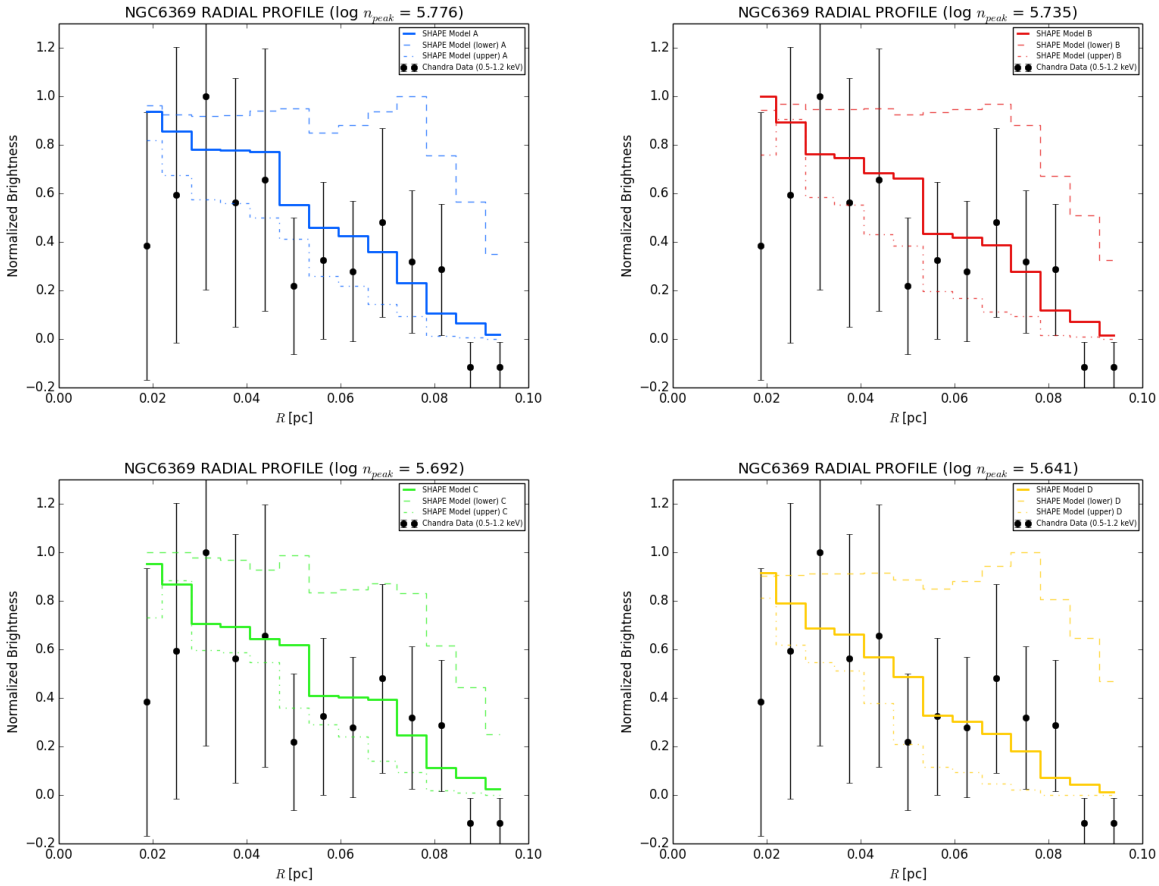

Figure 4.18: Best fit REP for the four density models used for NGC 6369. The configuration of this figure follows that of Fig. 4.10.

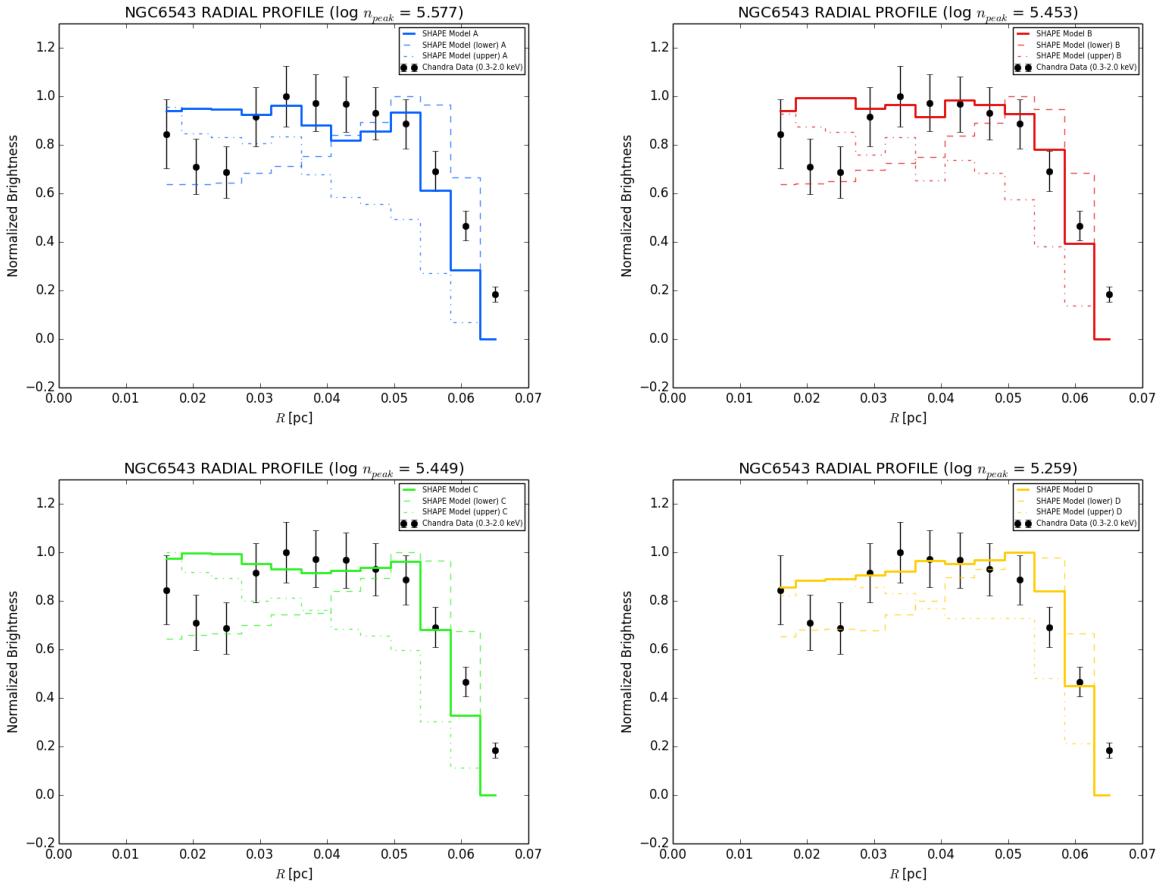

Figure 4.19: Best fit REP for the four density models used for NGC 6543. The configuration of this figure follows that of Fig. 4.10.

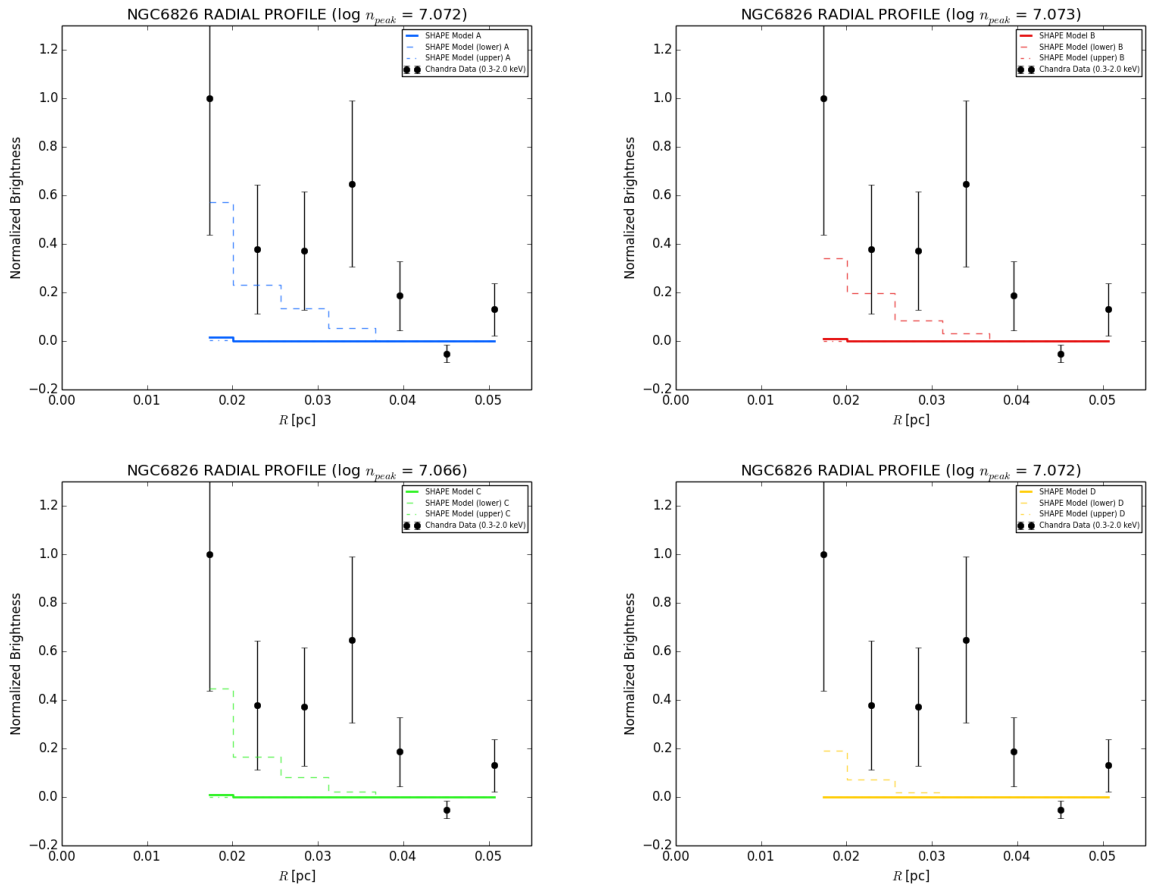

Figure 4.20: Best fit REP for the four density models used for NGC 6826. The configuration of this figure follows that of Fig. 4.10.

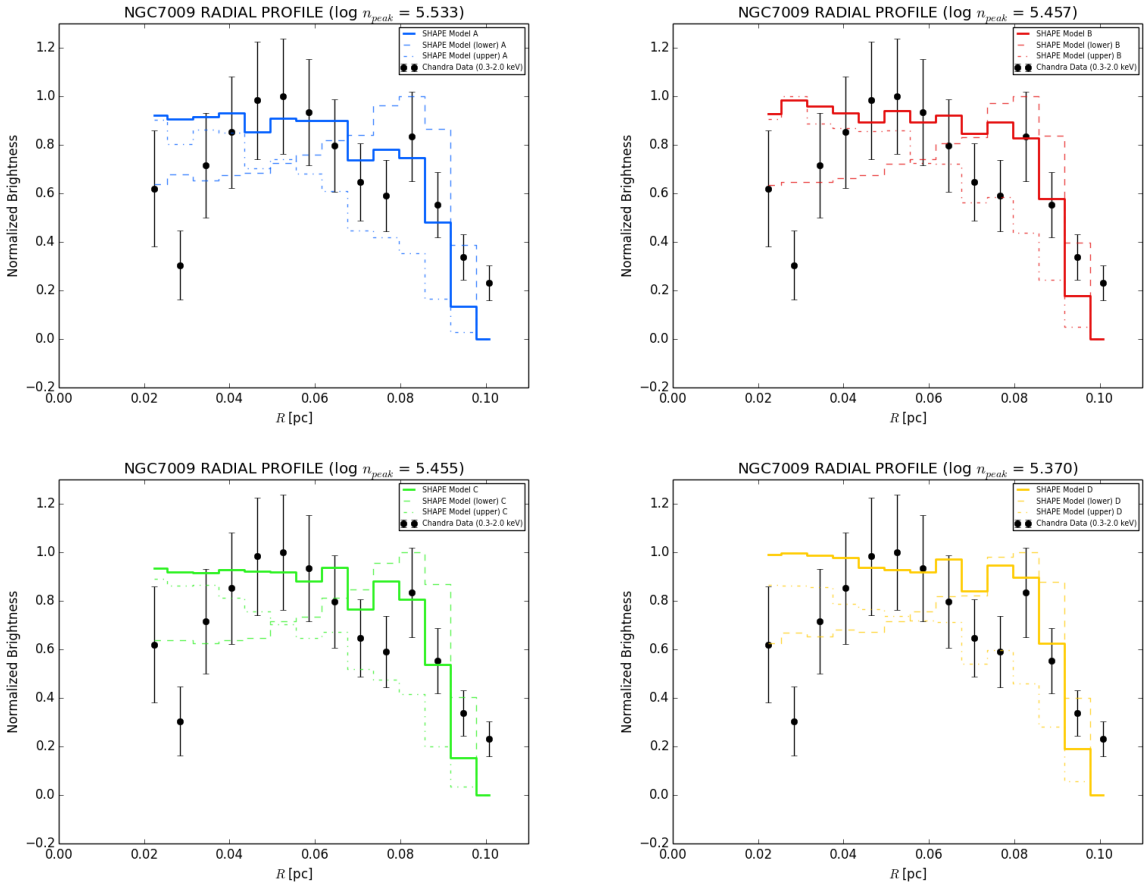

Figure 4.21: Best fit REP for the four density models used for NGC 7009. The configuration of this figure follows that of Fig. 4.10.

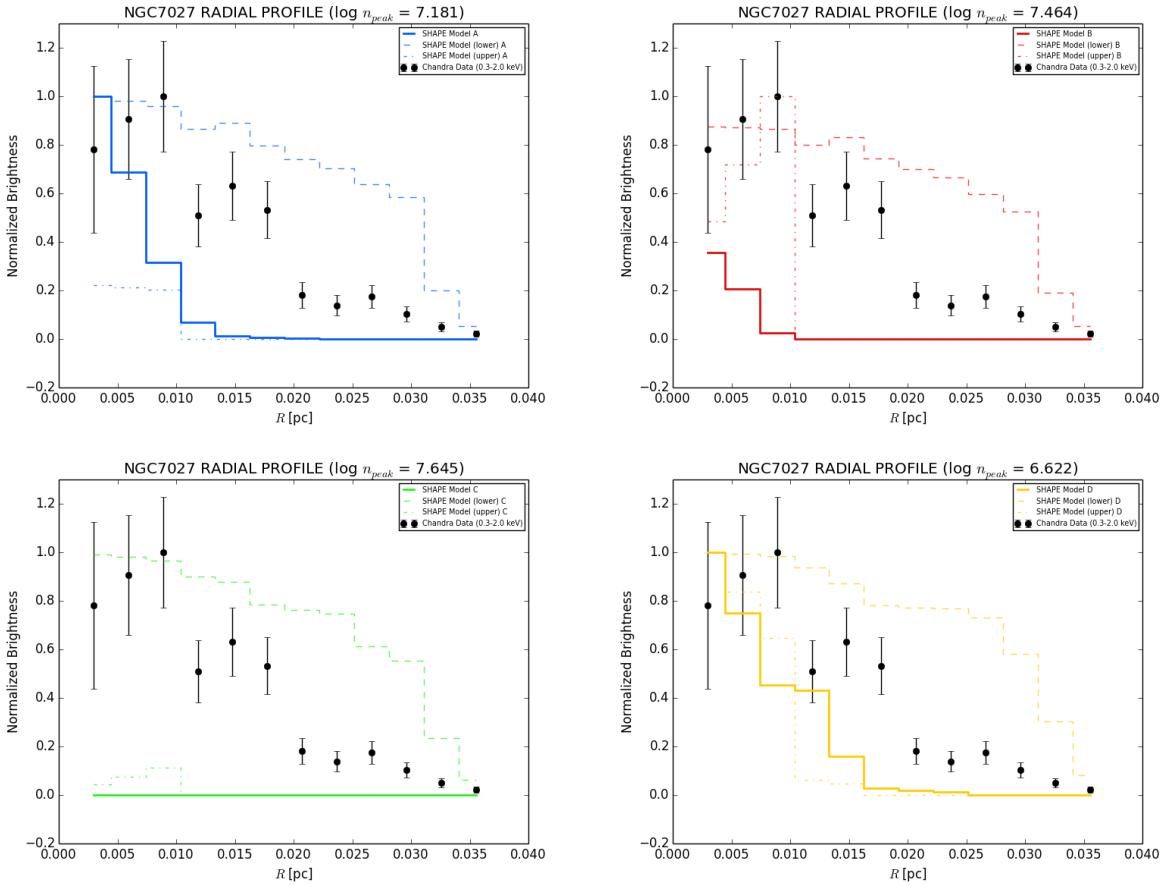

Figure 4.22: Best fit REP for the four density models used for NGC 7027. The configuration of this figure follows that of Fig. 4.10.

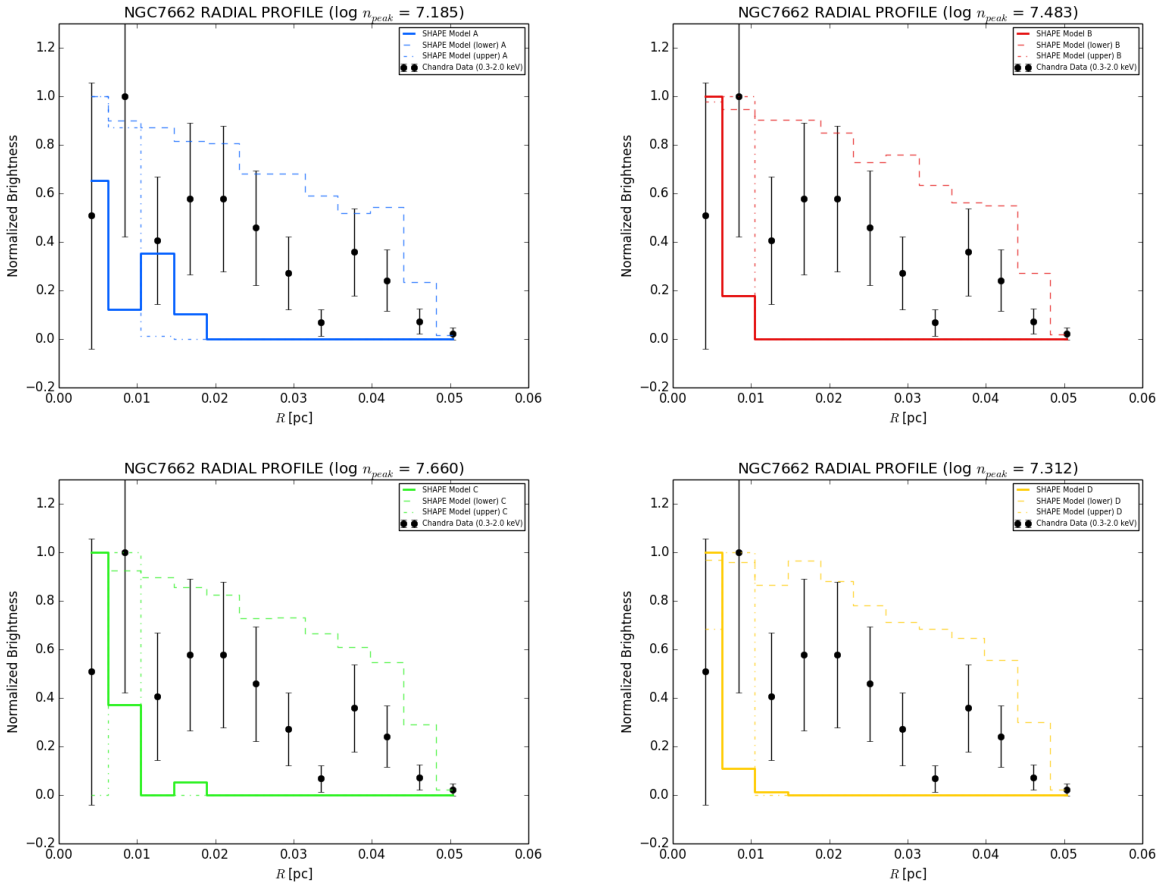

Figure 4.23: Best fit REP for the four density models used for NGC 7662. The configuration of this figure follows that of Fig. 4.10.

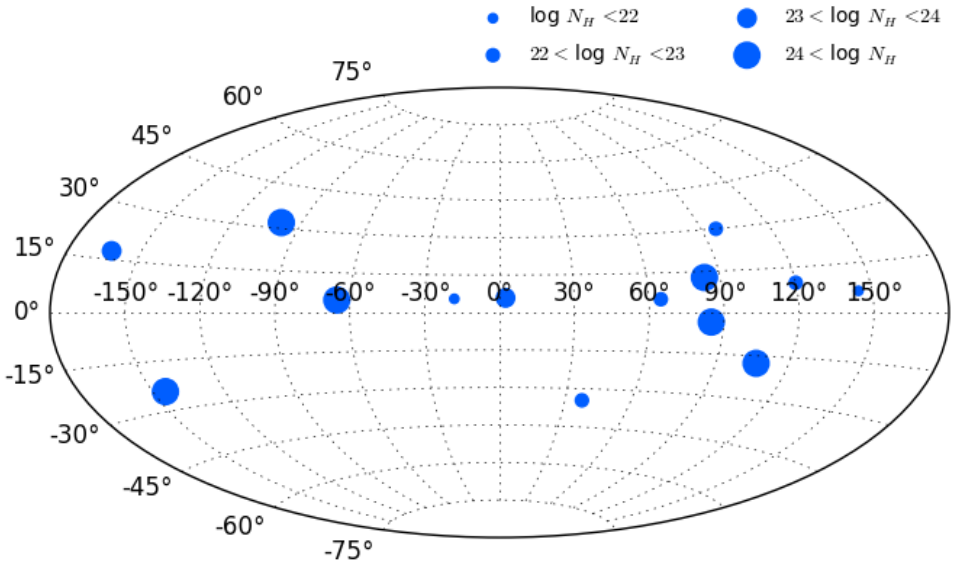

Figure 4.24: Map of our sample PNe including estimated column density. Here we use the A density model because there is a negligible difference between the $N_{\rm H}$ values calculated for A and the other density models. The estimated $N_{\rm H}$ appears independent of the location of the nebula in the galaxy.

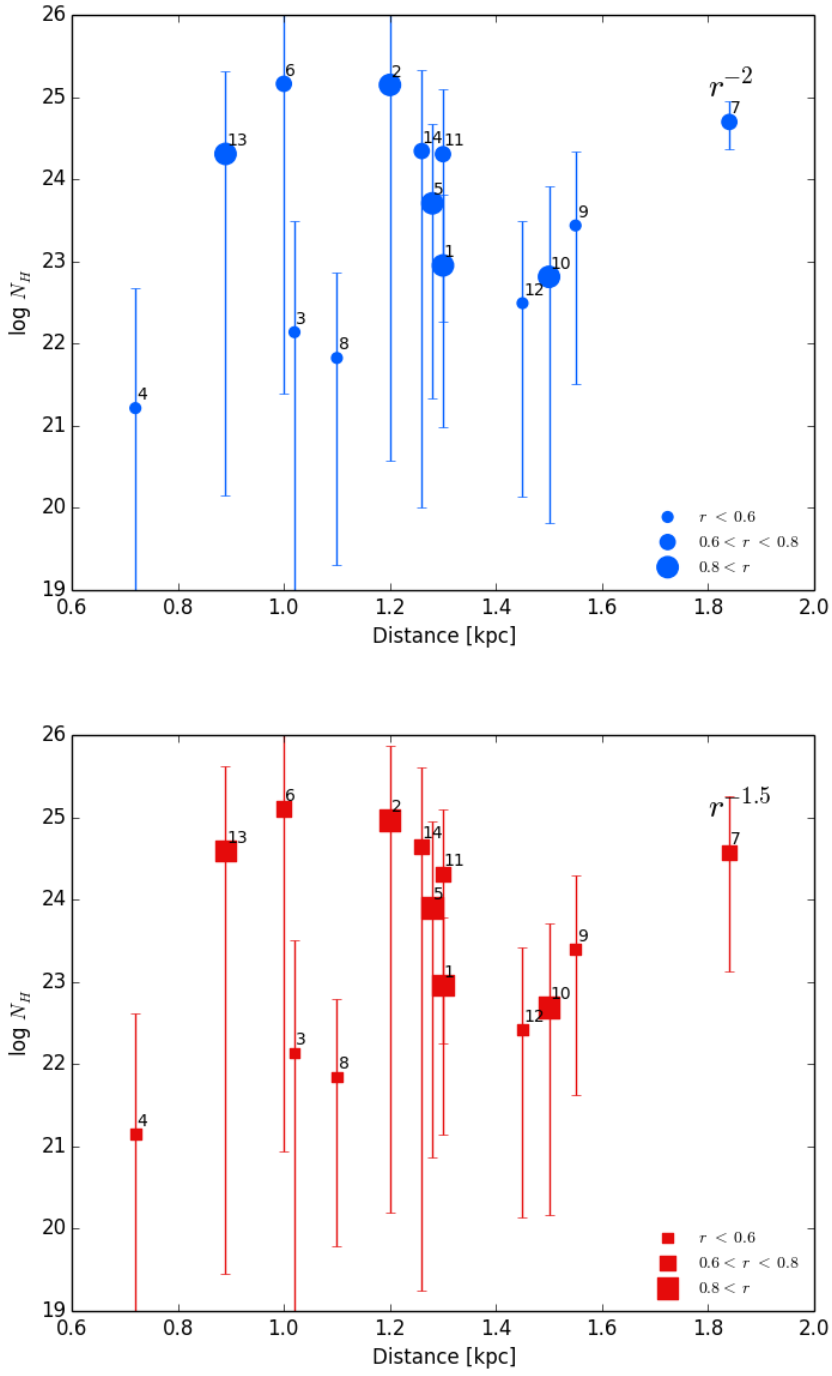

Figure 4.25: Estimated N_{H} compared to distance for models A and B.

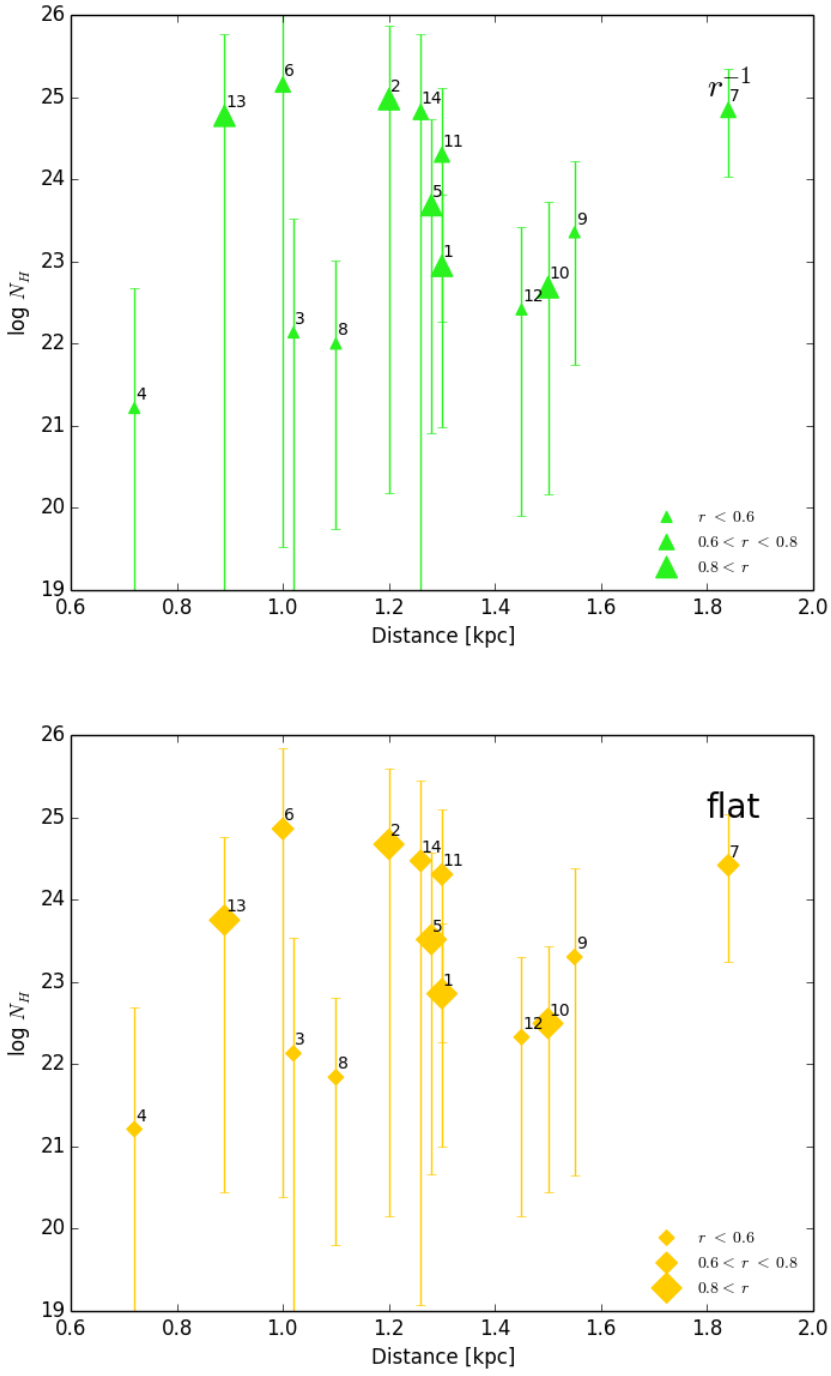

Figure 4.26: As with Fig. 4.25 with models C and D.

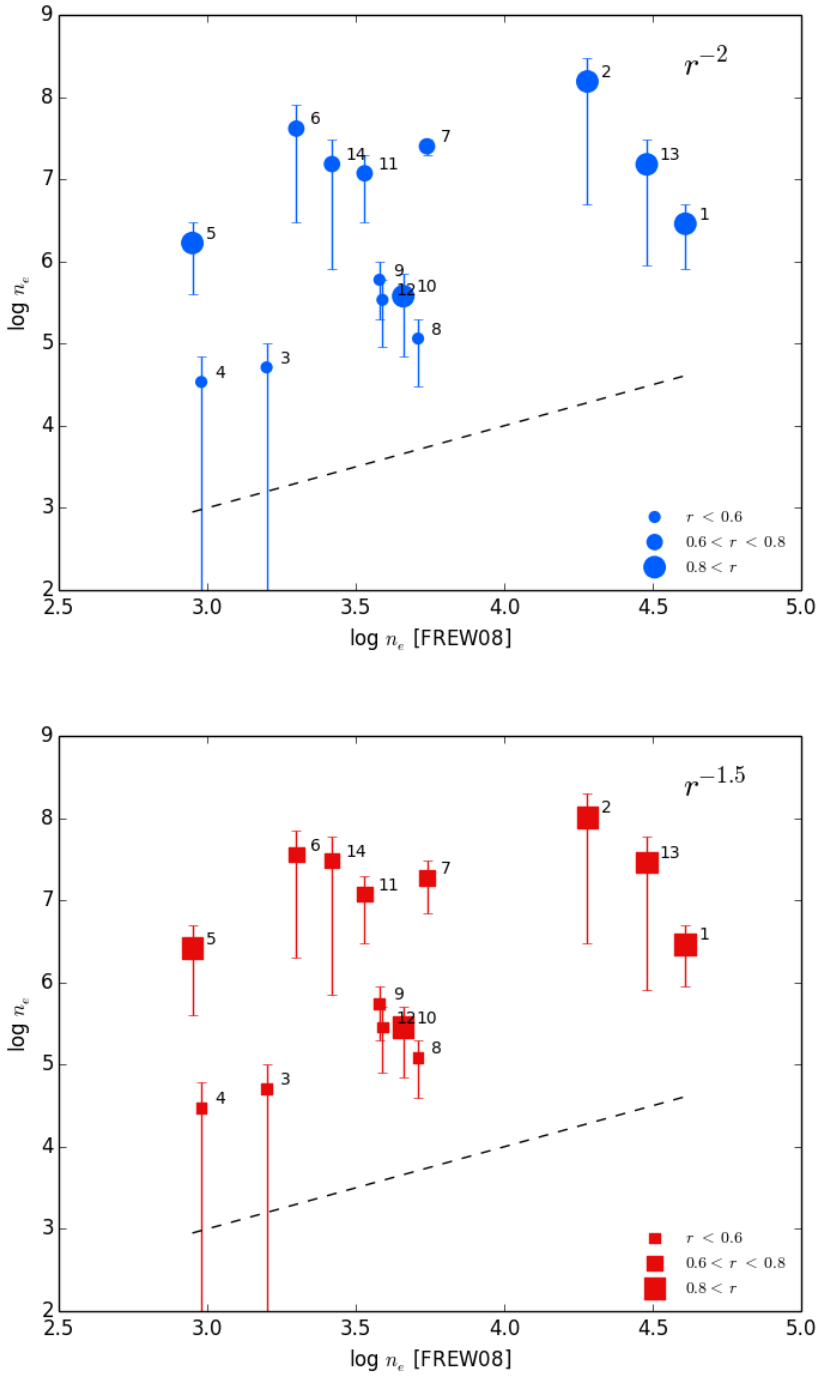

Figure 4.27: Nebular density versus previously published nebular density from Frew (2008) for density models A and B. The dashed line indicates a 1:1 agreement between the toy model densities and those reported by Frew (2008).

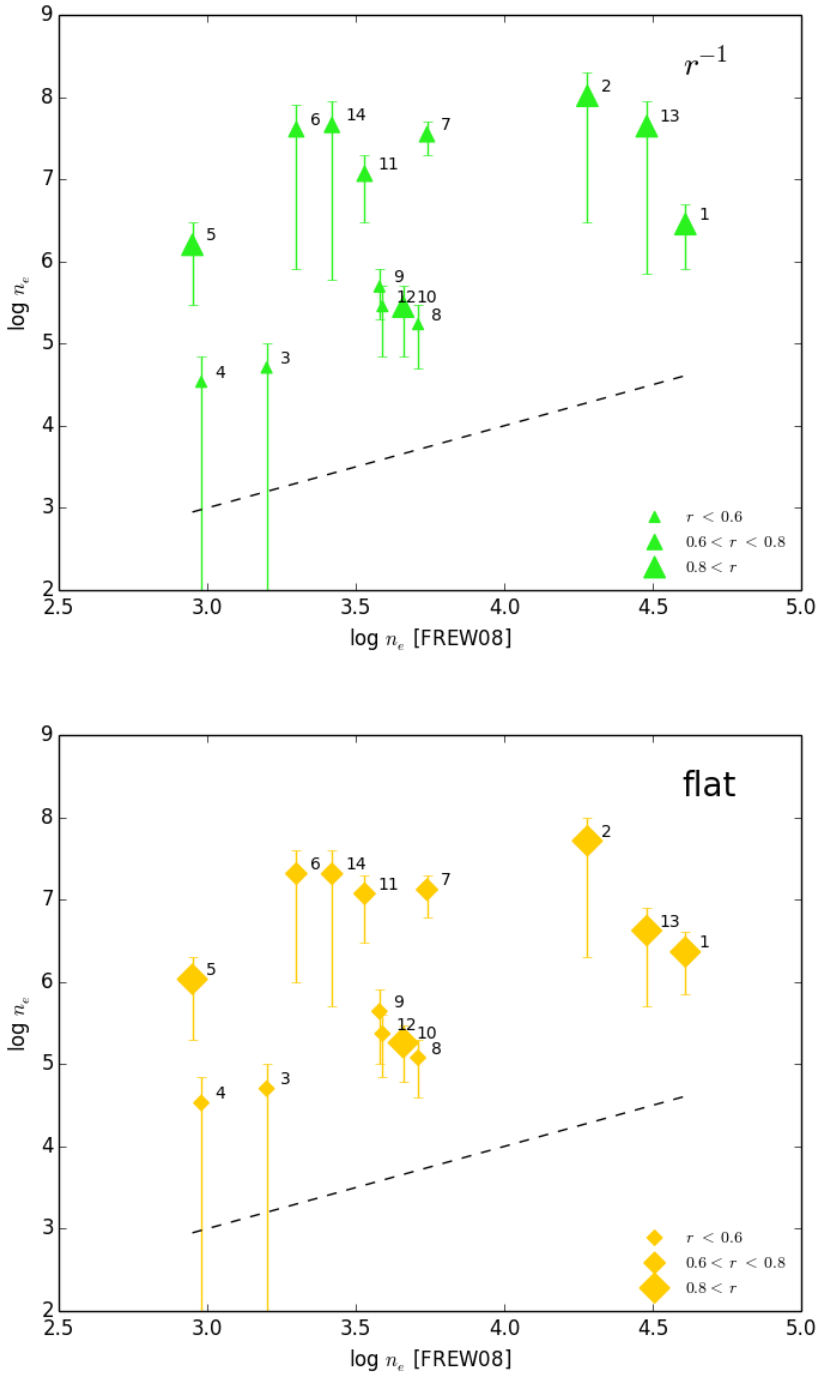

Figure 4.28: As in Fig. 4.27 for density models C and D.

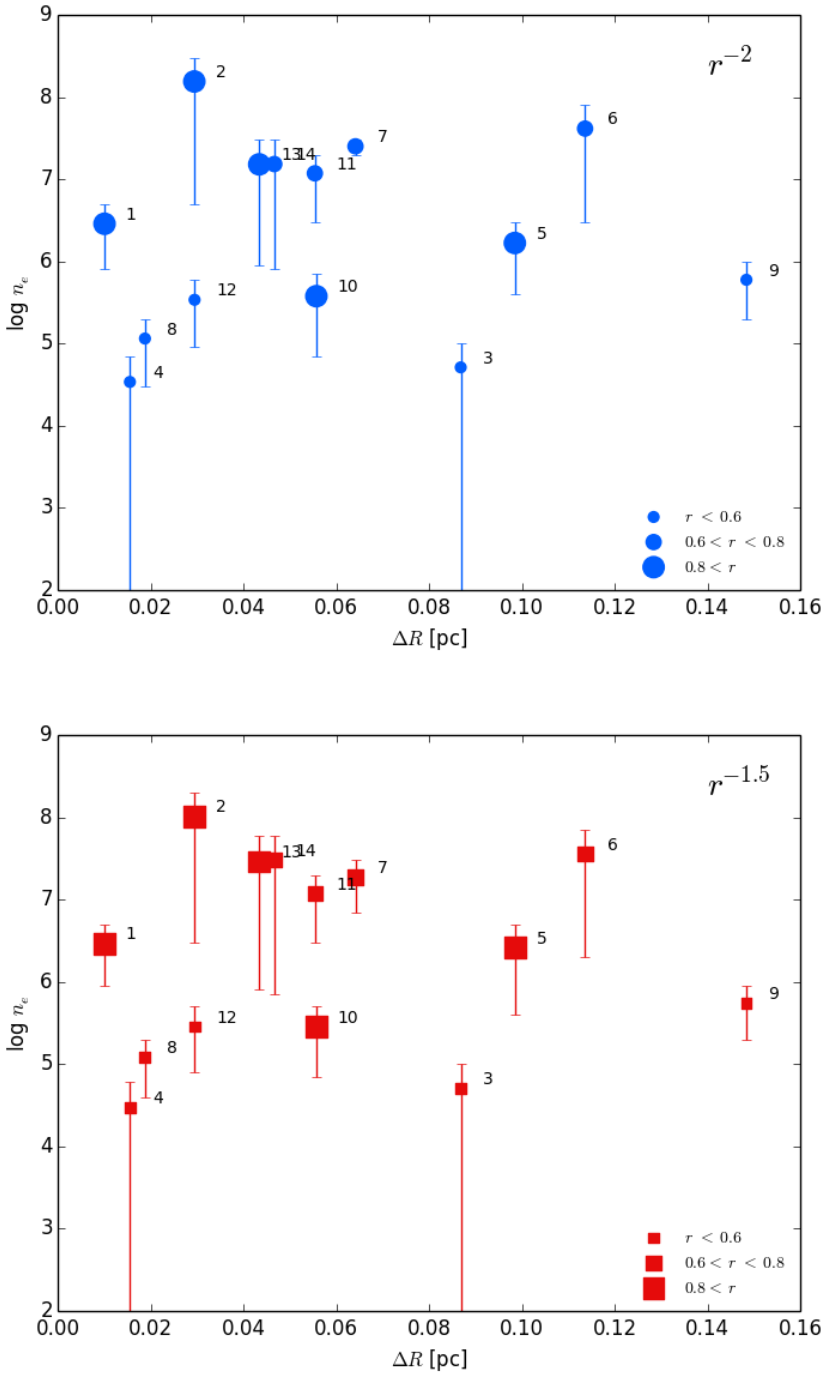

Figure 4.29: Nebular density versus shell thickness ΔR for density models A and B.

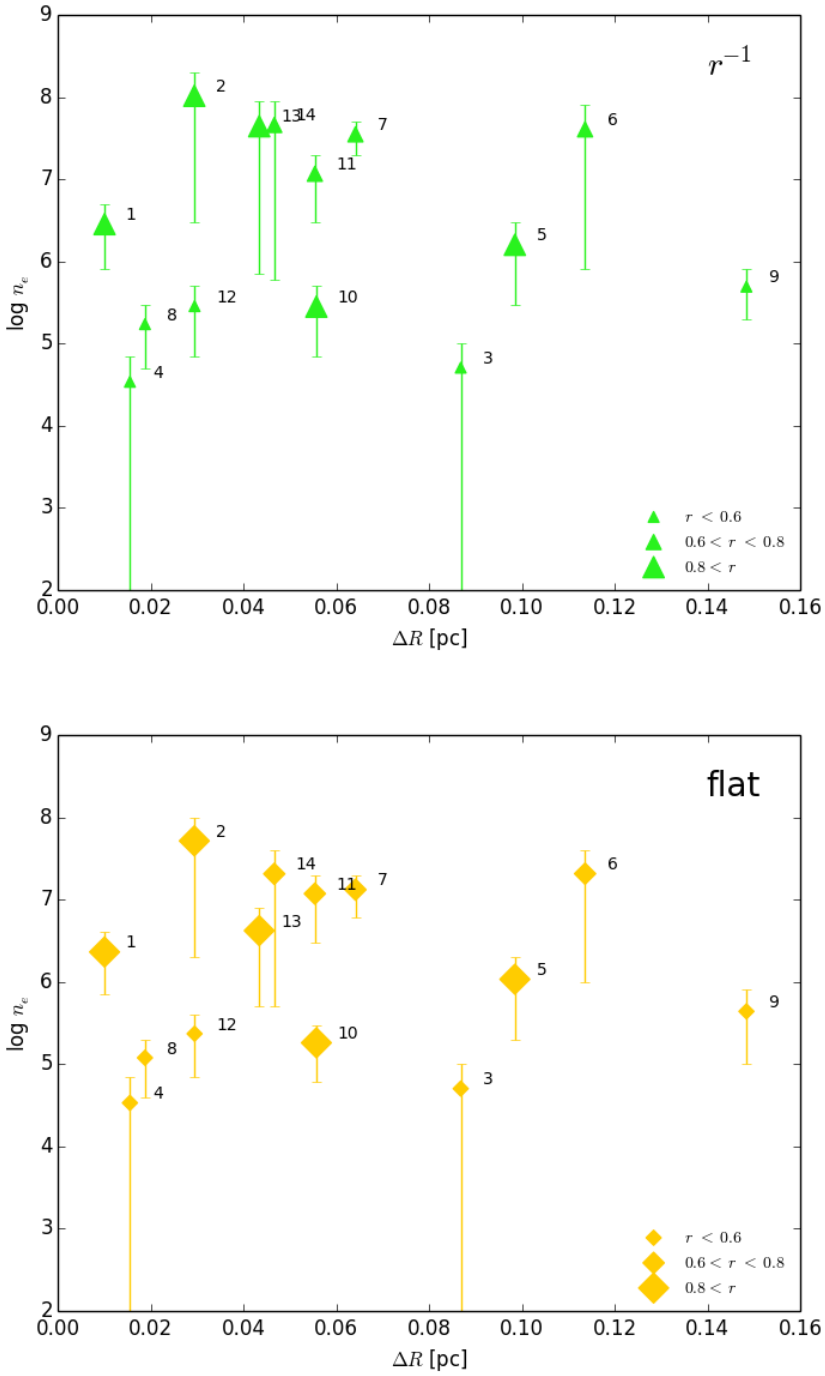

Figure 4.30: As in Fig. 4.27 for density models C and D.

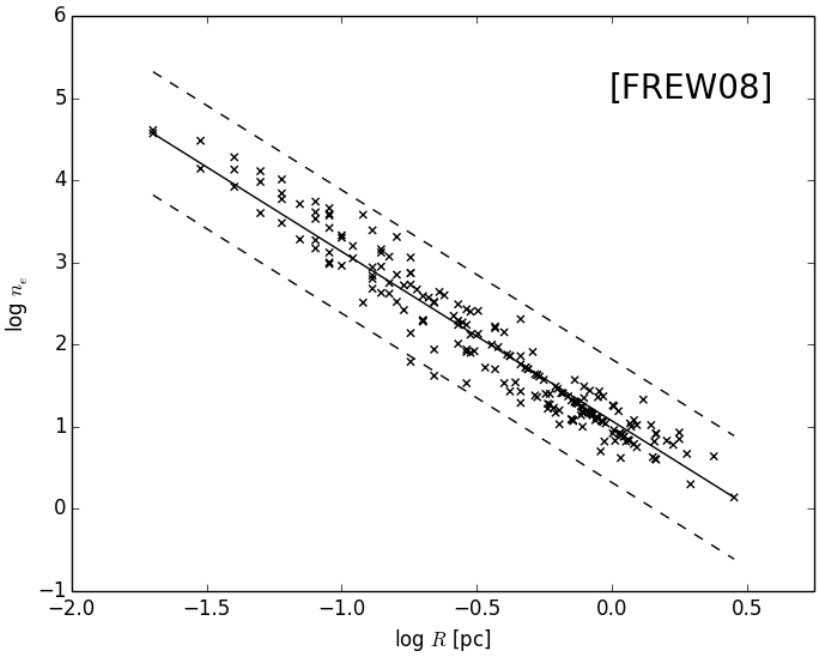

Figure 4.31: Nebular density n_e versus radius R based on Frew (2008) data. The solid line represents the best fit to the distribution, and the dashed lines represent a spread in density values of ± 0.75.

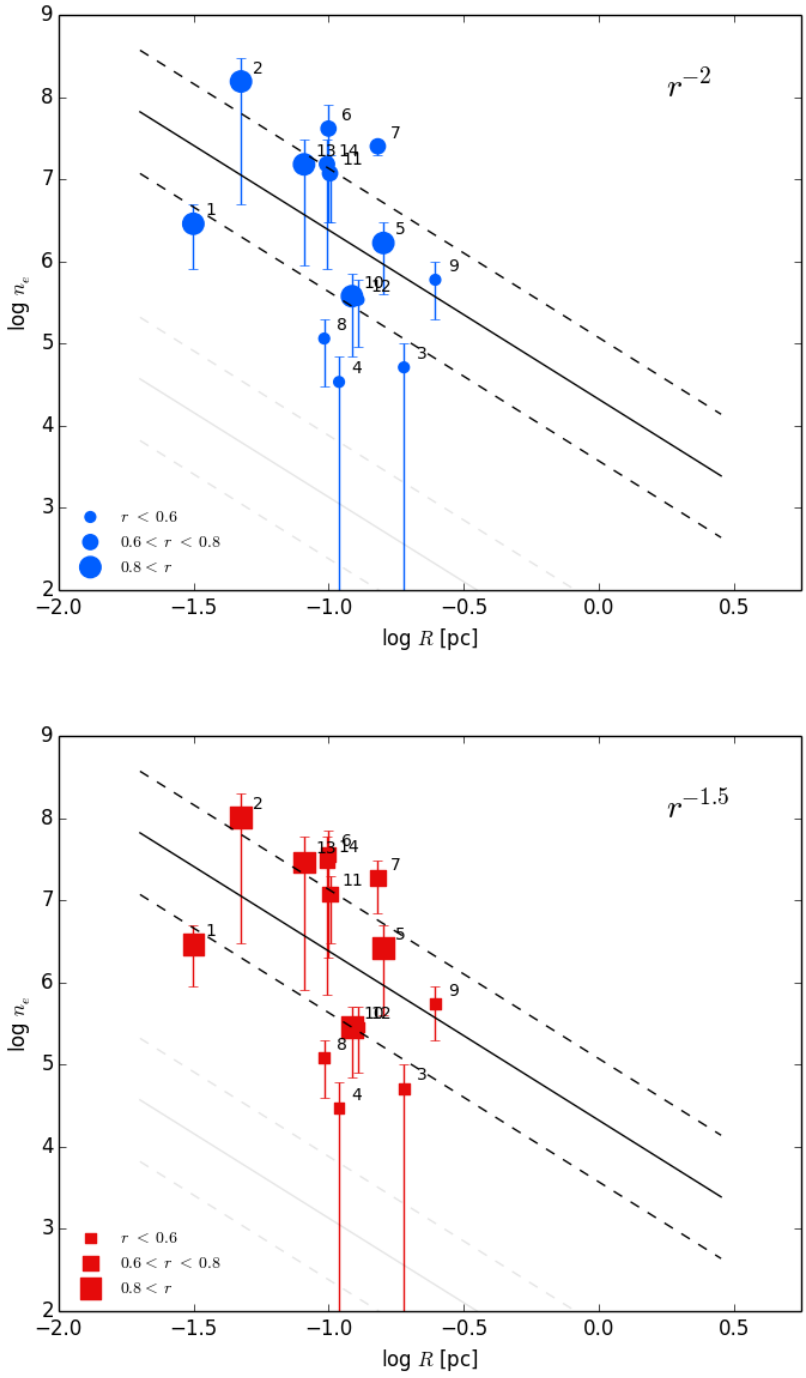

Figure 4.32: Nebular density n_e versus radius R for our toy models for density models A and B. The solid line represents the best fit to the Frew (2008) distribution, scaled by 3.25 to fit our range of values. The dashed lines again represent $\log n_{e,\mathrm{FREW}} \pm 0.75$.

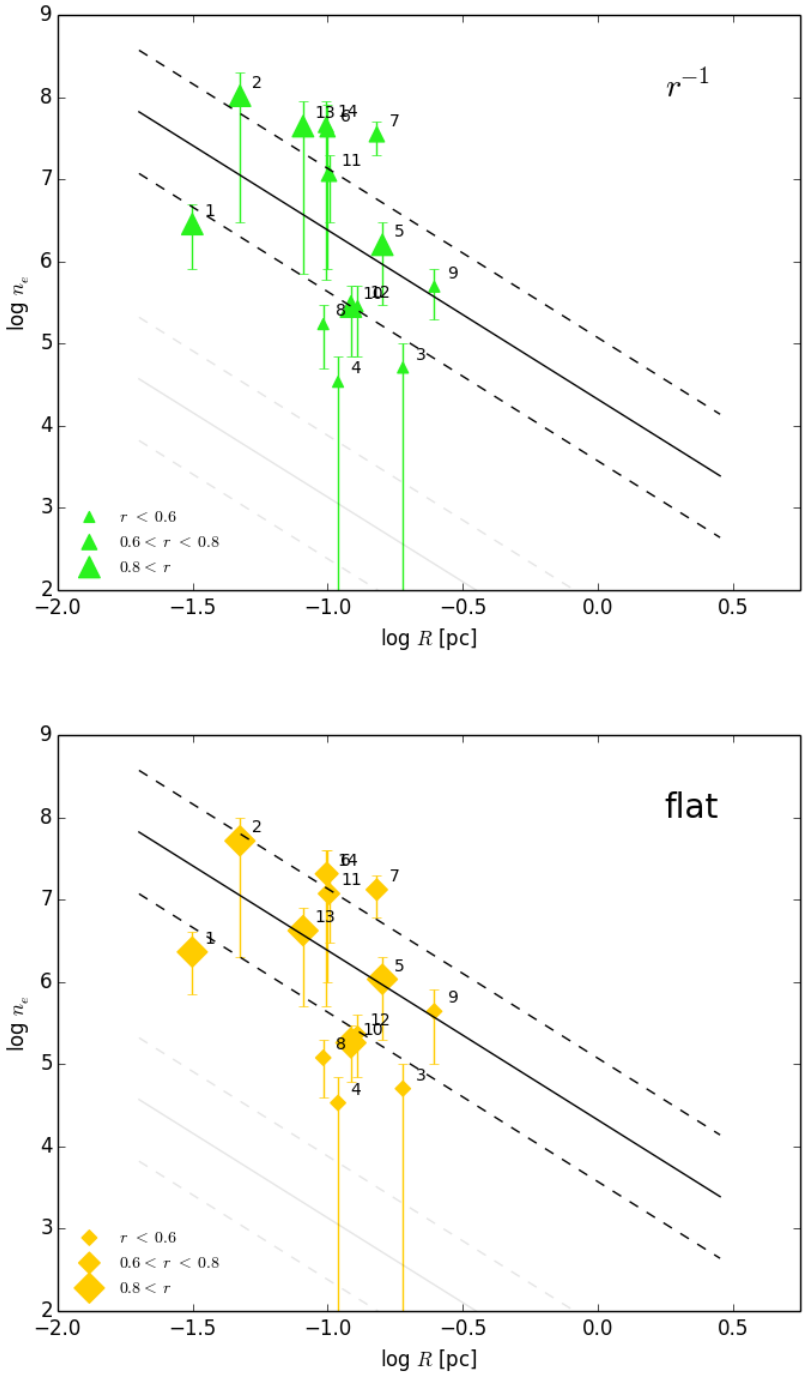

Figure 4.33: As with Fig. 4.32 with models C and D.

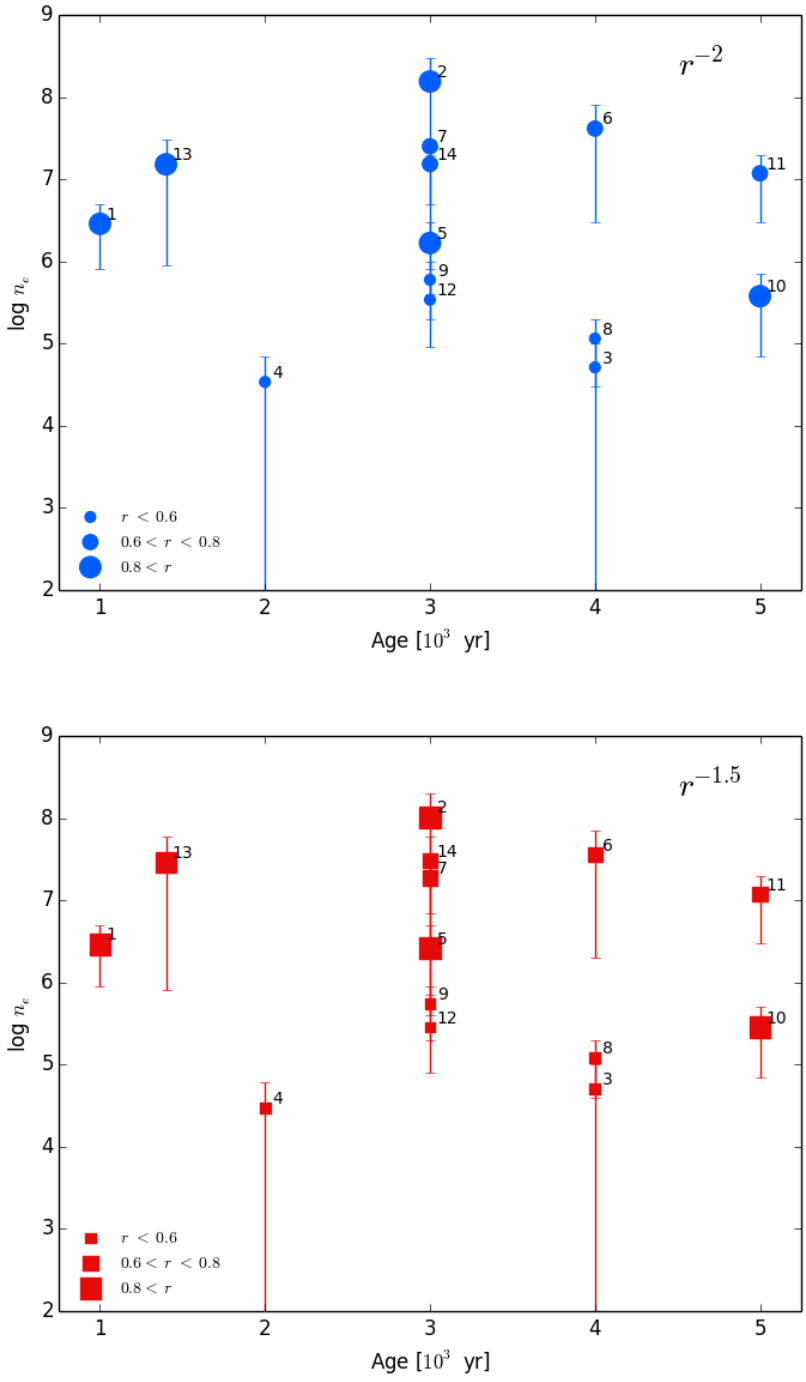

Figure 4.34: Nebular density n_e versus nebular age for density models A and B. The age of each nebula is a factor of 1000 yr and is measured based on the expansion velocity and radius of the nebula.

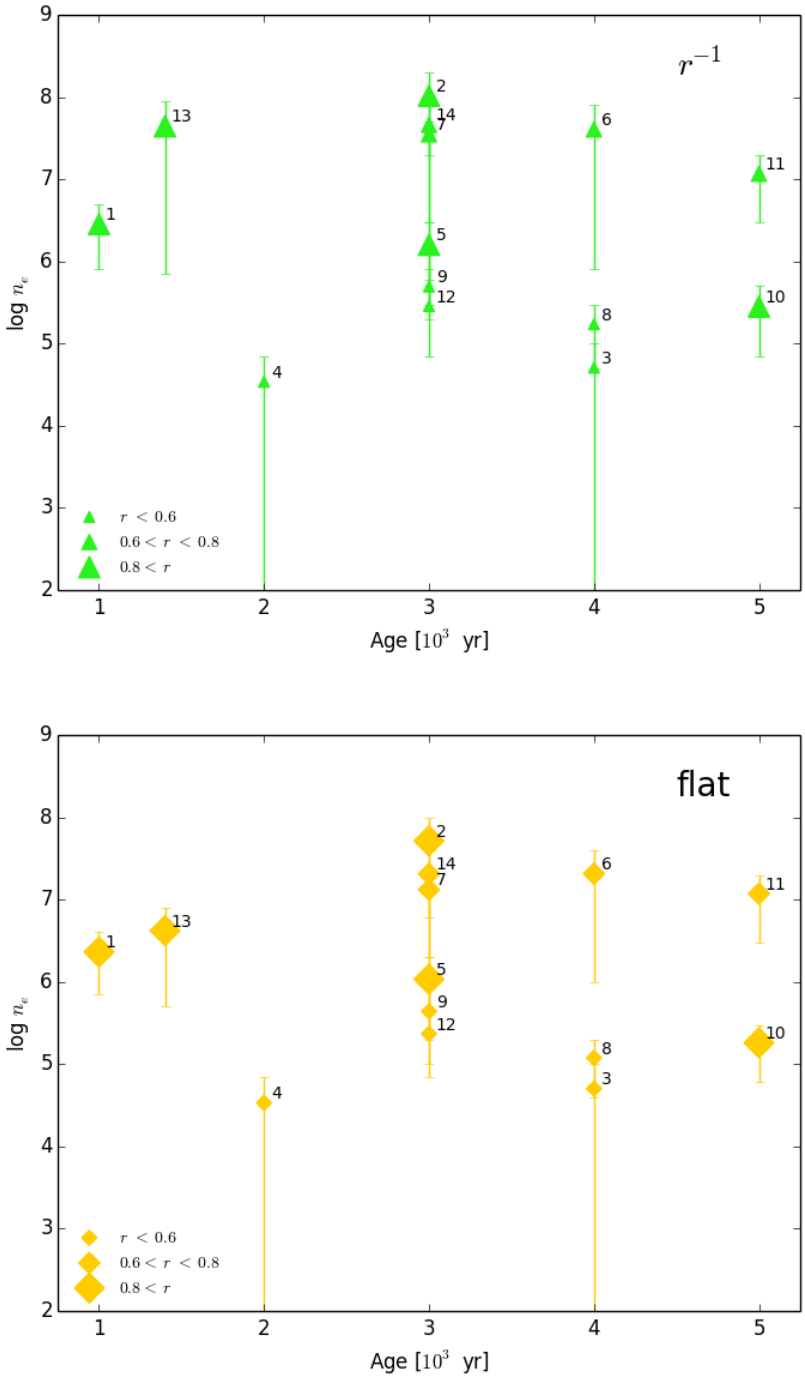

Figure 4.35: As with Fig. 4.34 with models C and D.

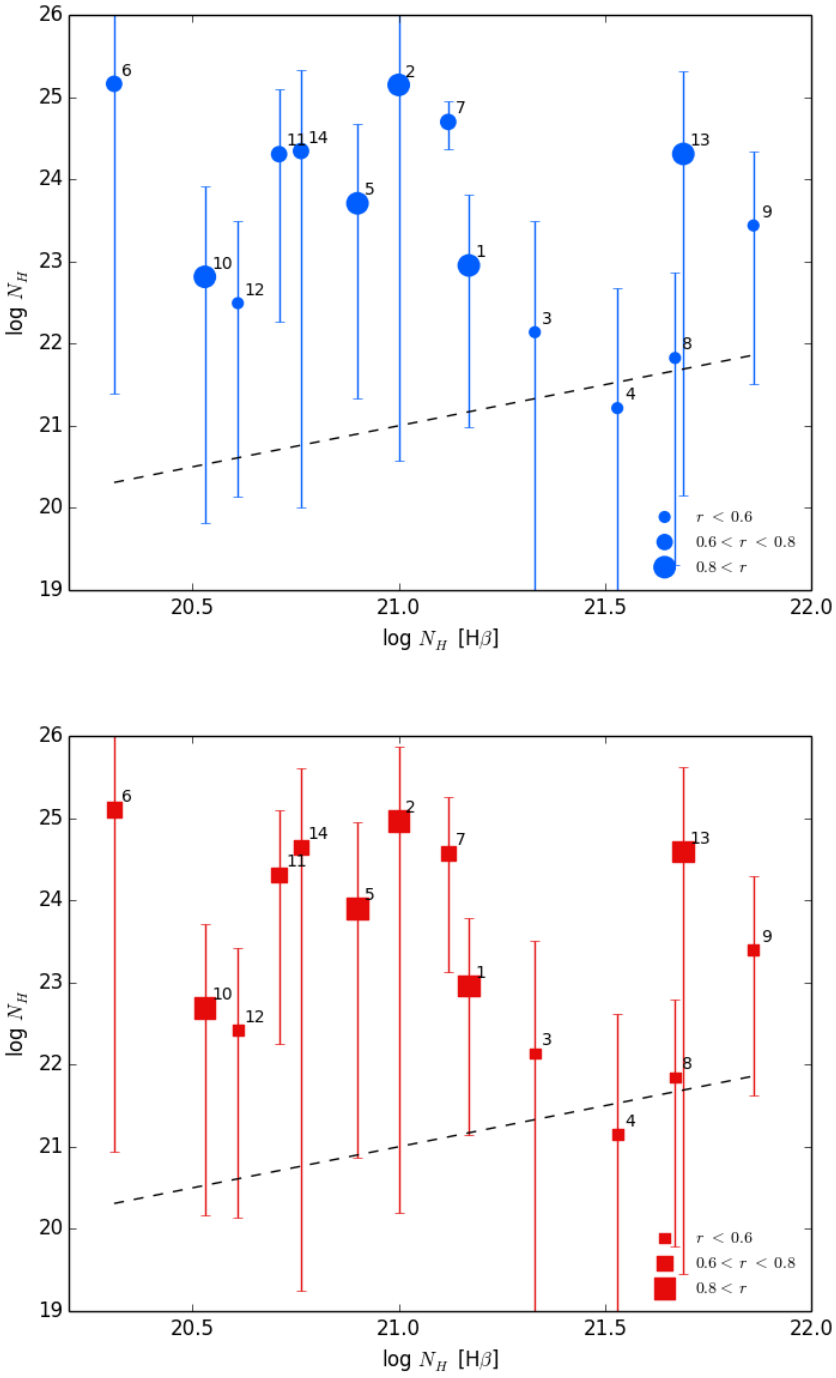

Figure 4.36: Estimated column density $N_{\rm H}$ compared to $N_{\rm H}$ determined from measurements of $c_{{\rm H}\beta}$ for density models A and B. The dashed line represents a 1:1 ratio to the $c_{{\rm H}\beta}$ column density values.

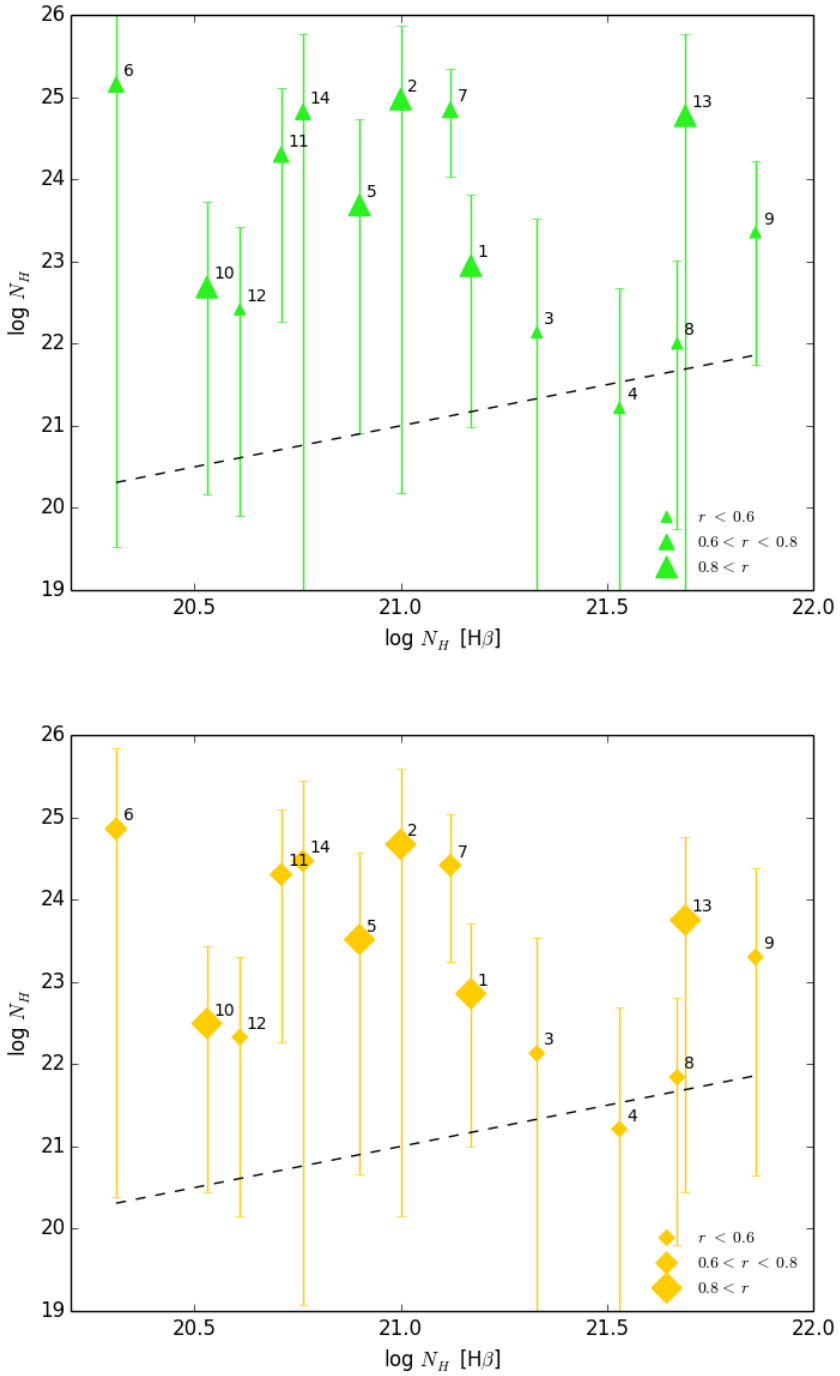

Figure 4.37: As with Fig. 4.25 with models C and D.

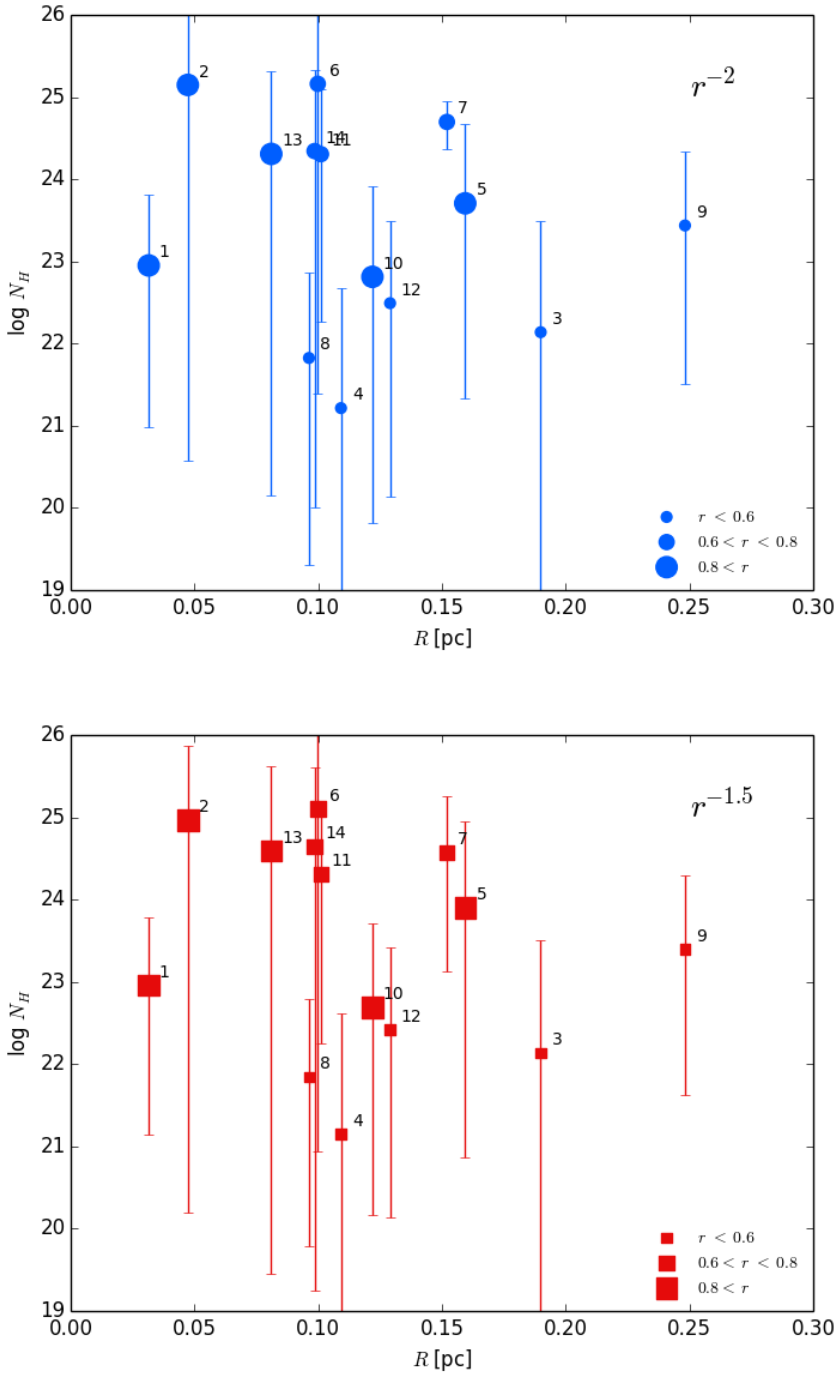

Figure 4.38: Estimated column density $N_{\rm H}$ and nebular radius R for density models A and B.

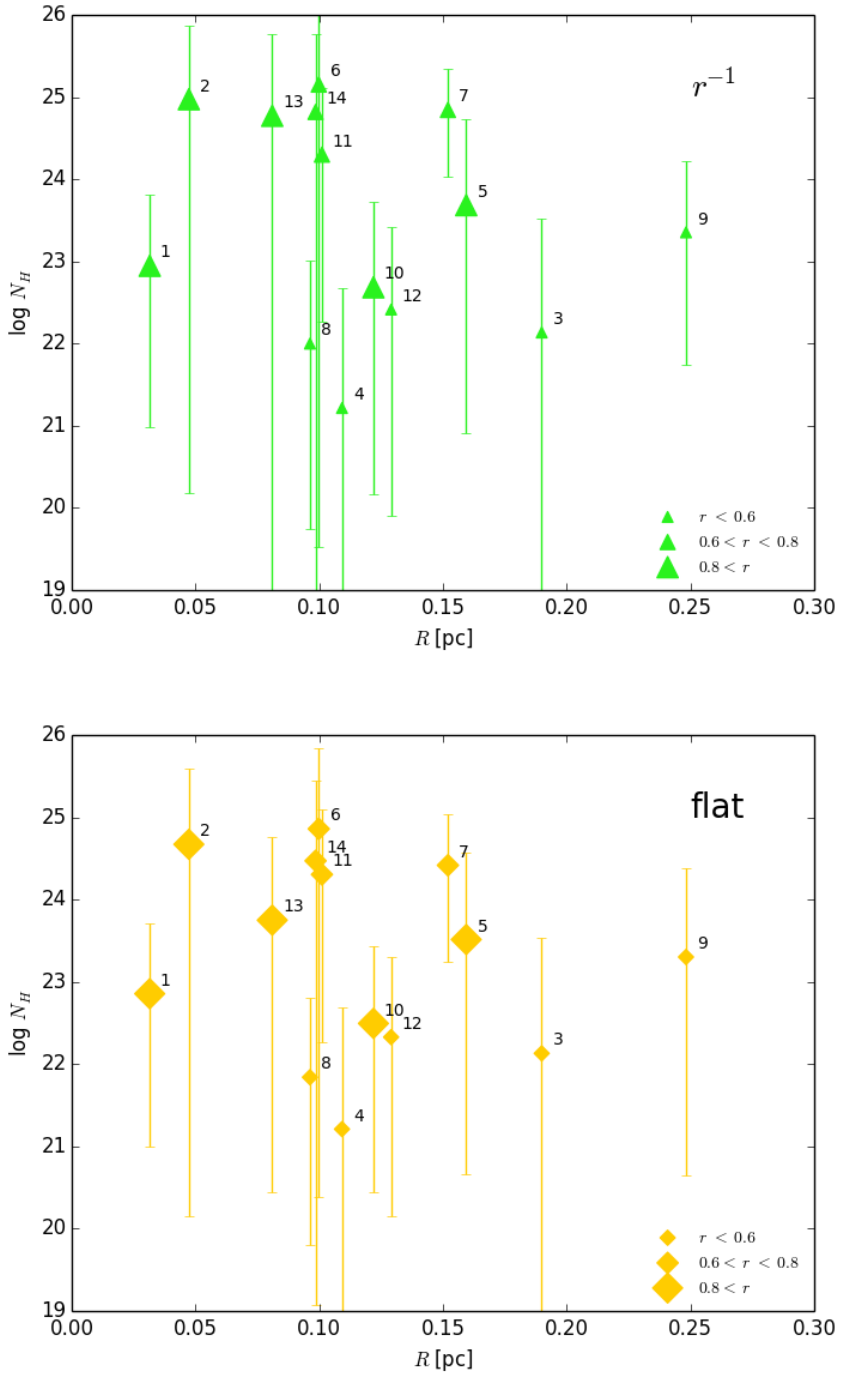

Figure 4.39: As with Fig. 4.38 with models C and D.

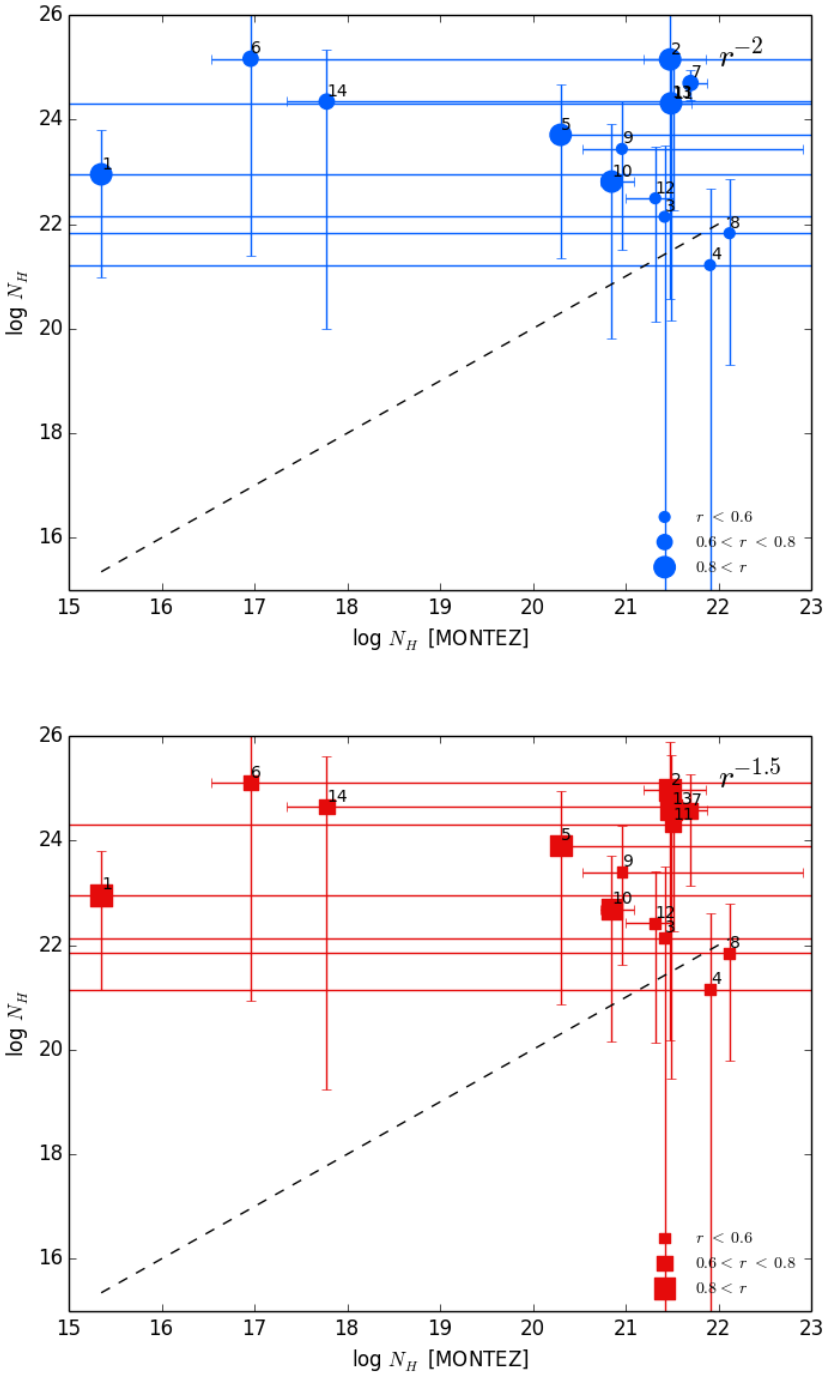

Figure 4.40: Estimated column density $N_{\rm H}$ compared to $N_{\rm H}$ determined from X-ray spectra for density models A and B. The dashed line represents a 1:1 ratio to the column density values from X-ray fitting.

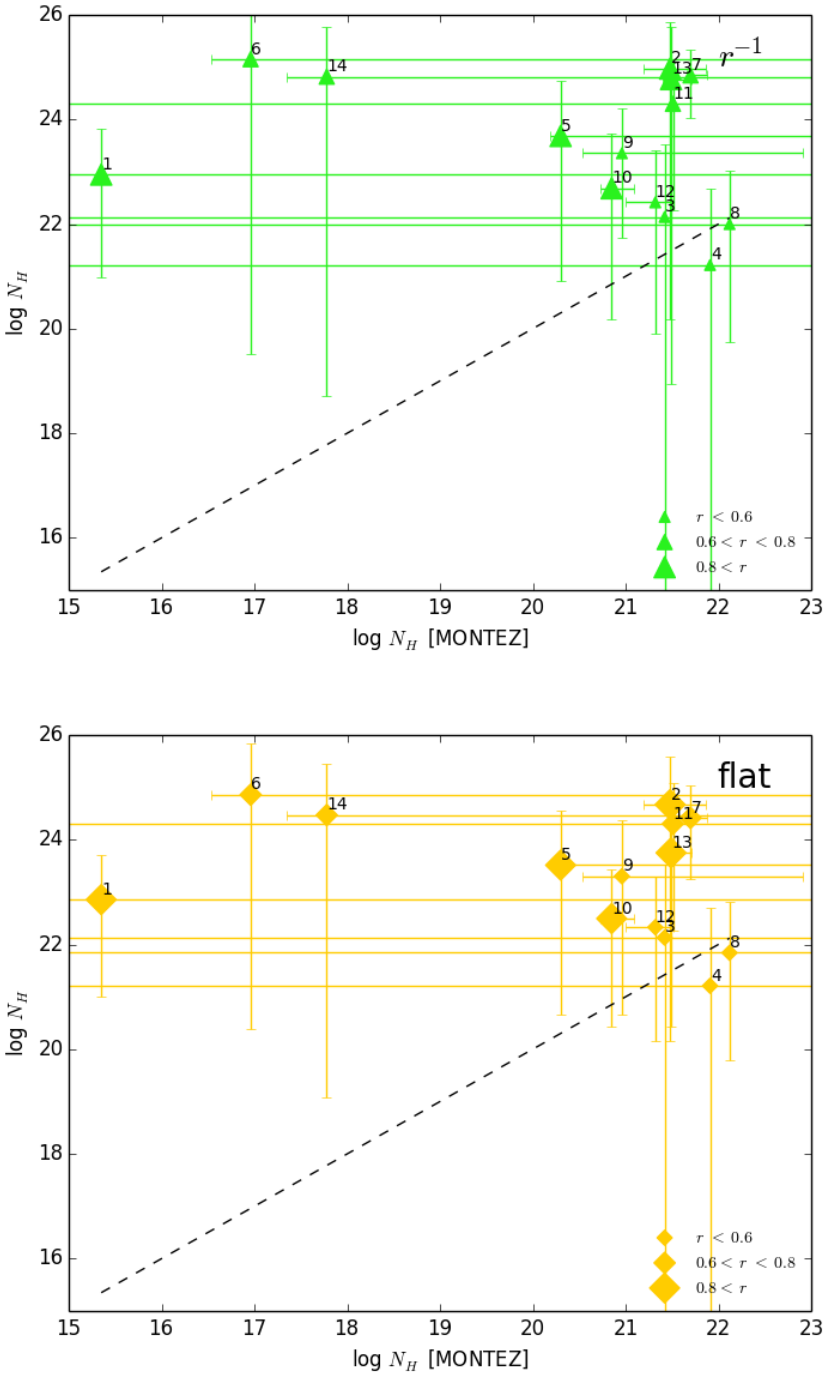

Figure 4.41: As with Fig. 4.40 with models C and D.

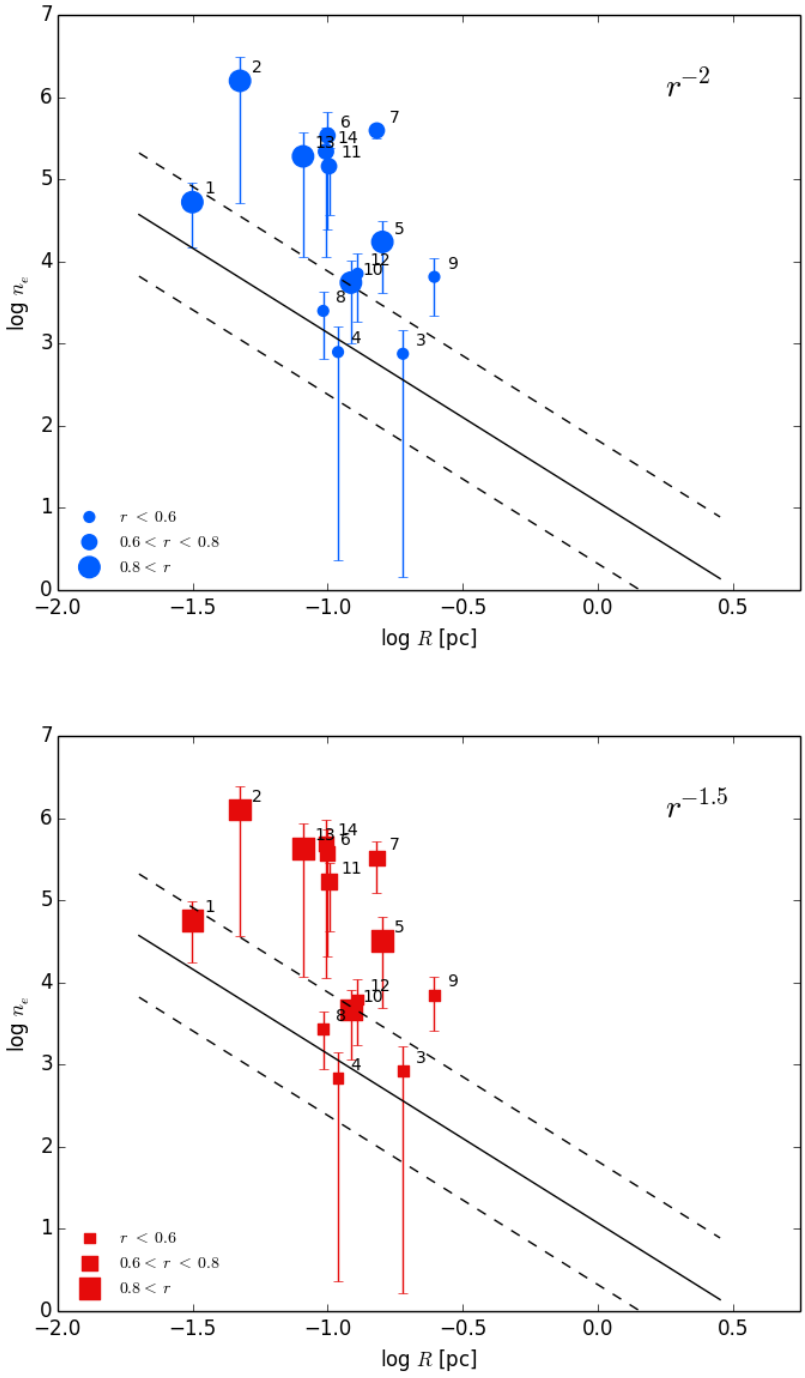

Figure 4.42: Nebular density n_e normalized using the X-ray spectral fit of BD+30 versus radius R for our toy models for density models A and B. The solid line represents the best fit to the Frew (2008) distribution, and the dashed lines represent $\log n_{e,\mathrm{FREW}} \pm 0.75$.

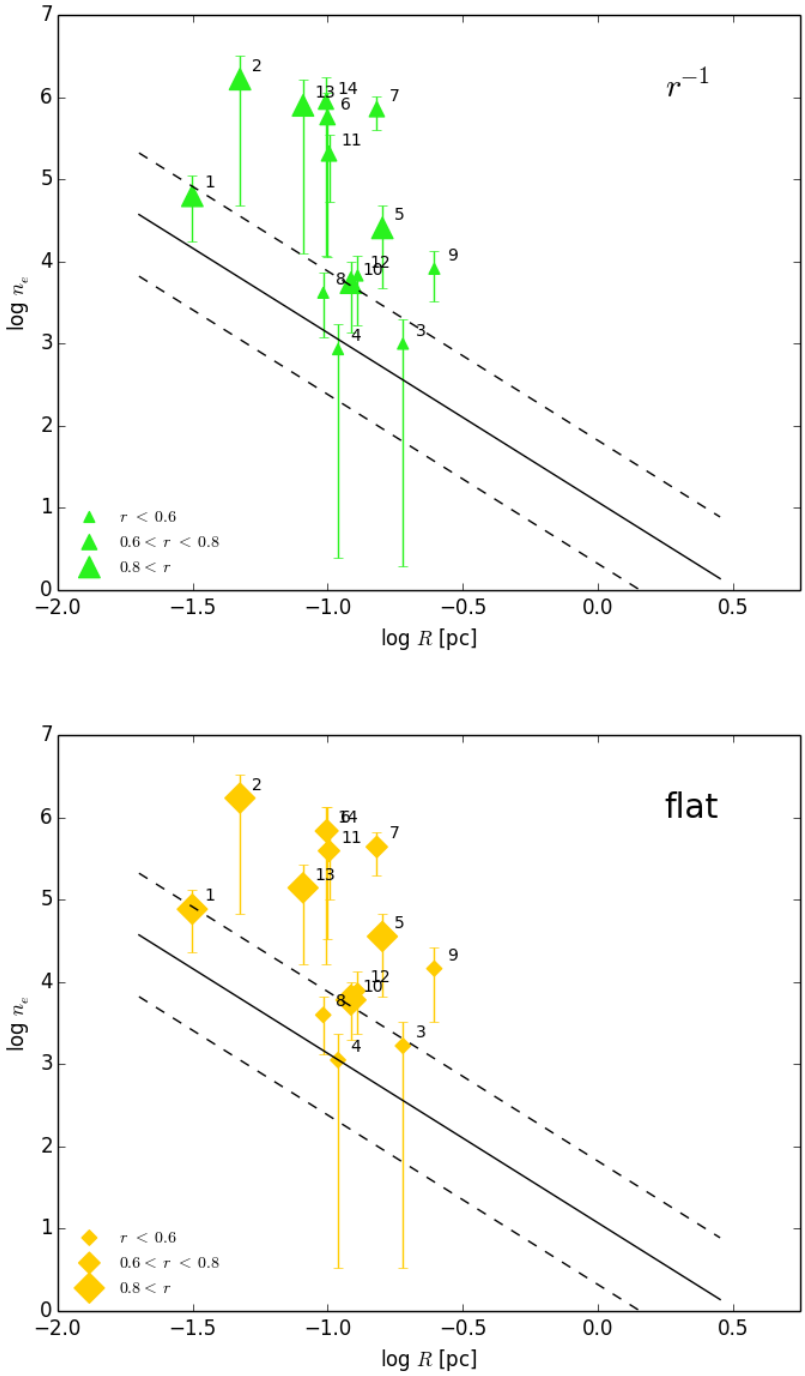

Figure 4.43: As with Fig. 4.42 with models C and D.

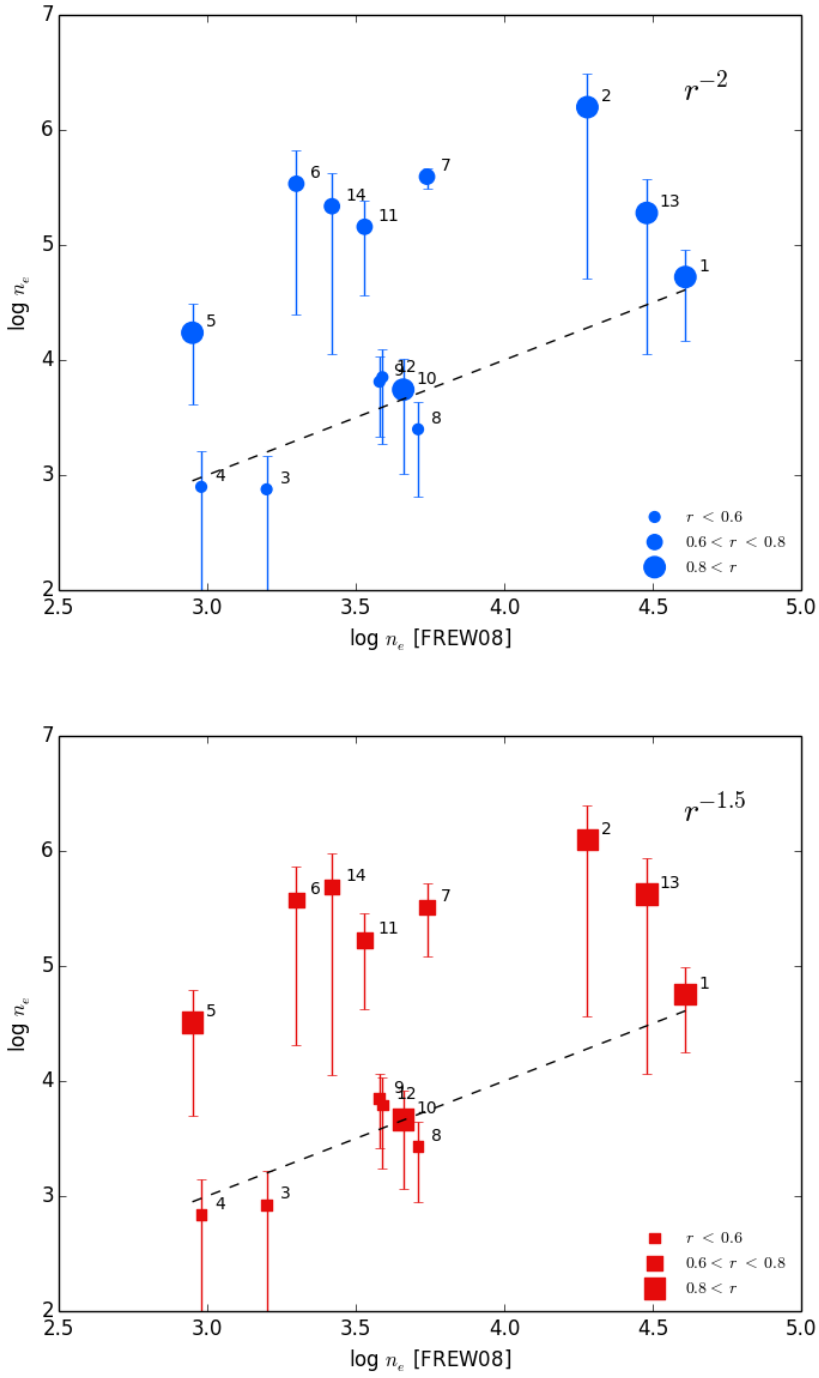

Figure 4.44: Nebular density normalized using the X-ray spectral fit of BD+30 versus previously published nebular density from Frew (2008) for density models A and B. The dashed line indicates a 1:1 agreement between the toy model densities and those reported by Frew (2008).

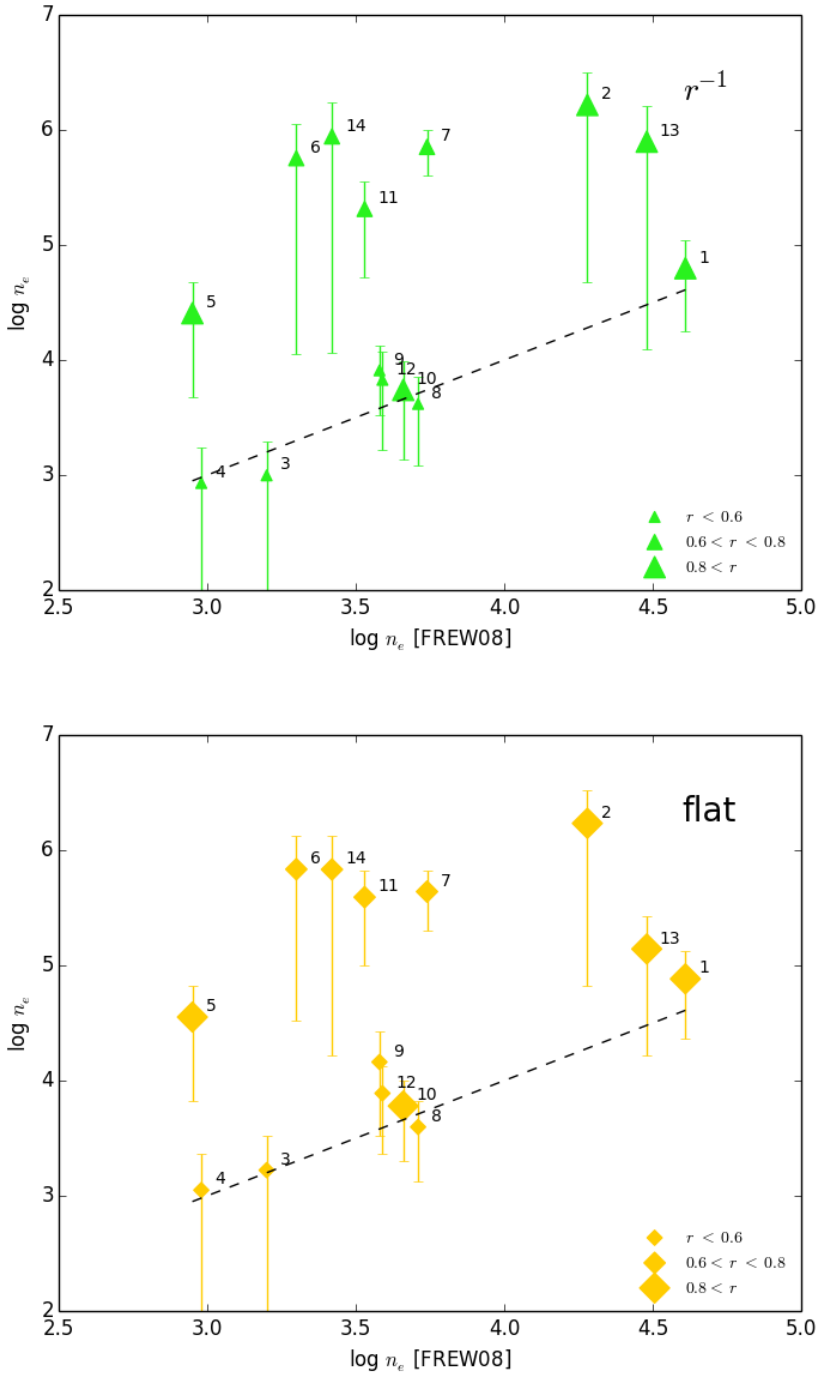

Figure 4.45: As in Fig. 4.44 for density models C and D.

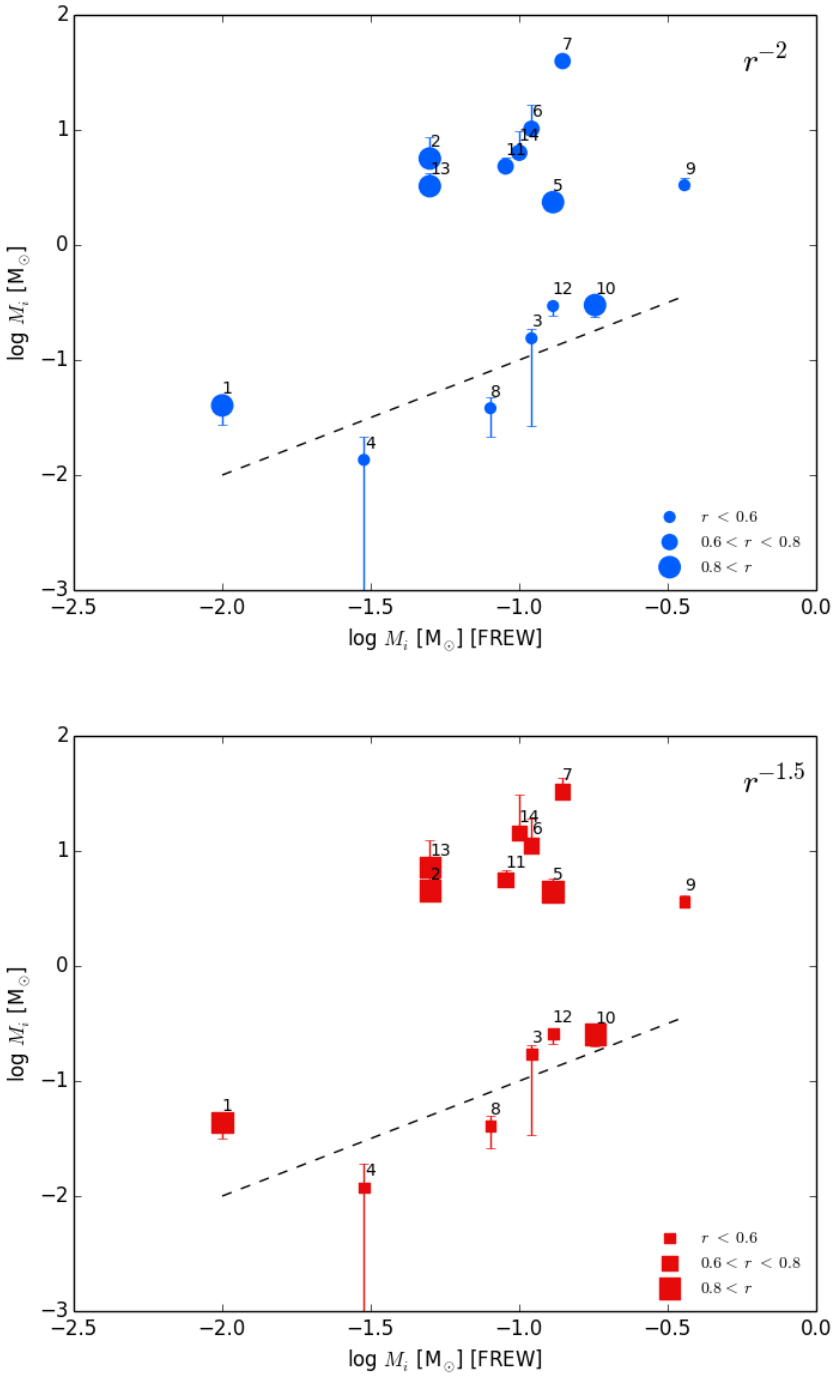

Figure 4.46: Ionized mass versus previously published ionized mass from Frew (2008) for density models A and B. The dashed line indicates a 1:1 agreement between the toy model masses and those reported by Frew (2008).

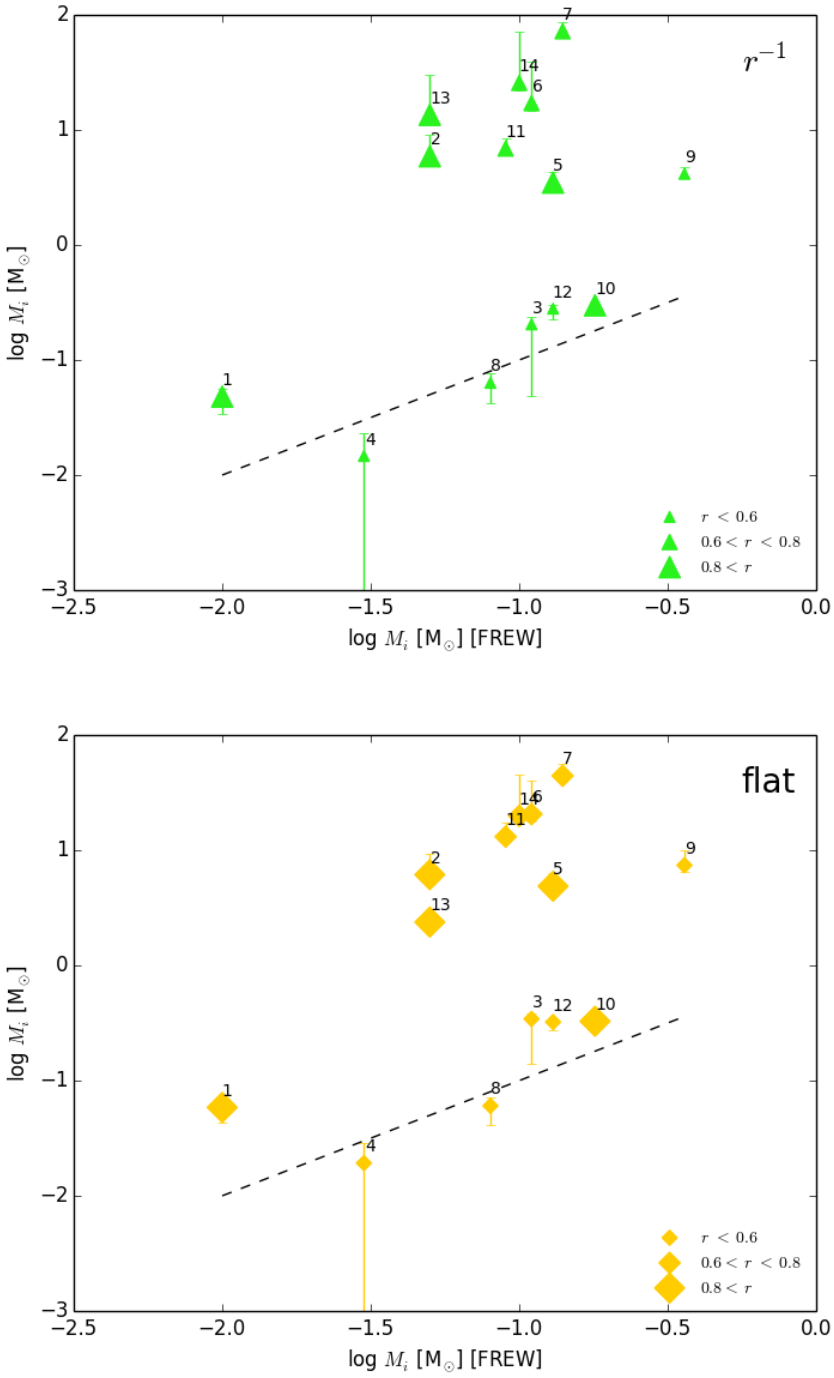

Figure 4.47: As in Fig. 4.46 for density models C and D.

CHAPTER 5

A MULTIWAVELENGTH 3D MODEL OF BD+30°3639

5.1 Introduction

Given our point of view from Earth, we are often limited in our understanding of 3-dimensional structures of astronomical objects. In the context of this thesis, recent attempts to model PNe in 3D have revealed that the projected morphology can be quite different from the 3D structure. Structures that appear circular or elliptical are in fact found to be bipolar (Jones et al., 2012). Information about the 3D morphology and kinematics of a handful of PNe have been analyzed in the past, but multiple interpretations of the data can help elucidate different structures and morphologies. By combining data from X-ray through radio regimes we are able to better compare PNe with different projected morphologies, physical properties, and CSPN-types in order to identify the most important processes that are involved in the formation of PNe.

In this thesis we present a multiwavelength study of BD+30°3639 (henceforth BD+30), a thoroughly investigated PNe. As one of the brightest and youngest ($\sim 10^3$ yr) PNe observed in the solar neighborhood, BD+30 has been the target of many observations across the electromagnetic spectrum. Upon first glance, BD+30 appears as an elliptical nebula with an internal, ring-like structure, a feature that appears in many other PNe, though here the ring is boxy (Fig. 5.1).

Figure 5.1: Composite *HST* and *Chandra* (blue emission) image of BD+30°3639 (credit: NASA/CXC/STScI/J.Kastner et al.).

It hosts a Wolf-Rayet-type (WR) central star, identified as [WC9]-type, which is responsible for dominating the ultraviolet spectrum of the nebula (Bernard-Salas & Tielens, 2005). Very Large Array (VLA) and IRAM observations suggested a prolate ellipsoidal morphology with unusual high velocity molecular CO emission (Masson, 1989; Bachiller et al., 2000). Optical emission line observations performed by *Hubble Space Telescope (HST)* of BD+30 highlight the asymmetrical nature of the nebula, revealing its clumpy nature caused in part by dust extinction (Arnaud et al., 1996). The projected *Chandra* radial emission profile of the diffuse X-ray emission appears to also suffer from moderate nebular extinction, which may in part be due to the orientation of the nebula, and thus supports the proposed prolate ellipsoidal model.

The purpose of this study is to develop a fully-realized 3D model of BD+30 with the aim of unraveling the complex structures and kinematics therein, and connecting the morphology and shape of this object with other PNe that appear morphologically different. We incorporate here previously published radio, infrared (IR), optical, and X-ray data as the basis for our model. Using the 3D astrophysical modeling tool *SHAPE*, we are able to build a multiwavelength, morpho-kinematic 3D model that incorporates radiative transfer and velocity information.

This chapter is composed as follows. In §5.2 we present the multiwavelength data and observations used to interpret the morphology of BD+30 and construct our 3D model, followed by §5.3

where we discuss the 3D modeling software *SHAPE* and our approach to constructing the model. We explore the resulting model in §5.4, followed by a survey of BD+30 at different projected orientations to compare with other PNe in §5.5. In §5.6 we summarize the results of this model and its implications for PNe evolution and shaping.

5.2 Observations and Data

BD+30 has been the target of multiple observations across various wavelength regimes (Table 5.1), illuminating various features and regions of the nebula. Below we discuss previously published observations across the electromagnetic spectrum of BD+30 that guided us in the construction of our model.

5.2.1 Radio/Millimeter

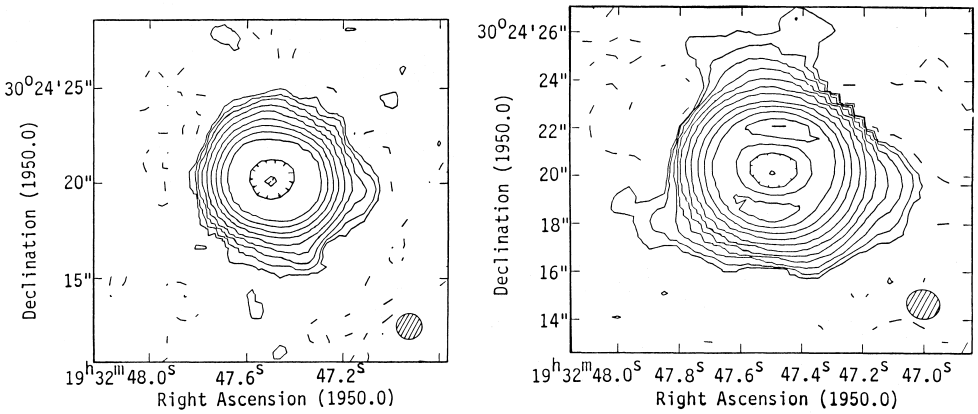

Figure 5.2: 20 and 6 cm images of BD+30; Fig. 2 from Basart & Daub (1987).

BD+30 was observed at 1.465 GHz (20 cm) and 4.885 GHz (6 cm) using the VLA in A and B array configurations respectively by Basart & Daub (1987) in May and August 1982. The 6 cm map revealed a limb-brightened shell, strongly confined to a double-peak structure oriented N-S, with a decrease in intensity towards the center, while the 20 cm map maintained the central decrease in brightness but lacked the prominent peaks (Fig. 5.2). Later VLA observations at 14.94 GHz (2 cm)

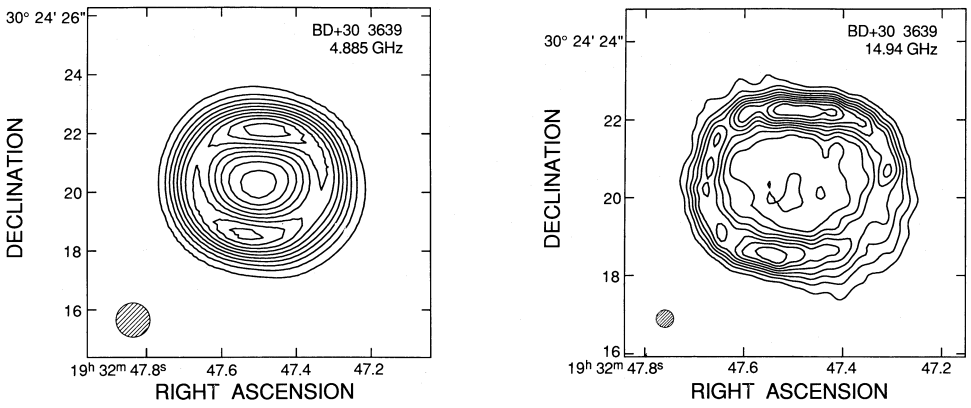

Figure 5.3: 6 and 2 cm images of BD+30; Fig. 1 from Masson (1989).

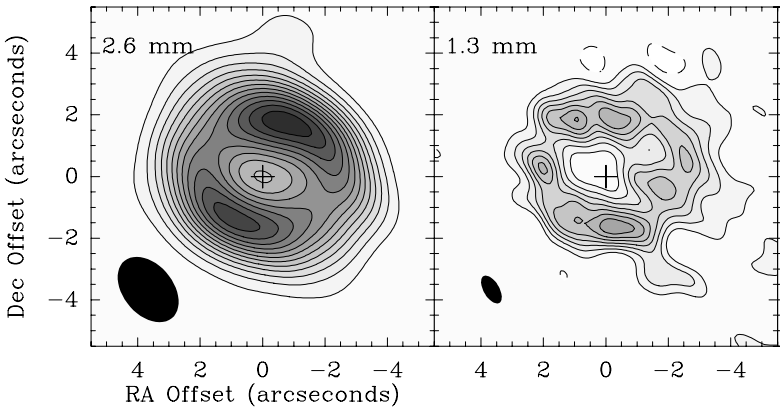

Figure 5.4: 2.6 and 1.3 mm images of BD+30; Fig. 1 from Bachiller et al. (2000).

Table 5.1: Observations of BD+30 Reported in the Literature

Wavelength Regime	Wavelength	Telescope	Instrument	Source	Year	Reference
Radio	230.538 GHz	IRAM 5-antenna interferometer	-	CO J=2-1	1998	Bachiller et al. (2000)
	115.271 GHz	”	-	CO J=1-0	1998	”
	2.6 mm	”	-	continuum	1998	”
	1.3 mm	”	-	continuum	1998	”
	20 cm	VLA	A Array	-	1987	Basart & Daub (1987)
	6 cm	”	B Array	-	1987	”
	6 cm	”	-	-	1986	Masson (1989)
	2 cm	”	-	-	1986	”
	6 cm	MERLIN	-	-	1995	Bryce et al. (1997)
	21 cm	WSRT	-	H I	1987	Taylor et al. (1990)
Infrared	10 μm	WIRO	-	dust	1979	Bentley et al. (1984)
	23 μm	”	-	”	”	”
	19.5 μm	”	-	”	”	”
	8.7 μm	”	-	”	1981	”
	11.4 μm	”	-	”	1981	”
	2.2 μm	SO[1] 2.3m	Hg:Cd:Te array	continuum	1989	Hora et al. (1993)
	10.0 μm	”	MIRAC	dust	1991	”
	11.2 μm	”	MIRAC	dust	1991	”
	12.4 μm	”	MIRAC	dust	1991	”
	12.8 μm	”	MIRAC	dust	1991	”
	13.2 μm	”	MIRAC	dust	1991	”
	2.213 μm	Hale Telescope	NICMOS3	H_2	1994	Shupe et al. (1998)
	3.6-4.2 μm	ISO	ISOCAM/SWS	continuum	1996	Persi et al. (1999)
	5.0-16.5 μm	”	LWS	continuum		”
	8.8 μm	*Subaru*	COMICS	continuum	2004	Matsumoto et al. (2008)
	9.7 μm	”	”	continuum	”	”
	10.5 μm	”	”	continuum	”	”
	11.7 μm	”	”	continuum	”	”
	12.4 μm	”	”	continuum	”	”
	8.6 μm	”	”	UIR	”	”
	11.2 μm	”	”	UIR	”	”
	12.8 μm	”	”	[Ne II]	”	”
	6.4 μm	*SOFIA*	*FORCAST*	dust	2014	Guzman-Ramirez et al. (2015)
	7.7 μm	”	”	dust	”	”
	11.1 μm	”	”	dust	”	”
	11.3 μm	”	”	dust	”	”
	33.6 μm	”	”	dust	”	”
Optical	4884 Å	WIRO	-	Hβ	1980	Bentley et al. (1984)
	487 nm	*HST*	WFPC2	Hβ	1997	Harrington et al. (1997)
	656 nm	”	”	Hα	”	”
	588 nm	”	”	He I	”	”
	5007 Å	”	”	[O III]	”	”
	3277 Å	”	”	[O II]	”	”
	6300 Å	”	”	[O I]	”	”
	6584 Å	”	”	[N II]	”	”
	9532 Å	”	”	[S III]	”	”
	6724 Å	”	”	[S II]	”	”
X-ray	0.1-2.4 keV	*ROSAT*	PSPC	thermal plasma	1990	Kreysing et al. (1992)
	0.3-8.0 keV	*ASCA*	-	thermal plasma	1994	Arnaud et al. (1996)
	0.3-8.0 keV	*Chandra*	ACIS-S	thermal plasma	2000	Kastner et al. (2000)
	0.3-8.0 keV	”	LETG/ACIS-S	thermal plasma	2006	Yu et al. (2009)

and 4.885 GHz by Masson (1989) in September 1986 also showed the double-peaked structure, but a more pronounced decrease in intensity towards the center (Fig. 5.3). The same trend was seen in observations of free-free (continuum) emission at 2.6 and 1.3 mm, carried out with the IRAM 5-antenna interferometer at Plateau de Bure in January and March 1998 (Fig. 5.4; Bachiller et al.,

2000).

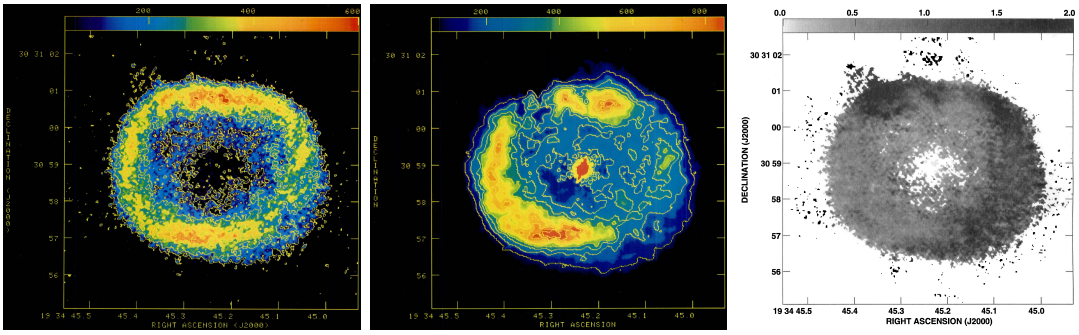

Figure 5.5: 6 cm map from combined MERLIN and VLA data (*left*), *HST* Hβ image (*center*), and a difference map of the radio map divided by the Hβ image (*right*) for BD+30; Figs. 1, 2, and 3 from Bryce et al. (1997). The elliptical beam size of the 6 cm radio map is 82×78 mas^2.

Based on models of ionization-bounded PNe from Masson (1990) we expect lower densities, and therefore weaker emission, along the poles of ellipsoidal nebulae, while the equator will be much denser, appearing brighter. The radio maps point to a morphology akin to a prolate ellipsoidal shell, with the polar regions being aligned with the major axis (E-W), and the equator with the minor (N-S). Additional 5 GHz observations collected with the Multi Element Radio Linked Interferometer Network (MERLIN) by Bryce et al. (1997) combined with Hβ *HST* observations served to expand upon this model. The similar spatial resolutions of *HST* Wide-Field Planetary Camera 2 (WFPC2) and the MERLIN observation provided a chance to see how the emission from ionized gas, as seen in radio (free-free) vs. optical (Hβ) emission, traces dust within the nebula, via the extinction of the Hβ photons relative to the radio continuum. The difference map generated by taking the ratio of the 5 GHz image to the Hβ image showed a brightness gradient from east to west, suggesting that there is more dust in the west, implying that the nebula is inclined with the eastern side closer to the observer (Fig. 5.5).

Taylor et al. (1990) made 21 cm of observations of BD+30 and four other nebulae at the Westerbork Synthesis Radio Telescope (WSRT) in 1987. The 21 cm spectra revealed that most nebulae had a blueshifted H I absorption feature, indicating that an atomic hydrogen outflow was present, while BD+30 was the only object to display an H I emission line. The emission was found

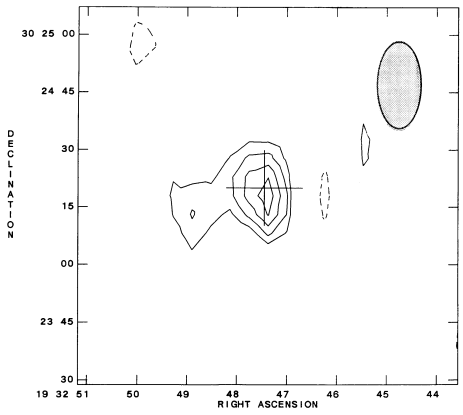

Figure 5.6: 21 cm contour plot of BD+30; Fig. 2 from Taylor et al. (1990). The neutral hydrogen emission around BD+30 is unresolved with the beam size of 0.3°, but its coincident with the nebula (marked with a cross).

to be surrounding the nebula up to 15″ away from the central star, as well as in an extension to the east (Fig. 5.6). The WSRT beam size of 11.5″ is insufficient to resolve features near the central star, making it difficult to compare any fine structure at this wavelength.

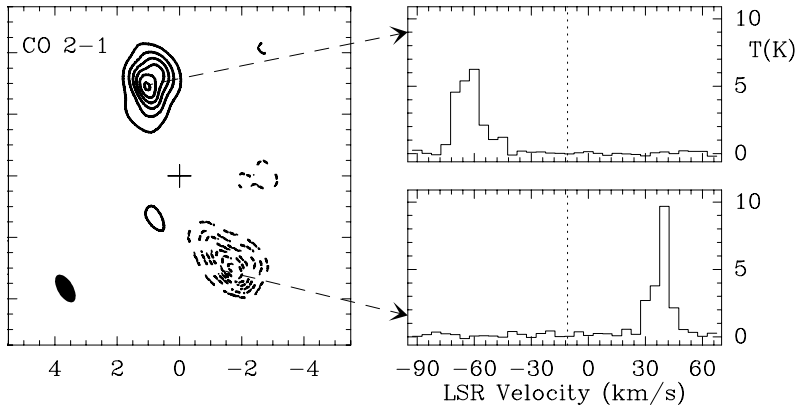

Figure 5.7: CO bullet image of BD+30 showing the velocity of both components; Fig. 1 from Bachiller et al. (2000).

Observations of the CO $J = 2 \rightarrow 1$ (1 mm) and $J = 1 \rightarrow 0$ (3 mm) lines in BD+30 carried out with the IRAM 30-meter telescope at Pico Veleta in June 1991 by Bachiller et al. (1991, 1992) revealed unusually high velocity molecular gas. Typical expansion velocities of red giants are on

the order of tens of km s^{-1}, while the CO line profiles range over an extent of 132 km s^{-1}. The separation of the red and blue-shifted peaks point to an expansion velocity of ∼50 km s−1 along the line of sight. Maps of the CO $J = 2 \rightarrow 1$ and $J = 1 \rightarrow 0$ lines taken with the IRAM 5-antenna interferometer at Plateau de Bure in 1998 exposed the emission as two high velocity ∼50 km s^{-1} "bullets" that appear spatially coincident with disruptions within the H_2 torus surrounding BD+30 (Fig. 5.7; Bachiller et al., 2000). In conjunction with the spectral line velocities, Bachiller et al. (1991, 1992, 2000) suggested that the origin of the bullets is closely tied to bipolar jets produced by the central star, however, no jets are directly detected within the nebula. This implies that the jets may have been present at a pre-nebula phase of the central star's evolution.

5.2.2 Infrared

There have been extensive IR studies of BD+30. Infrared observations from the 2.34 m telescope at Wyoming Infrared Observatory (WIRO) covering a range from 8.7 to 23 μm from September 1979 to November 1981 exposed a double peaked structure, perpendicular to the structure in the radio observed by Basart & Daub (1987) (Fig. 5.8; Bentley et al., 1984). When compared with the extent of the ionized region within the nebula, Bentley et al. (1984) found that there was no significant deviation between the morphologies of 8.7, 10.0, 11.4 μm emission and that of the Hβ emission. This suggests that the mid-IR emitting dust was well-mixed with the ionized gas, as seen by Bryce et al. (1997). Not only is the warm ($\sim$ 200 K) dust component evidently largely confined to the ionized region, but the 19.5 and 23.0 μm observations, which trace cooler ($T \sim 80$ K; Bentley et al., 1984) dust, also showed a lack of emission beyond the ionized region.

Hora et al. (1993) observed BD+30 in the mid-IR as well, using the Mid-IR Array Camera (MIRAC) on the Steward Observatory 2.3 m telescope. Images were taken at 2.2, 10.0, 11.2, 12.4, 12.8, and 13.2 μm and revealed a structure similar to that of the radio continuum (Basart & Daub, 1987; Masson, 1989), with the double-peaked emission aligned N-S rather than E-W (Fig. 5.9). Again, there is very little physical deviation from the radio and ionized emission regions. When comparing the unidentified infrared features at 11.2 and 12.4 μm, and the [Ne II] 12.8 μm feature

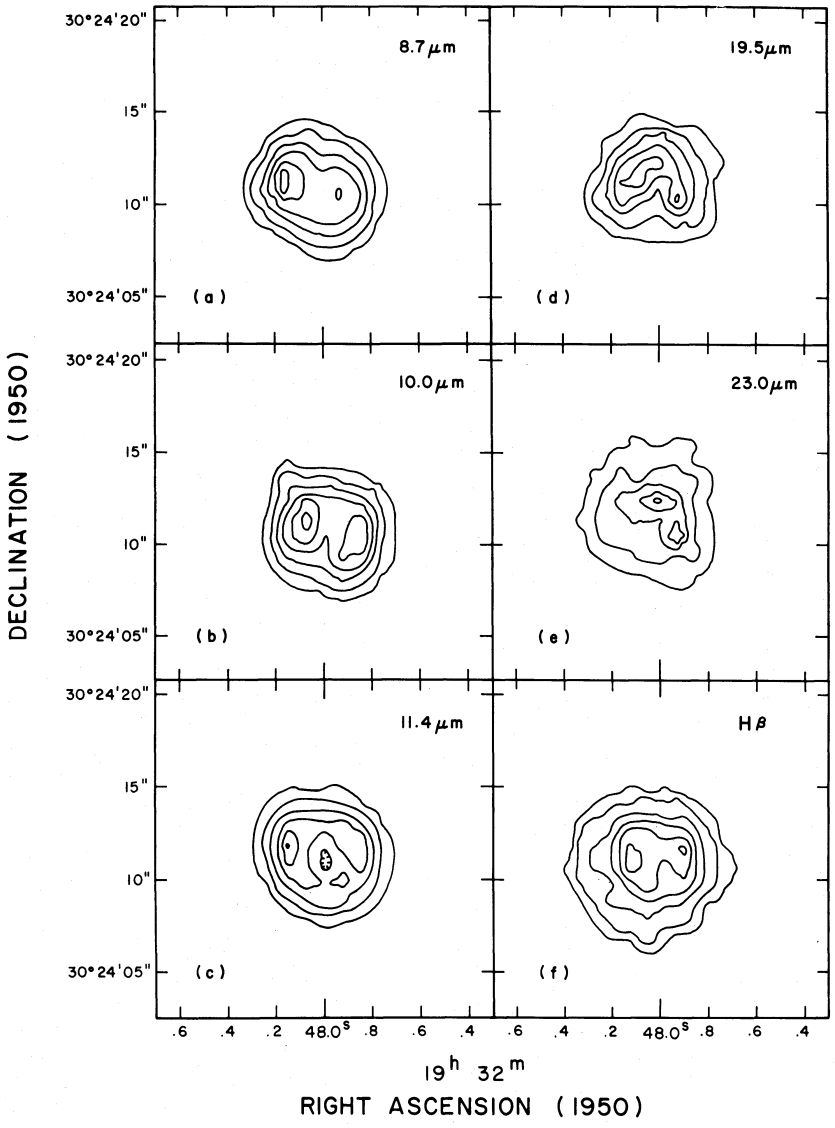

Figure 5.8: Mid-IR contour maps of BD+30; Fig. 1 from Bentley et al. (1984).

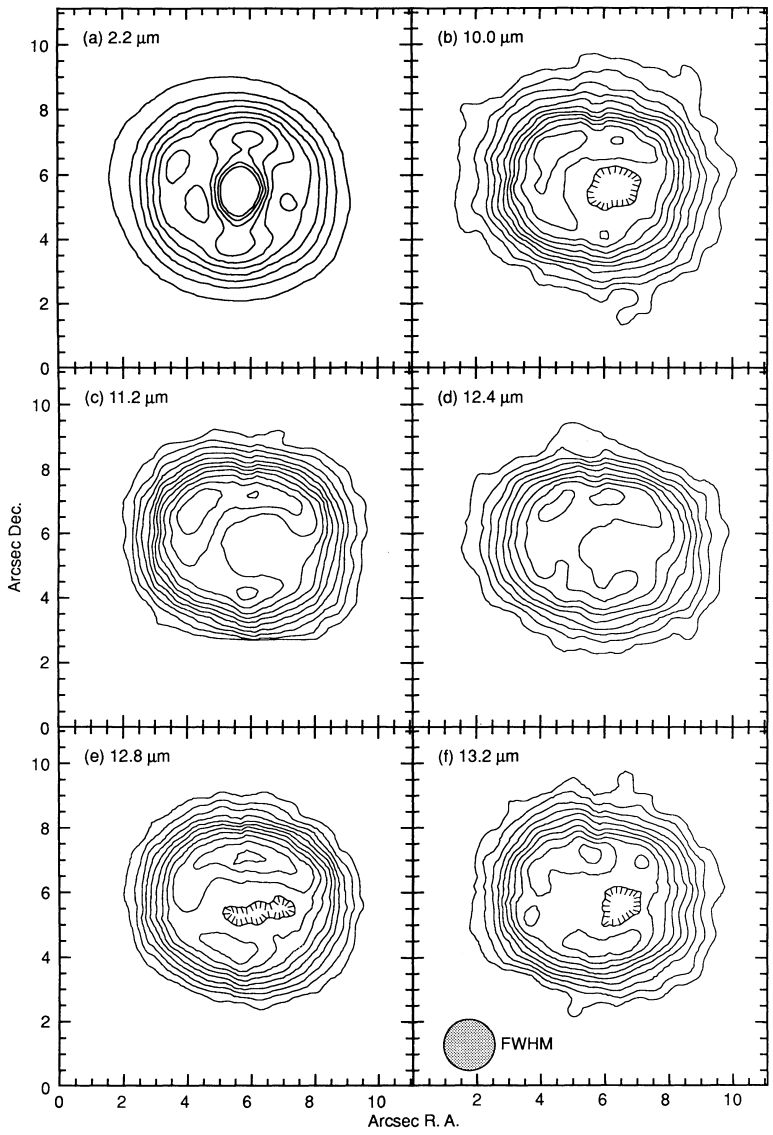

Figure 5.9: Mid-IR contour maps of BD+30; Fig. 1 from Hora et al. (1993).

to the 10.0 and 13.2 μm mid-IR continuum images, differences in the internal dust structure come to light (Fig. 5.10). Hora et al. (1993) found that the 11.2 μm emission extended farther than the continuum, especially in the northeast and southwest. Additionally, the 10.5 μm emission is confined to smaller region, mostly interior to the 11.2 μm emission.

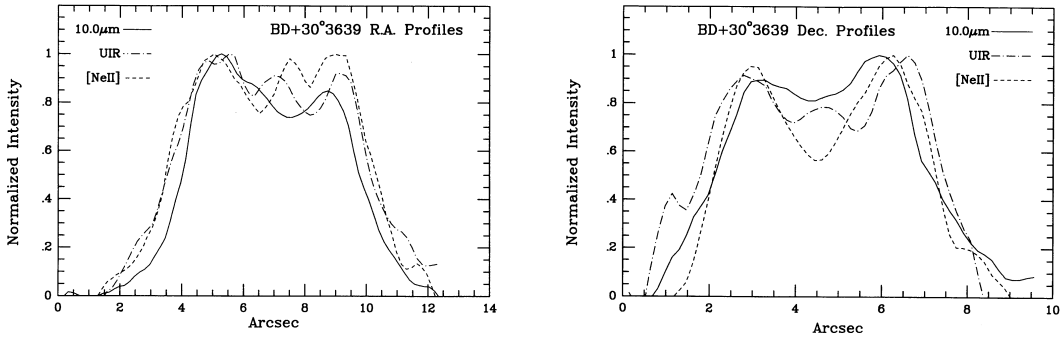

Figure 5.10: Radial profiles of mid-IR lines of BD+30; Fig. 4 from Hora et al. (1993). Left: East-West profile. Right: North-South profile.

Radial profiles across BD+30 in the E-W and S-N directions also show that the UIR 11.2 μm feature is extended beyond the continuum dust emission, though the [Ne II] 12.8 μm emission only shows this extension in the E-W direction (Fig. 5.10). The [Ne II] emission can be used as a tracer of the distribution of ionized gas, and it compliments the 6 cm radio emission peaks in the north and southern regions (Masson, 1989; Bryce et al., 1997). From a density map constructed from their mid-IR observations, Hora et al. (1993) concluded that the morphology of BD+30 is similar to that proposed by Masson (1989, 1990), with the equatorial region aligned N-S, and the less dense and warmer polar regions aligned E-W.

Spectroscopic observations of BD+30 across the mid-IR using the Infrared Space Observatory (ISO) took aim at the dust content of the nebula. Based on a model constructed by Siebenmorgen et al. (1994) it is believed that dust features of BD+30 are the result of polycyclic aromatic hydrocarbons (PAHs), carbonaceous dust, and silicate dust that are all spatially coincident. This is supported by spectrophotometric images taken using ISOCAM by Persi et al. (1999), who find that there is no significant spatial deviation from 6.2-12.8 μm. Additionally, scans from 2.4-45

μm using the Short Wavelength Spectrometer (SWS) on ISO revealed a bifurcated structure of the carbonaceous and silicate dust components. Waters et al. (1998) used a two-component dust model to replicate the dust distribution and found instead that the inner regions of the nebula that coincide with the PAH emission contain amorphous carbon grains. They report that the extended outer shell is composed of a mixture of amorphous and crystalline silicates, but the size of the region in their model is not well known.

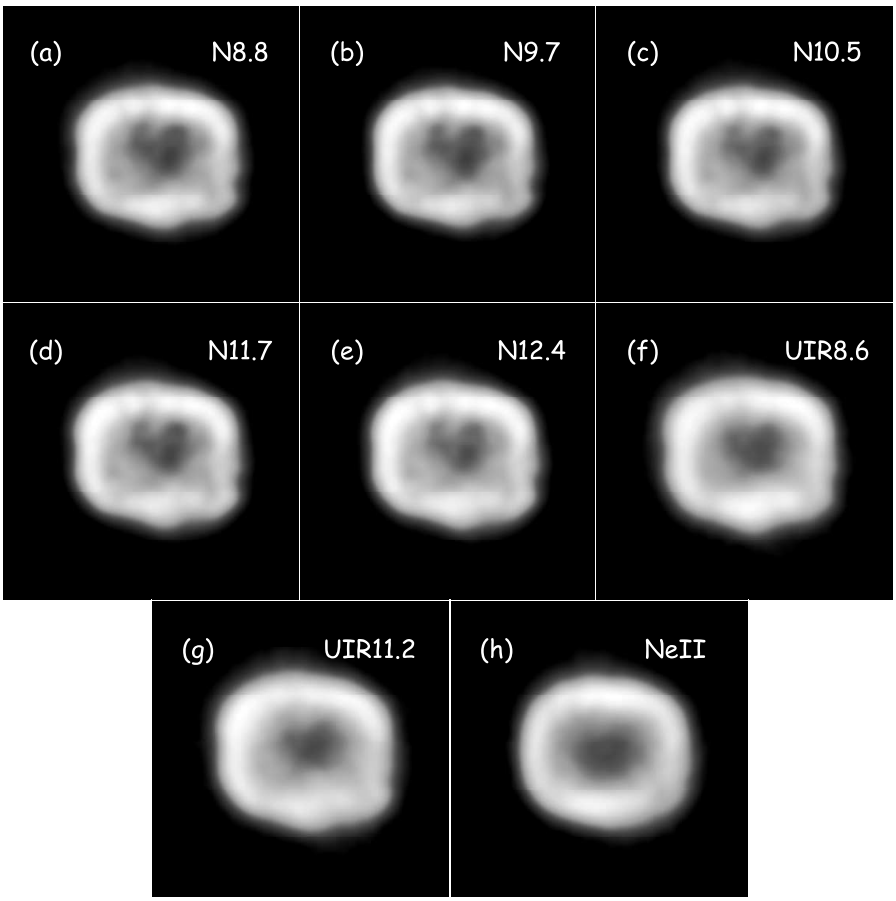

Figure 5.11: Mid-IR images of BD+30; Fig. 2 from Matsumoto et al. (2008). (a)-(e) use different filters to observe different parts of the mid-IR continuum, while (f), (g), and (h) target PAH and [Ne II] emission.

Subaru COMICS observations of BD+30 carried out by Matsumoto et al. (2008) using 8.8, 9.7, 10.5, 11.7, 12.4 μm medium-band filters and 8.6, 11.2, and 12.8 μm narrowband filters revealed

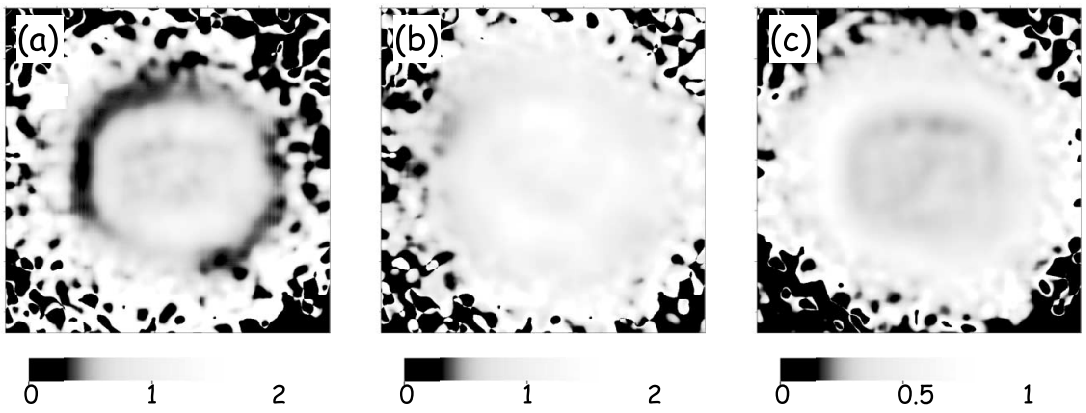

Figure 5.12: Band ratio images for BD+30; Fig. 4 from Matsumoto et al. (2008). The ratios are as follows (a) 8.6/11.2, (b) [Ne II]/11.2, and (c) 11.2/10.5

a boxier structure than previously observed in the mid-IR (Fig. 5.11). This is due to the higher resolution imaging capability of COMICS, which has a pixel scale of 0.13″ and point spread function of 0.35″ (based on FWHM at 11.6 μm). With these data, they produced a ratio image of 11.2 μm/10.5 μm that shows the same extended UIR feature as seen by Hora et al. (1993). They find that the 11.2 μm and the [Ne II] features are nearly coincident, save for a small 11.2 μm bump in the northeast of the nebula (Fig. 5.12). From the spectra they observed an absorption feature around 10 μm, which is attributed to silicate dust outside the ionized region, and therefore beyond the carbon rich shell, supporting the dual dust model for BD+30 proposed by Waters et al. (1998).

With the inclusion of 33.6 μm observations using the Faint Object InfraRed Camera (FORCAST) attached to the *Stratospheric Observatory for Infrared Astronomy (SOFIA) Telescope*, Guzman-Ramirez et al. (2015) were able to constrain the size of the silicate dust region to a radius of $7.5'' \pm 0.75''$, about 1.5 times the size of the carbon rich region (Fig. 5.13). It is in this region where the mid-IR emission around 10 μm is absorbed, as shown in the ISO spectrum of BD+30 (Persi et al., 1999; Guzman-Ramirez et al., 2015). Using an assumed expansion velocity of 10 km s^{-1}, Guzman-Ramirez et al. (2015) estimated the dynamical age for the silicate dust shell to be 4300 ± 740 yr and the age of the amorphous carbon shell to be 2800 ± 580 yr. These ages point to the transition window of the central star from [WO] to [WC] to be about 1500 yr. The analysis

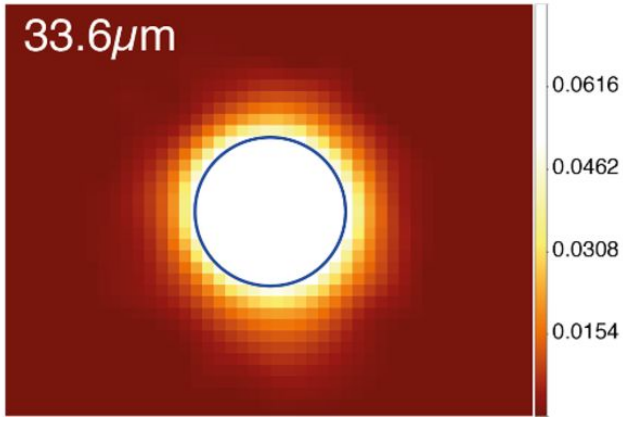

Figure 5.13: 33.6 μm image of BD+30; Fig. 1 from Guzman-Ramirez et al. (2015).

by Guzman-Ramirez et al. (2015) would also suggest that while the age of the nebula is estimated to be around 10^3 yr, the dusty components have existed more than twice as long.

In the near-IR regime, observations were made using the near-IR spectrograph on the 5 m Hale Telescope in May 1994, with the goal of investigating the kinematics of the H_2 emission surrounding the nebula (Shupe et al., 1998). The Shupe et al. (1998) H_2 $1-0$ $S(1)$ (2.1213 μm) maps revealed that the H_2 emission, first detected by Beckwith et al. (1978), falls within a ring or torus around the central ionized shell of BD+30, though the structure appears to be disrupted (Fig. 5.14). The central velocity gleaned from spectra across the torus ranges from -30 to 60 km s^{-1}, with regions in the southwestern tail showing velocities upward of 100 km s^{-1} (Fig. 5.15). The major part of the eastern side of the torus is redshifted compared to the ionized shell, while the majority of the western side is blueshifted (Shupe et al., 1998). Additional observations of the H_2 torus by Bachiller et al. (2000) show similar structure, and an interesting relation to the molecular CO bullets. A disruption along the northeastern part of the torus and a second in the south-southwest region, close to the southwestern tail, appear spatially coincident with the CO bullets, linking the torus structure with the origin of the CO (Fig. 5.16).

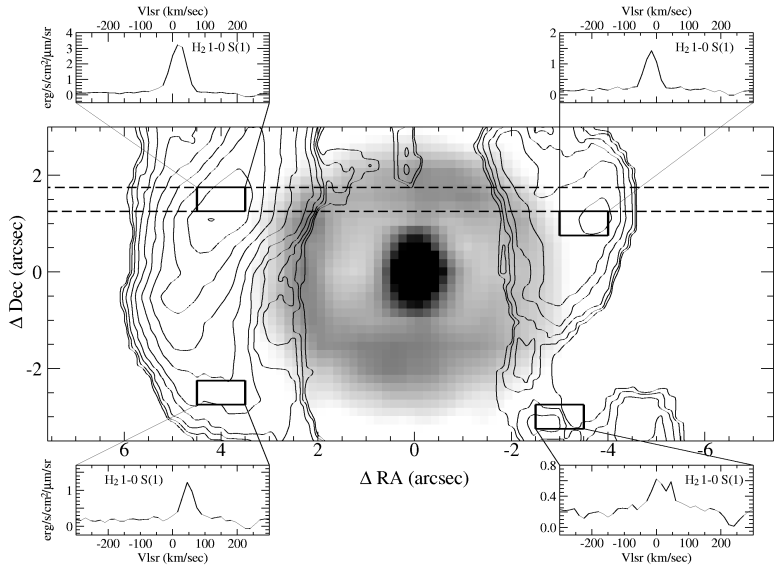

Figure 5.14: H_2 torus contours over image of BD+30; Fig. 1 from Shupe et al. (1998).

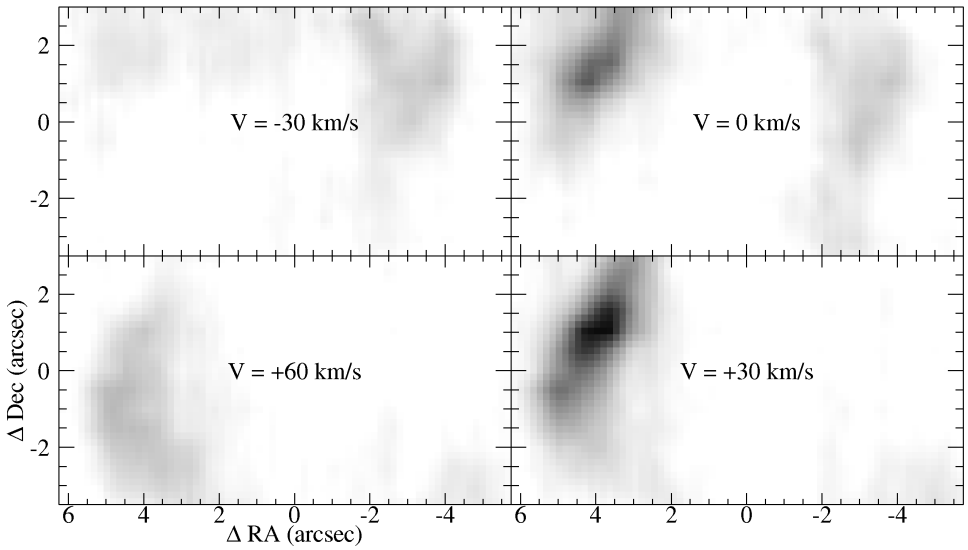

Figure 5.15: H_2 torus channel maps; Fig. 2 from Shupe et al. (1998). Each panel shows velocity slices of the H_2 emission, with the center local standard of rest (LSR) velocity indicated in the center of each frame.

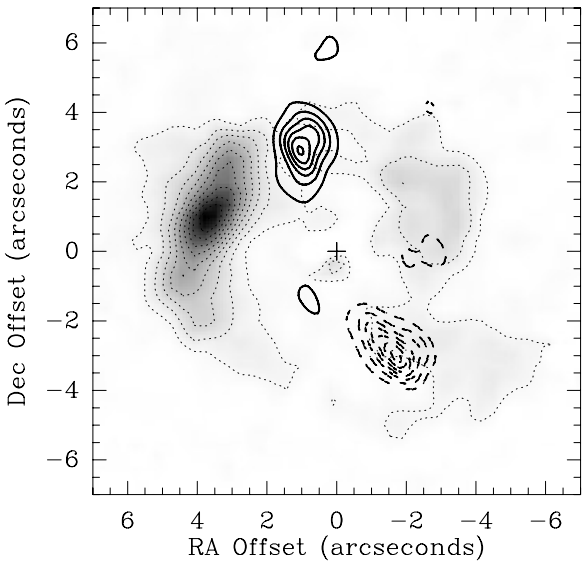

Figure 5.16: H_2 torus and CO bullet contours of BD+30; Fig. 3 from Bachiller et al. (2000).

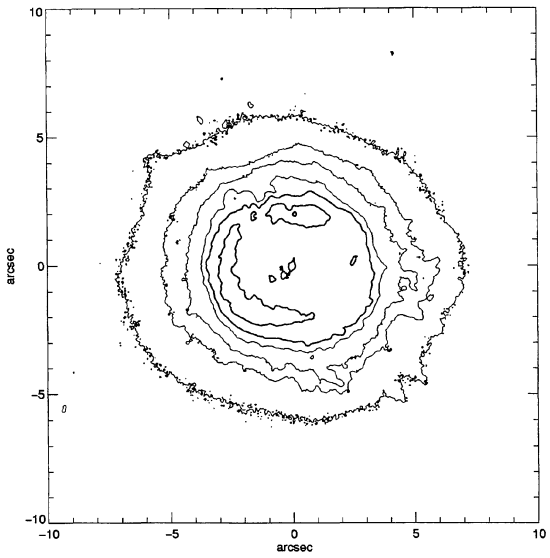

Figure 5.17: Hα image of BD+30; Fig. 2 from Harrington et al. (1997).

5.2.3 Optical

HST observations of BD+30 in Hβ, Hα, and optical lines of He I, [O III], [O II], [O I], [N II], [S III], and [S II] using Wide-Field Planetary Camera 2 (WFPC2) in 1994 by Harrington et al. (1997) showed an asymmetrical structure. Additionally, emission found in a halo around the nebula in the Hα narrow-band image (Fig. 5.17) was found to be light scattered by dust in the neutral halo. The ionized emission is coincident with 15 GHz VLA radio observations, though it does not share the same brightness features. The optical emission lines suffer from absorption along the western side of the nebula, and in the northeast, which is attributed to a dust blob. Harrington et al. (1997) suspected that this blob was separate from the nebula and due to an intervening component given its absence in a map of selective extinction, while the western extinction is regarded as the result of internal dust. The location of the northern extinction region appears close to the location of the northern CO bullet. The dust extinction is similar to that of the interstellar medium (ISM), implying a similar composition (Harrington et al., 1997).

The emission line observations display a stratification of the ionization. The higher ionization emission regions like [O III] and He I are found closer to the inner parts of the shell, while the lower ionization states are found to have stronger emission towards the edge of the shell (Harrington et al., 1997). This is expected given that the regions closest to the star will absorb more of its UV radiation, leaving little to ionize the outer portions of the nebula (Sabbadin et al., 2006).

Spatially resolved spectral observations of [N II] (6584 and 5754 Å) and [O III] (4959 and 5007 Å) taken by the William Herschel Telescope allowed Bryce & Mellema (1999) to cull velocity information from the nebula. Position-velocity (PV) diagrams of the [O III] region showed what appear to be high velocity outflows (HVOs), red-ward and blue-ward, close to the line-of-sight. These outflows correspond to gaps in the [N II] line profiles in the northeast and southwest (Fig. 5.18). The radial expansion velocity determined from the [N II] and [O III] spectral lines is 28 ± 1 and 35.5 ± 1 km s^{-1} respectively.

The small offset of the HVOs from the line of sight implies that the prolate nebula has a low inclination ($\sim 20°$). This configuration is also supported by additional *HST* observations using

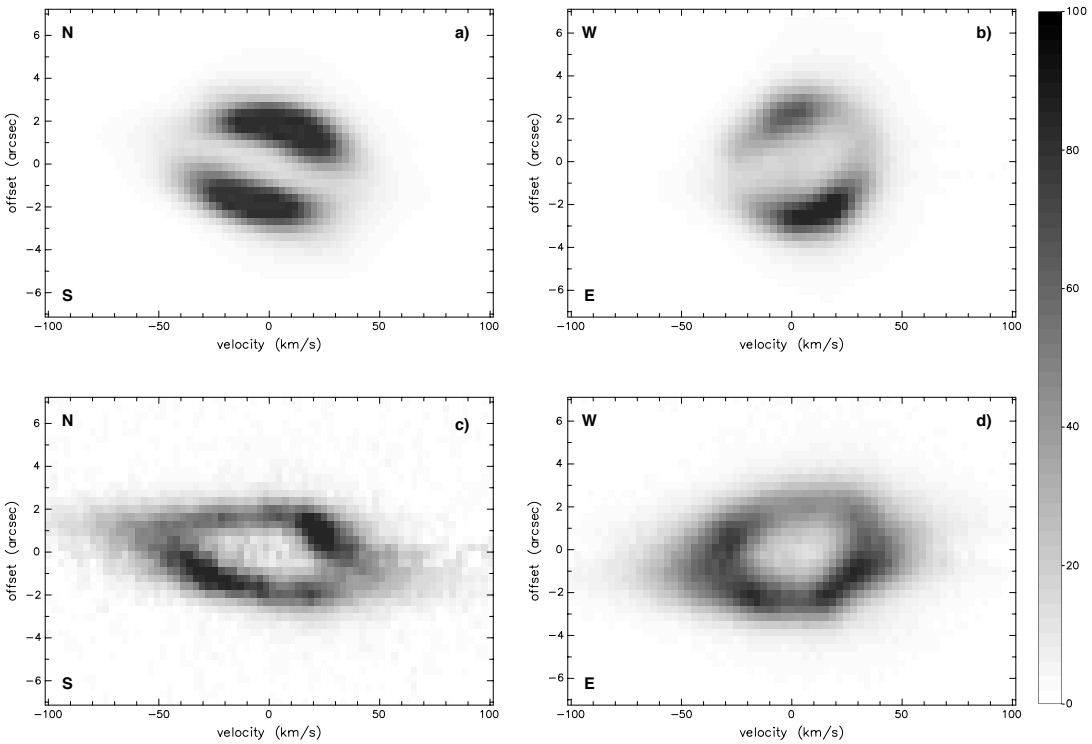

Figure 5.18: [N II] and [O III] position-velocity diagrams of BD+30; Fig. 2 from Bryce & Mellema (1999).

Hα and [N II] narrow-band filters by Li et al. (2002). In accordance with their kinematic model, they find that the expansion of the nebula is linearly proportional to the distance from the center, suggesting a homologous or Hubble expansion law. They propose that an ellipsoidal shell with an axial ratio of 1.5 to 1, inclined at an angle of 9.7° fits the observed line profiles. Indeed, when they compare their results with Bryce & Mellema (1999) they appear to be in agreement. Additionally, from their analysis of the expansion of BD+30, they surmise that material in the northeast moves towards the low density poles, particularly the regions lacking [N II] emission.

5.2.4 X-ray

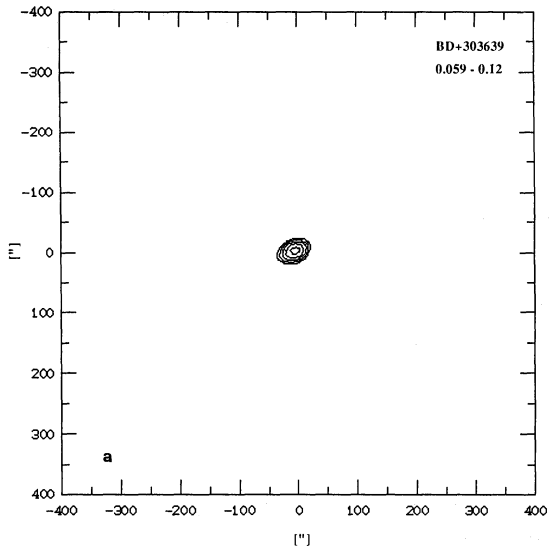

Figure 5.19: *ROSAT* X-ray image of BD+30 at 0.059-0.12 keV; Fig. 1 from Kreysing et al. (1992).

BD+30 was first detected as an X-ray source by Kreysing et al. (1992) using the Position Sensitive Proportional Counter (PSPC; Pfeffermann et al., 1987) on the *ROSAT* satellite in an energy range of 0.1-2.4 keV. Initially, due to the compact nature of the emission it was believed to be the result of a point source (Fig. 5.19). However, the temperature derived from fitting the X-ray spectra with a thermal bremsstrahlung model was found to be much too high (2.5×10^6 K) to be produced by the photosphere of the central star, suggesting an origin in wind shocks, although this

temperature is also an order of magnitude lower than expected given the wind speed of the central star (700 km s^{-1}; Leuenhagen et al., 1996; Marcolino et al., 2007).

The *ROSAT* observations were followed by observations using the *Advanced Satellite for Cosmology and Astrophysics* (*ASCA*; Tanaka et al., 1994) in October of 1994. Arnaud et al. (1996) fit the *ASCA* spectra from 0.4-1.7 keV with a MEKAL optically thin thermal plasma model, yielding a plasma temperature of 3×10^6 K indicative of a high abundance of carbon. Arnaud et al. (1996) surmise that the emitting plasma was most likely contained within the optical shell seen in *HST* observations, as predicted by the wind-blown bubble model (Kwok et al., 1978).

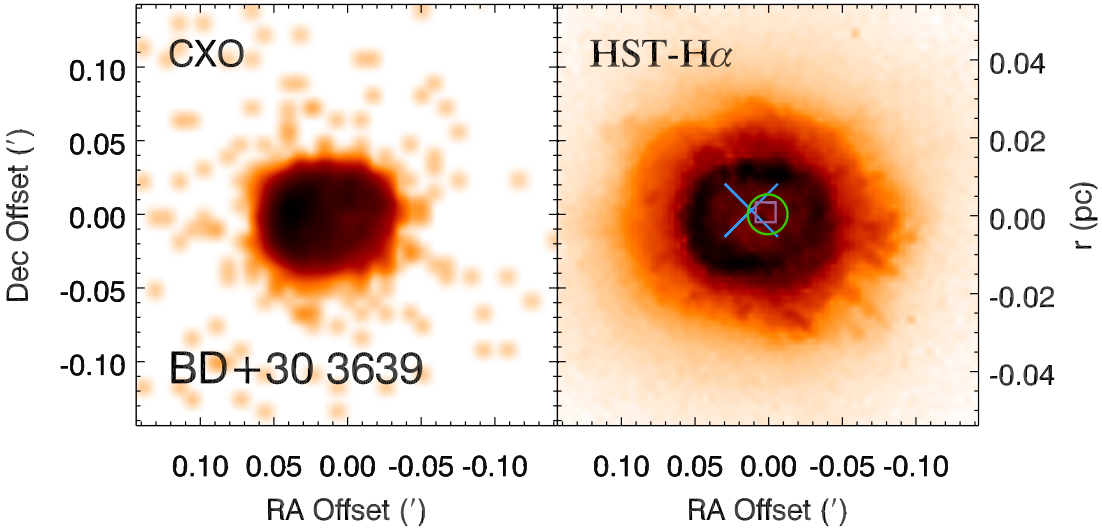

Figure 5.20: *Chandra* X-ray image of BD+30 at 0.3 to 2.0 keV; Fig. 2 from Kastner et al. (2012).

Higher resolution observations obtained using the *Chandra X-ray Observatory (CXO)* back-illuminated CCD in the Advanced CCD Imaging Spectrometer (ACIS) array revealed that the X-ray emission was elliptical and asymmetric (Kastner et al., 2000, 2002, 2012). Due to its superior spatial resolution, *CXO* was able to resolve the diffuse X-ray structure of BD+30 and uncover the asymmetric nature of the emission, which peaks east of the central star with weaker emission in the southwest (Fig. 5.20). This morphology corresponds with the inner cavity seen in IR and optical images, suggesting that the X-ray emission is confined to a hot bubble bounded by the ionized

and dusty regions. It is these regions that are expected to be responsible for the absorption of the X-rays rather than the ISM.

Additional *Chandra* observations using the Low Energy Transmission Gratings (LETG) spectrometer in conjunction with ACIS were taken in 2006 to investigate the X-ray spectrum in greater detail. The LETG/ACIS-S spectra revealed that BD+30 displays highly ionized emission lines of oxygen and neon (Yu et al., 2009). Using a two-component thermal plasma model with photoelectric absorption, Yu et al. (2009) obtained improved constraints on the elemental abundances in BD+30's hot bubble, and showed that carbon and neon are overabundant, while nitrogen is underabundant relative to solar, and iron is depleted. The fitted temperatures of the two-component model were 2.9 and 1.7×10^6 K, which is consistent with previous estimations of the plasma temperature, and suggests a temperature gradient within BD+30, though these temperatures are still lower than the expected 10^7 K given the CSPN wind speed.

Cooling mechanisms have been suggested for BD+30 to account for the temperature discrepancy (Soker & Kastner, 2002). Heat conduction across the boundary between the X-ray plasma interface and the ionized gas region, known as the contact discontinuity, could lead to evaporation of AGB material into the hot bubble, cooling it down to observed temperatures (Weaver et al., 1977; Steffen et al., 2008; Toalá & Arthur, 2014) Alternatively jets could be responsible for heating the gas interior to the ionized shell. The CO bullets may be associated with collimated jets launched at an earlier phase in BD+30's evolution (Bachiller et al., 2000; Akashi et al., 2008).

5.3 Morpho-kinematic Reconstruction

To develop a 3D model of BD+30, we used the 3D morpho-kinematic tool *SHAPE* (Steffen & López, 2006; Steffen et al., 2011), a software package developed for astrophysical modeling (see Chapter 2). We strive to construct a detailed morpho-kinematic model of BD+30 that incorporates multiwavelength information to date from the radio to the X-ray. Most previous models of BD+30 suggested an ellipsoidal shape with a homologous expansion law, where the velocity field decreases

with increasing distance from the central star (Li et al., 2002; Akras & Steffen, 2012). Here we begin with a prolate ellipsoid to represent the basic shape for most of the wavelength regimes employed for the model. The optical, IR, X-ray, and radio continuum morphologies all suggest such a shape, while the near-IR H_2 torus and the CO bullets require alternative shapes to fit the observed data. For the following modeling we assume a distance of 1.3 kpc to BD+30 (Frew, 2008). The published data that we used for reference can be found in Table 5.2.

Table 5.2: Observations of BD+30 used for *SHAPE* Modeling

Wavelength Regime	Wavelength	Telescope	Instrument	Source	Reference
Radio	230.538 GHz	IRAM 5-antenna interferometer	-	CO J=2-1	Bachiller et al. (2000)
	115.271 GHz	”	-	CO J=1-0	”
	6 cm	MERLIN	-	-	Bryce et al. (1997)
	21 cm	WSRT	-	H I	Taylor et al. (1990)
Infrared	2.213 μm	Hale Telescope	NICMOS3	H_2	Shupe et al. (1998)
	10.5 μm	*Subaru*	COMICS	continuum	Matsumoto et al. (2008)
	8.6 μm	”	”	UIR	”
	11.2 μm	”	”	UIR	”
	12.8 μm	”	”	[Ne II]	”
	33.6 μm	*SOFIA*	FORCAST	silicate dust	Guzman-Ramirez et al. (2015)
Optical	487 nm	*HST*	WFPC2	Hβ	Harrington et al. (1997)
	502 nm	”	”	[O III]	”
	656 nm	”	”	Hα	”
	658 nm	”	”	[N II]	”
	673 nm	”	”	[S II]	”
	953 nm	”	”	[S III]	”
X-ray	0.3-8.0 keV	*Chandra*	ACIS-S	thermal plasma	Kastner et al. (2000)

5.3.1 Optical

From the *HST* images it appears that the [N II] and Hα emission is coincident. Upon normalizing each image to its maximum intensity and dividing the [N II] image by the Hα, we find that the residual features are small and uniform (Fig. 5.21). We performed the same analysis for the other *HST* narrowband images (Hβ, [S II], [O III], and [S III]) and found that for all but the [O III], the size of the emission region did not vary greatly from that of the Hα emission (Fig. 5.22).

The [O III] shell is smaller, $\sim 5'' \times 4.3''$, and appears boxier than the other emission line regions. Using the kinematic data collected by Bryce & Mellema (1999) as a guide, we assumed a velocity

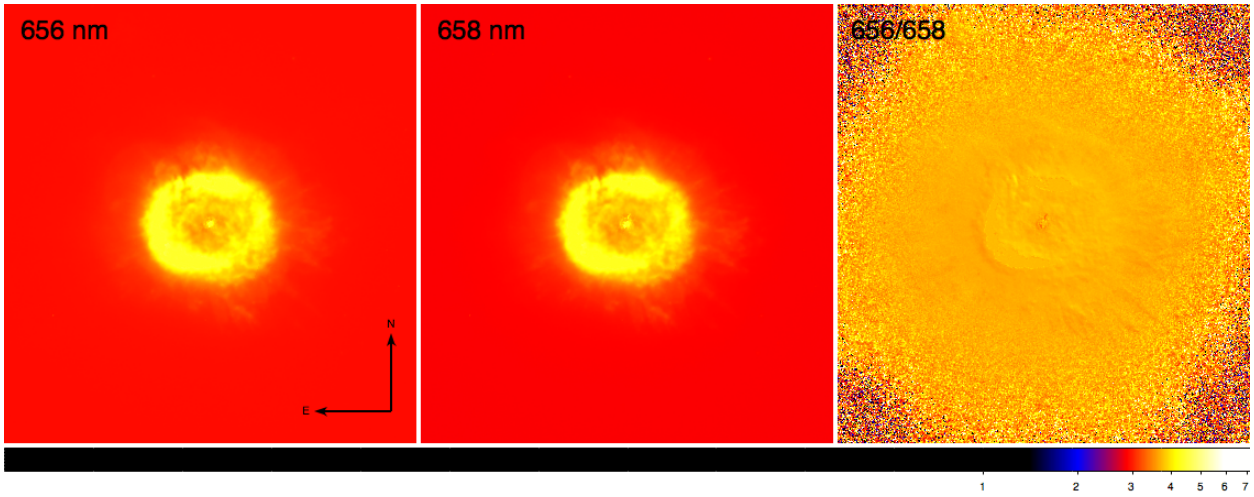

Figure 5.21: *HST* images of Hα (*left*), [N II] (*center*), and a ratio image of Hα/[N II] (*right*). The [N II] and the Hα images are normalized to the maximum intensity and then used to make the Hα/[N II] image, which is log normalized.

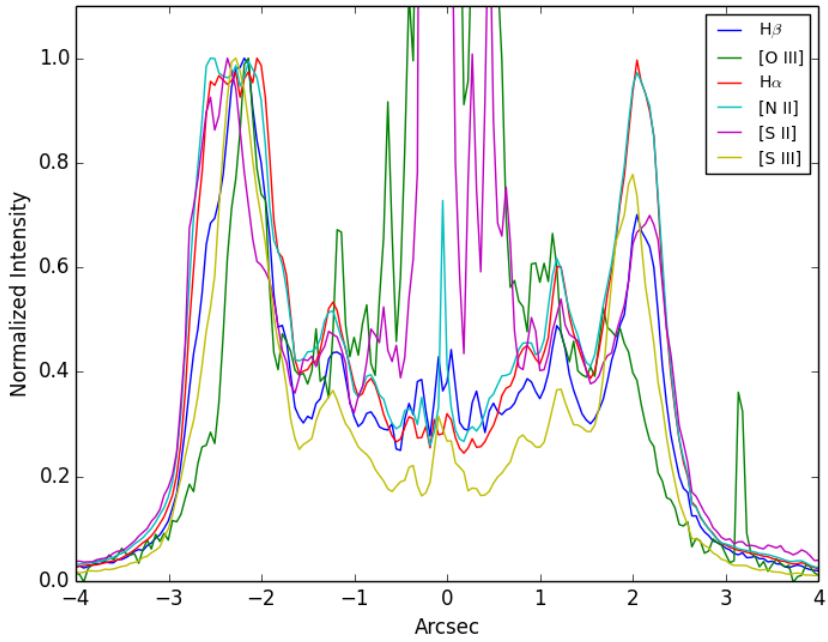

Figure 5.22: East-West radial profiles of optical emission features: Hα, Hβ, [O III], [N II], [S II], and [S III]. The central peaks are emission from the central star, while the secondary peaks to the east and west represent the optical ring of the nebula.

law

$$v = v_0 \frac{r}{r_{\rm neb}}\,, \tag{5.1}$$

where $r_{\rm neb} \sim 0.01$ pc, and v_0 for [O III] is 35.5 km s^{-1}. From the PV diagrams of [O III] from Bryce & Mellema (1999) we know that the nebula exhibits high velocity outflows nearly along the line-of-sight, which suggests an almost pole-on orientation. We expand our prolate ellipsoid along the z-axis by adding protrusions, which extend the velocity limit out to ~ 80 km s^{-1}.

Starting from the same shape as the [O III] emission region, we scale the shell to capture the larger $\sim 6'' \times 5''$ size of the [N II] emission region. The [N II] velocity field is expanding slower than the [O III], so we choose $v_0 = 28$ km s^{-1} (Bryce & Mellema, 1999). However, the outflows visible in the [O III] PV diagrams are not present in the [N II], or any of the other emission lines, so we concentrate the emission to a central shell, wrapped in an envelope that extends out to the [O III] outflows. Additionally, there is a "gap" in the PV diagram, indicating that there is a lack of material near the polar regions of the nebula. This suggests that the temperature of the poles is higher than the equator, akin to what is observed in NGC 7027 (Basart & Daub, 1987; Masson, 1989). To account for this, given that *SHAPE* does not incorporate heating, we lower the density of the emission along the poles using a n_r distribution that is constant out to the semi-minor axis and then decreases as r^{-2} combined with $n_\phi = \sin^2(\phi/2 + \pi/4)$ distribution while $n_\theta = 1$. Surrounding the [N II] and emission line regions is also a low density halo, which we model as a larger, prolate ellipsoid extending out to $\sim 14.5''$ from the central star. Additional protrusions were added to better fit the *HST* observations. All of the optical regions are set to a temperature of 8800 K (Bachiller et al., 2000).

For the emission properties of the emission line regions, we constructed Gaussian emission lines in *SHAPE* using the central wavelengths of the corresponding *HST* narrow-band filters (Table 5.2) and assuming a width of 0.1 Å. We apply a model for absorbing X-rays that is adapted from the

`xspec` `wabs` model,

$$M(E) = e^{-n_{\rm H}\sigma(E)}\,, \tag{5.2}$$

where $\sigma(E)$ is the photoelectric cross-section (Fig. 4.7; Morrison & McCammon, 1983). For the absorption we assume ISM abundances for the nebula, which has been shown to be similar to nebular abundances (though BD+30 is iron deficient; Yu et al., 2009).

5.3.2 Radio/Millimeter

To model the radio continuum, we chose the 6 cm MERLIN and VLA observations as a guide given the high resolution images (Bryce et al., 1997). The 6 cm emission closely resembles that of the Hβ region, therefore we use this shape as a base and adjust the size and shape accordingly to match the observations. Compared to the Hβ region, the 6 cm emission appears boxier, however the emission appears confined to a shell of similar thickness. We apply a homologous velocity expansion law here as well, with $v_0 = 21.5$ km s^{-1} based on the upper and lower limits of the expansion proposed by Basart & Daub (1987). The density model of the [N II] region is enhanced by an order of magnitude along the equatorial region ($n_\phi = 10\sin^2(\phi/2 + \pi/4)$) to model the high extinction found in the southwestern part of the nebula (Harrington et al., 1997; Kastner et al., 2002). Lastly, assuming that the dust and gas is well mixed, we keep the temperature distribution the same. The emission is modeled as a broad Gaussian with a central peak at 6 cm.

The only emission from CO was found in two discrete bullets at 1.3 and 2.6 mm, one in the northeast and the other in the southwest (Bachiller et al., 1991, 2000). We initially displace spheres to the northeast and southwest locations, respectively, of the bullets and begin applying various modifiers to adjust the shape to match the observations. From Bachiller et al. (2000) we set the expansion velocity of the bullets to -60 km s^{-1} for the northeastern bullet and 40 km s^{-1} for the southwestern bullet assuming homologous expansion. Each bullet was appropriately moved along the z-axis to match the channel maps such that the inclination of the bullets with respect to the

line-of-sight is approximately 45° (Bachiller et al., 2000). Given the small size of the bullets we leave the density constant and also give them a temperature of 40 K.

The atomic hydrogen 21 cm emission is unresolved and appears very extended and asymmetric (Taylor et al., 1990). To model this emission, we generate a large, oblate spheroid that measures $\sim 20''$ N-S and $\sim 17''$ E-W for the main component. Next we create a second spheroid to the east, $\sim 14'' \times 14''$ that is shorn and to which protrusions are added to match the contours of the 21 cm observation (Fig. 5.6). There is little detail for this region given the lack of observations, and the large beam size (0.3°) used for the H I observation. The temperature of the region is set to 1690 K, and the density is left as a flat distribution (Taylor et al., 1990).

The neutral regions of the nebula are expected to have some impact on absorption of light emitted from the optical regions, so we assume an initial gas-to-dust ratio of 300 (Siebenmorgen et al., 1994). The 6 cm (ionized) emission region is given an amorphous carbon absorption model while the (neutral, 21 cm) atomic hydrogen region is given a silicate dust absorption model with low density, which is expected given the well-known dual dust nature of BD+30 (Waters et al., 1998).

5.3.3 Infrared

While the mid-IR ISOCAM images show a relatively elliptical morphology for BD+30 (Persi et al., 1999), the *N*-band COMICS images reveal a more boxy nebula than seen in the optical emission lines, which is similar to the radio emission (Fig. 5.11). To generate a shape like this from a prolate ellipsoid requires squeezing the nebula in a manner similar to that used to model the 6 cm emission. Across the mid-IR, from the *N*-band to [Ne II], the shape of the nebula does not change greatly, though the size does vary. We model three *N*-band regions, 8.6, 11.2, and 10.5 μm. The 8.6 and 11.2 μm is expected to arise from PAHs while the 10.5 μm is emission from the warm dust continuum. From Matsumoto et al. (2008) it was shown that the 12.8 μm [Ne II] emission is coincident with the 11.2 μm, so we choose to model both forms of emission in one region. The smallest region is 10.5 μm, followed by 8.6 μm, and then 11.2 μm. The emission from all three

regions is modeled with Gaussian emission lines with central wavelengths at the four corresponding emission lines (8.6, 10.5, 11.2, and 12.8 μm). Given the expansion rate of the nebula, we apply an expansion velocity for each region of 22 km s^{-1}, with a nebular temperature of 200 K, and flat n_r and n_θ distributions combined with a $n_\phi = \sin^2(\phi/2 + \pi/4)$ distribution.

Surrounding BD+30 is a torus of molecular hydrogen that appears to be disrupted and incomplete. It is worth noting that given the observations we are working from, the shape of the torus may be affected by the low signal-to-noise ratio characteristic of the data. To model this region, we began by fitting a simple torus to the observation by Bachiller et al. (2000) to determine the rough orientation of the gas. From there we broke up the torus into three ellipsoids where the emission appeared strongest, east (H2E), northwest (H2NW), and southwest (H2SW) (Fig. 5.16). Once the complex 2-dimensional structure was extrapolated from the Bachiller et al. (2000) observation, we used PV diagrams and channel maps from Shupe et al. (1998) to extrapolate along the z-axis (Fig. 5.15). There is a large velocity gradient across the torus, with regions reaching upwards of -50 km s^{-1} to 100 km s^{-1}. The H2E region is the largest complete region of the torus, covering the entire velocity range, while both H2NW and H2SW are of comparable size and velocity dispersion. For emission, we assume a Gaussian emission line with a central wavelength of 2.213 μm to represent the H_2 1-0 $S(1)$ emission line. The density is expected to follow that of the optical emission regions ($n_r \sim r^{-2}$, $n_\phi = \sin^2(\phi/2 + \pi/4)$, $n_\theta = 1$) and is set to 1000 K (Shupe et al., 1998).

Both the mid-IR and H_2 torus sit within a large, silicate dust envelope that emits at 33.6 μm. This region was modeled with a simple prolate ellipsoid since the *SOFIA* observations were featureless (Guzman-Ramirez et al., 2015). A temperature of 100 K was assumed, and the density law is set to r^{-1}, while the expansion velocity is assumed to be 10 km s^{-1}. We choose to model the emission as a broad Gaussian with a central wavelength of 33.6 μm. The central star of BD+30 is believed to have evolved from an O-rich phase to a C-rich phase (Waters et al., 1998; Matsumoto et al., 2008). Following this model, and given the size of the torus and the larger 33.6 μm envelope, we take it that both were formed during the O-rich phase and apply a silicate dust model to act as an absorber. For the interior mid-IR regions $< 3''$ from the central star, we apply an amorphous

carbon absorption model to account for the C-rich phase of evolution.

5.3.4 X-ray

Using the *HST* [O III] observations as a guide, we generated a prolate ellipsoid, filled with an X-ray emitting plasma, that fits within the [O III] emission shell. This geometry was was chosen because the models for wind-blown nebulae predict that the hot bubble will lie interior to the ionized (optical) region (Weaver et al., 1977). Direct comparison of the *Chandra* and *HST* observations leads to the conclusion that the X-ray emitting region lies very close to the [O III] shell (Fig. 5.23). The *Chandra* observations show significant asymmetries in the hot bubble, which we believe is related to absorption by the surrounding nebula and therefore disregard for the initial modeling.

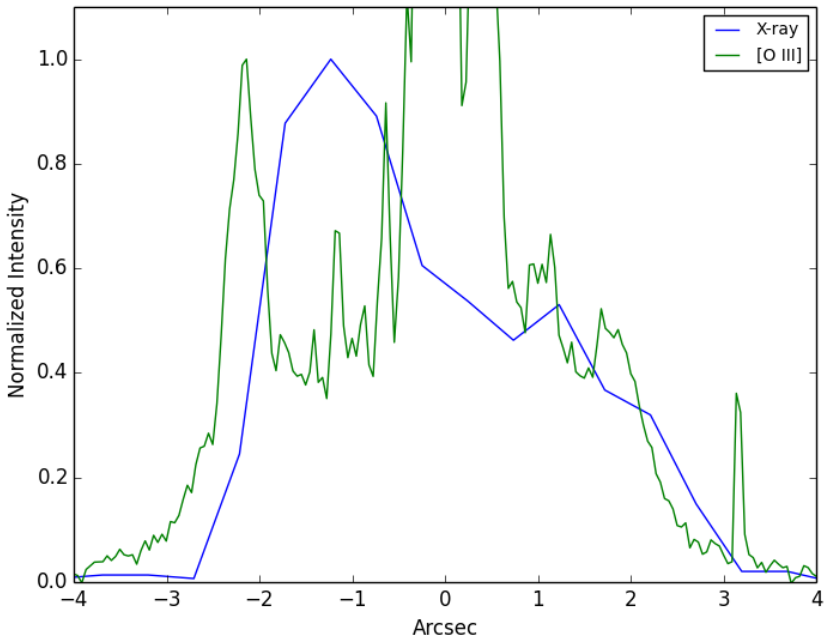

Figure 5.23: [O III] and X-ray East-West radial profiles.

There are no PV diagrams or velocity information available for the X-ray emission from BD+30. However, a wind velocity is assumed from the P-Cygni profiles to be 700 km s^{-1} (Leuenhagen et al.,

1996; Crowther et al., 2006; Marcolino et al., 2007). Given this wind speed, we expect a temperature of $\sim 2 \times 10^7$ K given

$$\frac{1}{2} m_{\rm H} v_w^2 = \frac{3}{2} kT \,, \tag{5.3}$$

where $m_{\rm H}$ is the mass of Hydrogen and v_w is the wind velocity. From fitting the *Chandra* X-ray spectrum with a variable `apec` thermal plasma model with a `wabs` absorption model using `xspec` (Fig. 5.24), we find that the temperature is $\sim 2.6 \times 10^6$ K, which is consistent with previously published temperatures for BD+30 (2.7×10^6 K, $1.9 - 2.9 \times 10^6$ K; Kastner et al., 2000; Yu et al., 2009, respectively). This is also a typical hot bubble temperature found for other PNe (Kastner et al., 2012; Freeman et al., 2014). The temperature discrepancy of an order of magnitude is believed to be due to a cooling mechanism, perhaps related to the contact discontinuity, which we do not include in this model (Toalá & Arthur, 2014). For our modeling purposes we adopt a temperature of 2.6×10^6 for the hot bubble.

To account for the X-ray emission in our model, we converted the `xspec` spectrum output into an emission coefficient model without any absorption such that it can be used by *SHAPE*. Based on the density profile model of Steffen et al. (2008) (Fig. 4.4), we assume that BD+30 has a naturally limb brightened hot bubble and confine the emission to a shell of thickness $\sim 3 \times 10^{-3}$ pc. We ignore self-absorption by the hot bubble, and no absorption model is applied for this region.

5.4 Results

The resulting 3D reconstruction of BD+30 can be found in Figs. 5.25-5.41. In the following section we will discuss the parameters of the resulting model that best fit the observations in reference to each wavelength regime.

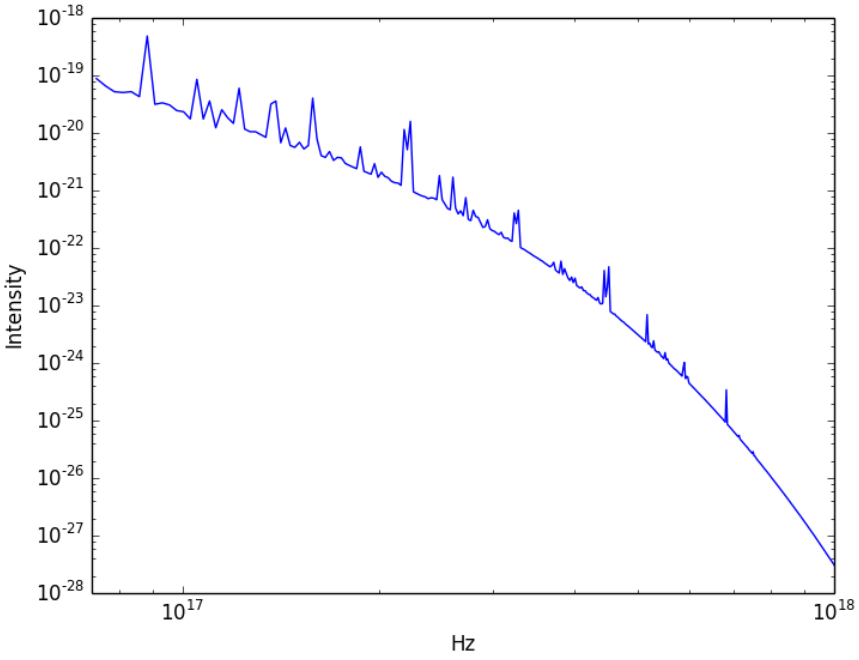

Figure 5.24: Unabsorbed `vapec` X-ray emission model from `xspec` fit to BD+30 *Chandra* data.

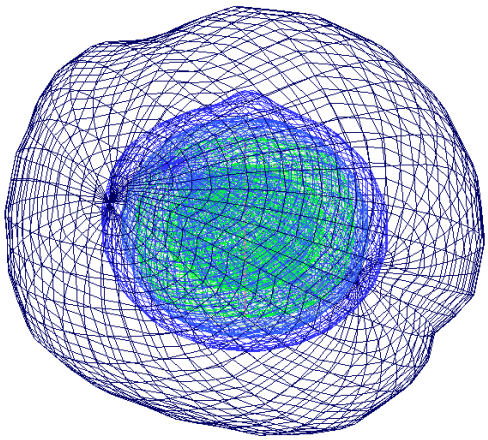

Figure 5.25: *SHAPE* model of the [O III], [N II], and Hα structure of BD+30. The green mesh represents [O III] emission, the blue represents the [N II] and Hα emission, and the navy blue mesh represents the halo of scattered optical light around BD+30.

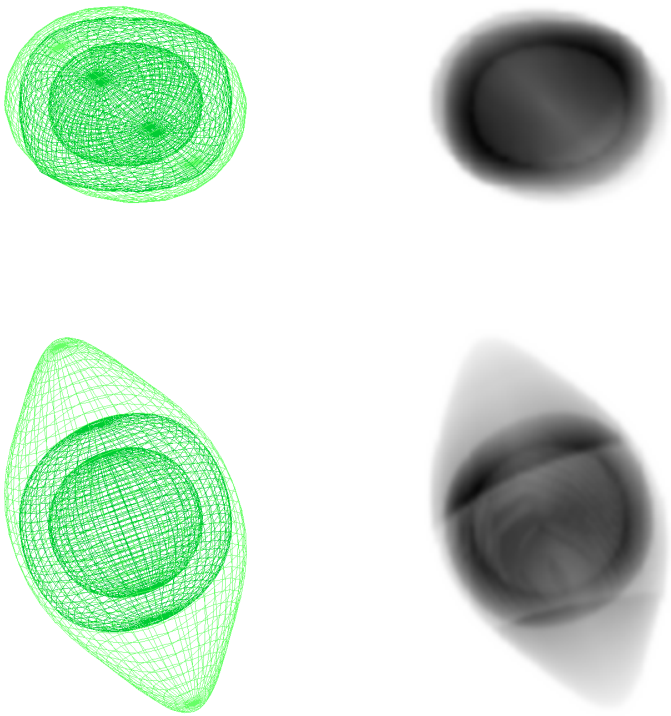

Figure 5.26: *SHAPE* models of the [O III] structure of BD+30 as viewed from Earth (*top*) and at an inclination of 90° (*bottom*). Meshes of the emission region are in the left column and the synthetic observations are found in the right. The field of view of each frame is $10'' \times 10''$.

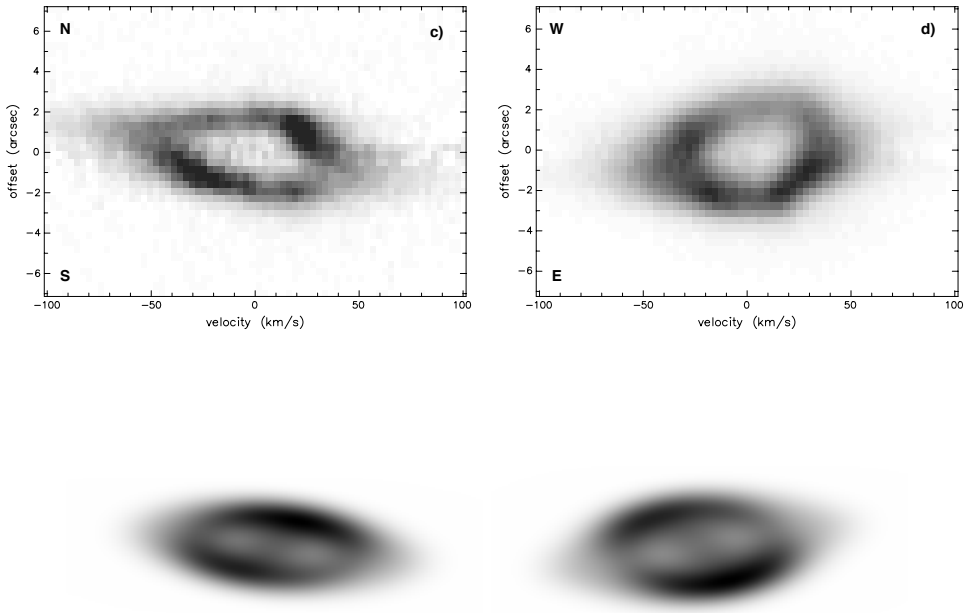

Figure 5.27: [O III] PV diagrams from Bryce & Mellema (1999) (*top*) and *SHAPE* synthetic PV [O III] (*bottom*).

5.4.1 Optical

The optical structure of BD+30 served as the basis for the reconstruction of the nebula (Fig. 5.25). Using an assumed homologous velocity expansion law we found that the Bryce & Mellema (1999) spectroscopic observations best fit a bipolar structure as seen in (Fig. 5.26). This structure encapsulates the HVOs seen in the [O III], and is in agreement with the morphology proposed by Lee & Kwok (2005). In order to fit the [O III] PV diagrams of Bryce & Mellema (1999) we adjusted the inclination and yaw (vertical rotation) of the model to 20° for both. Li et al. (2002) used variations in the surface brightness to fit an inclination of 9.7°, while Lee & Kwok (2005) fitted their model using observations from the radio to the optical to an inclination of 15°. We find an axial ratio of $z : x \sim 1.38$, and an inclination angle close to 20° fits the [O III] PV diagrams well (Fig. 5.27).

This orientation also fits the [N II] structure, with the understanding that the polar regions have a higher ionization parameter. In this case, lower densities at the poles favor higher ionization lines like [O III], while lower ionization lines like [N II] are mostly depleted. Comparison of the [N II] synthetic observation with the Bryce & Mellema (1999) observations can be found in Fig. 5.29. The [N II] emission is embedded in a low density halo with a morphology similar to that of the [O III] region with its HVOs. This region is believed to be the result of scattered emission due to dust in the surrounding nebula, rather than emission from gas.

Previously, Akras & Steffen (2012) modeled the [O III] and [N II] emission features of BD+30 using *SHAPE* in order to better determine the distance to the nebula. Their optical model produced a structure for BD+30 that differs from our own with a much less elongated structure (Fig. 5.30). This is due to their addition of a cylindrical velocity component to account for the HVOs instead of relying on a single homologous velocity law with a more elongated shape as we have done here. Akras & Steffen (2012) suggest that if a collimated outflow were to interact with the AGB wind that it may produce an elongated shape, as we see in our model. This morphology is predicted in hydrodynamical models that show if a jet is launched and followed by a fast wind, that it will yield an elliptical nebula like BD+30 (Huarte Espinosa et al., 2010).

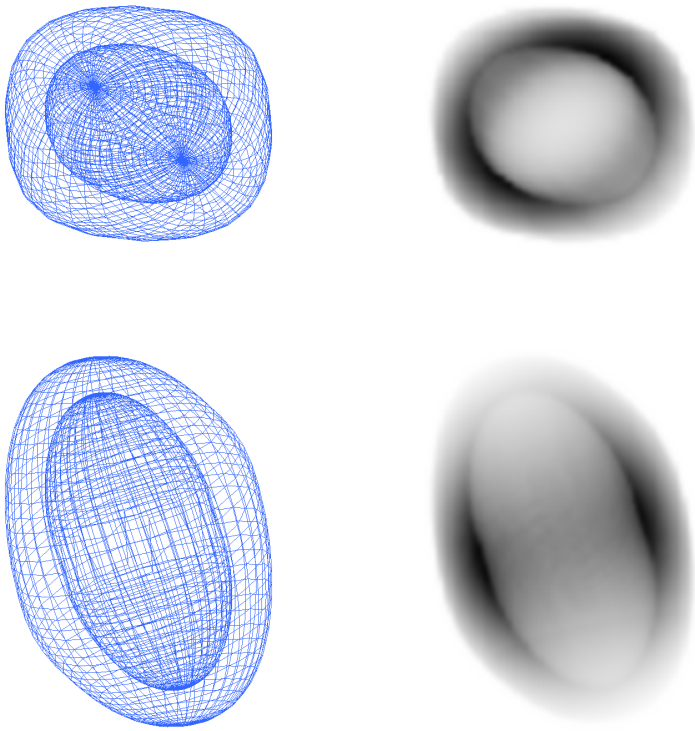

Figure 5.28: *SHAPE* models of the [N II] structure of BD+30 as viewed from Earth (*top*) and at an inclination of 90° (*bottom*). Meshes of the emission region are in the left column and the synthetic observations are found in the right. The field of view of each frame is $10'' \times 10''$.

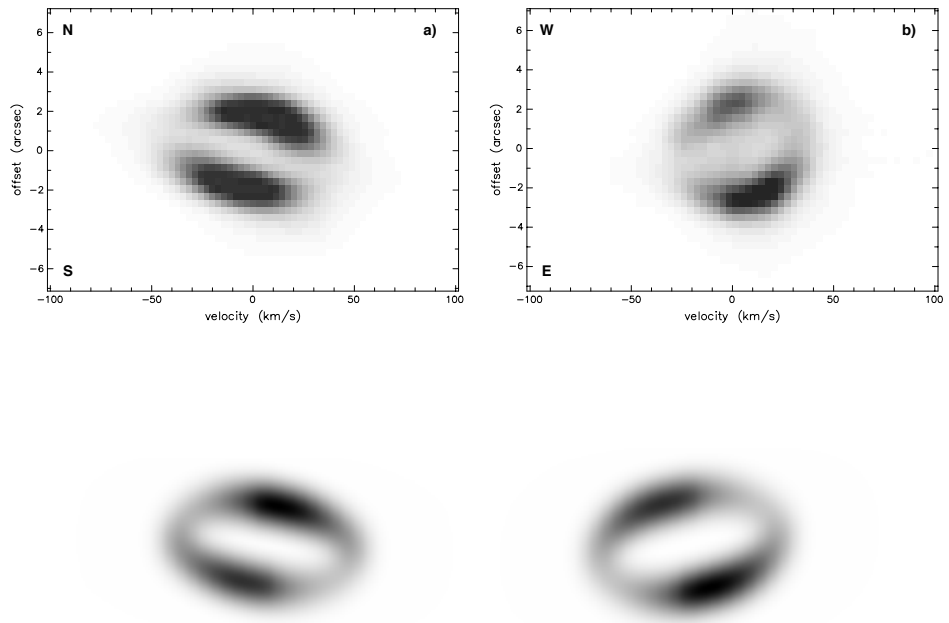

Figure 5.29: [N II] PV diagrams from Bryce & Mellema (1999) (*top*) and *SHAPE* synthetic PV [N II] (*bottom*).

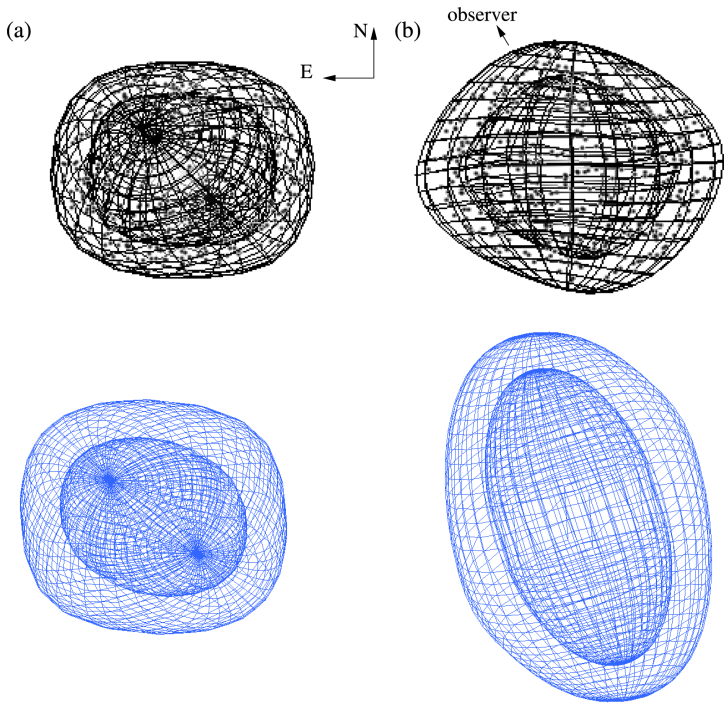

Figure 5.30: *SHAPE* models of the [N II] structure of BD+30. *Top:* Akras & Steffen (2012) model from the observers point of view and inclined 90°. *Bottom:* Our *SHAPE* model at the same inclinations.

5.4.2 Infrared

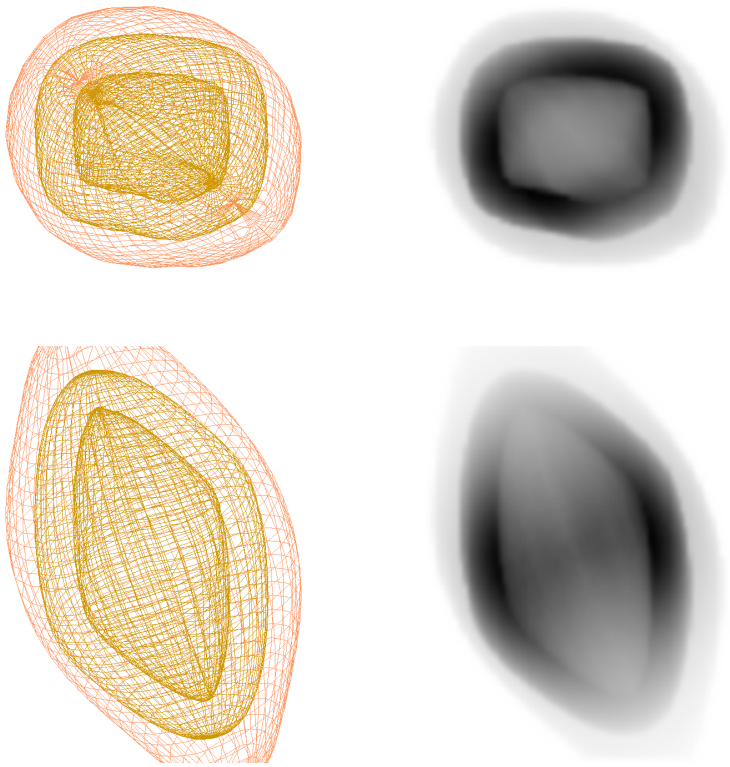

Figure 5.31: *SHAPE* models of the [Ne II] and 11.2 μm PAH structure of BD+30 as viewed from Earth (*top*) and at an inclination of 90° (*bottom*). Emission from both [Ne II] and PAHs are emitted from coincident regions and are thus modeled by a single mesh. Meshes of the emission region are in the left column and the synthetic observations are found in the right. The field of view of each frame is $10'' \times 10''$.

From the base structure of the nebula established by the optical emission, we reconstructed the mid-IR observations of BD+30 (Matsumoto et al., 2008). These regions, which represented emission from PAHs (8.6 and 11.2 μm), warm dust (10.5 μm), and [Ne II] (12.8 μm) showed a similar stratified structure as seen in the optical (Figs. 5.31, 5.32, and 5.33). The longer wavelength emission extended beyond the dust continuum at 10 μm and the warmer PAH line at 8.6 μm. The extent of each region only varies by fractions of an arcsecond. The overlap between the dust

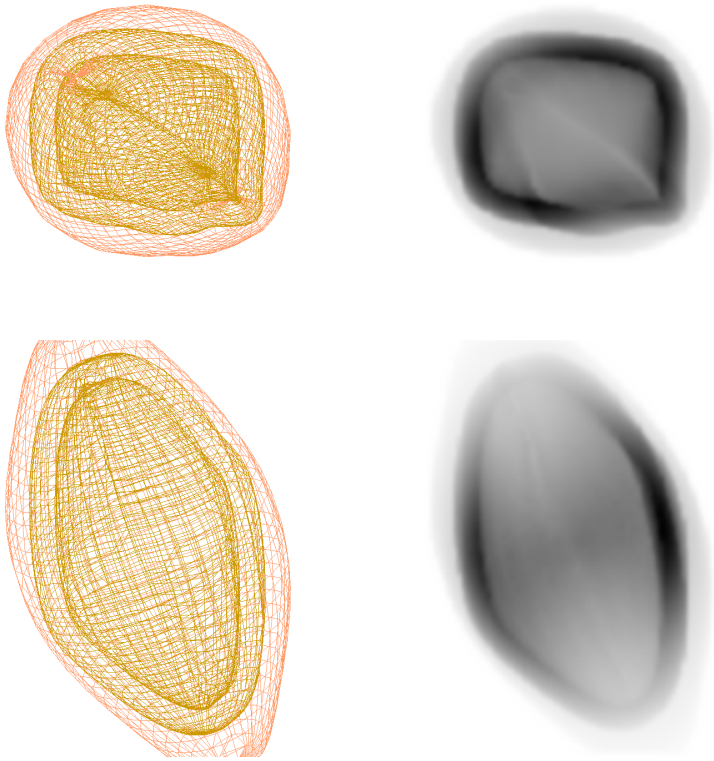

Figure 5.32: *SHAPE* models of the 8.6 μm PAH structure of BD+30 as viewed from Earth (*top*) and at an inclination of 90° (*bottom*). Meshes of the emission region are in the left column and the synthetic observations are found in the right. The field of view of each frame is $10'' \times 10''$.

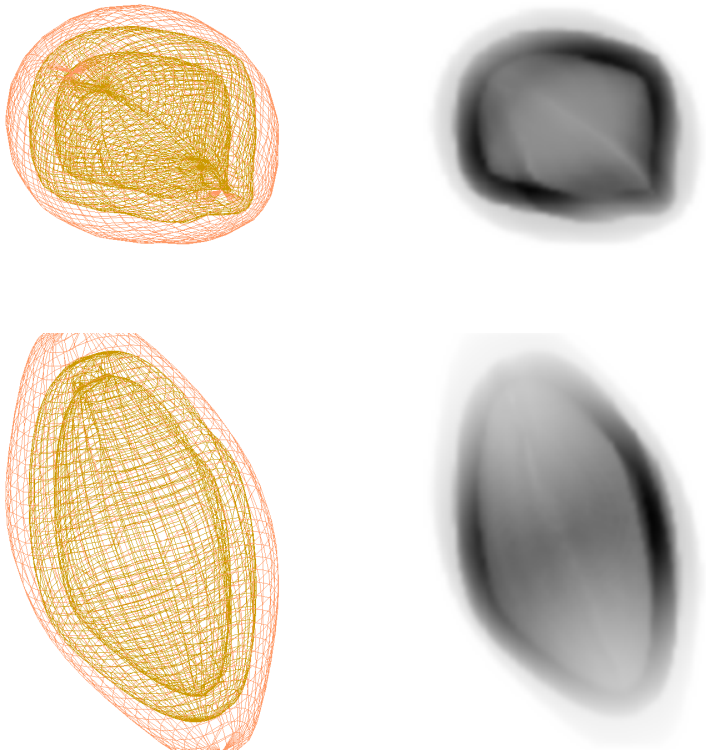

Figure 5.33: *SHAPE* models of the 10.5 μm continuum structure of BD+30 as viewed from Earth (*top*) and at an inclination of 90° (*bottom*). Meshes of the emission region are in the left column and the synthetic observations are found in the right. The field of view of each frame is $10'' \times 10''$.

features and the ionized gas shows that these regions are very well mixed, though the structure is quite different. The mid-IR regions appear more boxy than their optical counterparts. In order to achieve this structure in *SHAPE* the ellipsoid needed to be compressed along the equator, where the density is found to be highest. It is possible that the surrounding torus is in part responsible for the shape of the mid-IR regions more so than that of the ionized gas.

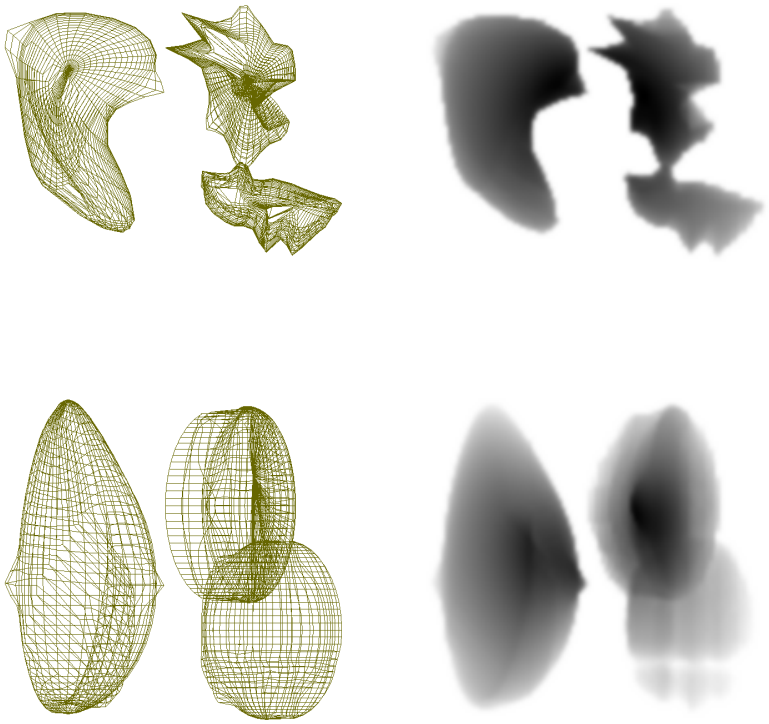

Figure 5.34: *SHAPE* models of the H_2 "torus" of BD+30 as viewed from Earth (*top*) and at an inclination of 90° (*bottom*). Meshes of the emission region are in the left column and the synthetic observations are found in the right. The field of view of each frame is $14'' \times 14''$.

Under the assumption of homologous expansion, the H_2 torus took on a shape that resembles more of a heavily disrupted shell than a torus (Fig. 5.34). This orientation of the torus differs from the morphology suggested by Bryce & Mellema (1999) who believed that the torus was expanding outward from the equatorial region of the nebula. The eastern part of the torus has a large range of

velocities, both blue and redshifted, while the western portions are broken up into blueshifted and redshifted portions. Comparison between the synthetic and observed channel maps can be found in Fig. 5.35.

The overall structure of the H_2 region nicely cradles the optical emission, and sits within the emission line halos, which are expected to actually be the result of scattered emission. The alignment between these regions corroborates this, given that scattering off of silicate dust in the torus is a likely origin of line emission so far from the central star.

All of the IR emission is enclosed by an envelope of silicate dust at 33.6 μm (Fig. 5.36). The *SOFIA* observations taken by Guzman-Ramirez et al. (2015) were the first to directly observe this region, which extends beyond $\sim 7.5''$ from the center of the nebula. We find that the density of this region needs to be much lower than that of the mixed dust regions in order to provide the appropriate absorption to match observations. Given that this region was created long before the planetary nebula was created the inherent shape may be quite different from the event that created the nebula, so we cannot put many constraints on the actual morphology beyond that it is close to spherical.

5.4.3 Radio/Millimeter

Unlike other nebulae like NGC 7027, the kinematics of the CO and H_2 are clearly distinct features with very different morphologies. While NGC 7027 hosts CO emission along the H_2 shell surrounding the nebula (Nakashima et al., 2010), BD+30 exhibits CO emission in the form of two distinct bullets that have no corresponding emission in other parts of the electromagnetic spectrum (Fig. 5.37). The alignment of the CO bullets on opposite sides of the nebula seems to suggest that they were the result of the same event. The inclination between the two is roughly 45°. It has been proposed that they may have formed from a jet, but no observations have found any direct evidence for a jet in the nebula (Bachiller et al., 2000). Their orientation is also off axis from the HVOs seen in the [O III] emission, however, it is possible that if a jet was responsible for creating the CO bullets, it could have precessed towards the major axis of the nebula some time after they

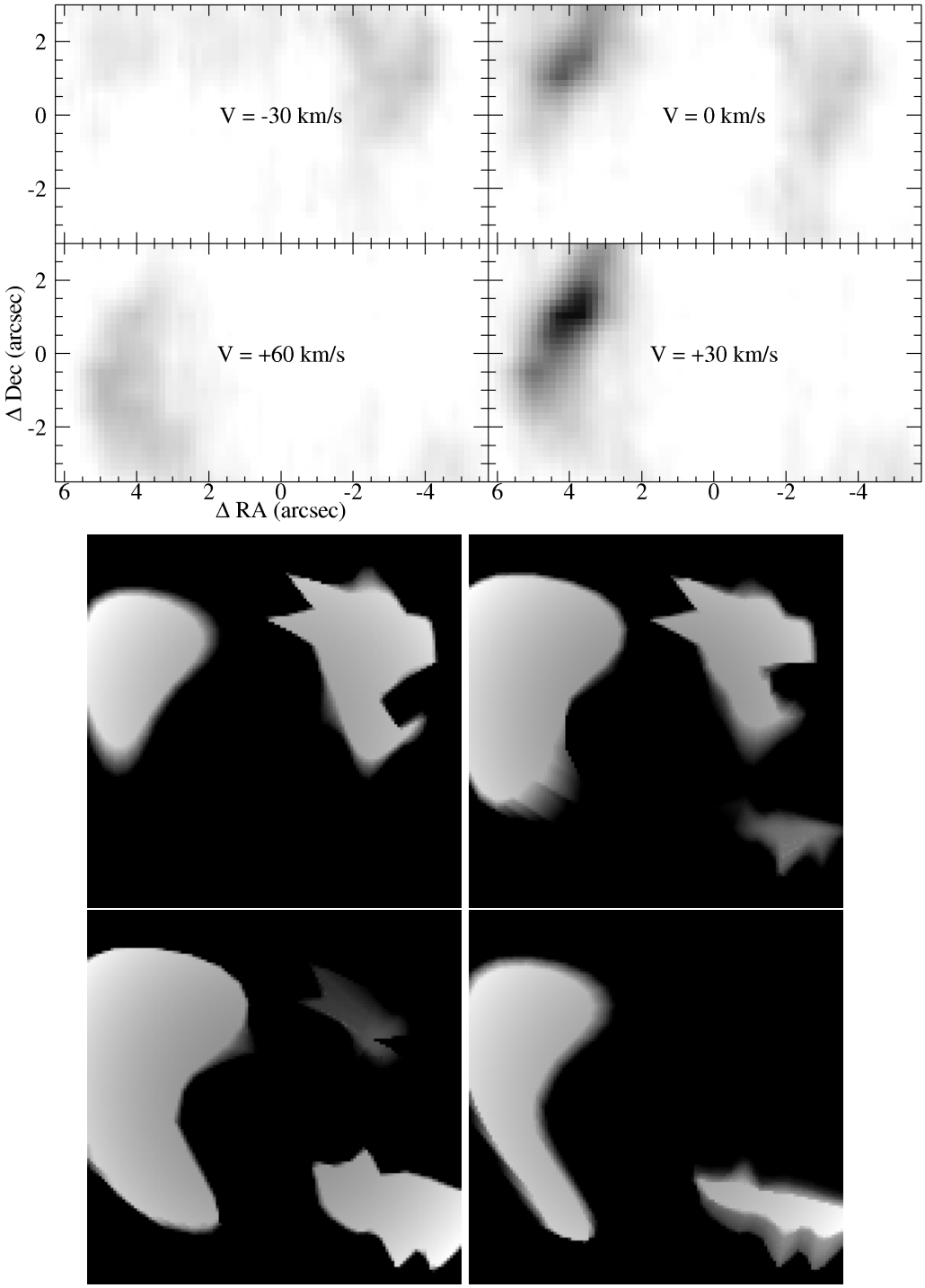

Figure 5.35: Shupe et al. (1998) channel maps of the H_2 structure surrounding the main nebula of BD+30 (*top*) compared to the synthetic *SHAPE* channel maps of the same structure (*bottom*). The *SHAPE* channel maps were generated using the same velocity cuts as the Shupe et al. (1998) maps (clockwise from top right: -30, 0, 60, and 30 km s^{-1}).

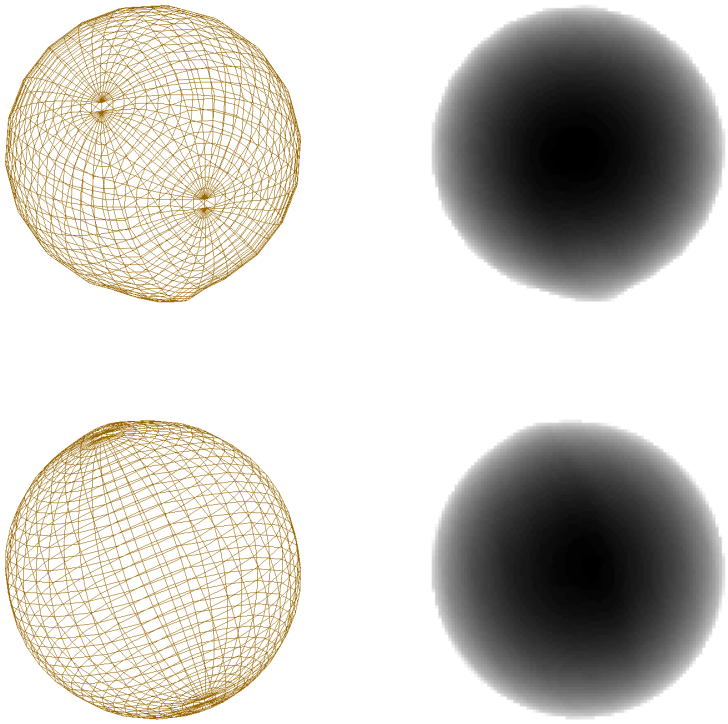

Figure 5.36: *SHAPE* models of the 33.6 μm silicate dust envelope of BD+30 as viewed from Earth (*top*) and at an inclination of 90° (*bottom*). Meshes of the emission region are in the left column and the synthetic observations are found in the right. The field of view of each frame is $22' \times 22''$.

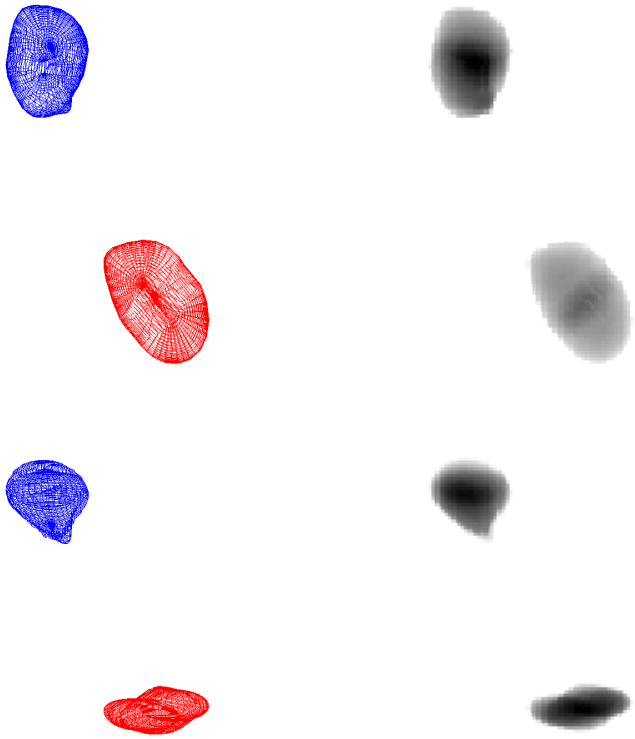

Figure 5.37: *SHAPE* models of the CO bullets of BD+30 as viewed from Earth (*top*) and at an inclination of 90° (*bottom*). Meshes of the emission region are in the left column and the synthetic observations are found in the right. The field of view of each frame is $10'' \times 10''$.

were launched. It is unclear from observations, and further modeling is required to get a better understanding of their formation and impact on the nebula.

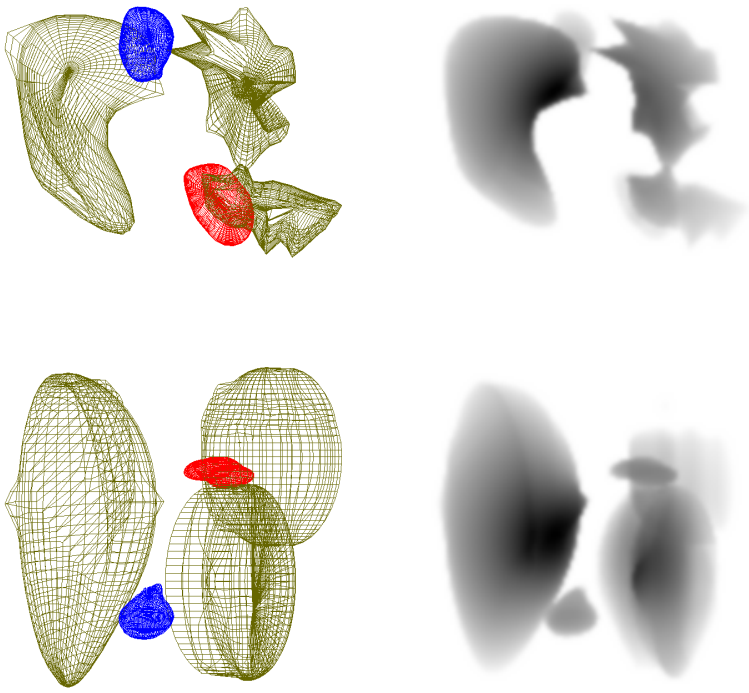

Figure 5.38: *SHAPE* models of the CO bullets of BD+30 overlaid with the H_2 regions as viewed from Earth (*top*) and at an inclination of 90° (*bottom*). Note that the southern bullet appears to be pushing into the western part of the torus, while the northern bullet is splitting the eastern H_2 feature from the northwestern portion. Meshes of the emission region are in the left column and the synthetic observations are found in the right. The field of view of each frame is $14'' \times 14''$.

Given the increasing velocity gradient from the ionized gas to the warm H_2, Shupe et al. (1998) inferred that the CO would have an asymmetric distribution that extended outside of the H_2 region in the form of an expanding shell. However, it appears that the physical disruption that caused the shape of the torus seems to have its origin in the CO bullets. The location of each bullet corresponds with low H_2 emission regions that break up the torus. When viewed from above the nebula it is further noted that the southern bullet appears to be pushing into the southwestern

portion of the torus, dragging it away from the main nebula (Fig. 5.38). The northern bullet looks to be breaking through the torus in the northeastern portion, splitting the two regions apart.

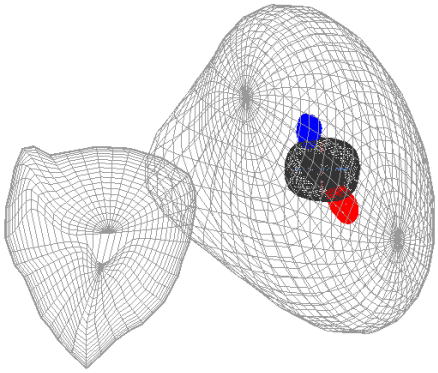

Figure 5.39: *SHAPE* models all of the radio emission regions of BD+30. The field of view of this image is $50'' \times 50''$.

The largest emission region related to BD+30 is the H I bubble it resides in (Fig. 5.39). The atomic emission extends $15''$ away from the central star in an odd shape with an additional component to the east. The secondary feature does not seem to be related to BD+30 and could be distinct. Unfortunately, the 21 cm observations were not able to distinguish it from the unresolved nebular H I (Taylor et al., 1990). Unlike the higher velocity components towards the outer edges of the main nebula, the H I bubble is found to be expanding close to 27 km s^{-1}, much slower than the H_2 torus or the CO bullets, and the corresponding region in our model is set to the same. Given that this emission is unresolved, it is difficult to confidently measure the impact this region has on our model.

The radio continuum varies somewhat at lower frequencies, but we model the emission here using the 6 cm observations from MERLIN and the VLA because they provide the most detail

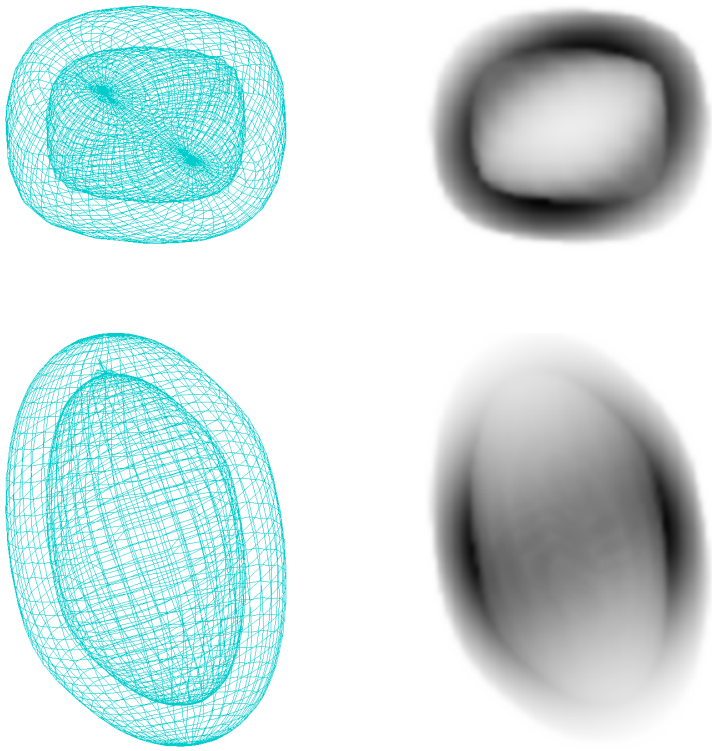

Figure 5.40: *SHAPE* models of the 6 cm emission of BD+30 as viewed from Earth (*top*) and at an inclination of 90° (*bottom*). Meshes of the emission region are in the left column and the synthetic observations are found in the right. The field of view of each frame is $10'' \times 10''$.

(Bryce et al., 1997). It is most evident from this region that the dust and gas is intermixed. The extent of the 6 cm is close to that of the Hβ and [N II] optical emission features, but the morphology shows a more complete and boxy shell due to a lack of absorption (Fig. 5.40). In particular, when reconstructing this region, we found it necessary to enhance the dust content in the southwestern part of the shell, in order to appropriately simulate the absorption in the synthetic observations. The structure of the prolate ellipsoid inclined to 20° shows the double-peaked emission expected from the observations and the model predicted by Masson (1989, 1990). Additionally, the shell thickness matches quite well, measuring close to 1/3 of the radius.

5.4.4 X-ray

The X-ray morphology based on observations of BD+30 from *Chandra* showed an asymmetrical nebula, with the peak emission located northeast of the central star. Comparison with optical and IR observations showed that the X-ray emission filled the central cavity well, and following from this we assumed that the morphology of the X-ray emission followed that of the [O III] region (Kastner et al., 2002, 2012). The resulting region we modeled is axisymmetric around the major axis (Fig. 5.41). The lower density in the polar regions allows for the X-ray emitting plasma to escape the dense equatorial region and fill the [O III] HVOs. Employing a `wabs` absorption model within the gas shells surrounding the central bubble reveals a synthetic image that closely matches the smoothed *Chandra* image.

5.5 Re-orienting BD+30

One of the many advantages of having a 3D model to play with is that we are no longer limited by our location on Earth. We can rotate our model, reorient it, and compare it with observations of other PNe. For our current analysis we have chosen four PNe: NGC 7027, NGC 6720, NGC 3132, and NGC 40 (physical parameters of these nebulae can be found in Table 5.3). In the following section we will investigate the relationship BD+30 has with other PNe of differing

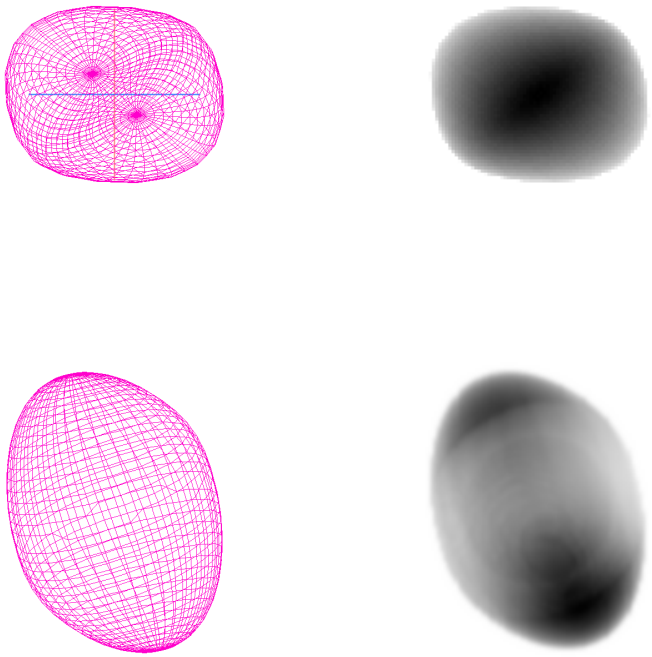

Figure 5.41: *SHAPE* models of the X-ray emission of BD+30 as viewed from Earth (*top*) and at an inclination of 90° (*bottom*). Meshes of the emission region are in the left column and the synthetic observations are found in the right. The field of view of each frame is $10'' \times 10''$.

projected morphologies, and connect the evolution of various PNe to a common path.

Table 5.3: Physical Parameters of Planetary Nebulae

Parameters	BD+30	NGC 7027	NGC 3132	NGC 6720	NGC 40	Units
R	0.02	0.03	0.13	0.13	0.11	[pc]
Age	1	1.4	6	6	4	10^3 [yr]
T_*	32	175	100	148	48	[kK]
Sp. Type	[WC9]	-	-	hgO(H)	[WC8]	-
Companion	-	-	A2IV-V	-	-	-
X-rays[a]	D	D,P	N	N	D	-

Notes.
[a]X-ray results key: P = point source; D = diffuse source; N = not detected.

5.5.1 NGC 7027

BD+30 is most commonly compared with another well-studied PNe, NGC 7027. NGC 7027 is often considered the poster-child for PNe given that it has emission from every part of the electromagnetic spectrum. These two nebulae have many structural commonalities. Both NGC 7027 and BD+30 are young PNe (1400 and 1000 yr, respectively) that are still in the active shaping phase of their evolution based on the presence of diffuse X-ray emission (Kastner et al., 2012; Freeman et al., 2014). The X-ray emission from both nebulae appear to have spatial distributions that correspond to low A_V where the X-ray emission peaks and weak emission towards areas of high A_V. These regions are located in the perimeters of the nebulae, and given the correspondence between low A_V and bright X-ray emission, suggests significant intranebular extinction in this region (Kastner et al., 2002). In the radio, NGC 7027 exhibits a similar limb-brightened, double-peak structure as seen in BD+30, which led Masson (1989) to suggest that the two might have the same morphology, with BD+30 appearing instead pole-on. Given the similar ages of the two nebulae, and the similar bipolar structure, it is possible that NGC 7027 represents the next stage of BD+30's evolutionary track.

For comparison, we rotated BD+30 to correspond with the inferred inclination of NGC 7027 (Cox et al., 2002) and generated synthetic observations of BD+30 [O III] emission (Fig. 5.42) using

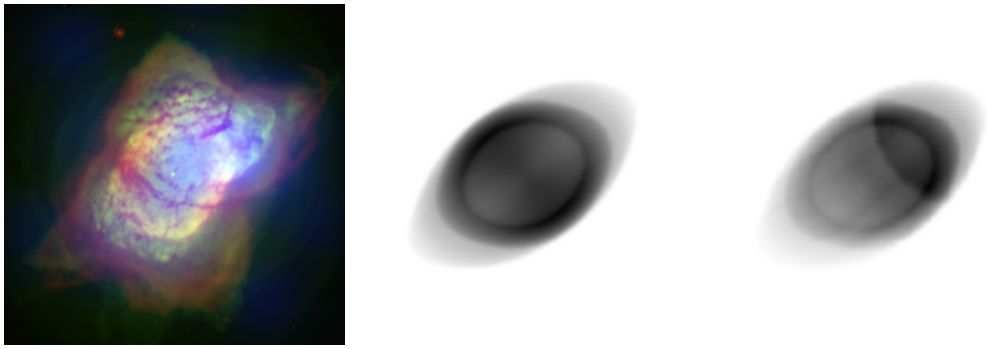

Figure 5.42: *HST* image of NGC 7027 (*left*) compared with the basic render (*center*) and physical render of BD+30 at a similar orientation (*right*).

the basic *SHAPE* renderer. The basic shape of the bipolar lobes match rather well between the two nebulae. Using the physical renderer to observe the [O III] emission region with the 6 cm absorption region acting as an absorber, we see that physically both PNe still look very different, even at a similar orientation (Fig. 5.42). While the basic morphology may be similar, the chemical composition is different, which has resulted in different structures in the gas and dust. NGC 7027 is known to have a molecular CO shell surrounding the main nebula, while BD+30 only has CO emission in bullets (Nakashima et al., 2010).

The spectral type of the central star of NGC 7027 is unknown due to difficulty observing it within the optical nebula. The similarities between the morphology of both BD+30 and NGC 7027 point to a possible common origin and stellar engine. In this case, it would imply that at the heart of NGC 7027 is a WR-type central star. However, the overall content of each nebula paints a different origin story. NGC 7027 is a carbon rich nebula, surrounded by amorphous carbon, which is very different from the bifurcated structure of carbonaceous and silicate dust in BD+30. The source of NGC 7027's chemical complexity is the progenitor of the central star, which has been estimated to be 3-4 $M_{\odot}$ Bernard-Salas et al. (2001), while the central star of BD+30 is known to have changed chemically during its progenitor phase from oxygen-rich to carbon-rich. The mass of the progenitor of BD+30's central star is not well known, but is estimated to be above 3 $M_{\odot}$ (Bernard-Salas et al., 2003). The change in BD+30's central star's composition could have put it

on a path similar to what NGC 7027 is now, but without more details of the central stars of both nebulae, and more modeling, it is difficult to confirm how much BD+30's future will emulate NGC 7027.

5.5.2 NGC 6720

NGC 6720, also known as the Ring Nebula, is one of the most famous examples of a planetary nebula and it is immediately evident that there are structural similarities with BD+30. The Ring Nebula appears as an elliptical ring in optical and mid-IR images while in the far-IR it is surrounded by a dusty halo (van Hoof et al., 2012). They both share similar radio structure as well, which reveals the same double-peak intensity feature aligned in the N-S direction. Unlike BD+30, NGC 6720 has no detectable X-ray emission, which is believed to be due to its advanced age of 6000 yr.

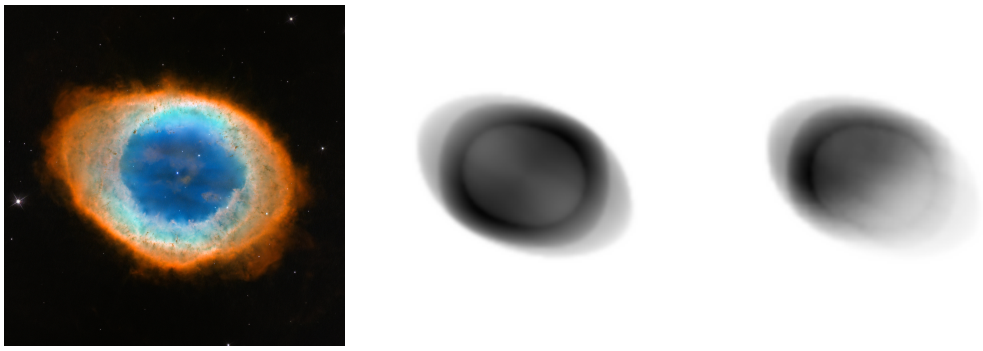

Figure 5.43: *HST* image of NGC 6720 (*left*) compared with the basic render (*center*) and physical render of BD+30 at a similar orientation (*right*).

Both Masson (1990) and O'Dell et al. (2013) modeled the Ring Nebula as a prolate ellipsoid inclined 30° (330°) to the line-of-sight with enhancement along the minor axis. Masson (1990) suggested that BD+30 may have a similar morphology but viewed closer to pole-on. Reorienting BD+30 to an inclination close to 30° we find that the basic render resembles the Ring Nebula unambiguously (Fig. 5.43). When rendering using the physical renderer we see that much like in NGC 6720, the HVOs disappear due to their low density, and we are left with the prominent ring feature (Fig. 5.43). We don't see some of the brightness enhancements within the ring, which is

most likely due to differing internal knot structures, as well as features along the polar axis that aren't apparent in BD+30. The PV diagrams for [N II] and [O III] look very similar, showing identical ring structures, but lacking the strong brightness enhancements in the north and south (O'Dell et al., 2013).

The likeness between BD+30 and NGC 6720 suggest common ancestry and a similar future, although their central stellar engines are different. This is in part due to the later stage of NGC 6720 where the proto-white dwarf at the center of the nebula has been able to heat up to 148 kK compared to the nascent 32 kK of BD+30's central star. It is very likely that BD+30 will end up evolving into something that morphologically will appear very similar to NGC 6720, though there is the matter of the surrounding H_2 region. While BD+30 continues to push into the surrounding H_2 left behind by its AGB progenitor which has been disrupted by the CO bullets, NGC 6720 shows that the H_2 morphology closely matches that of the ring and outer halo (van Hoof et al., 2010). It is possible that this surrounding gas may impede BD+30's evolution further funneling the gas along the poles rather than radially out via the equator.

5.5.3 NGC 3132

The southern sky has its own version of the Ring Nebula known as NGC 3132, or the Eight-Burst Nebula. The nebula appears in the sky with a thin elliptical ring and its internal structure has been compared with that of NGC 7027. As with NGC 6720, NGC 3132 has no detectable diffuse X-ray emission, likely due to its dynamical age of 6000 yr. Sahu & Desai (1986) modeled NGC 3132 as an expanding ellipsoidal shell based on [O III] observations with the major axis aligned northwest to southeast (PA 146.5°). Observations of CO further supported that it has a geometry similar to BD+30 with a high density waist and lower density poles (Sahai et al., 1990), though the CO emission was found in a shell around the main nebula, similar to NGC 7027. An alternative morphology has been suggested by Monteiro et al. (2000), which posits that NGC 3132 is a diabolo shape, similar to the Butterfly Nebula.

Adjusting BD+30's inclination to match that of NGC 3132 we find that the basic view of the

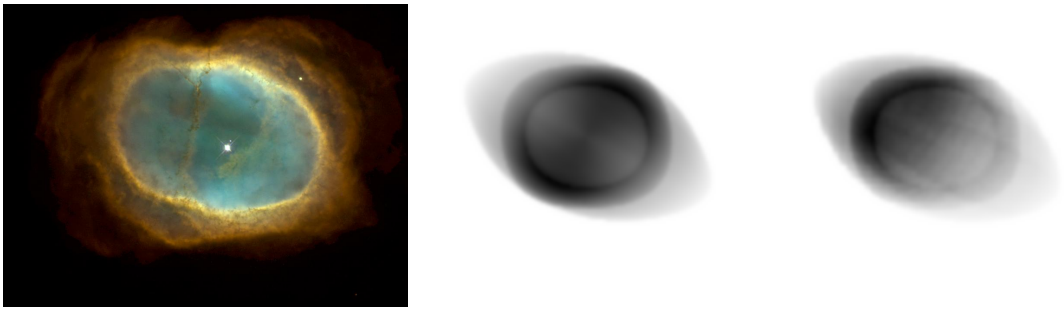

Figure 5.44: *HST* Hα image of NGC 3132 (*left*) compared with the basic render (*center*) and physical render of BD+30 at a similar orientation (*right*).

nebula resembles the optical elliptical shell (Fig. 5.44). Using the physical renderer we see that the view of the nebula changes a bit, most likely due to the differing dust morphology surrounding the ellipsoid (Fig. 5.44). Varying the composition and density of the dust shells of BD+30 could make it possible to find a configuration that more closely matches the observed morphology of NGC 3132, however, the correlation between the basic shapes serves as a proof of concept.

As with NGC 6720, the resemblance of the BD+30 model to NGC 3132 suggests that both lie on a common evolutionary path. The binary at the center of NGC 3132 is not expected to play any role in the shaping of the nebula given a separation of 1310 AU between the two components. That being said, the central star of BD+30 is believed to have once been a binary which coalesced into a single star, possibly launching jets and subsequently the CO bullets, however, the modern day stellar engine is a single [WC]-type star. Most PNe are believed to be the product of a binary central star, but many companion stars have yet to be unveiled. The similarities of BD+30 and NGC 3132 may yield indirect evidence that NGC 3132 is actually the product of a triple star system, provided BD+30's binary history can be exposed.

5.5.4 NGC 40

NGC 40 is another well-studied PN that contains a slightly elliptical central core with filamentary structures. Compared to BD+30, the central shell of NGC 40 appears more spherical, however,

it does show evidence for HVOs and a similar gap in the [N II] emission is seen in the PV diagrams (Monteiro & Falceta-Gonçalves, 2011). Observations made at 5 GHz show a double-peak structure as expected of a ellipsoidal morphology with a high density equatorial region and low density poles (George et al., 1974). NGC 40 has also been detected by *Chandra* (Montez et al., 2005), showing diffuse X-ray emission within the central shell much like BD+30. The shape of the X-ray emission differs between the two, with NGC 40 showing a limb-brightened structure while BD+30's emission fills the inner cavity completely. This difference may be the result of NGC 40's age (4000 yr) and that it is believed to be on the downward turn of the diffuse X-ray emission phase (Kastner et al., 2012).

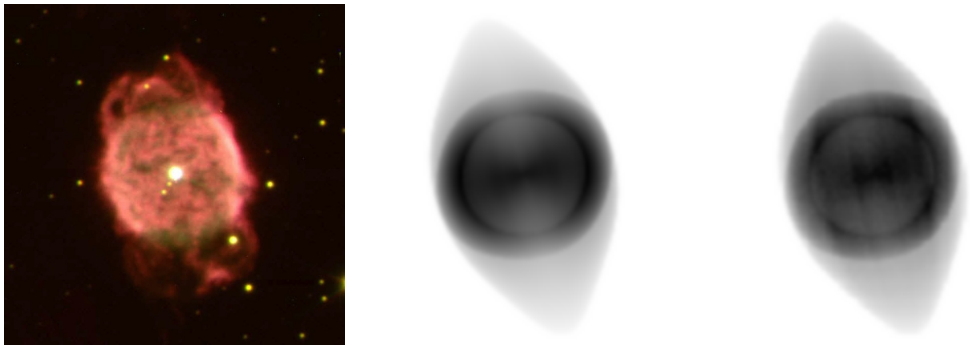

Figure 5.45: *HST* Hα image of NGC 40 (*left*) compared with the basic render and physical render of BD+30 at a similar orientation (*right*).

Tilting our model of BD+30 up to an inclination that brings the nebula nearly edge-on gives us our closest comparison to NGC 40. The basic shape of the nebula is elongated in the central region compared to NGC 40's more spheroidal central shell, but the overall morphology does appear similar (Fig. 5.45). When incorporating the physical renderer we see that the polar regions are not well modeled and there are no filamentary structures present in our model to adequately compare with NGC 40 (Fig. 5.45). The more spherical nature of NGC 40 may point to a single star evolutionary path, or that if there was a binary present, that it coalesced into a single star much earlier in its evolution than BD+30. Balick et al. (1987) suggested that the filamentary structure is the result of rapid expansion during the early stages of the formation of NGC 40, within $\sim$ 700 yr. This is

on the younger side of the age estimates for BD+30, so it is possible that such filaments may still form later given time to cool down and condense.

NGC 40 is the closest PNe morphologically to BD+30 that also hosts a [WC]-type central star. It is within a C-rich environment with possible evidence for silicate features, much like BD+30 (Delgado-Inglada & Rodríguez, 2014). The similarities in their morphologies and central stellar engines point to a similar origin and a evolutionary path. However, as mentioned before, the more spherical central shell is most likely indicative of single star evolution, while BD+30 shows a more elliptical central shell and the possible remnant of jets. More detailed modeling of NGC 40's morphology making use of kinematic information would provide a better comparison between these two nebulae.

5.6 Summary

BD+30 is one of the most well-studied PN in the solar neighborhood. It boasts emission from across the electromagnetic spectrum, including diffuse X-ray emission, and hosts a [WR]-type central star. Using previously published data and the astrophysical modeling software *SHAPE*, we have constructed a 3D morpho-kinematic model of BD+30. With the inclusion of multiwavelength data from radio to the X-ray, as well as radiative transfer with applied emission and absorption models, this reconstruction represents the most complete 3D model of a PN to date.

Our resulting model has similarities with previously published models (Masson, 1989; Bryce & Mellema, 1999; Lee & Kwok, 2005; Akras & Steffen, 2012) in which BD+30 is taken to be a prolate ellipsoid inclined between 10° and 20°. Based on kinematic data from optical emission lines, CO, and H_2 emission we were able to reconstruct the velocity components assuming a homologous velocity expansion law that showed evidence for HVOs along the major axis of the nebula. When comparing our synthetic observations with authentic ones from across the spectrum, we find that our model agrees well with the projected morphology.

We have gained new insight into the formation process of BD+30 from our 3D model. The

CO kinematic data of two distinct bullets offered a chance to appropriately orient them around the main shell, confirming that the two exist along an axis that is not aligned with the major axis. Furthermore, the orientation of the CO bullets and the kinematic disruptions in the H_2 region surrounding the nebula, suggest that the event that spawned the bullets is responsible for the disorganized structure of the so-called torus. We posit that given the silicate composition of the torus, that it was formed well before the nebula, and that the launching event for the CO bullets occurred during the pre-PN AGB phase.

As a young PN, BD+30 offers us the chance to peer into the early stages of PN evolution, particularly the evolution of other, more evolved PN like NGC 7027, NGC 6720, NGC 3132, and NGC 40. With the exception of NGC 7027, these nebulae are 3000-5000 yr older than BD+30, and based on our 3D model, it is likely that BD+30 will evolve along a similar trajectory.

- NGC 7027 serves as one of the most interesting PN. Comparing our 3D model of BD+30 with that of NGC 7027's projected morphology shows that the two share common structure, and that in many ways they may share common ancestry in the way of an energetic mass loss event or launching of jets.

- NGC 6720 is remarkably similar in basic morphology and kinematics to BD+30, though it has a different stellar engine. Additionally, BD+30 shows evidence of a violent mass loss event or jet launching that has disrupted its structure, whereas NGC 6720 shows a rather complete structure at all wavelengths.

- NGC 3132 shows a similar ellipsoidal structure to that of BD+30 and NGC 6720. The central visual binary is not believed to play a role in the shaping of this nebula given the large separation of the two components. The intrinsic morphology of NGC 3132 has been suggested to be more of a butterfly (diabolo) shape, however the striking resemblance between the BD+30 model and that of NGC 6720 seem to suggest that is indeed a prolate ellipsoid.

- NGC 40 is a PN that shares many physical components in common with BD+30. It has a bright inner shell surrounding a [WR]-type central star with low density outflows along the

poles, and diffuse X-ray emission has been detected from the central region. While NGC 40's central shell is more spherical than BD+30, it can still be considered a snapshot of two ends of hot bubble evolution for ellipsoidal PN with this type of internal structure.

Additional modeling will help to provide more detail for this reconstruction of BD+30, and more observations with modern observatories will help supply better data to work from. Hydrodynamic simulations of jet launching using BD+30's physical parameters would also be a useful measure of how accurate this model is, and a preliminary case can be done using *SHAPE*.

CHAPTER 6

SUMMARY AND FUTURE WORK

6.1 Investigating X-ray emission

The formation of PNe is typically modeled as being the result of the interaction between the progenitor AGB wind and the fast wind of the newly unveiled core. When the fast wind collides with the slower AGB wind, a shockwave forms, creating a hot bubble interior to the swept-up AGB material. At the speed at which the fast wind is traveling we expect the hot bubble to reach temperatures on the order of 10^7 K, well within the X-ray regime. In Chapter 3 we presented results of targeted observations of 59 PNe within the solar neighborhood by ChanPlaNS, which have placed constraints on the appearance and characteristics of X-ray emitting PNe. Combining data from the *Chandra* archive, as well as Cycle 12 and 14 observations of PNe, revealed that $\sim 54\%$ of all sample targets have some form of detectable X-ray emission, whether it is point-like, diffuse, or both.

Close to 40% of the ChanPlaNS sample host luminous X-ray point sources at their central stars. The soft ($\sim 0.6 - 1.0$ keV) point source emission is likely indicative of photospheric emission or wind shocks located close to the central star. The hard ($\gtrsim 1.0$ keV) emission is often related to binary companions of the central star. Accretion onto the companion star, collisions between the

winds of the two stars, or the photosphere of the secondary are all possible mechanisms leading to this form of emission. Within the ChanPlaNS sample, $\sim 60\%$ of the known binaries display this type of point-like X-ray emission.

We also found that $\sim 27\%$ of our sample hosted diffuse X-ray emission. Of these detections, 5 were PNe with [WR]-type central stars, which account for all of the [WR]-type PN in our sample. With the exception of Hb 5, all of the diffuse detections are linked to PNe that show compact ($R_{\rm neb} \lesssim 0.15$ pc) elliptical morphologies with closed structures or nested shells and high central electron densities ($n_e \gtrsim 1000$ cm^{-3}). These constraints point to a cutoff age of 5000 yr for the diffuse X-ray emission phase, suggesting that the impact of the central stellar wind on the shaping of the nebula occurs early on its evolution. The X-ray detection of this hot bubble phase appears largely independent of distance or the excitation of [O III] or Hβ lines, while the opposite holds true for point-like emission. The distance independence makes a strong case for expanding our sample to nebulae farther than 1.5 kpc from the Sun to increase our detection rate of diffuse X-rays from hot bubbles in PNe.

6.2 Unveiling diffuse X-ray morphology

ChanPlaNS revealed a host of PNe that exhibit diffuse X-ray emission from the hot bubble interior. Given the similarities between PNe and other wind-blown nebulae that exhibit X-rays, we anticipated that the morphology of the X-ray emission would also be similar, especially for those PNe with [WR]-type CSPNe. Diffuse X-rays found in the hot bubbles around WR stars have displayed limb-brightened morphologies, though the sample is few. To investigate the intrinsic structures of the diffuse X-ray emitting regions of PNe, we created simple, spherically symmetric, two-phase models using 14 PNe from the ChanPlaNS sample.

To create our models, we used the astrophysical modeling tool *SHAPE*, which had never been previously used to model X-ray emission. Our models consisted of an X-ray hot bubble and swept-up shell with the intent of investigating the X-ray morphology of these objects and the extinction

caused by the swept-up shell. The hot bubble was given a density distribution that would result in limb-brightening, with the density increasing sharply at its edge. We varied the density distribution of the swept-up shell from r^{-2} to a constant density, and the peak density was also varied from 10^2 to 10^9 cm^{-3}. Radial profiles were generated from our synthetic *SHAPE* data and compared with profiles generated from *Chandra* observations with the aim of finding a synthetic profile that best fit the observations, and in due course, a peak density estimate for the swept-up shell.

We found that very few ($\sim$ 21%) of the PNe in our sample display a limb-brightened morphology, and those that do suffer from poor photon statistics and poor fitting values, while the remaining sample are best-fit by limb-darkened hot bubbles. However, it is clear that the model of an intrinsically limb-brightened hot bubble with a surrounding shell of absorbing gas does fit the shape of the X-ray radial profiles well, suggesting that all PNe that are in an early stage of evolution with diffuse X-ray emission hide this structure. The density and corresponding column density values that we estimated are quite high, many orders of magnitude above previously estimated values using Hβ fluxes or via X-ray spectral fits, however our density estimates do follow the same trends as previously published data. We conclude that our model is seeing an "over-density" that may result from X-ray self-absorption, additional absorption components not considered here, or may be an artifact of our simplistic *SHAPE* model.

6.3 Modeling BD+30

Understanding the 3D structure of PNe can help untangle the projected morphology from its intrinsic shape, as well as reveal information about the history of the nebula. As a case study, we constructed a multiwavelength morpho-kinematic model of the thoroughly studied, brightest X-ray PN BD+30°3639 using *SHAPE*. BD+30 emits energy across the entire electromagnetic spectrum, including X-ray, which is believed to originate from the central hot bubble. Additionally, BD+30 hosts a [WC]-type central star, which makes it an interesting target for not only comparison to other PNe, but to larger WR wind-blown bubbles. In Chapter 5 we discussed the published

multiwavelength data accumulated for the construction of our model, which included radio, IR, optical, and X-ray observations. With the addition of kinematic data from spectra, we were able to reconstruct the 3D shape of BD+30.

We compared the resulting model with previously published models and found that synthetic observations of our 3D reconstruction agree well with previous observations. The basic shape of a prolate ellipsoid was consistent with most observations, but we required that the ellipsoid be elongated along the major axis, as revealed by high velocity outflows seen in the [O III] emission. Previously, these outflows were modeled by Akras & Steffen (2012) with a separate cylindrical velocity component in addition to the assumed homologous expansion law. We were able to fit the outflows without the need for this additional component, and such a morphology matches well with the shape and kinematics of the nebula across the spectrum. Additionally, we were able to model the molecular CO bullets associated with the nebula, and using the kinematic data we were able to model their position in reference to the nebula and the central star. The bullets appear to lie along an axis at an inclination of 45°, and have had an impact on the surrounding H_2, as made apparent from the reconstruction. We believe that these CO bullets, based on their distance from the central star and their interaction with the H_2 torus, were launched by a jet earlier in the life of BD+30's central star, possibly during its AGB phase while it was still a binary.

This model represents the most complete 3D model of a PN to date, and includes the first 3D modeling of X-ray emission using *SHAPE*. By comparing this model with other, older PNe, we were able to investigate how BD+30 will likely evolve and suggest a common evolutionary path between different PNe. Both NGC 7027 and BD+30 show evidence for some sort of energetic mass loss event, possibly by way of jets, which result in a sort of multipolar structure. NGC 6720 and NGC 3132 are ellipsoidal nebulae that share a similar ring-like structure in the optical as BD+30. NGC 40 also has polar outflows though it appears like a more spherical version of BD+30 at a higher inclination ($\sim 90°$). Both host [WR]-type central stars and diffuse X-ray emission, though NGC 40 is four times older. These two appear most closely linked and very well may be snapshots of two points along the evolutionary path of PNe with [WR]-type central stars. Being able to rotate and

alter our model to more closely resemble others has given us insight into similarities in evolutionary processes, physical parameters, and morphologies of PNe.

6.4 Future Work

Through the course of this dissertation we have gained new understanding of the X-ray emission properties of PNe, as well as insight into the multiwavelength 3D structure of BD+30. That being said, there is still more work to be done in the investigation of PNe via X-ray observations and 3D modeling.

6.4.1 Expand the ChanPlaNS Sample

The ChanPlaNS sample is mostly complete of compact PNe within $\lesssim$ 1.5 kpc of the Sun, however there are additional PNe within the solar neighborhood and beyond that we expect to detect X-ray emission from given the trends we have seen thus far. Objects such as NGC 5189 and NGC 5882 exhibit structures that are characteristic of diffuse X-ray emission, and have nebular densities above the observed cutoff limit of $\log n_e \geq 2.69$. Observations of more PNe like these and their central stars will expand our sample of X-ray emitting objects and provide better statistics, leading to answers for remaining questions:

- How does the lifetime of the hot bubble shaping phase relate to the mass of the CSPN progenitor?
- What is the relationship between diffuse X-ray emission and the final mass of the core, i.e. the WD remnant?

Currently, the X-ray detection rate of binary central stars of PNe is $\sim$ 60%, however there are PNe that display point-like emission from their central stars that are not confirmed binaries. By collecting additional data on the known binary central star systems and better observations of the central stars of PNe that exhibit point-like emission we will be able to establish trends based

on binary properties such as separation and companion type. Observations of additional PNe that exhibit highly bipolar morphologies can also lead to more X-ray point source detections and answer questions like:

- What is the relationship between binary period/separation and X-ray point source emission?
- What are the characteristics of secondaries within binaries that do exhibit X-ray emission?

6.4.2 Flesh Out the Toy Model

The current status of the toy model used for diffuse X-ray analysis is quite limited. There are several ways that we can expand upon this model to make a more robust tool for determining not only the ionized gas density, but also the morphology of the X-ray emission:

- Including ellipsoidal and bipolar shapes would result in a better test for each individual nebula's morphology, and more accurately reproduce the observed structures in the *Chandra*.
- Refining the density steps over which the fitting takes place can further constrain the density of the swept-up shell.
- Appropriately modeling the contact discontinuity will add an additional contribution to the absorption, enhancing our density fits.
- More advanced density models can be adapted for *SHAPE* and be applied to the swept-up shell, providing better estimates of the density of the ionized regions of the nebula.
- Using a variable abundance model for the X-ray absorption based on individual elements would provide better calibration of the nebular density with respect to the X-ray emission and nebular content.

6.4.3 Refine the BD+30 3D Model

Our 3D model of BD+30 represents one of the most complete models of a PN by including multiwavelength observations and data. In the time since many of the observations were originally

taken, new equipment and observing techniques have been developed which we could take advantage of to refine our model, providing a more accurate representation of the nebula. Proposing for Very Large Telescope observations using the Spectro-Polarimetric High-contrast Explanet REsearch (SPHERE) instrument will allow us to examine scattered light from dust near the central star, giving us a better look at the inner region of BD+30. There is also the matter of more recent observations of the CO bullets to measure the extent of their expansion in the past 20 years. Having additional positional data for these bullets will allow us to better determine their trajectory and thus the origin of the gas.

BD+30 represents a large class of PNe and by comparing our 3D model with these other PNe we will be able to draw connections between them. In Chapter 5 we compared BD+30 with four PNe on a basic level. Collecting published data for PNe with a wide set of physical parameters and comparing it with our BD+30 model using both the basic and physical renderer of various orientations will place better constraints on the evolutionary path of PNe of particular types and answer questions about what effect the central stellar engine has on the resulting morphology, and how that morphology appears to evolve over time.

6.4.4 Further 3D Modeling Using AstroBEAR

One of the major problems that is not only exhibited by PNe, but also by massive wind-blown bubbles, is that the temperatures of the X-ray hot bubbles are found to be lower than expected. To investigate this so-called "low temperature PN hot bubble" problem (Soker et al., 2010) we look to model the underlying mechanisms of the hot bubble by making use of the adaptive mesh refinement magnetohydrodynamics code AstroBEAR (Carroll-Nellenback et al., 2012). The capacities of the code to model wind blown bubbles in which magnetically controlled heat conduction plays a significant role make AstroBEAR a particularly useful tool for the PN X-ray problem.

This project will investigate PNe with a range of physical parameters representative of those for which we have detected diffuse X-ray emission. It is imperative to incorporate and rework the theory and models to better interpret the observations, both to improve our understanding of PNe

and to provide guidance in selecting targets for future *Chandra* and XMM observations. We expect our models to constrain the evolution of PN hot bubbles and hot bubble cooling mechanism(s) to thereby establish the specific PN kinematics and physical conditions that separate diffuse X-ray detections and nondetections.

BIBLIOGRAPHY

Acker, A., Jasniewicz, G., Koeppen, J., & Stenholm, B. 1989, A&AS, 80, 201

Akashi, M., Meiron, Y., & Soker, N. 2008, , 13, 563

Akashi, M., & Soker, N. 2013, MNRAS, 436, 1961

Akras, S., & Steffen, W. 2012, MNRAS, 423, 925

Aleman, I., et al. 2014, A&A, 566, A79

Arnaud, K., Borkowski, K. J., & Harrington, J. P. 1996, ApJL, 462, L75

Bachiller, R., Forveille, T., Huggins, P. J., Cox, P., & Maillard, J. P. 2000, A&A, 353, L5

Bachiller, R., Huggins, P. J., Cox, P., & Forveille, T. 1991, A&A, 247, 525

Bachiller, R., Huggins, P. J., Martin-Pintado, J., & Cox, P. 1992, A&A, 256, 231

Bagnulo, S., Landstreet, J. D., Fossati, L., & Kochukhov, O. 2012, A&A, 538, 22

Balick, B., & Frank, A. 2002, ARAA, 40, 439

Balick, B., Owen, R., Bignell, C. R., & Hjellming, R. M. 1987, AJ, 94, 948

Basart, J. P., & Daub, C. T. 1987, ApJ, 317, 412

Beckwith, S., Gatley, I., & Persson, S. E. 1978, ApJL, 219, L33

Bentley, A. F., Hackwell, J. A., Grasdalen, G. L., & Gehrz, R. D. 1984, ApJ, 278, 665

Bernard-Salas, J., Pottasch, S. R., Beintema, D. A., & Wesselius, P. R. 2001, A&A, 367, 949

Bernard-Salas, J., Pottasch, S. R., Wesselius, P. R., & Feibelman, W. A. 2003, A&A, 406, 165

Bernard-Salas, J., & Tielens, A. G. G. M. 2005, A&A, 431, 523

Bilíková, J., Chu, Y.-H., Gruendl, R. A., & Maddox, L. A. 2010, AJ, 140, 1433

Bilíková, J., Chu, Y.-H., Gruendl, R. A., Su, K. Y. L., & De Marco, O. 2012, ApJS, 200, 3

Bodman, E. H. L., Schaub, S. C., & Hillwig, T. 2012, JSARA, 5, 19

Boffin, H. M. J., Miszalski, B., Rauch, T., Jones, D., Corradi, R. L. M., Napiwotzki, R., Day-Jones, A. C., & Koppen, J. 2012, Science, 338, 773

Bohigas, J. 2001, RevMexAA, 37, 237

Bond, H. E., & Livio, M. 1990, ApJ, 355, 568

Bryce, M., & Mellema, G. 1999, MNRAS, 309, 731

Bryce, M., Pedlar, A., Muxlow, T., Thomasson, P., & Mellema, G. 1997, MNRAS, 284, 815

Bujarrabal, V., Castro-Carrizo, A., Alcolea, J., & Sánchez Contreras, C. 2001, A&A, 377, 868

Cahn, J. H., & Amd, S. 1978, in IAU Symposium, Vol. 76, Planetary Nebulae, ed. Y. Terzian, 3–9

Carroll-Nellenback, J., Shroyer, B., Frank, A., & Ding, C. 2012, in Astronomical Society of the Pacific Conference Series, Vol. 459, Numerical Modeling of Space Plasma Slows (ASTRONUM 2011), ed. N. V. Pogorelov, J. A. Font, E. Audit, & G. P. Zank, 291

Cassinelli, J. P., Cohen, D. H., Macfarlane, J. J., Sanders, W. T., & Welsh, B. Y. 1994, ApJ, 421, 705

Chu, Y.-H., Guerrero, M. A., & Gruendl, R. A. 2003, in IAU Symposium, Vol. 209, Planetary Nebulae: Their Evolution and Role in the Universe, ed. S. Kwok, M. Dopita, & R. Sutherland, 415

Chu, Y.-H., Guerrero, M. A., Gruendl, R. A., Williams, R. M., & Kaler, J. B. 2001, ApJL, 553, L69

Chu, Y.-H., et al. 2011, AJ, 142, 75

Clayton, G. C., De Marco, O., Nordhaus, J., Green, J., Rauch, T., Werner, K., & Chu, Y.-H. 2014, AJ, 147, 142

Clegg, R. E. S., Harrington, J. P., Barlow, M. J., & Walsh, J. R. 1987, ApJ, 314, 551

Corradi, R. L. M., Perinotto, M., Villaver, E., Mampaso, A., & Gonçalves, D. R. 1999, ApJ, 523, 721

Corradi, R. L. M., et al. 2011, MNRAS, 410, 1349

Cox, P., Huggins, P. J., Maillard, J.-P., Habart, E., Morisset, C., Bachiller, R., & Forveille, T. 2002, A&A, 384, 603

Crowther, P. A. 2007, ARAA, 45, 177

Crowther, P. A., De Marco, O., & Barlow, M. J. 1998, MNRAS, 296, 367

Crowther, P. A., Morris, P. W., & Smith, J. D. 2006, ApJ, 636, 1033

Daub, C. T. 1982, ApJ, 260, 612

De Marco, O. 2008, in Astronomical Society of the Pacific Conference Series, Vol. 391, Hydrogen-Deficient Stars, ed. A. Werner & T. Rauch, 209

De Marco, O. 2009, PASP, 121, 316

De Marco, O., Long, J., Jacoby, G. H., Hillwig, T., Kronberger, M., Howell, S. B., Reindl, N., & Margheim, S. 2015, MNRAS, 448, 3587

De Marco, O., Passy, J.-C., Frew, D. J., Moe, M., & Jacoby, G. H. 2013, MNRAS, 428, 2118

De Marco, O., Passy, J. C., Moe, M., Herwig, F., Mac Low, M. M., & Paxton, B. 2011, MNRAS, 411, 2277

De Marco, O., & Soker, N. 2002, PASP, 114, 602

Delgado-Inglada, G., & Rodríguez, M. 2014, ApJ, 784, 173

DePew, K., Parker, Q. A., Miszalski, B., De Marco, O., Frew, D. J., Acker, A., Kovacevic, A. V., & Sharp, R. G. 2011, MNRAS, 414, 2812

Douchin, D., et al. 2014, MNRAS, submitted

Drew, J. E., et al. 2014, MNRAS, 440, 2036

Dwarkadas, V. V., & Rosenberg, D. L. 2013, HEDP, 9, 226

Ercolano, B., Morisset, C., Barlow, M. J., Storey, P. J., & Liu, X. W. 2003, MNRAS, 340, 1153

Ercolano, B., Wesson, R., Zhang, Y., Barlow, M. J., De Marco, O., Rauch, T., & Liu, X.-W. 2004, MNRAS, 354, 558

Feibelman, W. A. 1998, ApJS, 119, 197

Frank, A., Balick, B., Icke, V., & Mellema, G. 1993, ApJL, 404, L25

Freeman, M., et al. 2014, ApJ, 794, 99

Freeman, P. E., Kashyap, V., Rosner, R., & Lamb, D. Q. 2002, ApJS, 138, 185

Frew, D. J. 2008, PhD thesis, Macquarie University, Department of Physics, Macquarie University, NSW 2109, Australia

Frew, D. J., Bojičić, I. S., Parker, Q. A., Pierce, M. J., Gunawardhana, M. L. P., & Reid, W. A. 2014a, MNRAS, 440, 1080

Frew, D. J., Parker, Q. A., & Bojicic, I. S. 2015, ArXiv e-prints

Frew, D. J., Parker, Q. A., & Bojičić, I. S. 2014b, MNRAS, submitted

Freyer, T., Hensler, G., & Yorke, H. W. 2003, ApJ, 594, 888

García-Díaz, M. T., Clark, D. M., López, J. A., Steffen, W., & Richer, M. G. 2009, ApJ, 699, 1633

García-Segura, G., Langer, N., & Mac Low, M. M. 1996a, A&A, 316, 133

García-Segura, G., Mac Low, M. M., & Langer, N. 1996b, A&A, 305, 229

Gehrels, N. 2004, in American Institute of Physics Conference Series, Vol. 727, Gamma-Ray Bursts: 30 Years of Discovery, ed. E. Fenimore & M. Galassi, 637–641

George, D., Hartsuijker, A. P., & Kaftan-Kassim, M. A. 1974, A&A, 35, 219

Getman, K. V., Feigelson, E. D., Broos, P. S., Townsley, L. K., & Garmire, G. P. 2010, ApJ, 708, 1760

Giacconi, R., et al. 1979, ApJ, 230, 540

Golovatyi, V. V., & Demchyna, A. V. 2014, Astronomy Reports, 58, 692

Gonçalves, D. R., Wesson, R., Morisset, C., Barlow, M., & Ercolano, B. 2012, in IAU Symposium, Vol. 283, IAU Symposium, 144–147

Gruenwald, R., & Aleman, A. 2007, A&A, 461, 1019

Guerrero, M. A. 2006, in IAU Symposium, Vol. 234, Planetary Nebulae in our Galaxy and Beyond, ed. M. J. Barlow & R. H. Méndez, 153–160

Guerrero, M. A., Chu, Y.-H., Gruendl, R. A., Williams, R. M., & Kaler, J. B. 2001, ApJ, 553, L55

Guerrero, M. A., & De Marco, O. 2013, A&A, 553, 23

Guerrero, M. A., Toalá, J. A., Medina, J. J., Luridiana, V., Miranda, L. F., Riera, A., & Velázquez, P. F. 2013, A&A, 557, 12

Gutierrez-Moreno, A., Moreno, H., & Cortes, G. 1986, PASP, 98, 488

Guzman-Ramirez, L., et al. 2015, MNRAS, 451, L1

Hajduk, M., Zijlstra, A. A., & Gesicki, K. 2010, MNRAS, 406, 626

Harrington, J. P., Lame, N. J., White, S. M., & Borkowski, K. J. 1997, AJ, 113, 2147

Herald, J. E., & Bianchi, L. 2011, MNRAS, 417, 2440

Herwig, F. 2001, , 275, 15

—. 2005, ARAA, 43, 435

Hillwig, T. C., Bond, H. E., Afşar, M., & De Marco, O. 2010, AJ, 140, 319

Hillwig, T. C., Frew, D. J., Louie, M., De Marco, O., Bond, H. E., Jones, D., & Schaub, S. C. 2015, AJ, 150, 30

Hora, J. L., Deutsch, L. K., Hoffmann, W. F., Fazio, G. G., & Shivanandan, K. 1993, ApJ, 413, 304

Hua, C. T., Dopita, M. A., & Martinis, J. 1998, A&AS, 133, 361

Huarte Espinosa, M., Frank, A., Balick, B., De Marco, O., Kastner, J. H., Sahai, R., & Blackman, E. G. 2010, ArXiv e-prints

Huckvale, L., et al. 2013, MNRAS, 434, 1505

Jacob, R., Schönberner, D., & Steffen, M. 2013, A&A, 558, A78

Jeffries, R. D., & Stevens, I. R. 1996, MNRAS, 279, 180

Jones, D., Boffin, H. M. J., Miszalski, B., Wesson, R., Corradi, R. L. M., & Tyndall, A. A. 2014a, A&A, 562, 9

Jones, D., Mitchell, D. L., Lloyd, M., Pollacco, D., O'Brien, T. J., Meaburn, J., & Vaytet, N. M. H. 2012, MNRAS, 420, 2271

Jones, D., Santander-Garcia, M., Boffin, H. M. J., et al. 2014b, in Asymmetrical Planetary Nebulae VI conference, Proceedings of the conference held 4-8 November, 2013. Edited by C. Morisset, G. Delgado-Inglada and S. Torres-Peimbert.

Jordan, S., Bagnulo, S., Werner, K., & O'Toole, S. J. 2012, A&A, 542, 4

Jordan, S., Werner, K., & O'Toole, S. J. 2005, A&A, 432, 273

Kahn, F. D., & West, K. A. 1985, MNRAS, 212, 837

Kaler, J. B. 1986, ApJ, 308, 322

Kastner, J. H. 2007, in Asymmetrical Planetary Nebulae IV, 5

Kastner, J. H., Li, J., Vrtilek, S. D., Gatley, I., Merrill, K. M., & Soker, N. 2002, ApJ, 581, 1225

Kastner, J. H., Montez, Jr., R., Balick, B., & De Marco, O. 2008, ApJ, 672, 957

Kastner, J. H., Soker, N., Vrtilek, S. D., & Dgani, R. 2000, ApJL, 545, L57

Kastner, J. H., Vrtilek, S. D., & Soker, N. 2001, ApJL, 550, L189

Kastner, J. H., Weintraub, D. A., Gately, I., Merrill, K. M., & Probst, R. G. 1996, ApJ, 462, 777

Kastner, J. H., et al. 2012, AJ, 144, 58

Keenan, F. P. 1991, , 186, 277

Koeppen, J., Acker, A., & Stenholm, B. 1991, A&A, 248, 197

Kreysing, H. C., Diesch, C., Zweigle, J., Staubert, R., Grewing, M., & Hasinger, G. 1992, A&A, 264, 623

Kwok, S., Purton, C. R., & Fitzgerald, P. M. 1978, ApJ, 219, L125

Latter, W. B., Kelly, D. M., Hora, J. L., & Deutsch, L. K. 1995, ApJS, 100, 159

Leão, I. C., de Laverny, P., Mékarnia, D., de Medeiros, J. R., & Vandame, B. 2006, A&A, 455, 187

Lee, T.-H., & Kwok, S. 2005, ApJ, 632, 340

Leone, F., Corradi, R. L. M., Martínez González, M. J., Asensio Ramos, A., & Manso Sainz, R. 2014, A&A, 563, A43

Leone, F., Martínez González, M. J., Corradi, R. L. M., Privitera, G., & Manso Sainz, R. 2011, ApJL, 731, 4

Leuenhagen, U., Hamann, W.-R., & Jeffery, C. S. 1996, A&A, 312, 167

Li, J., Harrington, J. P., & Borkowski, K. J. 2002, AJ, 123, 2676

Li, J., Kastner, J. H., Prigozhin, G. Y., Schulz, N. S., Feigelson, E. D., & Getman, K. V. 2004, ApJ, 610, 1204

López, J. A., García-Díaz, M. T., Steffen, M., Riesgo, H., & Richer, M. G. 2012, ApJ, 750, 8

Maciel, W. J., & Pottasch, S. R. 1980, A&A, 88, 1

Madejski, G. 2005, in American Institute of Physics Conference Series, Vol. 801, Astrophysical Sources of High Energy Particles and Radiation, ed. T. Bulik, B. Rudak, & G. Madejski, 21–30

Maercker, M., et al. 2012, Nature, 490, 232

Marcolino, W. L. F., Hillier, D. J., de Araujo, F. X., & Pereira, C. B. 2007, ApJ, 654, 1068

Marten, H., & Schönberner, D. 1991, A&A, 248, 590

Masson, C. R. 1989, ApJ, 346, 243

—. 1990, ApJ, 348, 580

Matsumoto, H., et al. 2008, ApJ, 677, 1120

Mayer, A., et al. 2014, A&A, 570, A113

Mendez, R. H., Herrero, A., & Manchado, A. 1990, A&A, 229, 152

Middlemass, D. 1990, MNRAS, 244, 294

Minkowski, R., & Aller, L. H. 1954, ApJ, 120, 261

Miszalski, B., Corradi, R. L. M., Boffin, H. M. J., Jones, D., Sabin, L., Santander-Garcia, M., Rodríguez-Gil, P., & Rubio-Díez, M. M. 2011, MNRAS, 413, 1264

Monet, D. G., et al. 2003, AJ, 125, 984

Monteiro, H., & Falceta-Gonçalves, D. 2011, ApJ, 738, 174

Monteiro, H., Morisset, C., Gruenwald, R., & Viegas, S. M. 2000, ApJ, 537, 853

Monteiro, H., Schwarz, H. E., Gruenwald, R., & Heathcote, S. 2004, ApJ, 609, 194

Montez, Jr., R., De Marco, O., Kastner, J. H., & Chu, Y.-H. 2010, ApJ, 721, 1820

Montez, Jr., R., & Kastner, J. H. 2013, ApJ, 766, 7

Montez, Jr., R., Kastner, J. H., Balick, B., & Frank, A. 2009, ApJ, 694, 1481

Montez, Jr., R., Kastner, J. H., De Marco, O., & Soker, N. 2005, ApJ, 635, 381

Montez, Jr., R., Kastner, J. H., Freeman, M. J., et al. 2015a, in prep.

Montez, Jr., R., et al. 2015b, ApJ, 800, 8

Morrison, R., & McCammon, D. 1983, ApJ, 270, 119

Nakashima, J.-i., Kwok, S., Zhang, Y., & Koning, N. 2010, AJ, 140, 490

Nordhaus, J., Blackman, E. G., & Frank, A. 2007, MNRAS, 376, 599

O'Dell, C. R., Ferland, G. J., Henney, W. J., & Peimbert, M. 2013, AJ, 145, 92

Osterbrock, D. E., & Ferland, G. J. 2006, Astrophysics of gaseous nebulae and active galactic nuclei

Parker, Q. A., et al. 2005, MNRAS, 362, 689

Parthasarathy, M., Acker, A., & Stenholm, B. 1998, A&A, 329, L9

Patriarchi, P., & Perinotto, M. 1991, A&A, 91, 325

Peña, M., Rechy-García, J. S., & García-Rojas, J. 2013, RevMexAA, 49, 87

Perinotto, M., Schönberner, D., Steffen, M., & Calonaci, C. 2004, A&A, 414, 993

Persi, P., Cesarsky, D., Marenzi, A. R., Preite-Martinez, A., Rouan, D., Siebenmorgen, R., Lacombe, F., & Tiphene, D. 1999, A&A, 351, 201

Peterson, B. M. 2001, in Advanced Lectures on the Starburst-AGN, ed. I. Aretxaga, D. Kunth, & R. Mújica, 3

Pfeffermann, E., et al. 1987, in Society of Photo-Optical Instrumentation Engineers (SPIE) Conference Series, Vol. 733, Soft X-ray optics and technology, 519

Phillips, J. P. 2002, ApJS, 139, 199

—. 2004a, MNRAS, 353, 589

—. 2004b, , 9, 391

—. 2005, MNRAS, 362, 847

Pierce, M. J., Frew, D. J., Parker, Q. A., & Köppen, J. 2004, , 21, 334

Planck Collaboration et al. 2015, A&A, 573, A6

Pottasch, S. R. 1980, A&A, 89, 336

Pottasch, S. R., & Bernard-Salas, J. 2010, A&A, 517, 12

Ramos-Larios, G., Guerrero, M. A., Vazquez, R., & Phillips, J. P. 2012, MNRAS, 420, 1977

—. 2013, ArXiv e-prints

Sabbadin, F., Turatto, M., Ragazzoni, R., Cappellaro, E., & Benetti, S. 2006, A&A, 451, 937

Sahai, R., Morris, M. R., & Villar, G. G. 2011, ApJ, 141, 31

Sahai, R., & Trauger, J. T. 1998, AJ, 116, 1357

Sahai, R., Wootten, A., & Clegg, R. E. S. 1990, A&A, 234, L1

Sahu, K. C., & Desai, J. N. 1986, A&A, 161, 357

Schmidt-Voigt, M., & Koppen, J. 1987, A&A, 174, 223

Schönberner, D., Jacob, R., Lehmann, H., Hildebrandt, G., Steffen, M., Zwanzig, A., Sandin, C., & Corradi, R. L. M. 2014, Astron. Nachr., 335, 378

Schönberner, D., & Steffen, M. 2003, in IAU Symposium, Vol. 209, Planetary Nebulae: Their Evolution and Role in the Universe, ed. S. Kwok, M. Dopita, & R. Sutherland, 147

Schwartz, D. A. 2004, International Journal of Modern Physics D, 13, 1239

Shimansky, V. V., Pozdnyakova, S. A., Borisov, N. V., Bikmaev, I. F., Vlasyuk, V. V., Spiridonova, O. I., Galeev, A. I., & Mel'Nikov, S. S. 2009, Astrophysical Bulletin, 64, 349

Shklovsky, I. S. 1956, Astron. Zh., 33, 222

Shupe, D. L., Larkin, J. E., Knop, R. A., Armus, L., Matthews, K., & Soifer, B. T. 1998, ApJ, 498, 267

Siebenmorgen, R., Zijlstra, A. A., & Krügel, E. 1994, MNRAS, 271, 449

Soker, N. 1994, AJ, 107, 276

—. 2004, , 9, 399

Soker, N., & Kastner, J. H. 2002, ApJ, 570, 245

Soker, N., & Livio, M. 1994, ApJ, 421, 219

Soker, N., Rahin, R., Behar, E., & Kastner, J. H. 2010, ApJ, 725, 1910

Soker, N., & Rappaport, S. 2000, ApJ, 538, 241

Stasińska, G. 2002, ArXiv Astrophysics e-prints

Steffen, M., Hubrig, S., Todt, H., Schöller, M., Hamann, W.-R., Sandin, C., & Schönberner, D. 2014, A&A, 570, A88

Steffen, M., Schönberner, D., & Warmuth, A. 2008, A&A, 489, 173

Steffen, W., Koning, N., Esquivel, A., García-Segura, G., García-Díaz, M. T., López, J. A., & Magnor, M. 2013, MNRAS, 436, 470

Steffen, W., Koning, N., Wenger, S., Morisset, C., & Magnor, M. 2011, IEEE Transactions on Visualization and Computer Graphics, Volume 17, Issue 4, p.454-465, 17, 454

Steffen, W., & López, J. A. 2006, in Revista Mexicana de Astronomia y Astrofisica Conference Series, Vol. 26, Revista Mexicana de Astronomia y Astrofisica Conference Series, 30–31

Su, K. Y. L., et al. 2007, ApJ, 657, L41

Tanaka, Y., Inoue, H., & Holt, S. S. 1994, , 46, L37

Taylor, A. R., Gussie, G. T., & Pottasch, S. R. 1990, ApJ, 351, 515

Terzian, Y. 1968, in IAU Symposium, Vol. 34, Planetary Nebulae, ed. D. E. Osterbrock & C. R. O'dell, 87

Toalá, J. A., & Arthur, S. J. 2011a, ApJ, 737, 100

Toalá, J. A., & Arthur, S. J. 2011b, in Revista Mexicana de Astronomia y Astrofisica, vol. 27, Vol. 40, Revista Mexicana de Astronomia y Astrofisica Conference Series, 185–186

—. 2014, arXiv:1407.1421

Toalá, J. A., Guerrero, M. A., Chu, Y.-H., Gruendl, R. A., Arthur, S. J., Smith, R. C., & Snowden, S. L. 2012, ApJ, 755, 77

Tocknell, J., De Marco, O., & Wardle, M. 2014, MNRAS, 439, 2014

Trümper, J., et al. 1991, Nature, 349, 579

Tylenda, R. 1996, in Astronomical Society of the Pacific Conference Series, Vol. 96, Hydrogen Deficient Stars, ed. C. S. Jeffery & U. Heber, 101

Ueta, T., et al. 2014, A&A, 565, A36

van der Hucht, K. A., Conti, P. S., Lundstrom, I., & Stenholm, B. 1981, , 28, 227

van Hoof, P. A. M., et al. 2010, A&A, 518, L137

van Hoof, P. A. M., et al. 2012, in IAU Symposium, Vol. 283, IAU Symposium, 41–44

Vázquez, R., Miranda, L. F., Torrelles, J. M., Olguín, L., Benítez, G., Rodríguez, L. F., & López, J. A. 2002, ApJ, 576, 860

Villaver, E., Manchado, A., & García-Segura, G. 2002, ApJ, 581, 1204

Vlemmings, W. H. T. 2007, in IAU Symposium, Vol. 242, IAU Symposium, ed. J. M. Chapman & W. A. Baan, 37–46

Waters, L. B. F. M., et al. 1998, A&A, 331, L61

Weaver, R., McCray, R., Castor, J., Shapiro, P., & Moore, R. 1977, ApJ, 218, 377

Webster, B. L., Payne, P. W., Storey, J. W. V., & Dopita, M. A. 1988, MNRAS, 235, 533

Weidmann, W. A., Gamen, R., van Hoof, P. A. M., Zijlstra, A., Minniti, D., & Volpe, M. G. 2013, A&A, 552, A74

Whitelock, P. A. 1985, MNRAS, 213, 59

Wrigge, M. 1999, A&A, 343, 599

Wrigge, M., Chu, Y.-H., Magnier, E. A., & Wendker, H. J. 2005, ApJ, 633, 248

Wrigge, M., & Wendker, H. J. 1996, in Roentgenstrahlung from the Universe, ed. H. U. Zimmermann, J. Trümper, & H. Yorke, 287–288

Wrigge, M., Wendker, H. J., & Wisotzki, L. 1994, A&A, 286, 219

Yu, Y. S., Nordon, R., Kastner, J. H., Houck, J., Behar, E., & Soker, N. 2009, ApJ, 690, 440

Zhang, C. Y. 1995, ApJS, 98, 659

Zhang, Y., Liu, X.-W., Wesson, R., Storey, P. J., Liu, Y., & Danziger, I. J. 2004, MNRAS, 351, 935

Zhekov, S. A. 2014, MNRAS, 443, 12

Zhekov, S. A., & Park, S. 2011, ApJ, 728, 135

Zijlstra, A. 2015, ArXiv e-prints

Zuckerman, B., & Gatley, I. 1988, ApJ, 324, 501